INDIRECT NEUTRON-CAPTURE CROSS SECTIONS FOR THE WEAK R-PROCESS

By

Rebecca L. Lewis

A DISSERTATION

Submitted to
Michigan State University
in partial fulfillment of the requirements
for the degree of

Chemistry — Doctor of Philosophy

2019

ABSTRACT

INDIRECT NEUTRON-CAPTURE CROSS SECTIONS FOR THE WEAK R-PROCESS

By

Rebecca L. Lewis

Understanding the production of the heaviest elements requires a wealth of information on the nuclear properties of short-lived nuclei. The rapid neutron capture process (r-process) is responsible for the majority of the production of the heaviest elements. The r-process utilizes neutron-capture reactions on heavy, neutron-rich nuclei. The nuclei involved in the r-process are very neutron-rich, short-lived, and very difficult to produce, so little information is known about them. The lack of directly measured neutron-capture cross sections has led to the development of indirect techniques that can be used to reduce the uncertainty in the neutron-capture cross sections, which can vary by orders of magnitude between different calculations. The β-Oslo method is one indirect technique which aims to reduce the uncertainty in the two statistical properties of the nucleus that contribute the largest sources of uncertainty in the r-process calculations: the nuclear level density (NLD) and γ-ray strength function (γSF). Both are required to calculate a neutron-capture cross section in the Hauser-Feshbach statistical framework, along with the neutron optical model. The β-Oslo method utilizes β decay to populate high-energy excited states in the same nucleus that would have been formed in the neutron-capture reaction of interest. The γ rays from the de-excitation are observed in the Summing NaI (SuN) detector to determine the total excitation energy of the nucleus as well as the γ-ray cascade to the ground state. With this information, the NLD and γSF can be extracted, after normalization to other data or theoretical calculations. With experimentally constrained NLD and γSF, the overall uncertainty of a neutron-capture cross section has been showed to be significantly reduced.

The neutron-capture cross sections of four neutron-rich nuclei (^{73}Zn, ^{70,71,72}Ni) were experimentally constrained using the β-Oslo method. The ^{73}Zn$(n,\gamma)^{74}$Zn data was also used to compare the constrained neutron-capture cross sections obtained from three different Hauser-Feshbach codes to determine additional sources of systematic uncertainty. The three Ni reactions were also compared to the ^{68,69}Ni cross sections that were previously constrained using the β-Oslo method.

To my nuclear family, in every sense of the term. Thank you for everything.

ACKNOWLEDGMENTS

Let's make this easy–thank you to everyone! It has taken what feels like a million people to get me to this point, and I really appreciate every one of you. I have had incredible friends and mentors everywhere I've been, from Northeastern to Michigan State, but also at Oak Ridge National Laboratory, Massachusetts General Hospital, the Nuclear Chemistry Summer School, and Los Alamos National Laboratory.

Of course, the mentor who has put up with me the longest is my advisor, Sean Liddick. Five years is a long time to listen to my terrible jokes and watch me do math wrong every time I try, and I really appreciate (and admire) your patience. I think I've gotten involved in almost every kind of science that is happening at the lab while working with you, which really helped me decide what I wanted to do after graduate school. Thank you for helping me make the time to do the other things I love as well, especially outreach.

Thank you to my committee: Dave Morrissey, Paul Mantica, and Artemis Spyrou. I didn't just see you once a year to update you on my progress—instead, I was able to talk to any one of you whenever I needed help or advice. I would also like to acknowledge the wonderful support and approachability of all of the faculty and staff that I've reached out to at the NSCL. I always felt like I could ask anyone a question, and I've become more confident in my ability to solve problems because I could rely on support from the whole lab.

I can't forget the beta group members, past and present, who helped me learn the ropes and let me tag along to experiments until I figured out what I was doing. And especially to Katie Childers, Ben Crider, and Andrea Richard—we had way more fun than we should have, but I have also learned more than I could ever image from working with you. Thank you Katie for letting me talk about everything going on. Ben, your support and encouragement

got me through some difficult projects. And Andrea, you are always ready to help me solve problems or just stand behind me while I run codes in a panic.

The other graduate students and the postdocs at the NSCL have been amazing, and I've made some of my closest friends while I've been here, especially Krystin Stiefel, Kalee Fenker, Amy Lovell, Wei Jia Ong, and Stephanie Lyons. I have to thank Amy and Wei Jia for your support, weekend breaks, knitting parties, and dinner together. I'm always excited to spend time with both of you! Kalee, thank you for answering questions whenever I had them and always being ready for a Wine Night or coffee adventure. And Krystin, you survived with me for over four years in the same office, which is amazing. Thank you for ignoring all the times I threatened my computer and for helping me turn our office into a safe place to cry, laugh, and just take a break from everything. Stephanie, I could never thank you enough for putting up with me while setting up my experiment. I know that I couldn't have done it without you, and you haven't stopped helping me in every way you can since.

The people who have supported me the most (and put up with me for the longest) are my family. Amanda, it's a good thing I like you because having my little sister doing the same science as me, and being better at it, would be terrible otherwise. I'm extraordinarily proud of you for finding what you love and learning everything about it, and proud of me for finding it first so I can always say that you followed me. You've stepped up to help me more times than I can remember, and I'll always be there to help you back. Mom and Dad—I've discovered so many amazing things because you've always encouraged me to try new things and take risks, even when I didn't want to. Thank you for making me get out of the car over and over again. I always know that you're proud of me, and I'm always excited to share my accomplishments with you because I know you'll be just as excited. I love you!

TABLE OF CONTENTS

LIST OF TABLES

LIST OF FIGURES

Chapter 1

Introduction

1.1 Production of heavy elements

There are many pathways to the creation of the elements that we see in the universe. Fusion of light nuclei can explain how everything up to iron is produced, but that process stalls for heavier elements as fusion is no longer energetically favorable. To move beyond iron there needs to be another pathway, one that isn't hindered by the large Coulomb barrier that exists between charged particles. Neutron capture processes are the solution. The addition of a neutron to a heavy nucleus is generally easier than adding a charged particle, so the production of the majority of the elements above iron proceeds by neutron capture reactions. There are two main processes for neutron capture in the universe–the slow neutron capture process (s-process), and the rapid neutron capture process (r-process). As the names imply, the difference between the two is the timescale on which neutrons are captured by the heavy nuclei. In the s-process, the neutron density is low and the average time between neutron captures is longer than the β-decay half-life of the nuclei involved, so they will undergo β decay before capturing another neutron. This keeps the isotopes produced by the s-process close to stability. In the r-process the neutron density is much higher which leads to a higher rate of neutron captures. Nuclei will therefore capture many neutrons before β decaying, leading to the production of isotopes very far from stability. When the neutron density

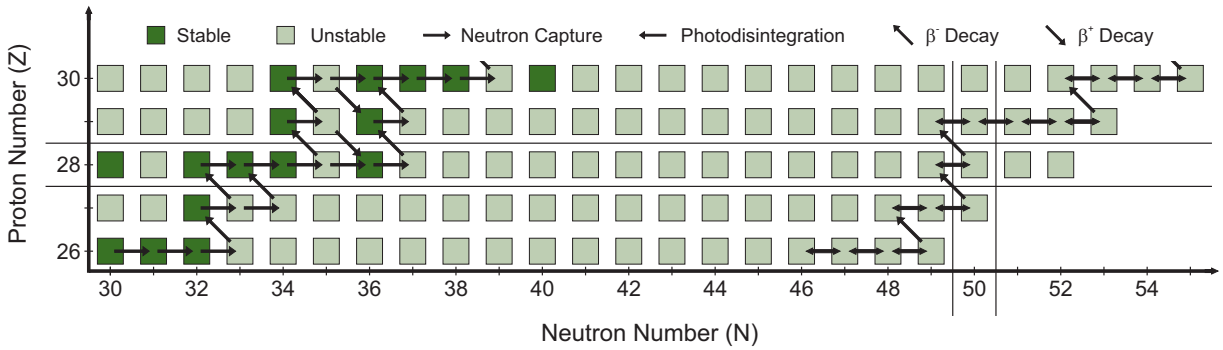

Figure 1.1: Section of the nuclear chart in the Ni region with the known s-process pathway [1] in the upper left, near stability. A representative r-process pathway has been added to the very neutron-rich region, though the exact pathway is unknown.

drops, the very neutron-rich nuclei will β decay back to stability. The relative locations of the s-process and r-process in the Ni region can be seen in Fig. 1.1. The r-process path is only approximate due to the uncertainty of the properties of these very exotic nuclei and the uncertainty in the astrophysical conditions in which the process could occur.

1.2 The r-process

Most of the observed solar abundances of nuclei are thought to be produced in a combination of both the s-process and the r-process. The s-process is easier to model, as the stability or near-stability of the nuclei involved means that there are many direct measurements of the nuclear properties required for the models, such as masses, β-decay half-lives, and neutron-capture cross sections. The astrophysical conditions are also generally known. The solar r-process abundance pattern can be deduced by subtracting the s-process contribution from the total observed abundance pattern. The resulting r-process residual abundance pattern has three peaks around A=80, 130, and 195, which correspond to the neutron shell closures encountered by the very neutron-rich nuclei involved in the r-process.

The astrophysical location of the r-process is of great interest because it helps define astrophysical conditions. Many locations have been proposed, with supernova and neutron star mergers emerging as the leading candidates (e.g. see reviews [2, 3]). The rate of occurrence of supernova events in the universe seems to be consistent with the abundance of r-process nuclei observed, but modeling such events in multiple dimensions is difficult and does not always result in the ejection of products into the universe [3]. Neutron star mergers, which would supply the high density of neutrons needed for an r-process, were until recently considered less likely than supernova due to their expected low rate of events and longer evolution time.

The recent observation of the neutron star merger GW170718 [4] was the first confirmation of an r-process location. The light curves detected from the kilonova after the merger were consistent with the production of lanthanide elements [5, 6], indicating that an r-process had taken place in the merger as the light curves matched those predicted in an event in which lanthanides would be produced [7]. This exciting observation has not solved the whole mystery of the r-process, however. There is still much to learn about the astrophysical conditions that do (or do not) support an r-process, and the situation is made more complicated when the large mass range of nuclei produced is considered. Observations of a number of r-process-rich stars show a difference between heavy and light r-process elements [2], which has led to the development of the weak r-process to describe the production of the lighter r-process elements.

1.2.1 Weak r-process

The stellar observations shown in Fig. 1.2 highlight the difference between light and heavy r-process abundances. In panel (a), the residual solar s-process elemental abundance pattern,

represented by the blue lines, is compared to observations from different stars (the lines and data sets have been offset for clarity) [2]. The difference between each data set and the solar r-process residual abundance pattern is plotted in panel (b). The scatter in the difference is large for the lightest elements (Z<50) but not for the heavier elements. The scatter is evident for the lighter elements even when all of the data sets are averaged together, as can be seen in panel (c) with the difference between the average of the observational data sets and the solar system residual r-process abundance pattern. This indicates that there is a separate process responsible for at least some of the production of these lighter elements, which has been investigated as a result of high and low frequency supernovae events (e.g. Refs. [8, 9, 10, 11]), as well as in site-independent scenarios [12]. The best way to narrow down the set of likely astrophysical conditions to determine the exact set required to produce the observed abundance pattern would be to model many different conditions and compare the calculated abundances to the observed abundances. That process is made extremely difficult due to the large uncertainties in the nuclear physics inputs that are needed for the calculations, such as masses, β-decay half-lives, and neutron capture rates.

1.3 Nuclear physics uncertainties

The impact of uncertainties in nuclear physics inputs on calculated abundance patterns has been studied in detail for the heavy (main) r-process elements using Monte Carlo simulations [13]. The masses, β-decay half-lives, and neutron capture cross sections over a large mass range were varied using a probability distribution based on estimates of their theoretical uncertainties, with a new r-process abundance pattern generated each time a value was changed. The uncertainty in the abundance pattern calculated using three different mass

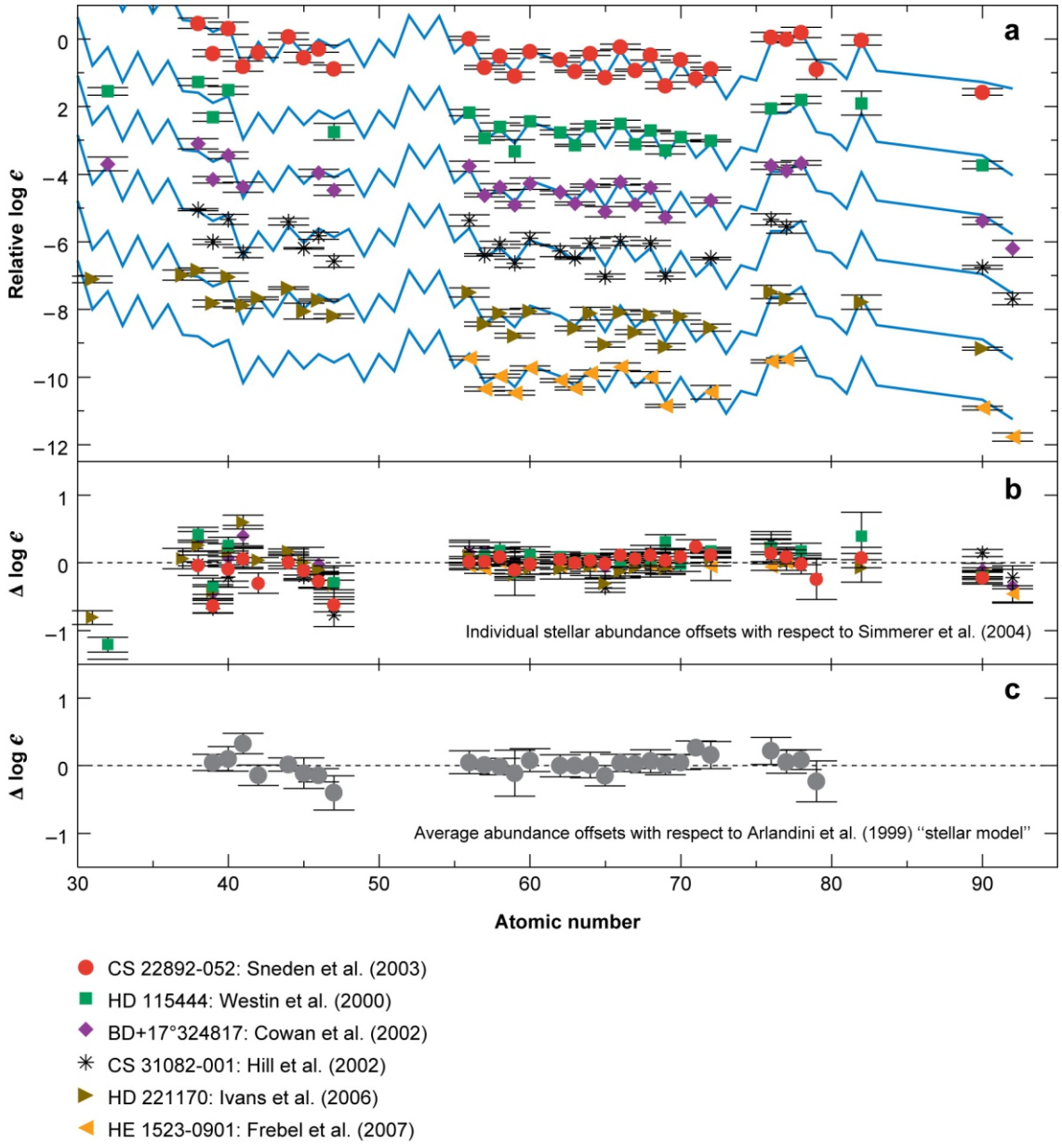

Figure 1.2: (a) Solar residual r-process abundance pattern (blue lines, shifted vertically for clarity) compared to observed r-process abundances in six r-process-rich stars (also shifted for clarity). (b) Difference between observed abundance and solar r-process abundance for each star. (c) Difference between average of all six stars and the solar r-process abundance. Republished with permission of Annual Reviews from [2]; permission conveyed through Copyright Clearance Center, Inc.

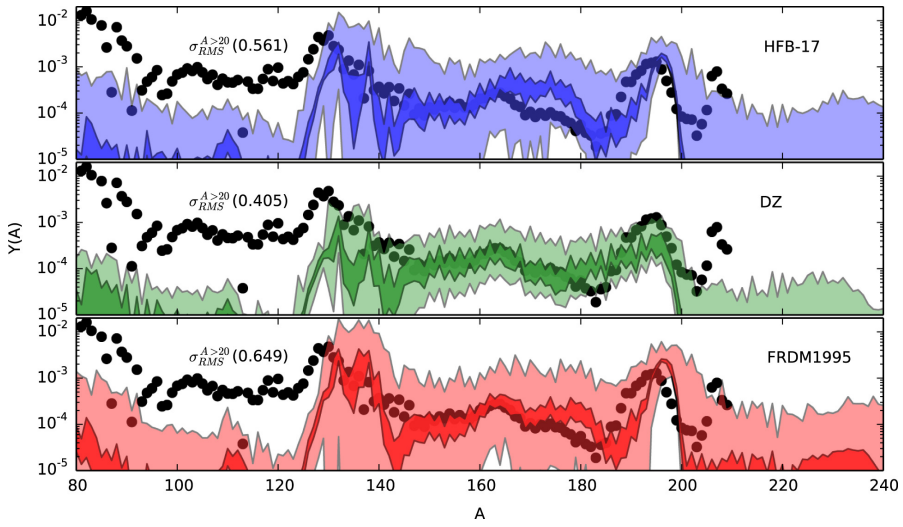

Figure 1.3: Solar r-process abundance pattern (black dots) compared to r-process abundance pattern calculated using three different mass models (model indicated in each panel). The lighter bands indicate the uncertainty in the calculated abundances with the rms error of the mass model compared to known masses. The darker bands indicate the uncertainty when the rms error is reduced to 100 keV. Reprinted from [13] with permission from Elsevier.

models (Fig. 1.3) can be very large, especially when considering the current experimental uncertainty of approximately 500 keV rms compared to known masses (light band). Even when artificially reducing the rms error to 100 keV (dark band), the uncertainty in the calculated abundance pattern remains large in areas, making it difficult to determine which mass model best fits the solar abundance pattern. The situation is similar when considering the current uncertainties in β decay half-lives (estimated to be a factor of $\sim$10) and neutron capture rates (estimated to be a factor of $\sim$1000), which can be seen in Fig. 1.4. Reducing the uncertainties in the nuclear physics inputs is the only way to differentiate between calculations run with different astrophysical conditions.

For weak r-process nuclei, the only detailed study on the impact of uncertain nuclear physics data is a recent sensitivity study focusing on neutron capture rates [14]. The study considered a number of astrophysical conditions that produced a weak r-process. The first set of mass fractions, calculated using reaction rate values from JINA REACLIB v1.0 [15],

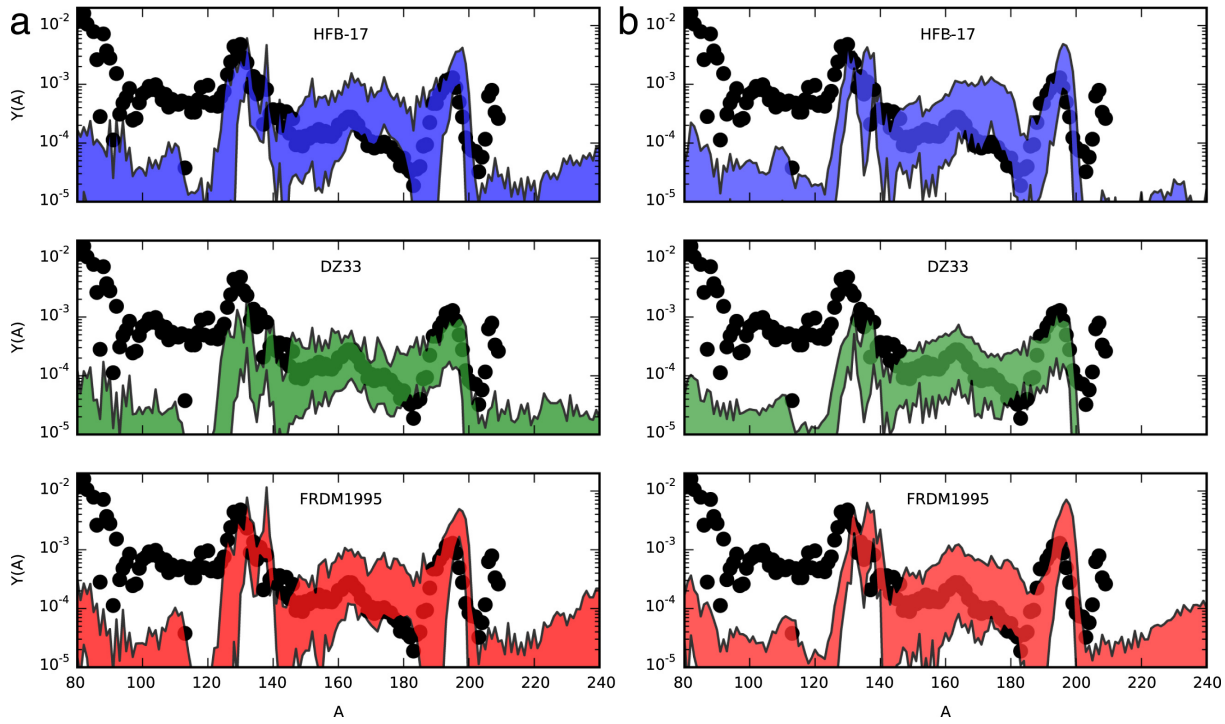

Figure 1.4: (a) Uncertainty in calculated abundance pattern for three different mass models (model indicated in panel, same as in Fig. 1.3) when considering the uncertainty in β-decay half-lives. (b) Same as (a) but considering the uncertainty in neutron-capture rates instead of β-decay half-lives. Reprinted from [13] with permission from Elsevier.

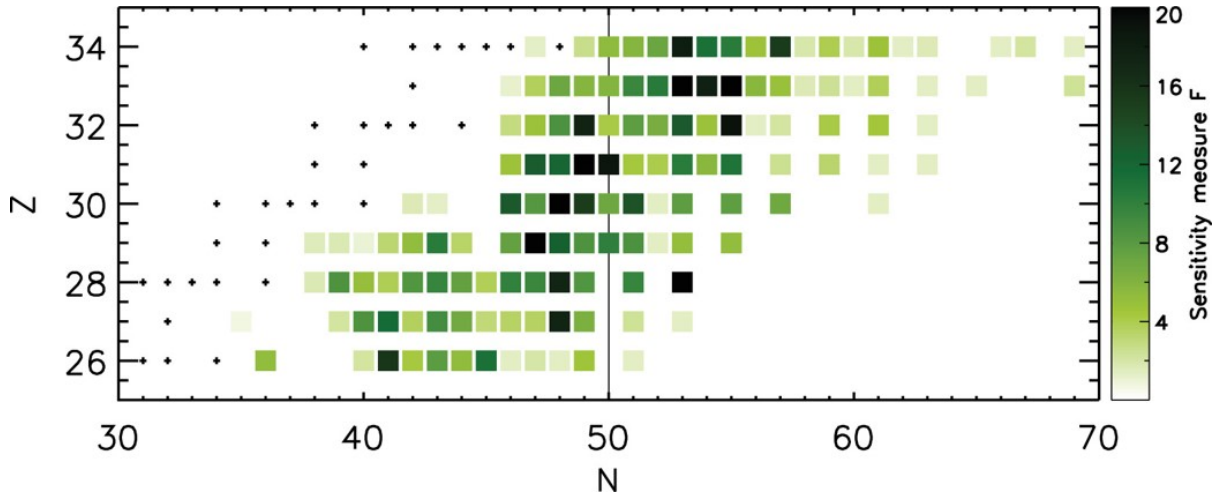

Figure 1.5: Sensitivity study from Ref. [14] of the impact of uncertain neutron capture rates on the calculated abundances for a weak r-process. Used in accordance with the Creative Commons Attribution (CC BY) license.

were set as the baseline [$X_{baseline}$(A)]. Then the neutron-capture rates of ≈300 nuclei were varied, individually, by a factor of 100. The resulting mass fractions [$X(A)$] were compared to their corresponding baseline values, and a sensitivity factor F was calculated, where

$$F = 100 \times \sum_{A} |X(A) - X_{baseline}(A)|. \tag{1.1}$$

The maximum F value over 55 sets of astrophysical conditions is shown in Fig. 1.5. The color gradient indicates the value of F, with white boxes indicating nuclei that did not have an F value greater than 0.5 for more than one set of conditions. Many nuclei have large values of F, confirming that large uncertainties in neutron capture rates also effects the abundances calculated for weak r-process nuclei, as was seen as in the heavier r-process nuclei. Reducing the uncertainties of nuclei with large F values in Fig. 1.5 is a good first step to determine what astrophysical conditions are needed to produce a weak r-process. The nuclei in this work have various F factors: ^{73}Zn has a value of 2, while ^{70,71,72}Ni have values of 9, 10, and 8, respectively.

The neutron capture rates do not have a large impact on the final abundances when the temperature is high because the neutron capture is in equilibrium with photodisintigration. When the temperature decreases, or if it never gets high enough, that equilibrium is not reached and the capture rates become very important for understanding the final abundance pattern.

The most straightforward way to reduce the uncertainty in a neutron capture rate is to directly measure the cross section. To do so generally requires a target of the nucleus of interest, which is not possible when considering the very short half-lives of nuclei involved in the weak r-process (seconds or less). Similarly, the short half-life of the neutron makes a neutron target extremely challenging. Therefore, indirect methods are required to place experimental constraints on the neutron-capture cross sections (for a review of the recent developments in indirect methods for neutron-capture cross sections, see Ref. [16]). Many of these methods rely on the Hauser-Feshbach model of neutron capture to calculate the cross section and reaction rate using statistical information about the nuclei involved, which can be constrained using experimental information.

1.4 Hauser-Feshbach model of neutron capture

When directly measuring a neutron-capture cross section is not possible, calculations are used. The Hauser-Feshbach model of neutron capture utilizes information about the reaction between the target nucleus and neutron (contained in the neutron optical model) and statistical information about the nucleus formed after the reaction between the target nucleus and the neutron–the nuclear level density (NLD) and γ-ray strength function (γSF). Hauser-Feshbach calculations provide a straightfoward way to determine the cross section

for large numbers of neutron-rich nuclei. The required statistical information, however, can have large uncertainties, which can lead to large uncertainties in the calculated cross sections. When possible, it is important to determine the NLD and γSF using experimental methods to constrain the needed inputs. Unfortunately, placing experimental constraints on the NLD and γSF is currently possible only for select regions of the r-process and weak r-process due to the difficulty in producing the desired nuclei at experimental facilities. For the majority of the nuclei involved in both processes, theoretical models of the NLD and γSF are the only viable method for calculating neutron-capture cross sections, so the large uncertainties away from stability are unavoidable. As more experimental information becomes available, even if it is just only a small subset of nuclei, both the NLD and γSF modeling can be improved to better represent these properties in regions where experimental data is not available, which will reduce uncertainties over the whole region involved.

1.4.1 Optical model

The neutron optical model describes the interaction between the target nucleus and the incoming neutron and has a long history. The target nucleus is assumed to be a uniform black body and the interaction between the target and neutron is modelled with a single interaction potential. In general, a spherical optical model potential (OMP) is used for r-process nuclei. The impact of including deformation has been found to have an minor impact, on the order of 10%, which is smaller than the other sources of uncertainty when calculating a neutron-capture cross section [17]. The standard OMP is that of Koning and Delaroche [18], where the parameters are determined through experimental scattering data when it is available. When not available, a global paramaterization is used. A semi-microscopic optical model, the Jeukenne-Lejeune-Mahaux (JLM) model [19] is also commonly used, and

generally results in a neutron-capture cross section that is within 20% of that obtained with the Koning-Delaroche model. For the nuclei in this work, the Koning and Delaroche OMP was used with global parameterizations. When considering nuclei far from the neutron drip line, the uncertainty in the neutron OMP is the smallest source of overall uncertainty in a Hauser-Feshbach calculation. Instead, the NLD and γSF provide the majority of the uncertainty in the final cross section calculation.

1.4.2 NLD models

The NLD also has a long history. The NLD function, ρ, represents the number of levels per unit energy, and can be described as a function of excitation energy (E_x), spin (J), and parity (π):

$$\rho(E_x, J, \pi) = N(E_x, J, \pi)/\Delta E_x, \tag{1.2}$$

where N is the number of levels of the specified spin and parity within the energy range ΔE_x. A total NLD can be produced by a summation over all spins and both parities, but converting from a spin- and parity-dependent NLD to a total NLD requires information about the distributions of both spin and parity in a given nucleus. This is particularly important when an experiment only populates a subset of levels and thus needs to be corrected to obtain a total NLD. An equal parity distribution is usually assumed, which has been shown to be valid [20], especially for heavy nuclei. The parity distribution of lighter nuclei, and those around shell closures, is less certain. The spin distribution is more complicated, as it is dependent on both the spin and excitation energy [21]. An average overall distribution function for the dependence of nuclear spin on excitation energy has been written as:

$$s(E_x, J) \simeq \frac{2J+1}{2\sigma^2(E_x)} e^{-\frac{(J+1/2)^2}{2\sigma^2(E_x)}}. \tag{1.3}$$

where $\sigma^2(E_x)$ is the so-called spin cut-off parameter. The above approximation is good for J below 30 [20]. By fitting a set of 310 nuclei and including only levels with experimental spin assignments, von Egidy and Bucurescu determined a structure-independent paramaterization of σ^2 [22]:

$$\sigma^2(E_x) = 0.391 A^{0.675}(E - 0.5Pa')^{0.312}, \tag{1.4}$$

where Pa' is the deuteron pairing energy, which can be calculated using mass excess values $M(A, Z)$ for a given nucleus with Z,A as:

$$Pa' = \frac{1}{2}[M(A+2, Z+1) - 2M(A, Z) + M(A-2, Z-1)]. \tag{1.5}$$

The nuclei used in the fit were either stable or very close to stability. An example of the difference in the spin distribution as the excitation energy changes can be seen in Fig. 1.6. At lower excitation energies the distribution strongly favors low spins, as is usually seen in experimentally determined spins at low energy. As the excitation energy increases the distribution shifts to higher spins. While this general trend is likely to hold, the shape of the spin distribution is not well known far from stability.

The Fermi Gas (FG) model is a well-known model for the NLD. Nucleons, which are fermions, must obey the Pauli exclusion principle, which requires each nucleon to have a unique set of quantum numbers. In the lowest energy configuration, the ground state, the nucleons fill up the lowest energy single-particle states. As excitation energy is added, nucleons are promoted to higher single-particle states, which determine the excited states

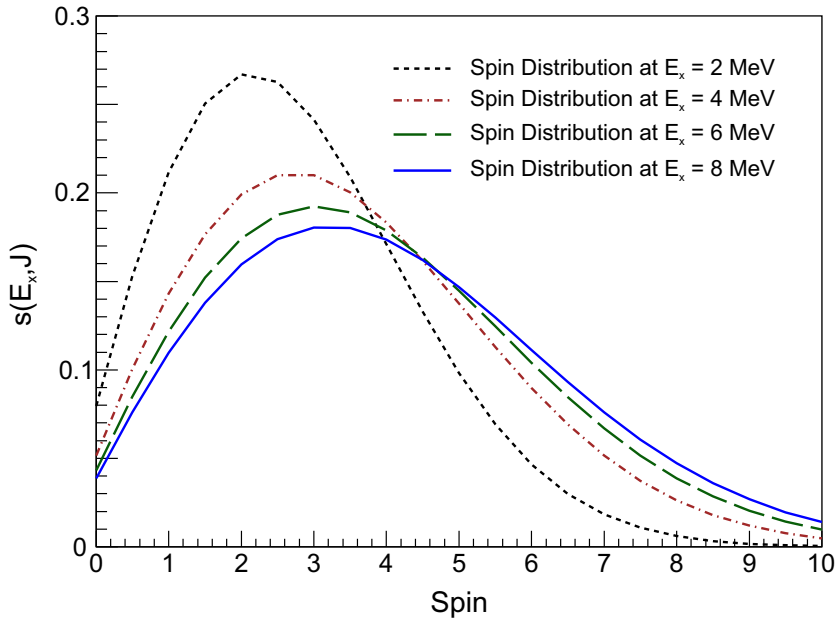

Figure 1.6: Spin distributions for different excitation energies from Eq. 1.3 using values for ^{74}Zn.

available to the nucleus. With only a small amount of excess energy, there are very few ways to promote the nucleons, and therefore very few levels per unit energy. With increasing energy added to the system, there are more configurations available and the density of levels per unit energy increases. This simple description was utilized by Bethe in 1937 to obtain an energy-dependent function for the level density [23]:

$$\rho(E_x) = \frac{\pi e^{2\sqrt{aE_x}}}{12a^{1/2}E_x^{5/4}}, \tag{1.6}$$

where E_x is the excitation energy of the nucleus and a is the level density parameter. a can be calculated using the spacing between the single particle states for protons and neutrons but is normally determined from experimental NLD information when it is available. Global systematics are used to determine values of a when it can't be derived from a known NLD. More recent determinations of a have included an energy dependence that account for the

energy-dependent shell effects that are not assumed in the simple description outlined above [24].

The assumption that nucleons do not interact within a nucleus is not correct, which has led to a modification of the FG model. The Back-shifted Fermi Gas (BSFG) model incorporates the effect of nucleon interactions with a shift parameter Δ, which takes into account the separation energy of a pair of nucleons that must be overcome before one can be promoted individually [25, 26]. The simple incorporation of Δ does not significantly alter the FG level density formula:

$$\rho(E_x) = \frac{\pi e^{2\sqrt{a(E_x-\Delta)}}}{12a^{1/2}(E_x-\Delta)^{5/4}}. \tag{1.7}$$

While Δ can be calculated as the pairing energy for neutrons and protons [27], both it and a can also be used as adjustable parameters to reproduce an observed NLD [24].

The FG and BSFG models do not reproduce the NLD at low excitation energies as well as they do at high excitation energies (above 5-10 MeV) [27]. On the other hand, the Constant Temperature (CT) model [21] describes the known low energy NLD for many nuclei, with the simple equation

$$\rho(E_x) = \frac{1}{T}e^{(E_x-E_0)/T}, \tag{1.8}$$

where E_0 and T are free parameters found through fitting experimental data. It has become common to use the CT model at lower excitation energies and connect it to the BSFG model to describe higher excitation energies (this is one of the methods available for the NLD in the RIPL-3 database [28], for example). The two models are connected at a matching energy, which is usually between 10-15 MeV for nuclei near stability [24]. For nuclei with incomplete

low-energy level schemes, the matching energy can be set to 0 MeV and only the BSFG model is used to describe the NLD [24].

The models described above fit well to experimental data, but they are not based on detailed structural information that would allow extrapolation far from stability where there is no experimental data. Microscopic level densities provide the best predictive power, but the computational challenges that arise when calculating mid- to large-mass nuclei have limited their application at present. The RIPL-3 database contains level densities calculated by Goriely et al. on a Hartree-Fock (HF) basis [29] for energies up to 150 MeV and spin values up to J=30. More recently, a combined Hartree-Fock-Bogolyubov (HFB) and combinatorial method [30] provides both spin- and parity-dependent level densities. A temperature-dependent version has also been published [31]. The fit to experimental data far from stability is hard to determine, due to the lack of data to compare to.

1.4.3 γSF models

The γ-ray transmission coefficient, $\mathcal{T}(E_\gamma)$, represents the average probability of a γ-ray escaping the volume of the nucleus, and is related to the γSF, $f(E_\gamma)$ through the expression

$$\mathcal{T}_{XL}(E_\gamma) = 2\pi E_\gamma^{(2L+1)} f_{XL}(E_\gamma), \tag{1.9}$$

where X is the electromagnetic character (electric E, or magnetic, M) and L is the multipolarity. Both $\mathcal{T}(E_\gamma)$ and $f(E_\gamma)$ describe the average properties of excited states, and are related as well to the reverse photoabsorption process. The photoabsorption strength can

be written as the average photoabsorption cross section $\langle\sigma_{XL}(E_\gamma)\rangle$:

$$\overrightarrow{f}_{XL}(E_f, J_f, \pi_f, E_\gamma) = \frac{1}{(2L+1)(\pi\hbar c)^2}\frac{\langle\sigma_{XL}(E_f, J_f, \pi_f, E_\gamma)\rangle}{E_\gamma^{(2L+1)}}, \tag{1.10}$$

where E_f is the final energy after the absorption and J_f and π_f are the spin and parity of the excited states at that energy. The shape of the photoabsorption cross section can be assumed, through the generalized Brink hypothesis [32, 33], to be independent of the energy at which the system starts, meaning the shape of the photoabsorption cross section on an excited state is the same as on the ground state. The "upward" strength function $\overrightarrow{f}_{XL}(E_f, J_f, \pi_f, E_\gamma)$, can be used to describe the "downward" strength function as well according to the principles of detailed balance. The γSF can be defined in a general way with the average partial radiative widths $\langle\Gamma_{XL}(E_i, J_i, \pi_i, E_\gamma)\rangle$ [34],

$$\overleftarrow{f}_{XL}(E_i, J_i, \pi_i, E_\gamma) = \frac{\langle\Gamma_{XL}(E_i, J_i, \pi_i, E_\gamma)\rangle\rho(E_i, J_i, \pi_i)}{E_\gamma^{(2L+1)}} \tag{1.11}$$

where E_i is the initial excitation energy bin of levels with spin J_i and parity π_i, and a level density of $\rho(E_i, J_i, \pi_i)$. The connection between the γSF and the photoabsorption cross section has allowed the γSF to be described as a low-energy extension of the Giant Dipole Resonance (GDR), a well-studied feature of the photoabsorption cross section of stable nuclei seen at high excitation energies (around 15-20 MeV). There is generally more data on the GDR shape than on the low-energy γSF shape, so models of the γSF have utilized the connection. This relationship also allows for a connection between the γSF and the lifetime of a state to be made–a small γSF value has a small partial width, which indicates a longer lifetime for that state, and vice versa.

The Standard Lorentzian (SLO) shape fits the GDR very well, so it has been used to represent the γSF in many cases. The SLO function was developed by Brink and Axel [32, 33] and is characterized by the strength (σ_{XL}), energy (E_{XL}), and width (Γ_{XL}) of the giant resonance:

$$f_{XL}(E_\gamma) = K_{XL}\frac{\sigma_{XL}E_\gamma\Gamma_{XL}^2}{(E_\gamma^2 - E_{XL}^2)^2 + E_\gamma^2\Gamma_{XL}^2}, \tag{1.12}$$

where the constant K_{XL} is:

$$K_{XL} = \frac{1}{(2L+1)\pi^2\hbar^2c^2}. \tag{1.13}$$

This shape has been used extensively for E1 radiation as well as M1 and E2, and even higher multipolarities when needed. E1 radiation is by far the most commonly used for the γSF due to the prevalence of the GDR across the nuclear chart. Currently, the SLO function is usually reserved for M1 and E2 radiation, as the Generalized Lorentzian (GLO) shape has been found to better represent the E1 shape [35].

The GLO function is based on the SLO function, but with a temperature-dependent limit that is non-zero for the lowest γ-ray energies. It was developed by Kopecky and Uhl [35] in response to the realization that the low-energy shape of the γSF can impact a neutron-capture cross section calculation (e.g. see Ref. [36]). The GLO form differs most significantly at low γ-ray energies (shown in Fig. 1.7, parameters detailed in Table 1.1), where data is more limited, but the change in shape was enough to bring calculated neutron-capture cross sections into agreement with measured values. The GLO is also described by the strength (σ_{E1}), energy (E_{E1}), and width (Γ_{E1}) of the giant resonance, and has the form:

$$f_{E1}(E_\gamma, T) = K_{E1}\Big(\frac{E_\gamma\tilde{\Gamma}_{E1}(E_\gamma)}{(E_\gamma^2 - E_{E1}^2)^2 + E_\gamma^2\tilde{\Gamma}_{E1}(E_\gamma)^2} + \frac{0.7\Gamma_{E1}4\pi^2T^2}{E_{E3}^3}\Big)\sigma_{E1}\Gamma_{E1}, \tag{1.14}$$

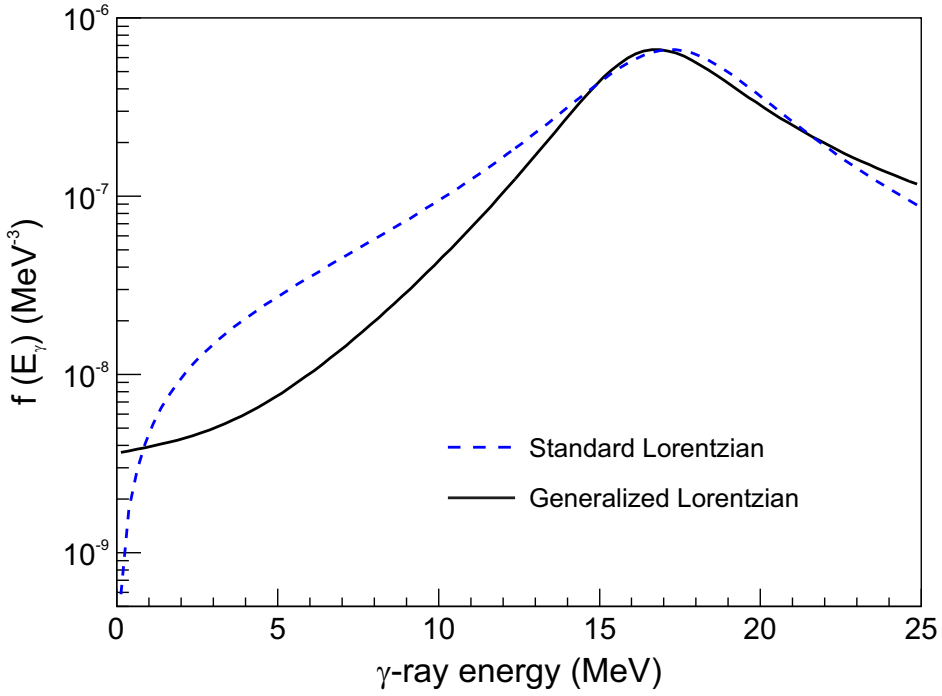

Figure 1.7: Comparison of the shape of the SLO and GLO models used to describe the γSF.

where:

$$\tilde{\Gamma}_{E1}(E_\gamma) = \Gamma_{E1}\frac{E_\gamma^2 + 4\pi^2 T^2}{E_{E1}^2}, \tag{1.15}$$

and T was originally meant to represent the Fermi Gas nuclear temperature, approximated by $T \approx \sqrt{E_x/a}$. As with the BSFG and CT models, where Δ, a, E_0, and T are parameters that can be adjusted to match a known NLD, T in the GLO function is often used as a free parameter when fitting measured γ, n data [24].

As with the NLD, microscopic models are desired for predicting the shape of the γSF far from stability. The quasi-particle random-phase approximation (QRPA) model has been incorporated into both HF [37] and HFB [38] models to build excited states. Hauser-Feshbach codes such as TALYS [39, 40] will often provide tabulated values from these microscopic calculations as another option for the γSF.

Table 1.1: GLO and SLO E1 default parameters for ^{74}Zn in TALYS used to generate the functions shown in Fig. 1.7.

E_{E1} (MeV)	17.485
σ_{E1} (mb)	133.069
Γ_{E1} (MeV)	6.144
T (GLO only)	0.7

In the last 15 years, experimental data at low γ-ray energies have shown an "upbend", where the strength increases as the γ-ray energy decreases, with a minimum usually around 2-4 MeV. Seen first in Fe isotopes [41], it has also been observed in many other nuclei (e.g. [42, 43, 44, 45, 46, 47, 48]). It is unclear if the strength is of magnetic or electric type, though current efforts to incorporate it into neutron-capture cross section calculations have used an M1 description. A recent Compton-polarization experiment of the ^{56}Fe(p, p') reaction using GRETINA [49] indicated the upbend may have a small bias towards magnetic transitions [50].

1.5 Indirect techniques

Indirect methods to constrain neutron-capture cross sections of short-lived nuclei rely on constraining at least one of the two major contributors to the uncertainty in a Hauser-Feshbach calculation–the NLD and γSF. There are four major indirect techniques currently being used: the Oslo method [51, 52, 53, 54], the β-Oslo method [55], the surrogate method [56], and the γSF method [57, 58]. The Oslo and surrogate methods both utilize charged particle reactions to populate the same compound nucleus that would be formed in the neutron-capture reaction of interest, followed by observing the decay. This limits both

methods to nuclei near stability due to the high beam rates needed for such experiments. The γSF method relies on measuring (γ, n) reactions to determine the inverse (n, γ) cross section, which requires stable targets and again limits the method to nuclei very close to stability. The β-Oslo method utilizes the β decay of neutron-rich nuclei to populate the nucleus that would be formed in a neutron capture reaction, which allows for its application much further from stability. It is still limited by the statistical framework of the Hauser-Feshbach calculation, however, and cannot be applied to nuclei with low NLD (less than 10 levels per excitation energy bin at the neutron separation energy, S_n) or small Q_β values (below 3 MeV in the A$\sim$70 region in order to populate a high enough NLD).

1.6 Dissertation outline

The results for experimentally constrained neutron-capture cross sections and reaction rates for four neutron-rich nuclei are presented. In Chapter 2 the details of two experiments carried out at the National Superconducting Cyclotron Laboratory (NSCL) are described, along with information about the detectors that were used. The β-Oslo method is described in Chapter 3 using the extraction of the NLD and γSF for ^{74}Zn as an example. The calculation of the neutron-capture cross section and reaction rate for the ^{73}Zn(n,γ)^{74}Zn reaction using the experimentally-constrained NLD and γSF is also included. Chapter 4 contains a comparison of different Hauser-Feshbach codes, again using the ^{73}Zn(n,γ)^{74}Zn reaction as an example. The step-by-step extraction of the NLD and γSF for ^{71,72,73}Ni using the β-Oslo method is described in Chapter 5. The subsequent calculation of the cross section and reaction rates for the ^{70,71,72}Ni(n,γ)^{71,72,73}Ni reactions, as well as a comparison of the NLD, γSF, and

cross sections with lighter Ni isotopes can be found in Chapter 6. Finally, conclusions are presented in Chapter 7 and an outlook of future work is provided.

Chapter 2

Experimental Setup

2.1 NSCL experiment e14505

The first experiment, number e14505, was carried out in February 2014 at the NSCL. A primary beam of ^{86}Kr was accelerated to 140 MeV/u through the Coupled Cyclotron Facility and impinged on a 376 mg/cm^2 thick Be target. The fragments were separated in the A1900 fragment separator [59] and ∼10 isotopes were delivered to the end station in the S2 vault, centered on ^{71}Co. A 60 mg/cm^2 Al wedge was used in the Image 2 (I2) position, with a 0.5% momentum acceptance. The experimental setup consisted of the Summing NaI (SuN) detector [60] to detect β-delayed γ rays, with a Si double-sided strip detector (DSSD) in the center of SuN for ion implantation. A Si surface barrier detector was placed behind the DSSD for veto events, and two Si PIN detectors were placed upstream of SuN. The ions were identified using the energy loss in the PIN detectors and the time-of-flight (TOF) between a thin scintillator at the focal plane of the A1900 and the PIN detectors. A total of 557,331 ions of ^{74}Cu were delivered to the setup.

2.1.1 Summing NaI (SuN) detector

SuN consists of 8 optically-isolated segments of NaI surrounding a small (1.8 in) borehole. It is 16 inches in diameter and 16 inches long. Each segment is read out by three PMTs, and

Table 2.1: Final voltages and scaling factors after gain matching the SuN PMTs for e14505 using the ^{40}K background peak. All voltages are positive.

PMT Number	Voltage (V)	Scaling Factor	PMT Number	Voltage (V)	Scaling Factor
0	730	1.0920	12	835	1.0866
1	740	1.0000	13	820	1.0000
2	780	1.1099	14	821	1.0995
3	774	1.1302	15	831	1.0959
4	771	1.0000	16	865	1.0000
5	764	1.1195	17	824	1.1033
6	794	1.1148	18	889	1.1467
7	803	1.0000	19	853	1.0000
8	812	1.1316	20	831	1.1131
9	838	1.0949	21	909	1.0796
10	824	1.0000	22	930	1.0000
11	848	1.0993	23	892	1.1026

the signals of all three PMTs are added together to get the total signal in a segment. SuN is used for total absorption spectroscopy (TAS) due to its large volume and high efficiency (85(2)% for the 662 keV transitions in the decay of ^{137}Cs, for example). The total signal from all eight segments can be summed to determine the full energy deposited in the detector from all the γ rays in a cascade that occur within 200 ns, while an individual segment can be used to determine the energy of individual γ ray in the cascade. The sum peak in SuN is a measure of the excitation energy of the daughter nucleus after β decay.

The 24 PMTs needed to be gain matched, which was done in two steps. First, the voltages of the PMTs were adjusted until the 1460 keV peak from the decay of naturally occurring

Table 2.2: Calibration values for SuN segments in e14505.

Segment Number	Calibration Scale	Calibration Intercept
0	0.4193	-16.02
1	0.4195	-15.95
2	0.4113	-14.95
3	0.4260	-16.50
4	0.4191	-16.41
5	0.4216	-17.93
6	0.4046	-16.20
7	0.4172	- 14.74

^{40}K was roughly in the same channel number in the software across all the PMTs. The second step was done in software, where a scaling factor was applied so that the 1460 keV peak was centered at exactly the same channel number. The ^{40}K background peak was used because the γ rays were external to the detector. The PMT signals in a single segment will be different depending on where in the segment the γ ray is detected–the largest signal will be from the PMT closest to the interaction. The final PMT voltages and scaling factors are given in Table 2.1. Once the PMTs were gain matched, the three PMTs in a single segment could be summed together. The segments were then energy calibrated using a ^{60}Co source and a ^{137}Cs source. The resulting calibration factors are contained in Table 2.2. For this experiment a linear calibration was used. The excitation energy was obtained by summing the calibrated segments.

2.1.2 Double-sided silicon strip detector

The central implantation detector was a small, 2.54 x 2.54 cm^2, 1 mm-thick DSSD. The DSSD consisted of two sets of 16 strips, one on each side of the detector, and perpendicular to each other. The location of an event was defined by the intersection of the strips on the front and back of the detector that recorded the highest energy depostion. Two gain ranges were used to differentiate between the implantation of an ion, which deposited 1000s of MeV in the DSSD, and β-decay electrons, which deposited tens of keV.

The DSSD strips were gain matched in both gain ranges. The high gain (used for detecting β-decay electrons) was gain matched using the 5.423 MeV particles from a ^{228}Th source. The response of each strip was scaled so that the peak was centered in the same channel. The low gain (used for detecting implanted ions) could not be gain matched until after the experiment started because standard sources do not produce α radition with high enough energies for the low gain range (in the thousands of MeV). The maximum energy peak from ion deposition in the DSSD was used, and was scaled for each strip so that the peak was centered in the same channel. The high gain and low gain scaling factors for each strip are given in Table 2.3, and are very similar as expected.

2.2 NSCL experiment e16505

A second experiment, number e16505, was carried out in September 2017 at the NSCL to expand on the data collected in experiment e14505, with an emphasis on the β decay of more neutron-rich Co isotopes. A primary beam of 45pnA of ^{82}Se was accelerated to 140 MeV/u through the Coupled Cyclotron Facility and impinged on a 470 mg/cm^2 thick Be target. The fragments were separated in the A1900 fragment separator [59] and a cocktail

Table 2.3: Scaling factors for gain matching the front and back strips of the DSSD in e14505.

Front Strip Number	Low Gain Scaling Factor	High Gain Scaling Factor	Back Strip Number	Low Gain Scaling Factor	High Gain Scaling Factor
0	0.752	1.035	0	1.102	1.191
1	0.818	1.067	1	0.962	1.099
2	0.762	1.044	2	0.952	1.054
3	0.863	0.998	3	0.978	1.089
4	0.786	0.955	4	0.986	1.125
5	0.773	0.997	5	1.087	1.092
6	0.823	1.015	6	1.000	1.152
7	0.758	0.993	7	0.933	1.094
8	0.742	0.972	8	0.973	1.083
9	0.765	0.923	9	1.025	1.139
10	0.772	1.027	10	0.965	1.092
11	0.781	0.981	11	1.008	1.102
12	0.774	0.964	12	1.007	1.132
13	0.804	0.992	13	0.966	1.104
14	0.564	0.932	14	0.996	1.149
15	0.814	0.981	15	0.973	1.135

Table 2.4: Final voltages and scaling factors after gain matching the SuN PMTs for e16505 using the ^{40}K background peak. All voltages are positive.

PMT Number	Voltage (V)	Scaling Factor	PMT Number	Voltage (V)	Scaling Factor
0	736	0.9685	12	839	0.9866
1	745	0.9873	13	821	0.9779
2	793	1.0391	14	836	0.9403
3	781	1.0354	15	833	0.9354
4	776	0.9648	16	869	0.9900
5	766	1.0052	17	828	0.9612
6	802	0.9993	18	893	1.0010
7	807	1.0082	19	852	0.9458
8	816	1.0364	20	833	0.9294
9	843	1.0444	21	908	0.9321
10	825	1.0186	22	929	0.9762
11	851	1.0613	23	891	0.9332

beam of ∼35 isotopes was delivered to the end station in the S2 vault, centered on ^{71}Fe. A 20 mg/cm^2 kapton wedge was used in the I2 position, with a full 5% momentum acceptance. The experimental setup was the same as for e14505, except that the TOF was determined between a position-sensitive scintillator in the I2 position and the PIN detectors upstream of SuN. The more neutron-rich beam was able to produce more exotic fragments for the measurement.

Table 2.5: γ-rays used for calibrating SuN segments in e16505.

Energy (keV)	Calibration Source
59.5409(1) [61]	^{241}Am
569.698(2) [62]	^{207}Bi
661.657(3) [63]	^{137}Cs
1063.656(3) [62]	^{207}Bi
1173.228(3) [64]	^{60}Co
1332.492(4) [64]	^{60}Co
2614.511(10) [65]	^{208}Tl (^{228}Th source)

2.2.1 SuN calibration

The voltages for each PMT used in e16505, as well as the scaling factors needed for the gain matching, are shown in Table 2.4. The segments were then energy calibrated using the γ-rays listed in Table 2.5. A linear calibration fit was found to represent the data as well as a second-order polynomial, and can be seen in Fig. 2.1 for each segment. The calibrated segment energies were added together to get the TAS energy with no additional calibration required.

2.2.2 DSSD gain matching

The DSSD high gain was gain matched using four ^{228}Th peaks (5.423, 5.685, 6.288, 6.778 MeV) and a ^{241}Am peak (5.486 MeV). Each peak was scaled to match the channel number on strip 7 for both the front and the back sets. The average scaling factor from the five peaks was used. The signals of low gain were gain matched after the experiment started by applying a scaling factor to each stip so the maximum energy peak was located in the same

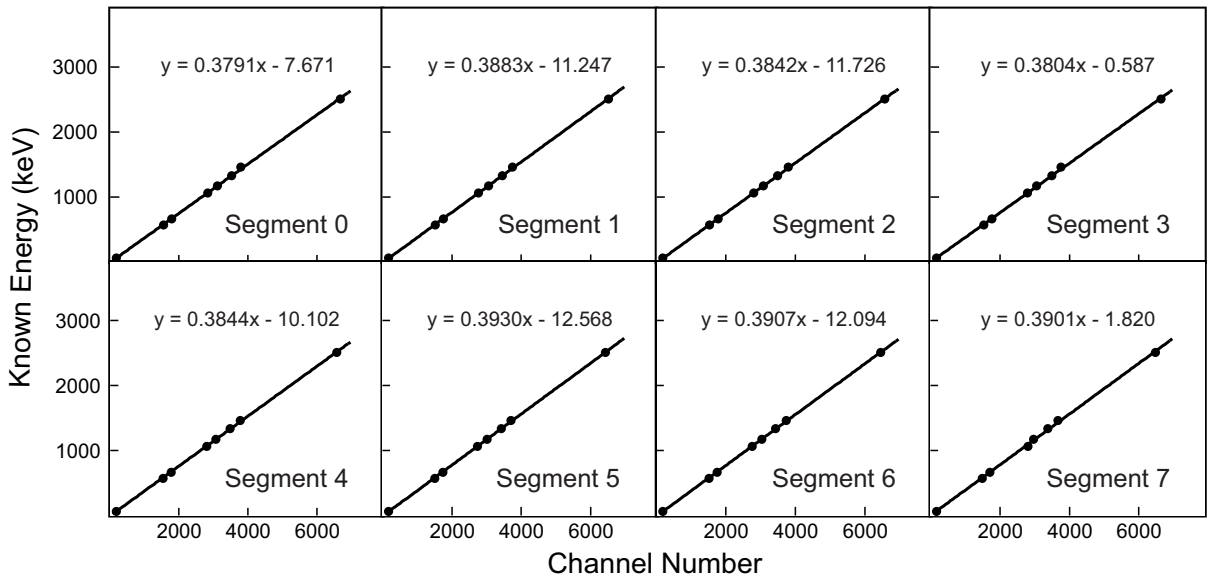

Figure 2.1: Calibration for each SuN segment in e16505 using the γ-rays listed in Table 2.5. Each panel is labeled with the segment number.

channel number of the peak of strip 7 on the front and back. The high gain and low gain scaling factors for each strip are detailed in Table 2.6. The results of the gain matching for the high gain (decays) can be seen in Fig. 2.2, while the results of the gain matching for the low gain (ions) can be seen in Fig. 2.3.

2.3 Correlation of implants and decays

The separated ions of interest were delivered to the experimental station and came to rest inside the DSSD. A short time later a given ion would undergo β decay. The signal from the β-decay electron was correlated with the previously implanted ion based on both time and the position within the detector by requiring that the ion and the decay were detected in either the same pixel or a 3x3 pixel window surrounding the decay (see Fig. 2.4). The choice of pixel field has to be chosen carefully based on the arrival rate of ions in the experiment. The higher the rate, the more difficult it becomes to accurately correlate ions and decays due

Table 2.6: Scaling factors for gain matching the DSSD in e16505.

Front Strip Number	Low Gain Scaling Factor	High Gain Scaling Factor	Back Strip Number	Low Gain Scaling Factor	High Gain Scaling Factor
0	1.104	1.002	0	1.067	1.176
1	0.969	1.002	1	1.025	0.998
2	0.932	1.041	2	1.007	0.947
3	1.162	0.994	3	1.004	1.185
4	1.081	0.982	4	1.057	1.031
5	1.023	0.974	5	1.030	1.045
6	1.980	0.999	6	1.074	1.100
7	1.000	1.000	7	1.000	1.000
8	0.997	1.010	8	1.017	1.085
9	1.001	0.975	9	1.050	1.094
10	1.292	1.037	10	1.011	1.043
11	1.151	0.979	11	1.050	1.066
12	1.087	1.058	12	1.058	1.141
13	0.956	0.937	13	1.035	1.067
14	1.008	1.132	14	1.066	1.113
15	1.000	0.899	15	1.018	1.046

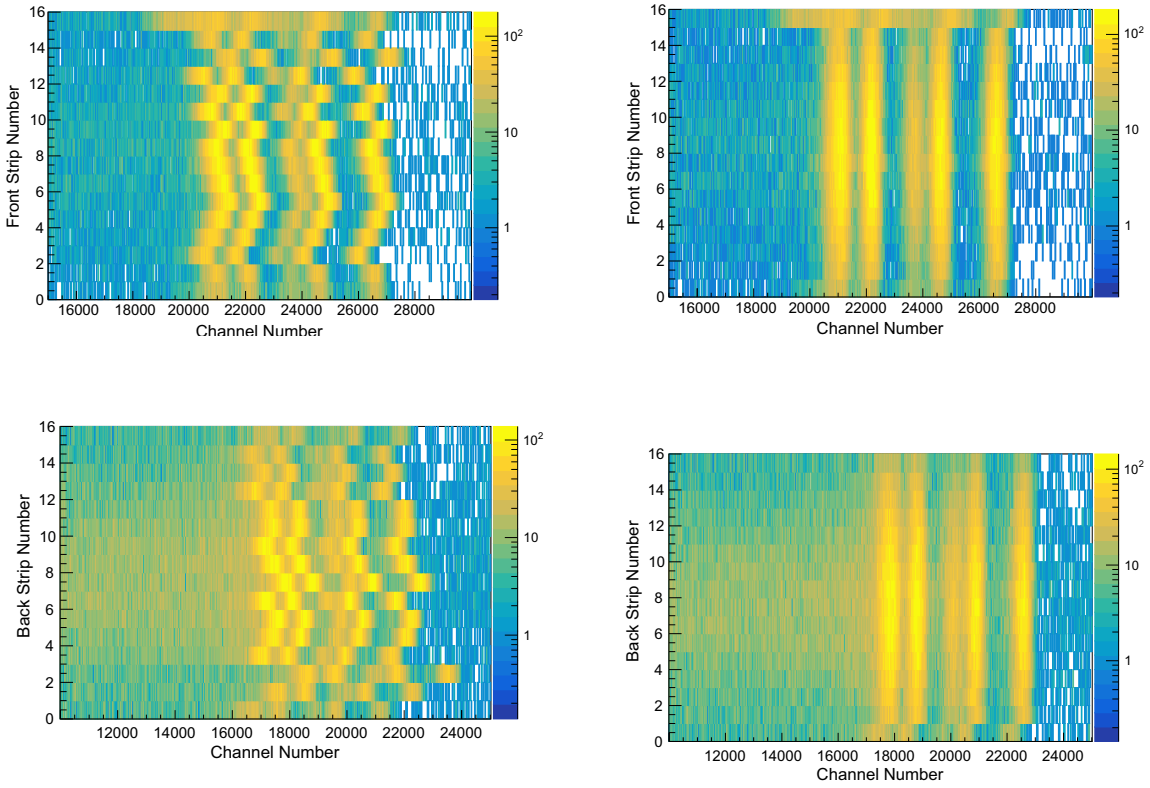

Figure 2.2: Gain matching the front (top) and back (bottom) of the DSSD high gain setting in e16505. The strip number is shown versus the channel number, and the five alpha peaks from a ^{228}Th source can be seen. A single scaling factor was obtained for each strip to align the peak energies. For both the front and back, the left panel shows the strip responses before gain matching, while the right panel shows the strip responses after gain matching with the five peaks seen in the same channels for each strip.

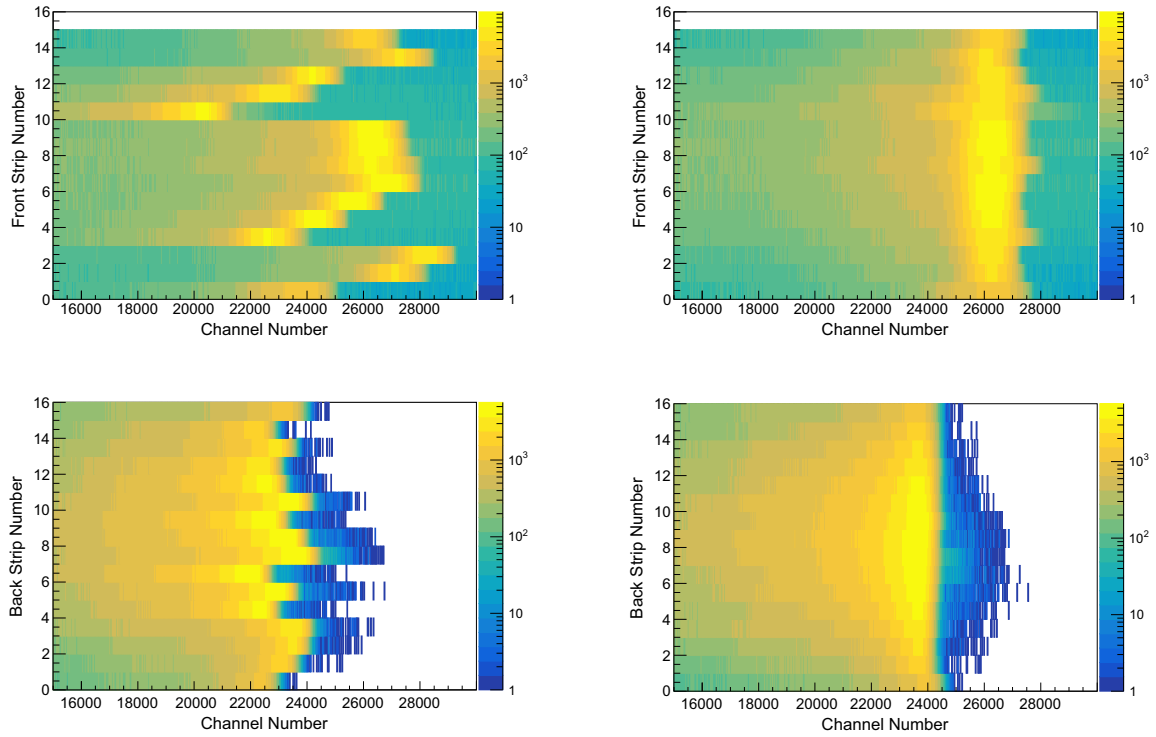

Figure 2.3: Gain matching the front (top) and back (bottom) of the DSSD low gain setting in e16505. The strip number is shown versus the channel number, as in Fig. 2.2. A source could not be used due to the gain range, so gain matching was performed using the maximum energy peak from ions during the experiment. The last strip on the front of the DSSD (strip 15) was not working during the experiment. As in Fig. 2.2, the left panels show the strip responses before gain matching, while the left panels show the strip responses after gain matching, with the maximum energy peak occuring in the same channels for all strips.

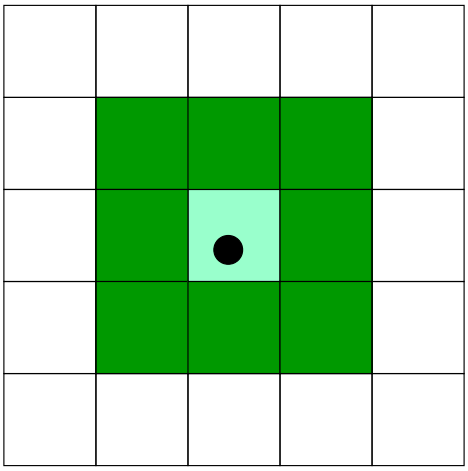

Figure 2.4: Model of a 5x5 DSSD, which can be read as 25 pixels. In this example, the decay (the black circle) was detected in the central pixel (the highest energy deposition was in the center strips on both the front and back). Two correlation pixel fields are possible for this decay. The first is the same pixel, shown here as the light green box where the decay is located. The second is a 3x3 field surrounding the decay pixel, shown here by the dark green box (and including the light green box). The white boxes are the remaining pixels that would not be considered in either correlation.

to random coincidences, so a single pixel correlation is preferred. For low rate experiments ($\sim$50 particles per second or less when using the small DSSD in SuN), the time between ion implantations in a single pixel can become long enough that using a 3x3 pixel field becomes more useful. In experiment number e16505, for example, the average rate of ions per pixel was 0.1/second, while the half-lives of the isotopes of interest were in the tens of ms. This allowed for a 3x3 pixel field to be used, as the average rate of ions within that field was still less than 1/second.

The correlation time window that can be used depends on the half-life of the nucleus of interest and the implantation rate on the detector (which was kept to below 100 pps in both experiments). The window needs to be long enough that the chance of seeing the decay is high, but not so long that the chance of another ion arriving within the pixel window is high. A good rule of thumb is to use a correlation window that is 2-3 times the half-life of the

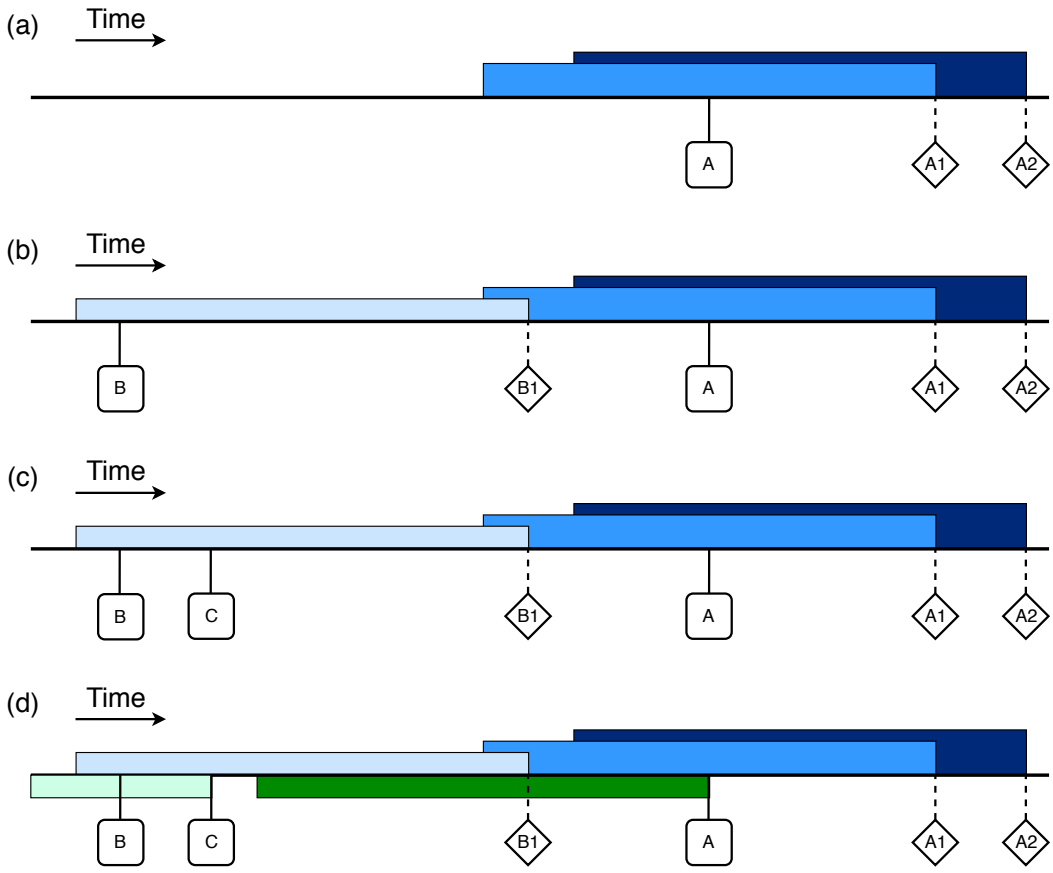

Figure 2.5: Organization of correlation logic (see text for details).

nucleus of interest with the low implantation rate used. With longer correlation windows the rate of random correlations increases. For ^{74}Cu, which has a half-life of 1.63(5) seconds [66], a correlation time of 5 seconds was used. A 150 ms correlation time was used for the three Co isotopes due to their shorter half-lives: 80(3) ms [67] for ^{71}Co, 59.9(17) ms [68] for ^{72}Co, and 42(3) ms [69] for ^{73}Co.

Figure 2.5 will be used to describe the correlation logic. In this example it is assumed that the ions and their decays are located in the same pixel in the detector. Ions are represented by squares, while decays are represented by diamonds. In panel (a), an ion A is detected in the DSSD, followed some time later by a decay A1 and then another decay A2. The

analysis of event proceeds forward in time, so the ion, along with the location and time of its detection, are saved. When the analysis reaches decay A1, a correlation is searched for. A correlation window (shown as the light blue bar) is opened to look backwards in time for an ion that arrived in that pixel that could be the source of the decay. Ion A, which falls within the correlation window, is then correlated to decay A1. The same procedure occurs when the analysis reaches decay A2, and is shown with the dark blue bar. Therefore, ion A has two decays correlated to it, which could correspond to the parent and daughter decay. In panel (b), the situation is made more complicated with the addition of another ion, B, that is implanted before ion A, along with its decay B1. When the analysis reaches decay B1, the correlation window (the lightest blue bar) is long enough that ion B is correlated to it. This correlation does not affect the correlation of ion A to decays A1 and A2, which proceeds as described in panel (a). Panel (c) adds another layer of complexity with the detection of ion C immediately after ion B. The decay from ion C does not happen to be detected. In this scenario, both ions B and C are saved, and when the correlation window is opened by the decay B1, both ions are within the window. The correlation is done between the decay and the ion closest in time to it, so decay B1 would be correlated to ion C, which would be incorrect. To help prevent these types of miscorrelations, a minimum time window between ions is enforced in the correlator. This concept can be seen in panel (d), which has the same ion and decay scheme as panel (c). The correlation of ion A, which was not affected by ion C in panel (c), now has an extra step to complete before the correlation is finalized. Decay A1 is correlated to ion A due to the correlation window, but then another window is opened, which starts with the detection of ion A and is the same length as the correlator window. This window, shown as the dark green bar, does not encounter another ion, so the correlation between ion A and decay A1 can proceed, as well as between ion A

and decay A2. The correlation of decay B1 does not proceed the same way. Decay B1 is correlated to ion C as in panel (c), but when the new window is opened from ion C (the light green bar), ion B is within the window. That means that decay B1 could be from ion B or ion C, so the correlation is halted and decay B1 is not correlated to an ion. To obtain the random correlation background, the correlation procedure is done backwards in time. For this procedure, the exact same correlation as in Fig. 2.5 is performed, but the time arrow is reversed [70]. The backwards in time procedure should take into account truly random correlations, including decays from longer-lived isotopes in the DSSD.

The window that opens to prevent a decay from being correlated to an ion that is too close in time to another ion is referred to as the "minimum implantation window". The minimum implantation window is set to be the same length as the correlation window to ensure there is only one ion present in the correlation window. The longer the correlation window, the longer the minimum implantation window and the higher the chance of there being another ion in the window, which lowers the number of successful correlations. Therefore, shorter correlation windows are preferred. There are less correlations in the first 150 ms of a 5 sec correlation than there are in the full 150 ms of a 150 ms correlation due to the minimum implantation window, as the number of decays that are not correlated to ions increases (see Chapter 5 for values for the decay of ^{71,72,73}Co).

Chapter 3

β-Oslo Method

The β-Oslo method [55] builds on the established Oslo method [51, 52, 53, 54] for extracting the NLD and γSF of a nucleus by populating highly excited states and detecting the subsequent γ-ray emission. The main difference to the Oslo method is that β decay is used to populate highly excited states instead of charged particle reactions. Populating the nucleus of interest through β decay allows for experimental information about the NLD and γSF to be extracted further from stability than other indirect methods, but is limited by the β-decay selection rules and Q values. The γ-rays that are detected are used to experimentally constrain those statistical properties so that they can be used to infer a neutron-capture cross section. The method is generally restricted to nuclei that have large β-decay Q values and a high NLD around S_n (see Introduction for general limits). The details of the β-Oslo method will be explained in detail using the β decay of ^{74}Cu, which was used to extract the NLD and γSF of ^{74}Zn in order to reduce the uncertainty in the ^{73}Zn(n,γ)^{74}Zn reaction cross section. The analysis contains four main steps:

1. Unfolding of the raw 2D matrix of γ-rays observed in SuN for a given ion.

2. Extraction of the primary γ-ray matrix. These are the first γ rays to be emitted from a level in a cascade to the ground state.

3. Simultaneous extraction of the functional forms of the NLD and $\mathcal{T}(E_\gamma)$ (see eq. 1.9 for translation of $\mathcal{T}(E_\gamma)$ to γSF).

4. Normalization of NLD and γSF.

Each step will be described in detail below. Fig. 3.1 is a flow chart that indicates the steps required for the analysis, including the physics information required. The MAMA code [71] handles the unfolding and primary extraction, which requires information about the response of the γ-ray detector. The other codes are responsible for the NLD and γSF normalization, and information such as the level density at the neutron separation energy [$\rho(S_n)$], the low-energy levels, and the spin of the target nucleus in the neutron-capture reaction of interest are all required.

3.1 Populating highly excited states through β decay

The β-Oslo method utilizes β decay to populate highly excited states of the nucleus of interest (the neutron-capture product, ^{74}Zn in this example) as indicated schematically in Fig. 3.2. Not every β-decaying nucleus is amenable to the β-Oslo method. The most important consideration is that the Q-value of the decay is large enough to produce statistical γ-ray decay in the daughter. Generally, Q-values of at least 4 MeV are preferred, with larger values providing a larger probability that there will be decays going through the statistical region (roughly above 2-3 MeV [72]). While not necessary, it is preferred that the Q-value is close to or even slightly above the neutron separation energy of the daughter nucleus so that the full excitation energy range can be accessed by β decay and γ-ray transitions. It is also assumed that only Gamow-Teller transitions are observed.

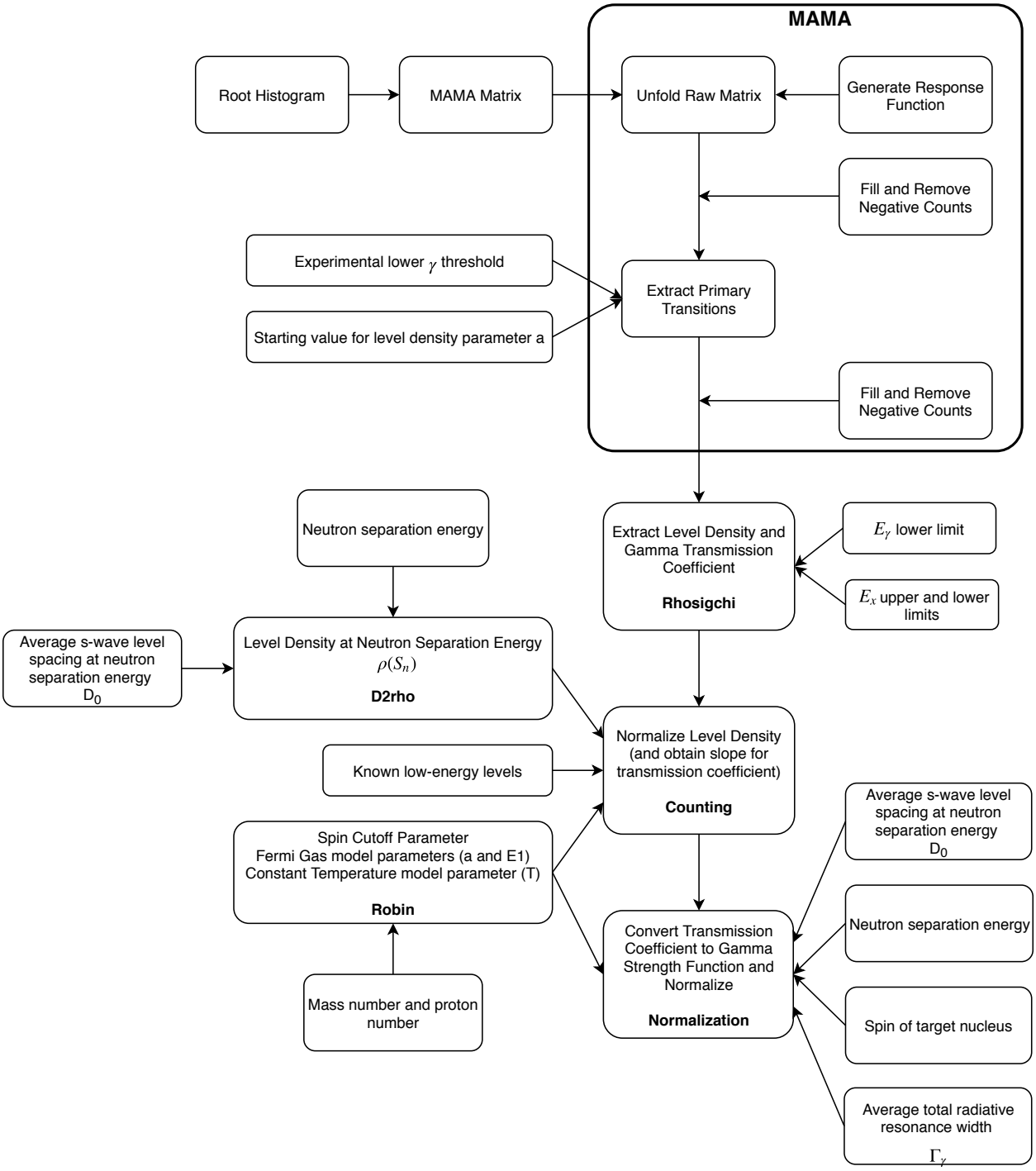

Figure 3.1: Flowchart showing the steps of the Oslo Method.

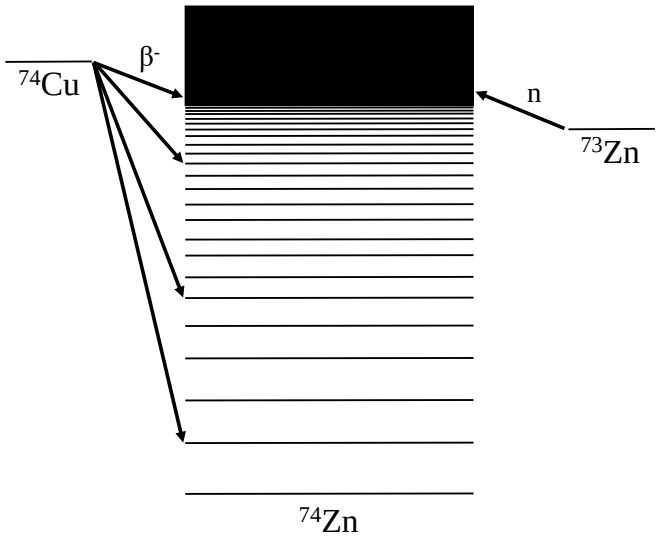

Figure 3.2: Schematic of the population of excited states in the same compound nucleus through both β decay and neutron capture for the example of using ^{74}Cu β decay to populate the ^{74}Zn nucleus that would be formed in a neutron-capture reaction on ^{73}Zn. The relative energies of each ground state are to scale.

The γ-ray energy (E_γ) and excitation energy (E_x) spectra in SuN for the β decay of ^{74}Cu are shown in Fig. 3.3. The level most strongly fed by β decay, at 605.9 keV ($I_\beta = 30(3)\%$ [66]) is clear, as is a set of levels between 2800-3000 keV that are also strongly fed (combined $I_\beta \approx 31\%$ [66]). The strongest γ-ray transition of 605.9 keV is clear as well. Both the E_γ and E_x spectra are consistent with the literature on the β decay of ^{74}Cu. The Q-value of the β decay of ^{74}Cu is 9.751 MeV, while ^{74}Zn has a S_n of 8.235 MeV. The raw E_x versus E_γ matrix for the decay of ^{74}Cu is shown in Fig. 3.4. This is the starting point for the β-Oslo analysis.

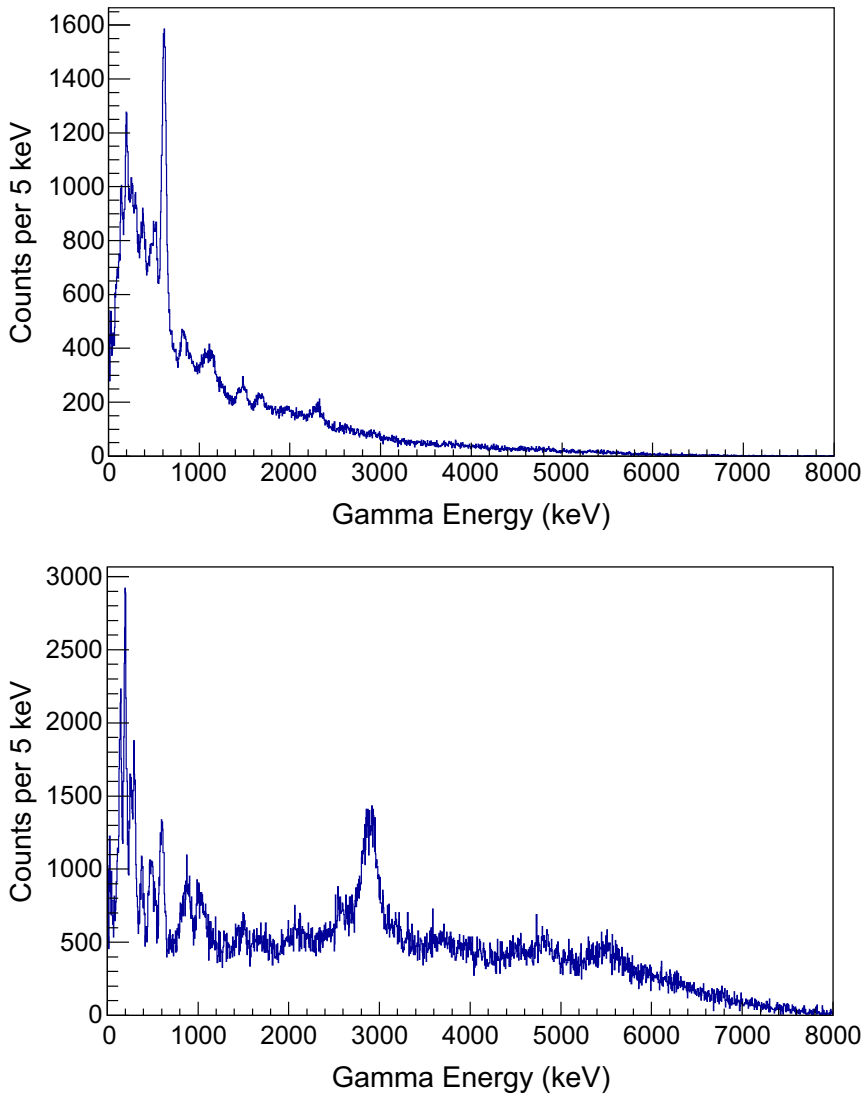

Figure 3.3: SuN spectra showing the γ-ray energies, E_γ (top), and excitation energies, E_x (bottom), from the decay of ^{74}Cu.

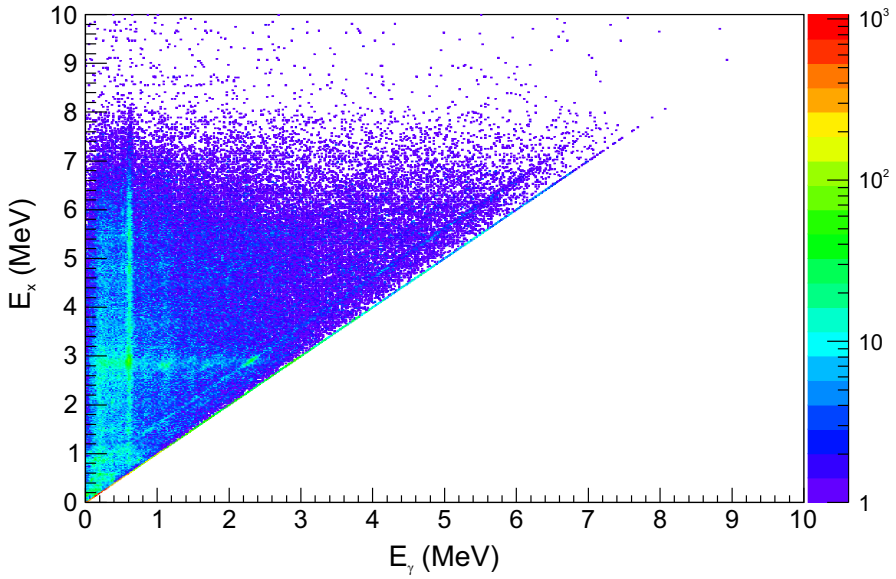

Figure 3.4: Raw E_x vs. E_γ matrix for the β decay of ^{74}Cu used to create the projections in Fig. 3.3.

3.2 Unfolding

The γ-ray energies in the raw matrix were obtained from individual segments in SuN. While the efficiency of detecting the total energy of a γ ray in the full volume of SuN is high, the efficiency of detecting the full energy in just one segment is lower, at around 40% for a 1 MeV γ ray. To account for this, the E$_\gamma$ spectrum has to be unfolded. The response function of the detector, which is a measure of the response to γ rays of varying energies, was constructed using the GEANT4 simulation code [73]. An iterative unfolding procedure was then used to determine the full γ-ray energies from the raw data collected, as described in Ref. [51].

The iterative method relies on folding trial spectra with the response matrix and altering the trial spectrum until the folded spectrum matches the experimental data. Letting f represent the folded spectrum, u represent the trial spectrum, and $\mathbf{R}$ the response function matrix (the full energy of the γ ray as a function of the energy deposited in the detector), the folding procedure can be represented as:

$$f = \mathbf{R}u, \tag{3.1}$$

which is compared to the observed spectrum r.

The observed spectrum is taken to be u^0, the first trial function. The first folded spectrum f^0 is calculated using Eq. 3.1 and compared to the observed spectrum. The next trial function becomes the sum of the original trial function and the difference between the first folded spectrum and the observed spectrum:

$$u^1 = u^0 + (r - f^0). \tag{3.2}$$

This procedure is repeated, generating new trial functions at each step, until the folded spectrum f^n matches the observed spectrum within the experimental uncertainties, based on a χ^2 test.

Only the four central segments of SuN were unfolded due to the large volume of the detector and the observation that very few γ rays deposit energy in the outer four segments. The unfolding procedure described resulted in the unfolded matrix shown in Fig. 3.5 for ^{74}Zn.

3.3 Extraction of primary γ rays

Primary γ rays are those that are emitted first in a cascade from any excited state. For this analysis, the primary matrix should contain only these γ rays. To achieve this, the γ rays that follow the first in a cascade must be subtracted. The procedure, as described in Ref. [52], is based on the assumption that the γ-ray emission probability from a given excited

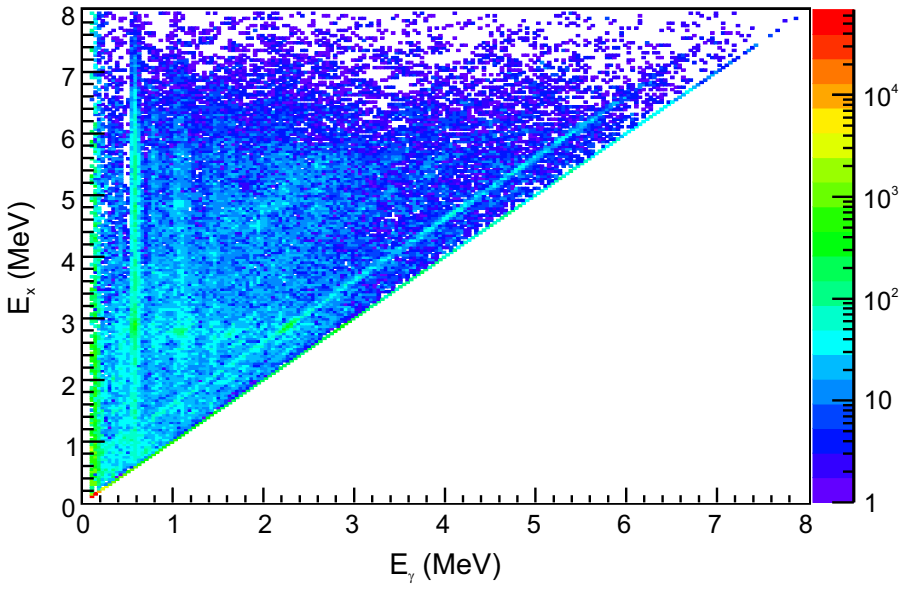

Figure 3.5: Unfolded E_x vs. E_γ matrix for the β decay of ^{74}Cu.

state is the same if the level is populated directly by β decay or by a γ transition from a higher excited state. Therefore, the unfolded spectra f_i are composed of all the possible γ rays decaying from excited states within the excitation energy bin i. The spectra $f_{j<i}$ contain the same γ-ray transitions except for the first γ-rays emitted from bin i, so the primary γ-ray distribution h_i for each bin i is estimated by

$$h = f_i - g_i, \tag{3.3}$$

where g_i is the sum of all spectra, weighted by w_{ij}, which represents the probability of the decay from bin i to states in bin j (normalized so that $\sum_j w_{ij} = 1$)

$$g_i = \sum_j n_{ij} w_{ij} f_j \tag{3.4}$$

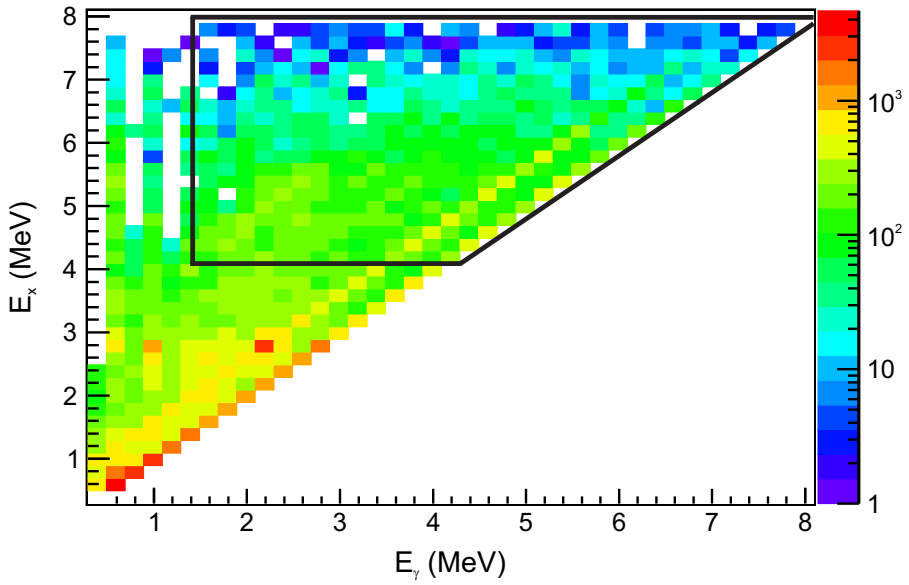

Figure 3.6: Primary E$_x$ vs. E_γ matrix for the β decay of ^{74}Cu.

and requires information about the average γ-ray multiplicity $\langle M_i \rangle$ and the number of counts in spectrum f_i, $A(f_i)$, so that

$$n_{ij} = \frac{\langle M_j \rangle A(f_i)}{\langle M_i \rangle A(f_j)}. \tag{3.5}$$

g can be thought of as the probability distribution $[P(E_x, E_\gamma)]$ that describes the probability that a γ-ray of a given energy will be emitted from a given excited state. The γ-ray spectra at lower excitation energy bins are subtracted from the bin of interest, leaving only the primary γ-rays. This is done at each excitation energy. The primary matrix obtained for ^{74}Zn is shown in Fig. 3.6.

3.4 Functional forms of the NLD and γSF

The NLD and γ-ray transmission coefficient $[\mathcal{T}(E_\gamma)]$ are extracted simultaneously from the primary matrix. The probability that a γ ray of a given energy will be emitted from a

given excited state can be related to the NLD and $\mathcal{T}(E_\gamma)$, ignoring the nuclear spin for the moment, as:

$$P(E, E_\gamma) \propto \rho(E - E_\gamma)\mathcal{T}(E_\gamma) \tag{3.6}$$

where $\mathcal{T}(E_\gamma)$ can be converted to the γSF using the equation

$$\gamma SF = \frac{1}{2\pi}\frac{\mathcal{T}(E_\gamma)}{E_\gamma^3}, \tag{3.7}$$

which is the same as Eq. 1.9 for the specific case of a dipole transition. This relationship assumes that the NLD and $\mathcal{T}$ are independent functions. The other major assumption at this stage is that $\mathcal{T}$ is independent of the excitation energy at which is it extracted, which has been shown to be valid in ^{238}Np [72].

The primary matrix needs to be normalized so that the γ-ray energies in each excitation energy bin sum to 1 for it to represent a normalized probability. The NLD and $\mathcal{T}(E_\gamma)$ extracted from the primary matrix are functional forms which satisfy the following equations [53]:

$$\rho(E - E_\gamma) = Ae^{\alpha(E-E_\gamma)}, \tag{3.8}$$

$$\mathcal{T}(E_\gamma) = Be^{\alpha E_\gamma}, \tag{3.9}$$

where the A, B, and α parameters are determined in the normalization procedure. The NLD (determined at the excitation energy of the nucleus after emission of a γ ray of energy E_γ) and $\mathcal{T}(E_\gamma)$ are extracted simultaneously from a region of the E_x, E_γ matrix that is

statistical. The region is chosen to exclude strong transitions (such as from the first excited state to the ground state) and low excitation energies, so that the γ emission proceeds through statistical rules instead of being dominated by strong transitions. The E_x upper limit of the range accounts for the energy of the first excited state in the β-delayed neutron daughter, so that γ-rays from that nucleus are not included. The extraction region for ^{74}Zn is indicated by the black outline in the primary matrix in Fig. 3.6.

3.5 Normalization of NLD and γSF

The functional forms of the NLD and γSF need to be normalized to determine A, B, and α. Three pieces of information are needed for the normalization. Typically, the known levels at low excitation energies and the level density at the neutron separation energy [$\rho(S_n)$] are used to determine A and α. B is usually determined using information from the GDR. Nuclei accessible in β-decay experiments have at least some known low-energy levels, but for short-lived nuclei there is little experimental information to determine $\rho(S_n)$ and the absolute γSF. Instead, they need to be obtained through systematics from nearby nuclei or theoretical calculations.

In the traditional Oslo method, $\rho(S_n)$ is calculated from the average s-wave level spacing at the neutron separation energy (D_0). D_0 is the inverse of the NLD at $\rho(S_n)$ for levels that would be populated in neutron capture–that is, levels that have $\pm 1/2$ spin compared to the ground state of the capturing nucleus. This value can be obtained using neutron capture experiments on the nucleus of interest, which is again not possible for short-lived nuclei. The value of B, the magnitude of the γSF, is calculated using the average radiative width at the neutron separation energy, Γ_γ. Γ_γ can also be determined in neutron capture experiments

and suffers from the same restrictions. Theoretical calculations or systematics need to be used when D_0 and Γ_γ values are not available. In the β-Oslo method, the $\rho(S_n)$ value is obtained from theoretical NLD calculations, while the magnitude of the γSF is determined using high-energy γSF information from nearby nuclei.

3.5.1 NLD

For the NLD normalization performed in this work all of the known low-energy levels in ^{74}Zn were used, and the $\rho(S_n)$ value was determined from theoretical calculations. The procedure for relating the calculated NLD to experimental information was described in Ref. [30], and involved using the cumulative levels calculated from the theoretical NLD. They were compared to the known cumulative levels, and the calculated levels were shifted in excitation energy to match the known levels. The known cumulative levels can be seen compared to the calculated cumulative levels in Fig. 3.7. The best E_x shift value of 0.4 $\pm$ 0.2 MeV was determined from a χ^2 minimization between the known levels and calculated levels in the 2 to 3.25 MeV range. The results of the χ^2 distribution can be seen in Fig. 3.8.

Once the excitation energy shifts was determined, it was also applied to the theoretical level density. With a shift of 0.4 $\pm$ 0.2 MeV the level density calculated at 3 MeV would need to be shifted to 3.4 MeV for the middle value, 3.2 MeV for the upper value, and 3.6 MeV for the lower value. The lower and upper designations refer to the new $\rho(S_n)$ value compared to the middle value–a larger shift moves a lower level density value to a higher excitation energy, therefore producing a lower $\rho(S_n)$ value. At higher excitation energies the NLD has an exponential increase, which should be the same for all three shifted data sets. Using a simple exponential fit of the form

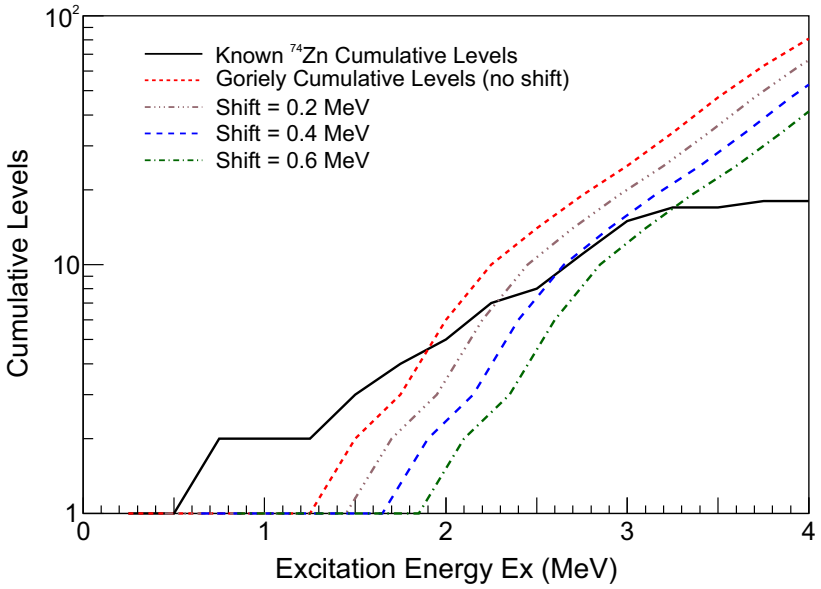

Figure 3.7: Calculated cumulative levels compared to known ^{74}Zn levels.

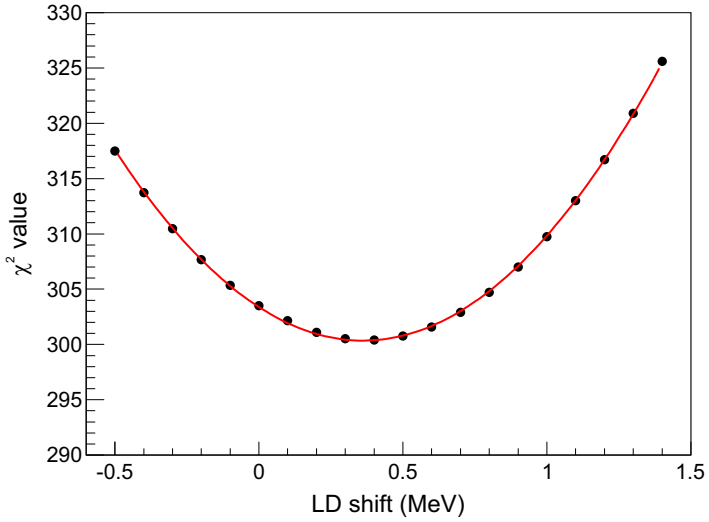

Figure 3.8: χ^2 value versus shift value for the shifting of ^{74}Zn theoretical cumulative levels from Ref. [30]. The calculated cumulative levels are shifted in excitation energy to match the known cumulative levels.

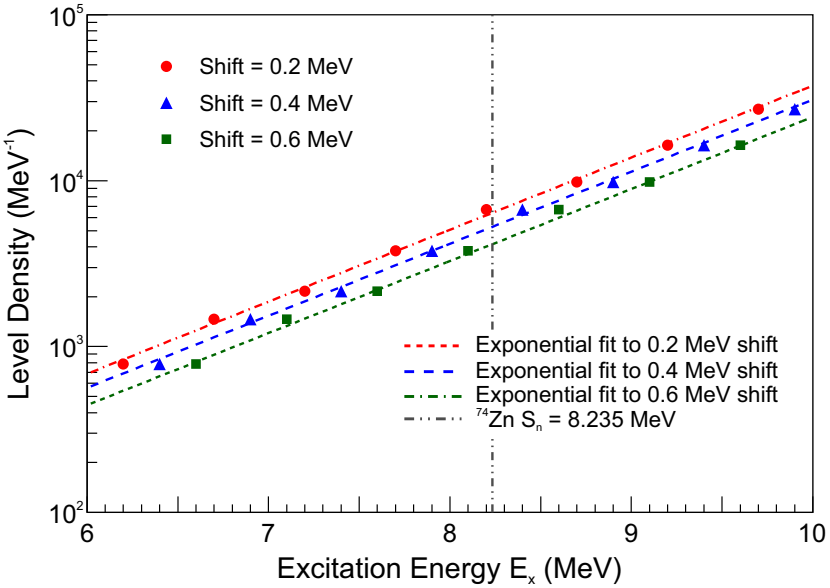

Figure 3.9: Goriely level densities (from Ref. [30] shifted in excitation energy according to the best shift value found, as shown in Fig. 3.1.

Table 3.1: Parameters used in exponential fit of Eq. 3.10 to shifted calculated NLD for ^{74}Zn and the resulting $\rho(S_n)$ values.

Shift Value	Constant (a)	Slope (b)	$\rho(S_n)$
0.2 MeV	1.7(2)	1.00(2)	6360(130)
0.4 MeV	1.4(2)	1.00(2)	5200(120)
0.6 MeV	1.1(2)	1.00(2)	4230(100)

$$y = ae^{bx}, \tag{3.10}$$

where a is the constant and b is the slope, the shifted theoretical NLD values produced $\rho(S_n)$ values of 4230 MeV^{-1}, 5200 MeV^{-1}, and 6360 MeV^{-1} at the S_n of 8.235(3) MeV [66]. The parameters are detailed in Table 3.1 and the fits are shown in Fig. 3.9.

A number of assumptions are contained within the NLD normalization. The parity distribution is assumed to be roughly equal at all excitation energies and spins, which is likely valid for heavy nuclei but may be less valid for lighter nuclei or those near closed shells. It is also assumed that the populated spin distribution from β decay is the same at all excitation energies, and the distribution at S_n is used from theory calculations, which are also assumed to be correct. Finally, the calculated NLD from theory is assumed to have the correct shape, as only the E_x dependence is altered to match the known levels, but the slope is not.

With both the known low-energy levels and $\rho(S_n)$, the NLD could be normalized. This was done through a simultaneous fit of the experimental NLD to the low-energy levels and to a CT model extrapolated from the $\rho(S_n)$ value. The parameters for the Constant Temperature model were determined through the fit. This provided both the A and α values in the NLD functional form, as well as α in the functional form of the γSF (see eq. 3.8 and 3.9). The normalized NLD is shown in Fig. 3.10, with the known levels and shifted Goriely NLD that were used for the normalization.

3.5.2 Limited spin population

The NLD is also a function of angular momentum, or nuclear spin. A limited range of spins is populated by the β-decay process, which needs to be taken into account in this analysis. The ground state of ^{74}Cu is 2^- [74], which would populate spins of 1^-, 2^-, and 3^- in an allowed β decay. After one dipole transition, the spins populated would be in the range of 0 to 4, of both parities. The primary γ rays observed in a β-Oslo experiment are restricted to that spin range, which impacts the normalization of the γSF. Because α was determined in the NLD normalization, the $\rho(S_n)$ value and the known levels have to be reduced based

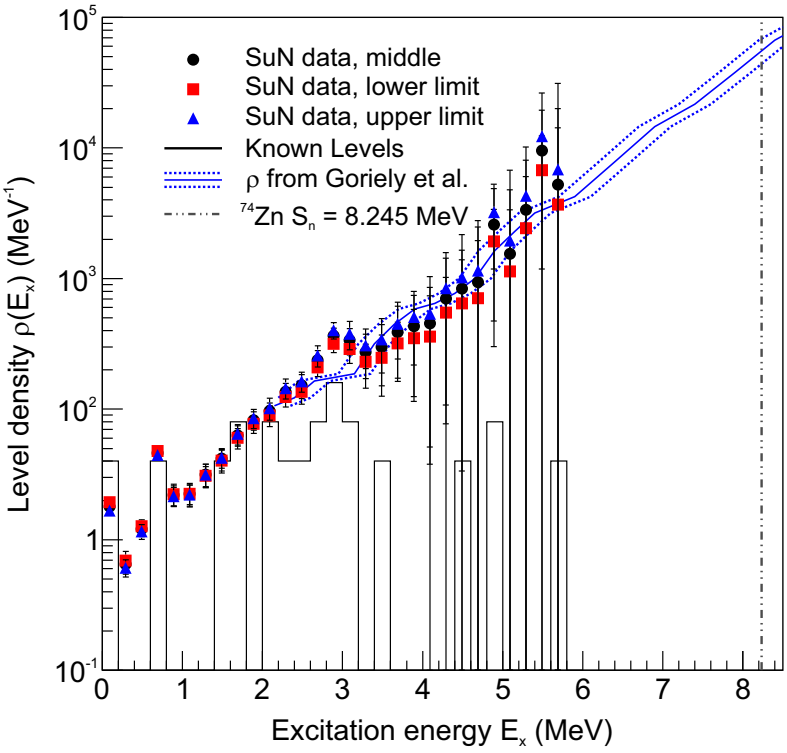

Figure 3.10: Nuclear level density for ^{74}Zn showing the experimental data (black circles) as well as upper and lower limits (red squares, blue triangles), known levels from NNDC (solid black line), and level density calculated in Ref. [30] (solid blue line). Dashed blue lines indicate uncertainties on the shift of the calculated level density.

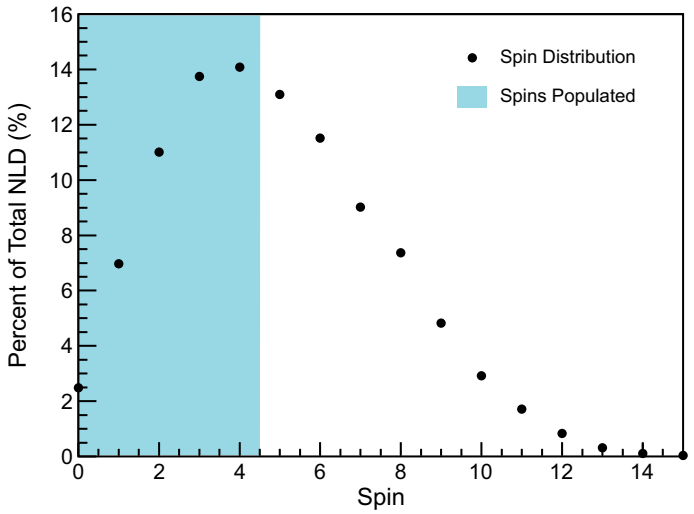

Figure 3.11: Distribution of spins for the levels in ^{74}Zn around the neutron separation energy based on tabulated spin- and parity-dependent NLD from Ref. [30]. Spins highlighted in blue are populated following an allowed β decay of ^{74}Cu and one dipole photon transition. The ground state of ^{74}Cu is 2^- [75].

on the expected spin population to determine α for the γSF normalization. To determine the reduction, the spin- and parity-dependent theoretical NLD from Goriely [30] was once again used. The percentage of the total NLD around the neutron separation energy for each spin was calculated (see Fig. 3.11), and the percentage that fell within the spin range of interest, highlighted in blue in the figure, was determined. For ^{74}Zn, 48% of the NLD fell within the spin range 0-4, leading to reduced $\rho(S_n)$ values of 2040 MeV^{-1}, 2510 MeV^{-1}, and 3070 MeV^{-1}. The known levels at low E_x used in the normalization with the reduced $\rho(S_n)$ were also reduced to include only levels are assigned spins that fall within the spin range of interest, which resulted in a reduction of 20%. The normalization parameters were similar between the full and reduced NLD, which was expected.

3.5.3 γSF

With the α value set by the NLD normalization (using the reduced normalization values), only the value of B was unknown. The γSF of nearby nuclei at high energies was used for the γSF normalization. For ^{74}Zn, photoabsorption data for ^{70}Zn and ^{74,76}Ge was used [76]. The γ, n cross section can be converted into a γSF using the equation

$$\gamma SF(MeV^{-3}) = \frac{\sigma_\gamma^2}{(3\pi\hbar)^2}, \tag{3.11}$$

where σ_γ is the photoabsorption cross section of the nucleus of interest.

The photoabsorption cross section is generally measured above the neutron separation energy of the nucleus, so it must be fit and extrapolated to lower energies to be used for normalization of the experimental γSF, which does not go above S_n. A GLO function [35] describes the shape of the γSF at high excitation energies very well, and has been traditionally used to estimate the low-energy shape of the γSF (see Section 1.4.3). Each available γ, n data set was fit with a GLO function, and the resulting average function was extrapolated to lower excitation energies where it overlapped with the experimental γSF data. The parameters for the GLO functions (one for each data set) are detailed in Table 3.2, along with the average values. A χ^2 minimization was performed to match the experimental γSF to the average from the GDR fits from 4 to 7 MeV to determine B. The normalized γSF, along with the γ, n data and GLO function extrapolations, are shown in Fig. 3.12. The green band in the figure indicates the uncertainty in the SuN data.

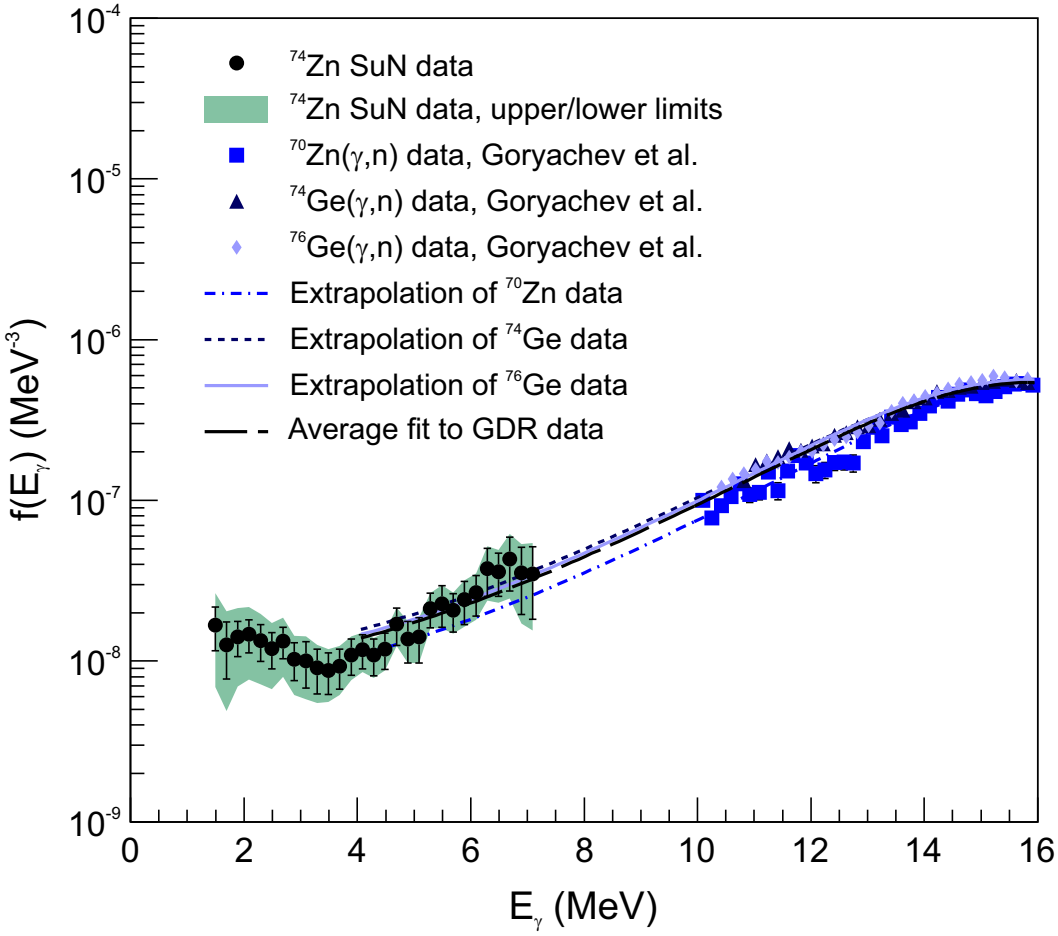

Figure 3.12: Gamma strength function for ^{74}Zn showing the experimental data (black circles), experimental data for ^{70}Zn and ^{74,76}Ge from Ref. [76] (blue squares, triangles, and diamonds), and the GLO fit to that data and extrapolation to lower energies (blue solid, dashed, and dot-dashed lines). The last 15 points of the experimental γSF were used to minimize the distance between the experimental γSF and the extrapolations of the (γ,n) data sets. The green band indicates the combined statistical and systematic uncertainty of the SuN data.

Table 3.2: GDR parameters from GLO fits to experimental data from Ref. [76]. E_{E1} is the energy of the giant resonance, Γ_{E1} is the width, and σ_{E1} is the strength. A value of 0.7 for T_f in the GLO function was adopted for all three data sets.

Nucleus	E_{E1} (MeV)	σ_{E1} (mb)	Γ_{E1} (MeV)
^{70}Zn	17.64(6)	97(1)	9.9(2)
^{74}Ge	17.86(10)	95(1)	12.4(4)
^{76}Ge	17.64(9)	101(1)	11.2(4)
Average	17.71(7)	98(1)	11.2(3)

3.6 Cross section and reaction rate calculation

The NLD and γSF obtained using the β-Oslo method technique were input into a Hauser-Feshbach reaction code to obtain the neutron-capture cross section. Previous β-Oslo results have been based on the TALYS reaction code [39, 40], and for consistency this choice was retained for the ^{73}Zn$(n,\gamma)^{74}$Zn reaction, as well as the Ni isotopes that form the basis of this work. TALYS v. 1.6 was used in all cases. A discussion on the differences among a select set of Hauser-Feshbach codes can be found in Chapter 4.

TALYS offers a lot of flexibility for describing both a NLD and γSF, which makes it easy to ensure the NLD and γSF that are used in the calculation represent the experimental data well. The NLD was input in a tabular form generated from a CT model fit to the experimental data, which assumed an equal parity distribution. The γSF was represented as an E1 GLO combined with an exponential function for the upbend. The GDR parameters used in the GLO+exponential fit for the ^{74}Zn data were the average values from the parameters in Table 3.2, which were used to normalize the γSF. The parameters for the upbend were allowed to vary to best fit the upper, middle, and lower γSFs, and the results are detailed in Table 3.3.

Table 3.3: Parameters for the upbend added to the GLO to describe the experimental γSF of ^{74}Zn.

Experimental data set	Exponential constant	Exponential slope
Lower limit	1E-7	-1.4
Middle	1E-7	-1.6
Upper limit	1E-7	-1.9

The GDR parameters were added to the input file for the calculation, but the exponential upbend was added directly to the source code.

The resulting ^{73}Zn$(n,\gamma)^{74}$Zn neutron-capture cross section and reaction rate are shown in Fig. 3.13. For both, the light band is the range in values due to all combinations of NLD and γSF models shown in Table 3.4, which is a subset of the NLD and γSF models available in TALYS, using default parameters. In v. 1.6 there are six NLD models and five γSF models available. One of the NLD models (temperature-dependent Hartree-Fock-Bogolyubov using the Gogny force [31]) and one of the γSF models (SLO [32, 33]) were not used in this work due to systematic disagreements with known data (see Ref. [77]), leaving five NLD and models and four γSF models. The neutron energy range chosen for the cross section (10 keV to 1 MeV) corresponds to likely weak r-process temperatures [14]. The temperature range shown in the reaction rate figure, however, is set by TALYS and can not be changed. The range (0.1 to 10 GK) corresponds to higher neutron energies of $\sim$4-40 MeV (these are the most probable energies in the Maxwell-Boltzman distribution). The dark band is the range in values with the inclusion of the experimentally-constrained NLD and γSF functions. The uncertainty in the neutron-capture cross section was reduced from a factor of 5 (maximum)

Table 3.4: Subset of NLD and γSF models available in TALYS used to determine the uncertainty in the cross section and reaction rate of neutron-rich nuclei.

NLD models	γSF models
CT+BSFG [21]	Kopecky-Uhl GLO [35]
BSFG [21, 78]	Hartree-Fock BCS + QRPA [37]
Generalized super fluid model [79]	Hartree-Fock-Bogolyubov + QRPA [38]
Hartree Fock using Skyrme force [29]	Modified Lorentzian [80]
Hartree-Fock-Bogoliubov (Skyrme force) + combinatorial method [30]	

to less than a factor of 2, while the uncertainty in the reaction rate was reduced from a factor of 11 (maximum) to less than a factor of 2.

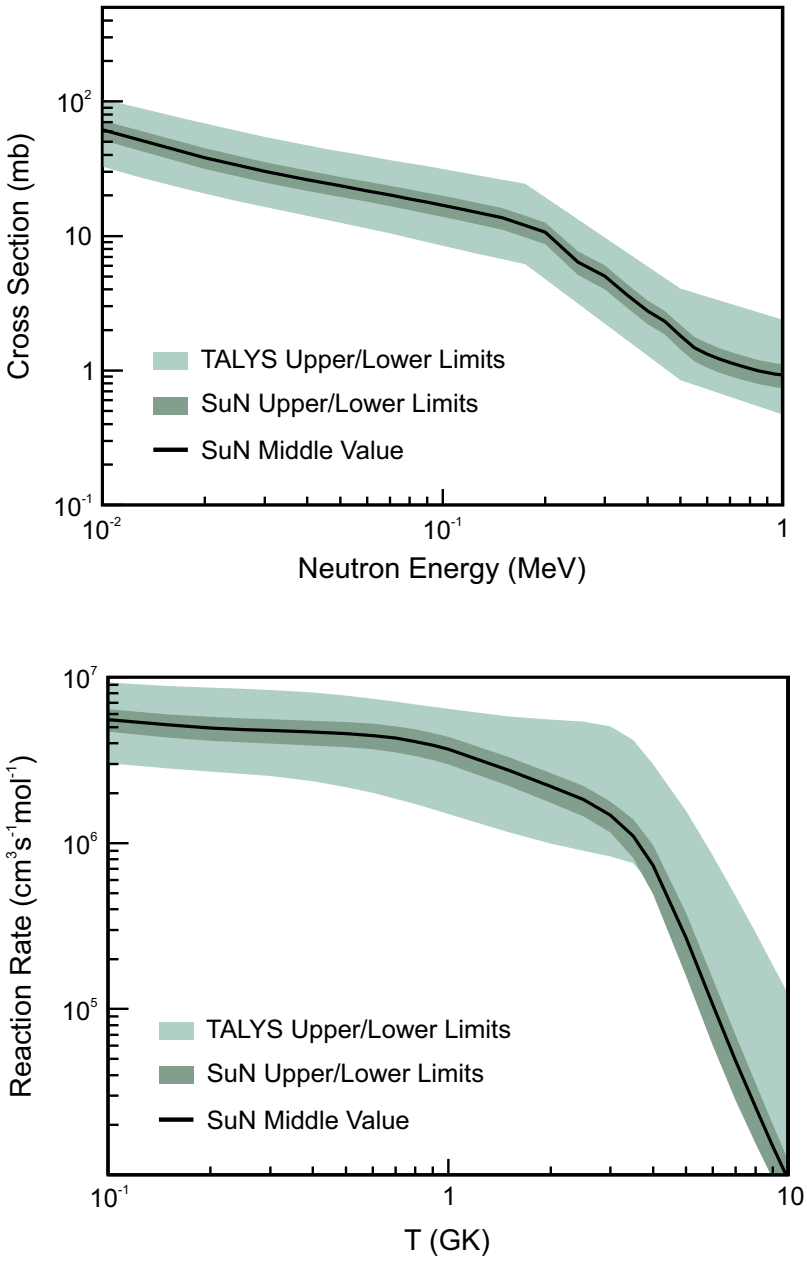

Figure 3.13: (Top) Cross section for the ^{73}Zn(n,γ)^{74}Zn reaction calculated in TALYS. The lighter band shows the variation in the cross section resulting from combinations of the available NLD and γSF options in TALYS. The darker band shows the uncertainty in the cross section when using the experimental NLD and γSF. (Bottom) Astrophysical reaction rate calculated by TALYS. The lighter and darker bands are the same as for the cross section calculation.

Chapter 4

Code Comparison

4.1 Hauser-Feshbach codes

There are many codes available to perform Hauser-Feshbach neutron-capture calculations. Some of the most commonly used codes for astrophysical calculations are TALYS [39, 40], EMPIRE [81], NON-SMOKER [82, 83], and CoH [84]. These codes utilize various forms of the NLD and γSF of short-lived, neutron-rich nuclei, which can lead to differences in how the NLD and γSF are represented in the codes. The uncertainty in both the NLD and γSF increase when moving away from stability [85, 86] for reasons discussed in the last chapter that is reflected in model differences for short-lived, neutron-rich nuclei, leading to large uncertainties in the calculated neutron-capture cross section even within one code (such as the large uncertainties in TALYS described in Chapters 3 and 6). In addition, the agreement between codes is not guaranteed. There have been previous attempts to determine the discrepancy between cross sections calculated by different codes for both stable nuclei [87] and fissionable nuclei [88]. One study with stable nuclei compared the neutron-capture rates calculated using four Hauser-Feshbach codes – TALYS, NON-SMOKER, CIGAR, and SAPPHIRE [89] – and found that variations in the model parameters among the codes resulted in factors of 2-3 difference at 30 keV even with the same model parameters [87]. Another study that focused on fissionable nuclei (^{238}U and ^{239}Pu) compared TALYS, EMPIRE, CoH, and

CCONE [90] (CCONE was developed specifically for actinides). By requiring all the parameters to be the same across the four codes, the authors were able to obtain neutron-induced fission cross sections and neutron inelastic cross sections for both nuclei that matched within 10%. This result is very promising, but does point to the amount of work that is required to make sure all of the parameters are consistent. Both studies used nuclei with well-known nuclear data, so here a new comparison of Hauser-Feshbach codes was performed to determine the uncertainty in the neutron-capture cross section calculated for a short-lived, neutron-rich, and only partially-studied nucleus, ^{73}Zn due to code differences.

Understanding the scale of the uncertainty inherent in the choice of Hauser-Feshbach code is particularly important when utilizing indirect methods to obtain experimentally-constrained NLD and γSFs. The shape of each function, especially the γSF, may not conform exactly to the model that is used in a particular code (the NLD is usually described by the CT or BSFG models and is less likely to vary strongly between codes). Learning how to run a Hauser-Feshbach code with experimental data involves determining what models are available, learning how to adjust the parameters, and understanding how the experimental NLD or γSF is manipulated between when it it included and when it is used in the neutron capture calculation. Checking model predictions between different codes is cumbersome and thus unlikely to be performed for every nucleus with an experimentally-constrained NLD and γSF. However, the potential variation among codes results in an additional source of uncertainty in the neutron-capture cross sections obtained using indirect methods that should be acknowledged. For the ^{73}Zn$(n,\gamma)^{74}$Zn reaction, the neutron-capture cross sections calculated by different codes differed by almost an order of magnitude,and could be reduced to a difference of about 10% only after requiring that the NLD, γSF, and level information were exactly the same.

4.2 Calculation with default settings

First, the neutron-capture cross section was calculated using the default settings for each code in a "black box" calculation. This involved running the Hauser-Feshbach neutron-capture calculation with only the minimum of inputs, such as the target nucleus (^{73}Zn) and neutron energies (0.01 MeV to 1 MeV). The three codes have different models of the NLD and γSF as the default. The TALYS default for the NLD is a CT+FG model [21] with a matching energy of 0 due to the small number of known levels in ^{74}Zn. CoH uses the BSFG model for the NLD, while EMPIRE has employed a generalized superfluid model (GSM) [79] that has been renormalized to discrete levels and S_n information specifically for the EMPIRE code. For the γSF, TALYS uses a GLO function for E1 radiation and SLO functions for all other multipolarities. CoH does the same, but restricts γ-ray emission to L = 1 transitions. EMPIRE uses a modified Lorentzian function (MLO), where the width of the GDR is determined using a semi-empirical expression [91]. The default NLD and γSF assumptions used in each code can be seen compared to the experimental values in Fig. 4.1. For tables of the default NLD and γSF, see Appendix A.

The resulting cross sections, shown in Fig. 4.2, show how different the results can be. Different models for the NLD and γSF affect both the shape and magnitude of the neutron-capture cross section as a function of neutron energy, and variations among models can be an order of magnitude.

4.3 Calculation with experimental data constraints

Tests of the impact of using the same NLD and γSF in each code were performed utilizing the experimentally-constrained NLD and γSF described in Chapter 3 for ^{74}Zn. The NLD was

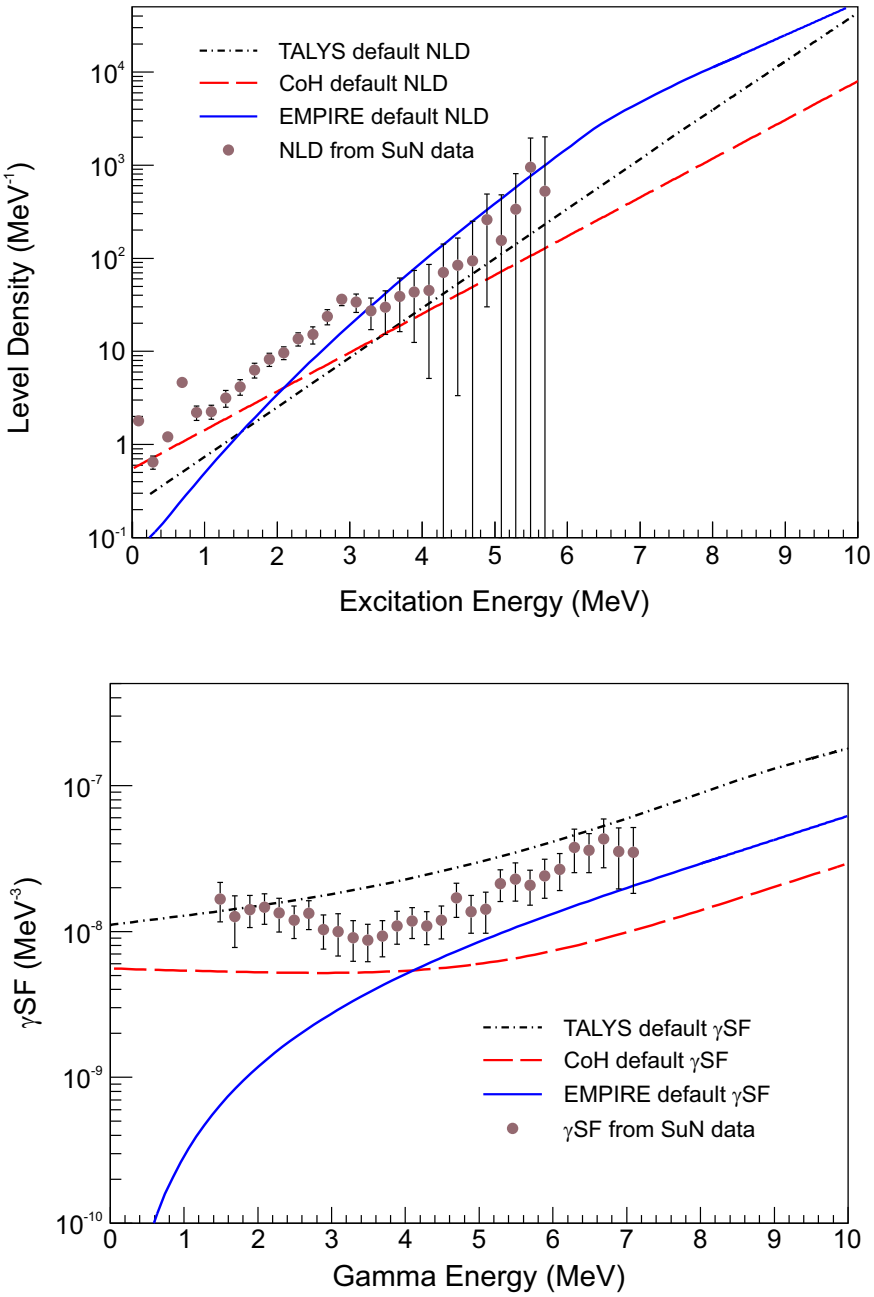

Figure 4.1: (Top) Default NLD for ^{74}Zn in TALYS, CoH, and EMPIRE compared to the experimental NLD obtained using the β-Oslo method. (Bottom) Default γSF for ^{74}Zn in TALYS, CoH, and EMPIRE compared to the experimental γSF obtained using the β-Oslo method.

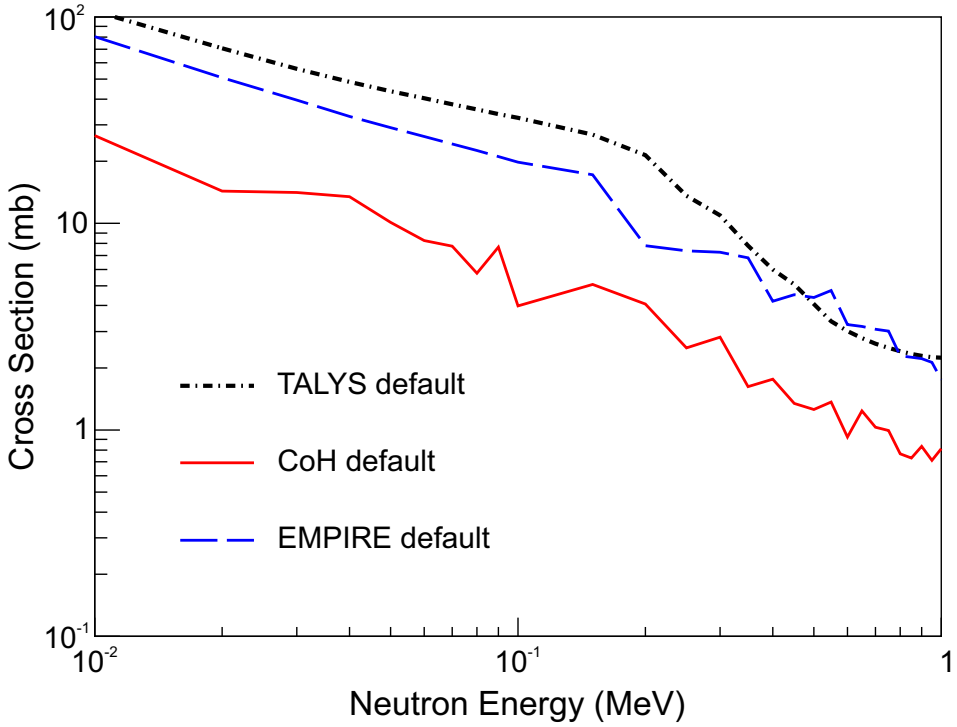

Figure 4.2: Neutron-capture cross section calculated using the default inputs and settings for each of the three codes.

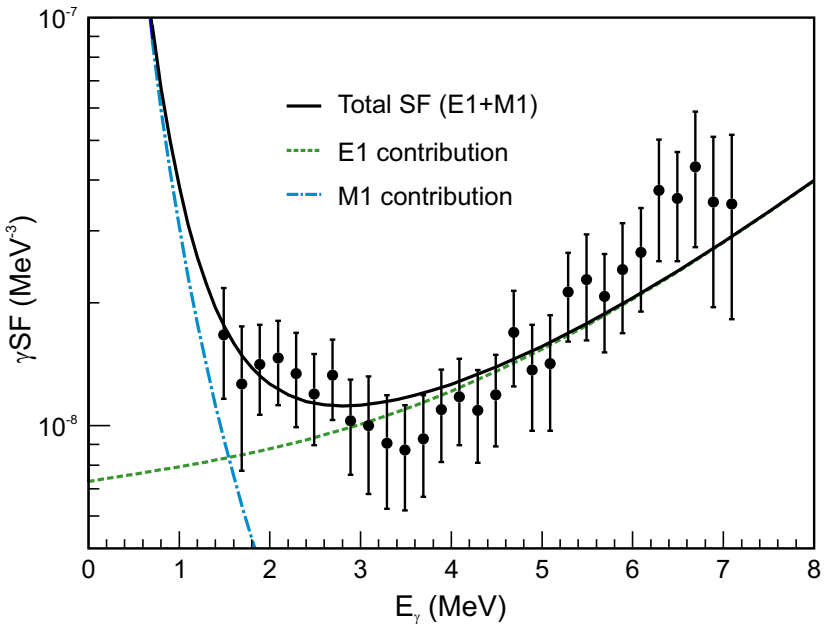

Figure 4.3: Experimental γSF for ^{74}Zn fit with an E1 GLO function plus an M1 SLO upbend.

fit with the CT model described in Chapter 3 to generate a table in the format appropriate for each code. In all cases, an equal parity distribution was assumed. The γSF had more limitations, particularly in CoH. The only model available for E1 radiation in CoH is a GLO function, and an M1 SLO function can be added to represent the upbend component. Due to this limitation, the experimental γSF was fit with a combination of an E1 GLO and an M1 SLO function. When incorporating the experimental γSF into TALYS for the calculation in Chapter 3, an exponential function was used to represent the low-energy upbend, which was incorporated directly into the source code. Direct modification of the source code for CoH and EMPIRE to incorporate the shape of the experimental γSF was more complicated and not pursued. The parameters used in the GLO+SLO fit are given in Table 4.1, while the fit to the experimental γSF is shown in Fig. 4.3.

With the addition of the experimental NLD and γSF, the results from the three calculations were closer, as shown in the top panel of Fig. 4.4. The major difference among them was the shape as a function of neutron energy–at $\sim$200 keV the TALYS calculation

Table 4.1: GLO E1 parameters and SLO M1 parameters used to fit the experimental γSF.

E_{E1} (MeV)	17.7(1)
σ_{E1} (mb)	98(2)
Γ_{E1} (MeV)	11.2(6)
E_{M1} (MeV)	4.63 x 10^{-7}(500)
σ_{M1} (mb)	39(9)
Γ_{M1} (MeV)	0.096(88)

decreased, while the EMPIRE and CoH calculations did not. The scale of these differences can also be seen in the bottom panel of Fig. 4.4, where the percentage deviation of EMPIRE and CoH from TALYS is shown. At low neutron energies, the CoH calculation was very close to TALYS, and even the EMPIRE calculation differed by less than 50%. At ∼200 keV, however, the deviation jumped to almost 200% for both. The TALYS cross section was chosen as the comparison model due to its unique shape at this step. The deviation at ∼200 keV can be explained by the first excited state of ^{73}Zn at 195.5(2) keV [92]. If the level was used in the code for neutron inelastic scattering on ^{73}Zn then the neutron-capture cross section would decrease at 195.5 keV. The decrease in the cross section calculated in TALYS indicated that inelastic scattering was present. In both CoH and EMPIRE, however, the level was not contributing to inelastic scattering. An investigation of the ^{73}Zn levels being in each code found that EMPIRE does not assign the 195.5 keV level a spin or parity, while CoH does but considers it a poorly known level, so it is not used in the calculation (see Table 4.2).

It is important to note that while the NLD is the same as used in the TALYS calculation in Chapter 3, the γSF is represented differently due to code restrictions. Therefore, the neutron-capture cross sections from TALYS in Fig. 3.13 and Fig. 4.4 are not comparable.

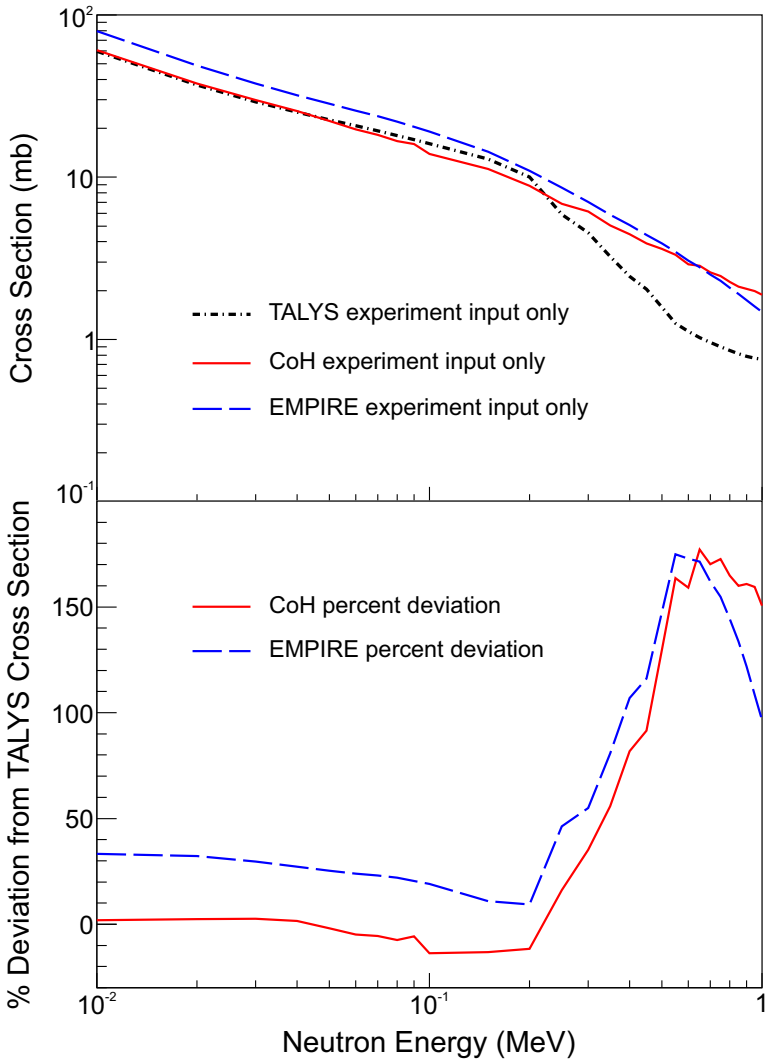

Figure 4.4: (Top) TALYS, EMPIRE, and CoH ^{73}Zn(n,γ)^{74}Zn cross sections using experimentally obtained NLD and γSF. All other aspects of the codes were left to default conditions. (Bottom) Percent deviation of the CoH and EMPIRE cross sections compared to the TALYS cross section after including the experimental NLD and γSF. See text for discussion of the kink at E_n $\sim$200 keV.

4.4 Final calculation

The details of the level energies and spin/parity assignments used in each code, as well as the suggested values in RIPL-3, are detailed in Tables 4.2 and 4.3. For consistency, most levels were given the spin/parity assignments used TALYS, which had the most complete assignments. When there is no suggested spin/parity assignment in RIPL-3, TALYS assigns a spin and parity based on statistical rules. Two assignments were changed from the original TALYS assignment–the 3^+ for the 1418.56 keV level was changed to 4^+ due to an updated ENSDF evaluation in 2017 that suggested a 4^+ assignment from Coulomb excitation [93], while the 5^- for the 2148.2 keV level was changed to 2^+ due to the suggested values of (1, 2^+) in RIPL-3. CoH in particular needed to have levels "turned on" for use. The results for the cross section calculations after the level assignments were adjusted are shown in Fig. 4.5. At this point the results from the three codes agreed very well, with EMPIRE about 10% above the TALYS and CoH calculations. This small discrepancy was due to the different methods for describing the width-fluctuation corrections (WFC). The WFC accounts for the correlation between the incident and exit channels in elastic scattering, and affects the neutron-capture cross section through the elastic scattering component of the neutron-nucleus interaction. CoH uses a WFC described in [94] based on the Moldauer approach [95] that is used in TALYS, so they are very similar. EMPIRE uses the HRTW (Hofmann, Richert, Teppel, and Weidenmöller) approach, which has been shown to produce different neutron-capture cross sections than the Moldauer formulation at the 10% level [96, 97].

In summary, it is possible to obtain similar neutron-capture cross sections for a neutron-rich nucleus with different Hauser-Fesbach codes when the differences in input and model

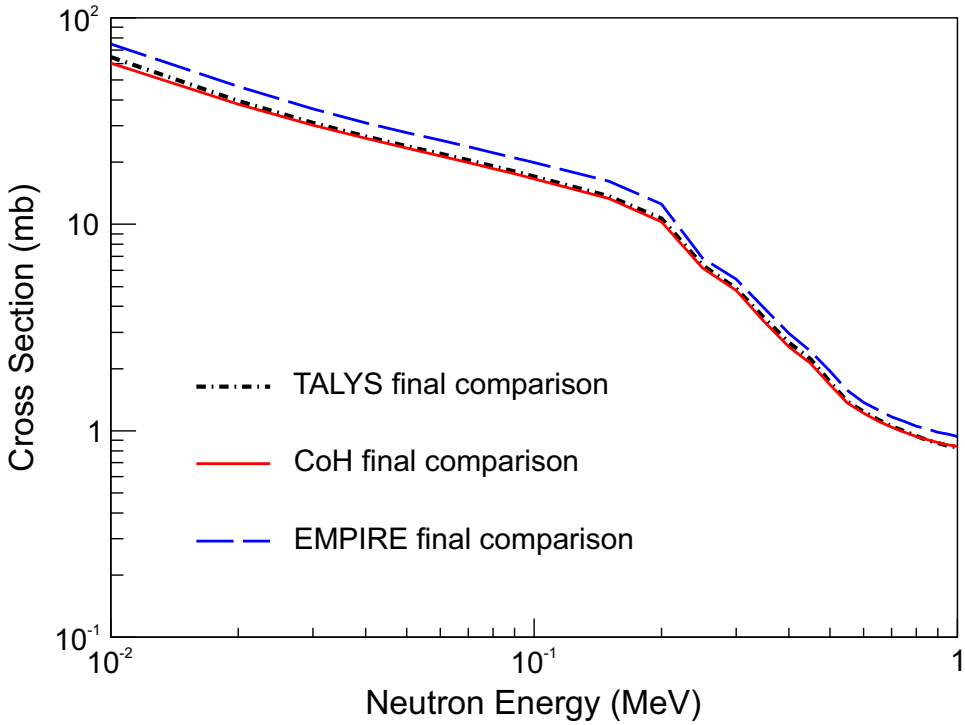

Figure 4.5: Neutron-capture cross section calculated after accounting for differences in the nuclear physics inputs between the codes.

Table 4.2: ^{73}Zn level energies, spins, and parities including the values assigned in TALYS, CoH, and EMPIRE, as well as the RIPL-3 suggested levels and the values used in the final comparison.

^{73}Zn level energy (keV)	Suggested spin/parity (RIPL-3)	Final spin/parity used	TALYS spin/parity	CoH spin/parity	EMPIRE spin/parity
0	$(1/2^-)$	$1/2^-$	$1/2^-$	$1/2^-$	$1/2^-$
195.5 [ab]	$(5/2^+)$	$5/2^+$	$5/2^+$	$3/2^+$	no assignment
307.2 [ab]	(5/2)	$5/2^+$	$5/2^+$	no assignment	no assignment
337 [ab]	none	$3/2^+$	$3/2^+$	$3/2^-$	no assignment
449.6 [ab]	$(3/2^-)$	$3/2^-$	$3/2^-$	no assignment	no assignment
502.2 [ab]	(5/2)	$5/2^-$	$5/2^-$	no assignment	no assignment
1124 [ab]	(5/2)	$5/2^-$	$5/2^-$	no assignment	no assignment
2008.9 [ab]	(5/2)	$5/2^-$	$5/2^-$	no assignment	no assignment

[a] Level not used by CoH.
[b] Level not used by EMPIRE.

Table 4.3: ^{74}Zn level energies, spins, and parities including the values assigned in TALYS, CoH, and EMPIRE, as well as the RIPL-3 suggested levels and the values used in the final comparison.

^{74}Zn level energy (keV)	Suggested spin/parity (RIPL-3)	Final spin/parity used	TALYS spin/parity	CoH spin/parity	EMPIRE spin/parity
0	0^+	0^+	0^+	0^+	0^+
605.9	2^+	2^+	2^+	2^+	2^+
1418.56 [a]	(0^+, 4^+)	4^+	3^+	no assignment	0^+
1670.25	(2^+)	2^+	2^+	2^+	2^+
1788.9 [a]	none	1^+	1^+	no assignment	0^+
2099.23 [a]	none	4^-	4^-	no assignment	0^+
2148.2 [a]	(1, 2^+)	2^+	5^-	no assignment	0^+
2353.6 [a]	none	3^+	3^+	no assignment	0^+
2551.88 [ab]	none	1^+	1^+	no assignment	no assignment
2657.6 [ab]	none	6^-	6^-	no assignment	no assignment
2698 [ab]	none	1^+	4^-	no assignment	no assignment
2809.04 [ab]	none	2^-	2^-	no assignment	no assignment
2904.73 [ab]	none	3^-	3^-	no assignment	no assignment
2969.3 [ab]	none	1^-	1^-	no assignment	no assignment
2985.9 [ab]	none	7^+	7^+	no assignment	no assignment
3063.9 [ab]	none	2^-	2^-	no assignment	no assignment
3067 [ab]	none	5^+	5^+	no assignment	no assignment
3571 [ab]	none	3^-	3^-	no assignment	no assignment
4562.4 [ab]	none	4^+	4^+	no assignment	no assignment
4861.8 [ab]	none	1^-	1^-	no assignment	no assignment
4896.8 [ab]	none	2^+	2^+	no assignment	no assignment
5628 [ab]	none	0^-	0^-	no assignment	no assignment

[a] Level not used by CoH.
[b] Level not used by EMPIRE.

assumptions are removed. The difficulty in verifying that all the inputs, and the NLD and γSF models, are the same is large, however, and the situation is made even more complicated by any limitations in structure information for such short-lived nuclei. The calculated cross sections are sensitive to the spins and parities of excited states in both the neutron-capture compound nucleus and the target nucleus. If those values are not known, they need to either be determined from theory or the level is disregarded completely (which is not physical), changing the resulting cross section calculation. The overall uncertainty in a neutron-capture cross section, even when constrained using experimental data from an indirect method, is therefore larger by some amount due to the choice of Hauser-Feshbach code used. For this case, the "black box" calculations deviated by up to 80%, which is not an insignificant source of uncertainty.

Chapter 5

Analysis of Co Decays

The β decay of three neutron-rich Co isotopes (71,72,73) was studied using the β-Oslo method to extract the NLD and γSF of the corresponding daughter isotopes. Details of the analysis, including the method for obtaining the particle identification as well as the β-Oslo analysis is presented.

5.1 Particle identification

The uncorrected particle identification plot (PID) is shown in Fig. 5.1. The energy loss was measured in an upstream PIN detector, while the time-of-flight (TOF) was measured between the I2 scintillator and the PIN detector. The momentum acceptance of the A1900 was set to 5%, which led to the broad distributions in TOF for each isotope. A second, smaller distribution was present at smaller TOF (approximately 2 ns) for each isotope. The smaller distribution was present in all experimentally recorded TOF signals, and was likely due to a trigger issue with the I2 scintillator used for the TOF. The identity of the isotopes with the shifted TOF were verified using known γ rays, which confirmed that each isotope delivered was observed at two separate TOF. A 2D gate was placed around each elemental band in an uncorrected PID that used the sum of the energy deposition in both PIN detectors (PIN1 + PIN2) instead of dE in a single PIN detector. The increased separation between the distributions when using the summed PIN energy can be seen in Fig. 5.2, which also

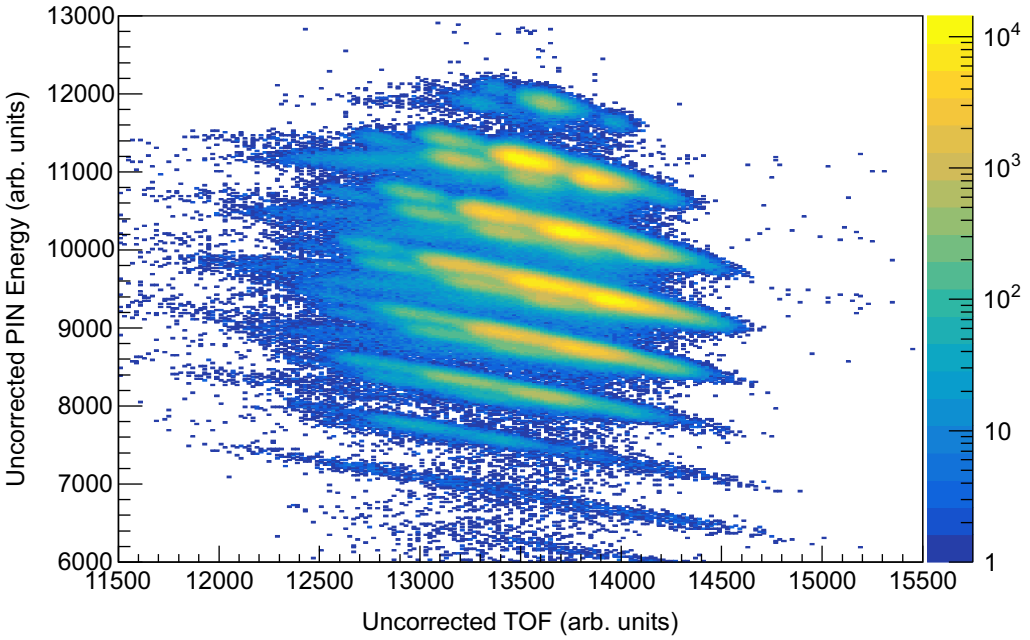

Figure 5.1: PID with uncorrected PIN energy versus uncorrected time-of-flight (determined between the I2 scintillator and a PIN detector).

contains the gates that were used to select only the major distribution. Approximately 10% of the data fell outside of the gates shown.

The remaining analysis utilized only the data within the gates shown in Fig. 5.2. Even after taking a cleaner cut of data, there were still multiple distributions as a function of I2 scintillator position, which can be seen as "wings" around the main distribution in Fig. 5.3. The position of the ion in the I2 scintillator was determined by taking the time difference between the signals from the two PMTs on either side of the scintillator. Only about 10% of the data was located outside of the main distribution, so a cut on the I2 position was used to remove the extra events. The location of the main distribution in the I2 position was slightly different for each element band, so a 2D gate was placed on the PIN energy versus I2 position spectrum (also shown in Fig. 5.3).

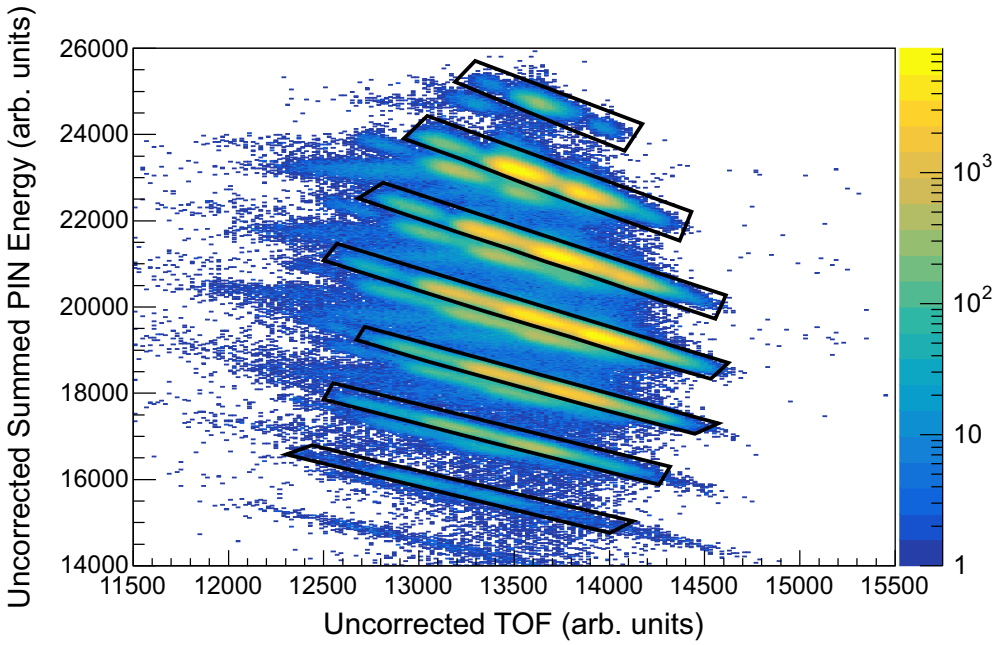

Figure 5.2: PID with uncorrected, summed PIN energy (energy deposited in both PIN detectors summed together) versus uncorrected TOF.

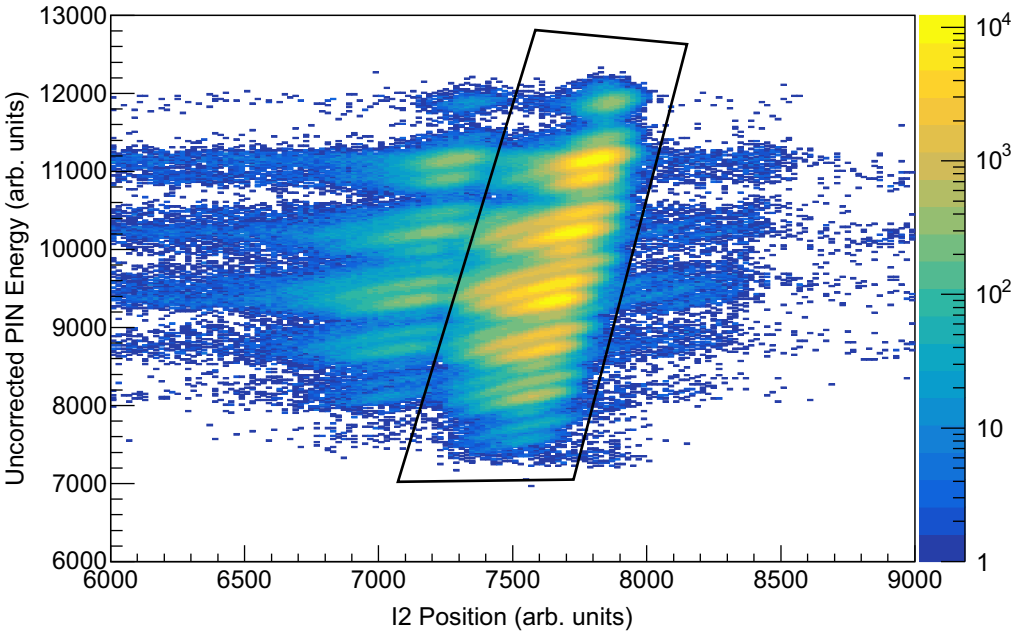

Figure 5.3: Uncorrected PIN energy versus I2 position (determined by the time difference between signals from the north and south PMTs on the I2 scintillator) for all data within the gates shown in Fig. 5.2.

5.1.1 I2 position corrections

The fragment beam is dispersed according to momentum at I2 and the TOF is correlated with position. When the slits are open to a momentum acceptance of 5%, the TOF of the ions needs to be corrected based on the location of the ion in the I2 scintillator in order to improve the PID because an ion that hits one side of the I2 scintillator has a lower velocity through the A1900 than if the same ion hit the opposite side. A correction to the TOF was applied so that the TOF of each isotope was independent of the position in the I2 scintillator. The difference between the uncorrected and corrected TOF for the Co isotopes can be seen in Fig. 5.4. In each figure, the TOF is plotted against the position in the I2 scintillator. The uncorrected TOF figure (top) also shows multiple distributions in the I2 position, while the corrected TOF figure (bottom) has the I2 position gate from Fig. 5.3 applied, so only the main distribution is present. The bands retain a slight curvature but the major dependence was removed.

The TOF was not the only parameter that needed to be corrected to improve the PID. The energy deposited in the PIN detectors was also dependent on the I2 position, which can be seen for the Co isotopes in the top panel of Fig. 5.5. The corrected dE of the Co isotopes for PIN1, plotted against the I2 position, is shown in the bottom panel of Fig. 5.5, with the I2 position gate applied. Figure 5.6 shows the final PID used in the analysis, and also has the ^{71,72,73}Co isotopes used in this work highlighted. The number of ions of each nucleus delivered to the end station is given in Table 5.1.

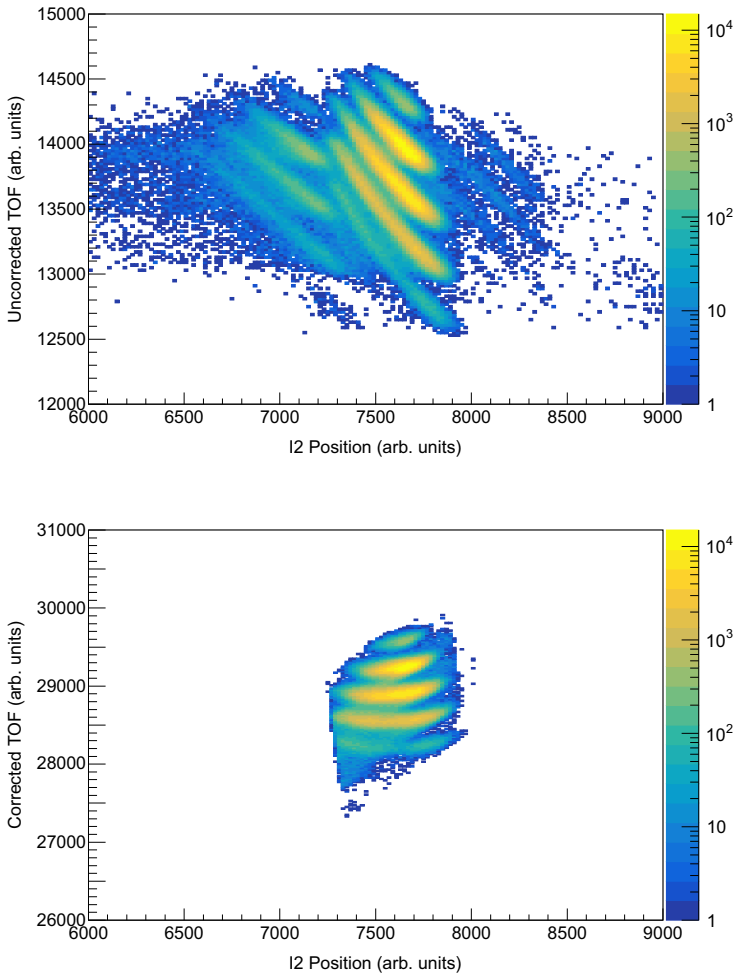

Figure 5.4: (Top) Uncorrected TOF versus I2 position for all Co isotopes. (Bottom) Corrected TOF versus I2 position for all Co isotopes, with the PIN energy versus I2 position gate shown in Fig. 5.3 applied.

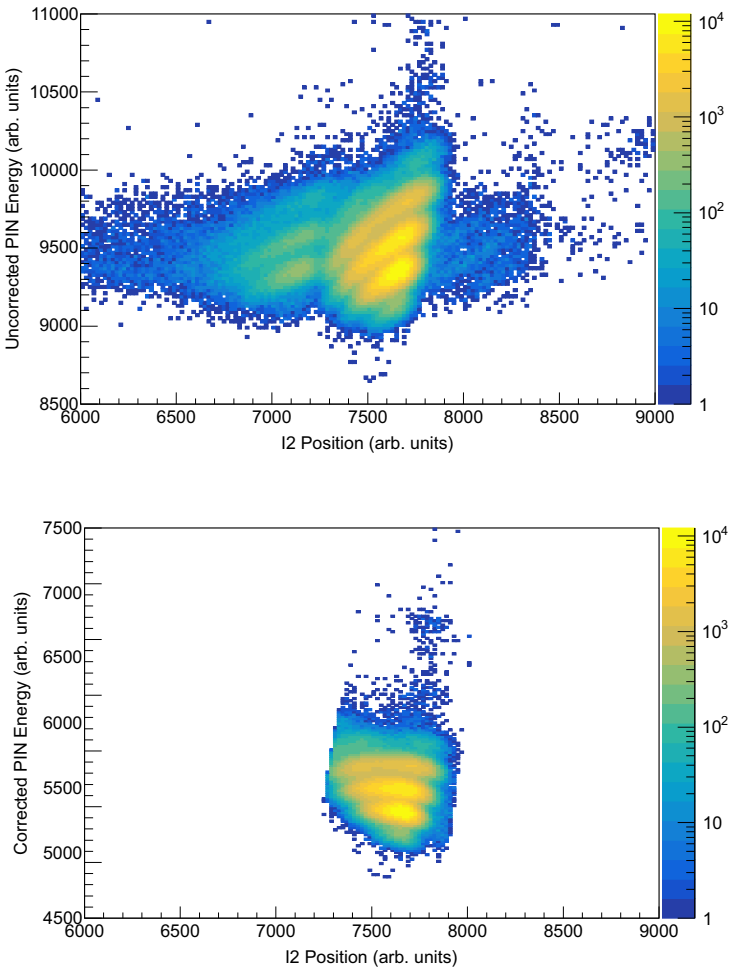

Figure 5.5: (Top) Uncorrected PIN energy versus I2 position for all Co isotopes. (Bottom) Corrected PIN energy versus I2 position, with the PIN energy versus I2 position gate shown in Fig. 5.3 applied.

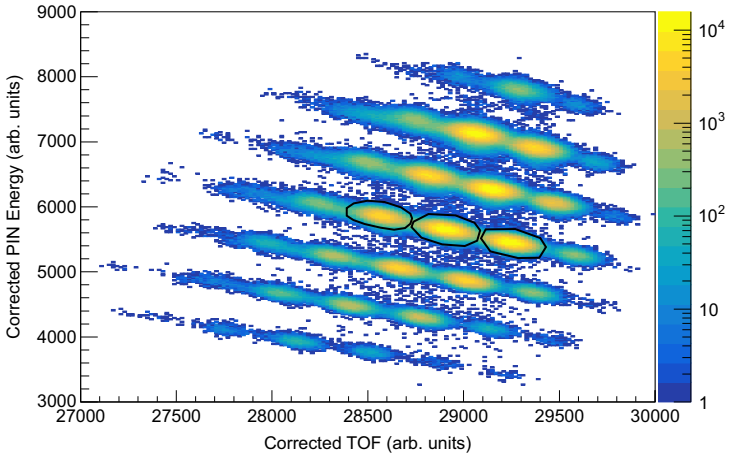

Figure 5.6: Final decay PID, with corrected PIN energy versus corrected TOF and all element gates (Fig. 5.2) as well as I2 position gate (Fig. 5.3) applied.

Table 5.1: Number of ions of each isotope delivered to S2 in e16505. Number was determined after the PID corrections but before the application of the correlator software.

Isotope	Number of Ions	Isotope	Number of Ions	Isotope	Number of Ions
^{64}Cr	154	^{70}Fe	203990	^{74}Ni	697393
^{65}Cr	1463	^{71}Fe	36073	^{75}Ni	326142
^{66}Cr	3371	^{72}Fe	3579	^{76}Ni	28828
^{67}Cr	474	^{73}Fe	88	^{77}Ni	1396
^{65}Mn	176	^{70}Co	13930	^{75}Cu	1587
^{66}Mn	2074	^{71}Co	605035	^{76}Cu	277236
^{67}Mn	41383	^{72}Co	633027	^{77}Cu	707004
^{68}Mn	33136	^{73}Co	247223	^{78}Cu	33693
^{69}Mn	8555	^{74}Co	18051	^{79}Cu	2558
^{70}Mn	526	^{75}Co	827	^{78}Zn	637
^{68}Fe	13999	^{72}Ni	295	^{79}Zn	18799
^{69}Fe	203581	^{73}Ni	98246	^{80}Zn	934

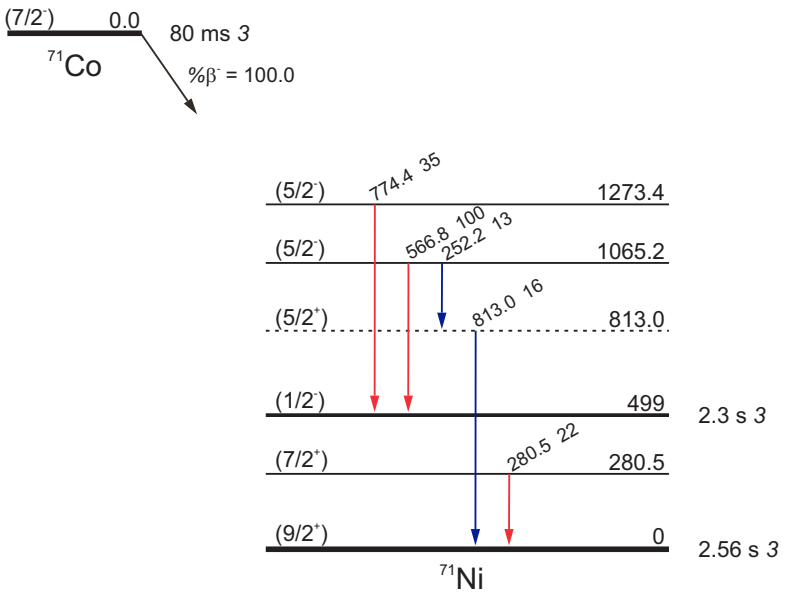

Figure 5.7: Known level scheme for the β decay of ^{71}Co. All γ-ray intensities are relative to the 566.8 keV transition.

5.2 ^{71}Co decay

The half-life of ^{71}Co is known to be 80(3) ms [67], so a correlation time of 150 ms was used. The decay curve for ^{71}Co was obtained from the time difference between correlated ions and decays, and includes contributions from the parent (^{71}Co) decay, daughter (^{71}Ni) decay ($t_{1/2}$=2.56 s [67]), and random correlations. The SuN spectra (both γ rays and TAS) contained all of these components, and the contribution from the daughter decays and random correlations needed to be removed to leave only γ rays from the decay of the parent. By fitting the full decay curve with a combination of all of the components, the number of daughter decays and random correlations was determined and could be removed, which is described in detail in this section.

The apparent half-life of the daughter ^{71}Ni was calculated because of a long-lived isomeric state at 499 keV. The isomer half-life, 2.3(3) s [98], is the same as the ground state half-life of 2.56(3) s [67] within uncertainties. Decays from both states were expected in the experiment,

as both the 1065 keV level and a corresponding level at 566 keV (detected when the 1095 keV level de-excited to the 499 keV β-decaying isomeric state) were observed (see level scheme in Fig.5.7). By fitting the TAS peaks at 1065 keV and 566 keV it was determined that 19(1)% of the ^{71}Ni decays were from the ground state, leading to an effective ^{71}Ni half-life of 2.3(4) seconds. The daughter half-life was fixed in the fitting procedure using the calculated value, as was the decay constant of the exponential background. The shape of the background was obtained from the backwards correlation by fitting the decay curve with a simple exponential function to extract the decay constant, which was used to fix the decay constant of the background component in the forward correlation. The half-life of the parent as well as the magnitude of the exponential background were left as free parameters in the fit.

The measured decay curve is shown in Fig. 5.8 as the black histogram, while the blue histogram represents the decay curve from the backwards correlation. The blue dotted line is the fit to the backwards correlator decay curve, which was used to set the decay constant of the background. The black line describes the combined fit to the decay curve, including the parent decay (red dot-dash line), the daughter decay (green dash line), and the background component (gold dot-dash line). From this fit, the parent half-life was extracted and compared to the known half-life. For ^{71}Co, the extracted half-life of 84(7) ms matched the known half-life of 80(3) ms [67]. The number of parent decays, daughter decays, and background counts (random correlations) in the 150 ms correlation window could also be obtained. These values are important for understanding how much of the daughter and background was contained in the raw SuN spectra, and therefore how much needed to be removed. The relevant values, including the number of counts in the decay curve from the backwards correlation, are given in Table 5.2.

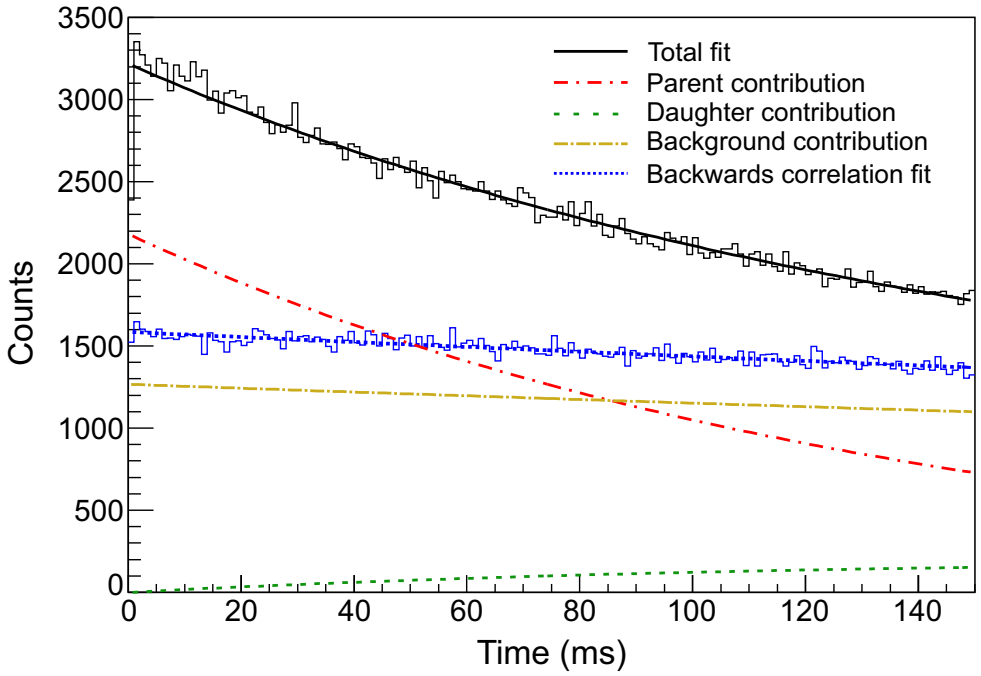

Figure 5.8: Full decay curve fit for the decay of ^{71}Co including the parent contribution (red dot-dash line), daughter contribution (green dotted line), and background contribution (gold dot-dash line). The black histogram is the full decay curve from the data, with the total fit (combination of parent, daughter, and background) shown with the black solid line. The shape of the background contribution was determined using a correlation backwards in time, shown as the blue histogram. The blue dashed line fit to the backwards correlation set the background contribution shape, and the magnitude was allowed to vary to determine the blue dot-dash line.

Table 5.2: Results of decay curve fit for ^{71}Co decay using a 150 ms correlation time (see Fig. 5.8).

Number of parent decays	157210(920)
Number of daughter decays	3954(18)
Number of random correlations	171070(150)
Number of events in backwards correlation	221190(36)

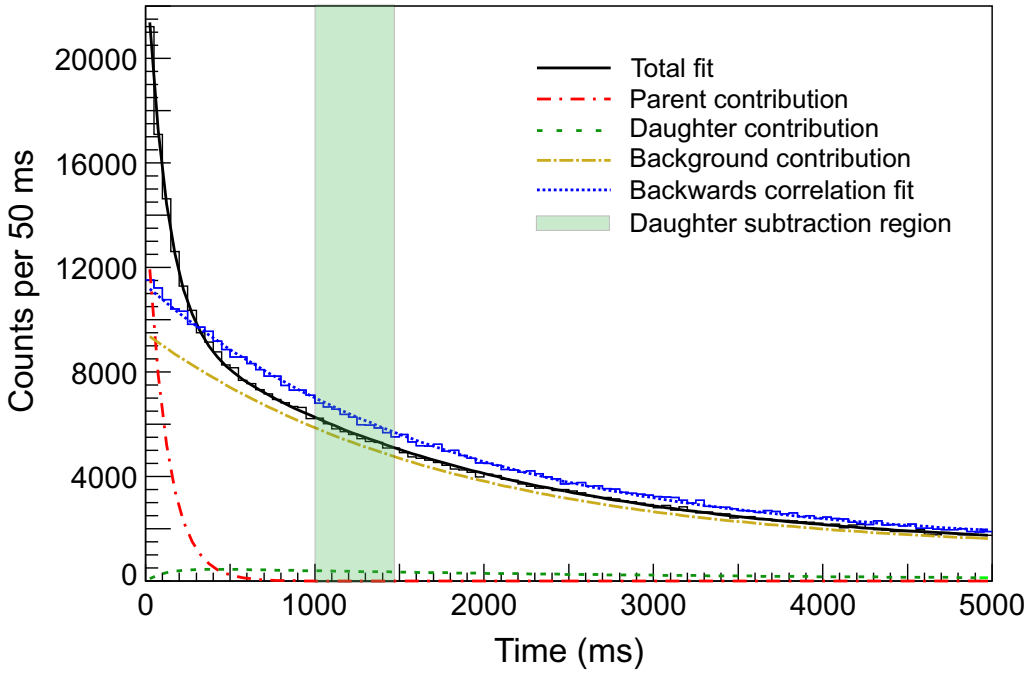

Figure 5.9: Long correlation time decay curve fit for the decay of ^{71}Co. The green band shows the time region used to remove the daughter contribution to the SuN spectra. The parent and daughter decay constants were set from the fit shown in Fig. 5.8. The background component was determined the same way as in Fig. 5.8.

Table 5.3: Results of decay curve fit for ^{71}Co decay using a 5 sec correlation time (see Fig. 5.9).

Number of daughter decays in subtraction region	3960(170)
Number of random correlations in subtraction region	50954(99)

A representative spectrum including the daughter and background γ-ray events was removed from the SuN spectra (segments and TAS) based on spectra from a time window where only daughter decays were occurring. To find such a time window, a longer correlation time was used–5 seconds instead of 150 ms. At long decay times the ^{71}Ni decays are expected to dominate the spectra. The decay curve from the 5 sec correlator, including all the components, can be seen in Fig. 5.9. The same fitting procedure was used for the longer correlator, with the daughter half-life set to the known value, the parent half-life set to the value obtained using the 150 ms correlator, and the background decay constant set by fitting the backwards in time correlation in the 5 sec correlator. Between 1000 ms and 1484 ms the same number of ^{71}Ni decays, 3960(170), occurred as with the 150 ms correlation time. A much longer time was needed to see the same number of decays because of the longer minimum implantation time, which resulted in a lower correlation efficiency (see Section 2.3). There was also background in that time window due to random correlations (see Table 5.3). After removing the daughter decays, 120100(100) background counts were left to be removed in the 150 ms correlation. The reverse time correlation was used to represent that background, scaled to the total number of counts that needed to be removed. The reverse time correlation had 221190(36) counts, while only 120100(100) counts needed to be removed. The backwards correlation was scaled appropriately to remove the correct amount of background remaining in the spectra.

The segments and TAS spectra for ^{71}Co are shown in Fig. 5.10. In each, the black histogram shows the raw SuN spectrum, the blue shows the scaled SuN spectrum from the backwards correlation, and the green shows the daughter contribution from the later time window. The red is the parent contribution, obtained by subtracting the blue and green spectra from the raw (black line) spectrum.

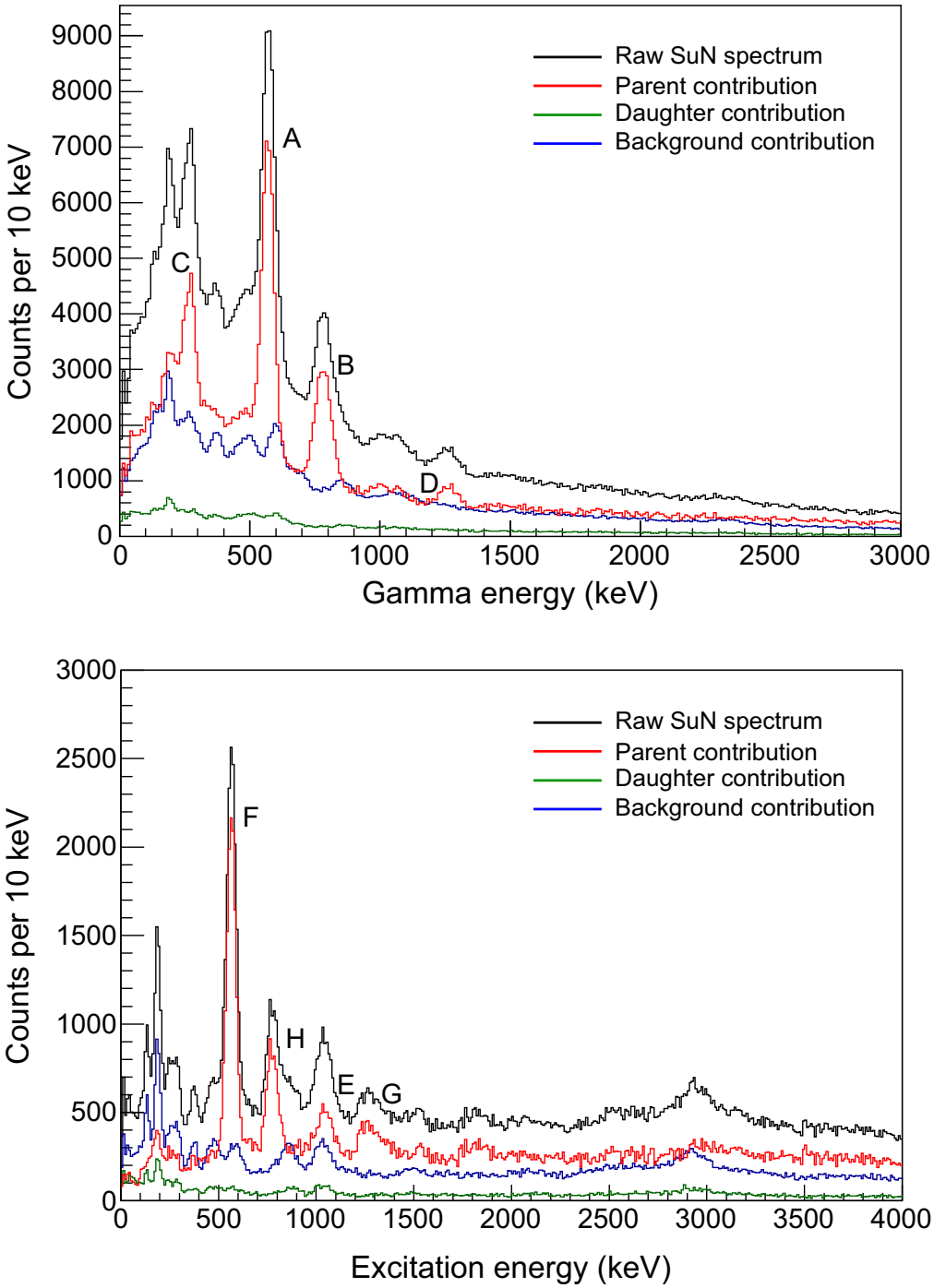

Figure 5.10: (Top) ^{71}Co SuN γ-ray spectrum showing the raw spectrum (black), daughter decay contribution (green), background contribution (blue), and parent decay contribution (red). (Bottom) TAS spectrum for the same decay.

The strongest β-delayed γ-ray transition following the decay of ^{71}Co into ^{71}Ni is known to be 566.8 keV [A], with a relative intensity of 100%. That peak was clearly observed in the parent segments spectrum, followed by the 774.4 keV transition [B] ($I_\gamma = 35\%$) and the 280.5 keV transition [C] ($I_\gamma = 22\%$). Another γ ray was seen at 1273 keV [D], which corresponds to the de-excitation of the 1273.4 keV level directly to the ground state, and has not been seen in the literature. The β-decay feedings for the decay of ^{71}Co are not well known, but the 1065.4 keV level [E] is the most populated. It de-excites to the long-lived isomer at 499 keV, as well as through a weaker branch that bypasses the isomer, so peaks at both 1065 keV and 566 keV [F] are seen in the TAS spectrum. The 1273.4 keV level [G], along with the 774 keV peak arising from transitions to the isomeric state [H] were clearly seen as well.

5.2.1 β-Oslo matrices

The β-Oslo matrix, with the total excitation energy, E_x, on the y-axis and the energy of a single γ ray, E_γ, on the x-axis, was obtained by taking the experimental spectrum and subtracting the daughter and background contributions (the starting matrix, as well as those with the daughter component and background component can be seen in Appendix B). The raw 2D matrix was then unfolded to remove the detector response and the primary γ spectra were obtained following the procedure described in Chapter 3. The raw matrix can be seen in Fig. 5.11, with 200-keV wide bins on both axes. The matrix was rebinned to 600 keV before unfolding in an attempt to mitigate the impact of the isomeric state in ^{71}Ni by combining each set of levels offset by 499 keV. The unfolded matrix can be seen in Fig. 5.12. The region of the primary matrix used to extract the NLD and γSF is highlighted in Fig. 5.13, and was restricted to $E_\gamma > 1000$ keV and $E_x \in (2400, 4800)$ keV. The upper E_x limit was set above the $\rho(S_n)$ of ^{71}Ni, which is 4.264(3) MeV [67]. The first excited state of ^{70}Ni has

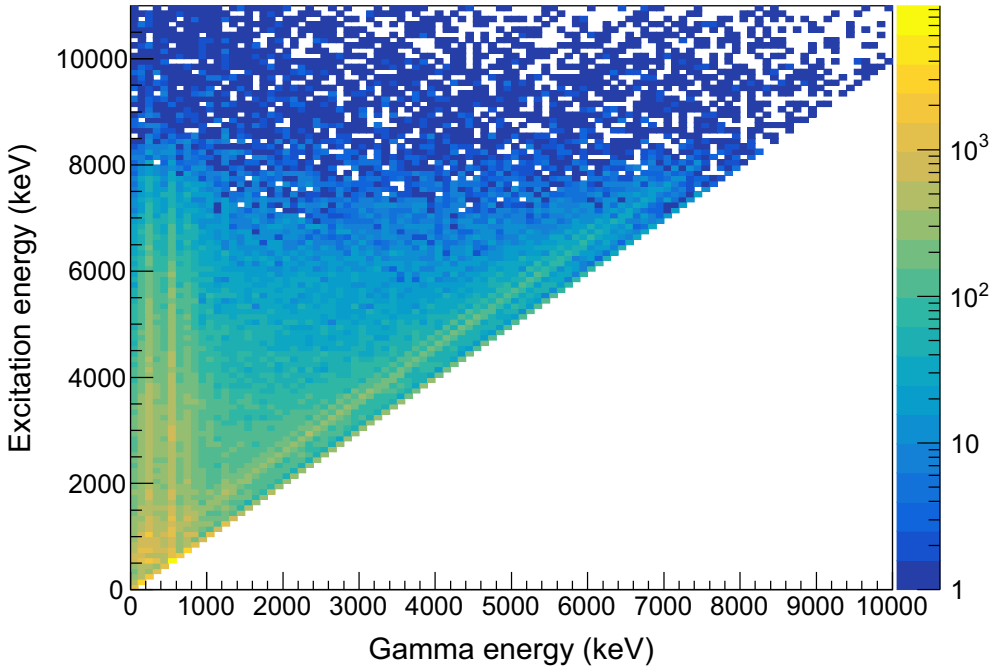

Figure 5.11: Raw 2D Oslo matrix for the decay of ^{71}Co into excited states of ^{71}Ni. The γ-ray energies obtained from the segments of SuN are plotted on the x-axis, while the excitation energy of the daughter nucleus, obtained from the total energy in the detector, is plotted on the y-axis.

an energy of 1259.55(5) keV [99], which allowed for the upper E_x limit to be increased to slightly above $\rho(S_n)$ without the possibility of contamination of γ rays from the β-delayed neutron daughter.

5.2.2 NLD normalization

As described in Chapter 3, the $\rho(S_n)$ value was determined using cumulative levels calculated by Goriely [30] and shifted in excitation energy to match the known low energy levels. There are 5 excited states known in ^{71}Co, all below 1.3 MeV. The known levels are all from β-decay experiments, so the calculated cumulative level distribution was reduced to include

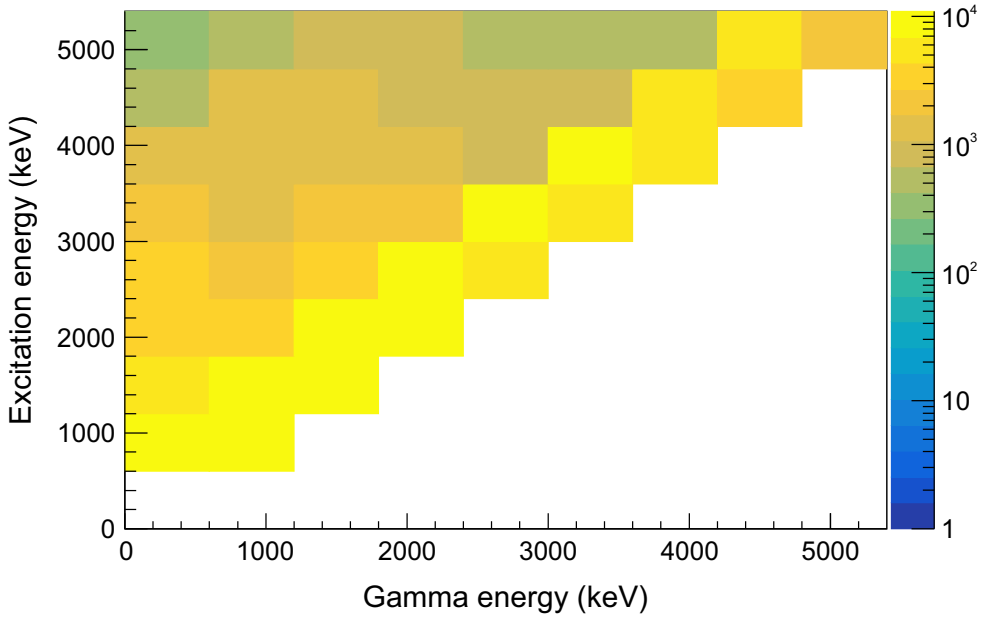

Figure 5.12: Unfolded 2D matrix for ^{71}Ni with 600 keV binning on both axis.

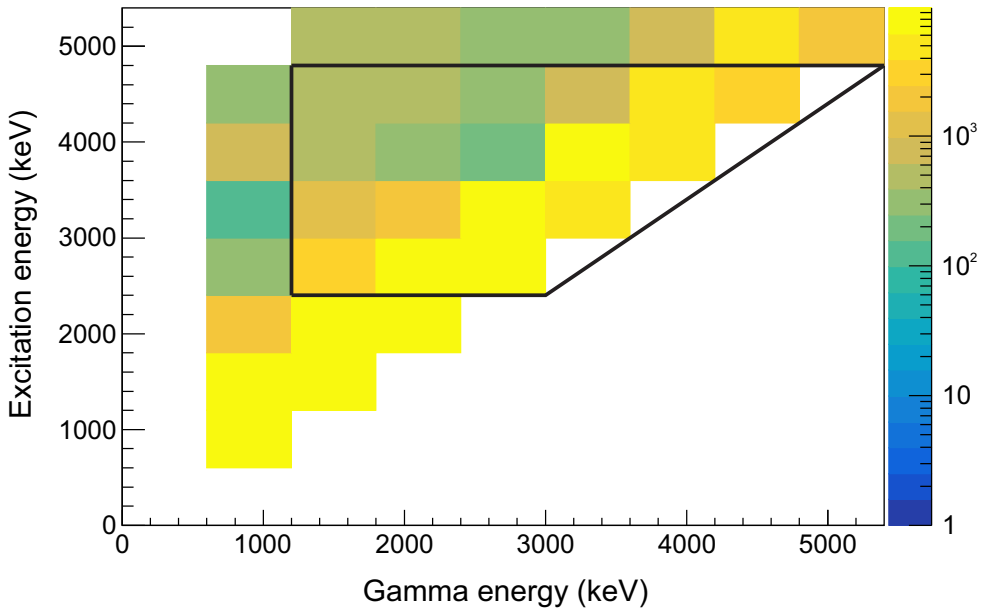

Figure 5.13: Primary 2D matrix for ^{71}Ni with 600 keV binning on both axis. The extraction region used for the NLD and γSF is outlined by the black lines.

Table 5.4: Parameters used in exponential fit to shifted calculated NLD.

Shift Value	Constant	Slope	$\rho(S_n)$ (MeV^{-1})
0 MeV	3.8(14)	1.02(7)	300(150)
0.25 MeV	3.0(12)	1.02(7)	230(120)
0.5 MeV	2.3(9)	1.02(7)	178(92)

only those with spins populated following an allowed β decay from the tentatively assigned $(7/2^-)$ ground state of ^{71}Co and one dipole transition, leading to a range of spins from 3/2 to 11/2. The χ^2 minimization result for the shifting of the reduced calculated cumulative levels is shown in Fig. 5.14. The second-order polynomial fit resulted in a best shift value of 0.25 $\pm$ 0.25 MeV. The reduced theoretical cumulative level distribution corresponding to the best shift, as well as the upper and lower limit shifts of 0 MeV and 0.50 MeV are shown in Fig. 5.15, compared to the known cumulative levels. The large uncertainty was due to the small number of known levels in ^{71}Ni. The shifted NLD around S_n was fit with an exponential function to determine the value of $\rho(S_n)$. The shifted calculated NLD are shown in Fig. 5.16, with the S_n of ^{71}Ni (4.264 MeV) shown in comparison to the energy range used in the fit to extract the $\rho(S_n)$ values. Due to the low S_n of ^{71}Ni, the calculated NLD was fit mostly above S_n, where it was more exponential in shape. The fit results are detailed in Table 5.4, and resulted in lower, middle, and upper values of $\rho(S_n)$ of 178(92), 230(120), and 300(150) MeV^{-1}, respectively.

The only information known about ^{71}Ni comes from β-decay experiments, so a full NLD could not be obtained due to the lack of known levels at low energies. Instead, the known levels at low energies from β decay and the reduced $\rho(S_n)$ value were needed to normalize the experimental NLD. The reduced $\rho(S_n)$ was determined using the same method as for the

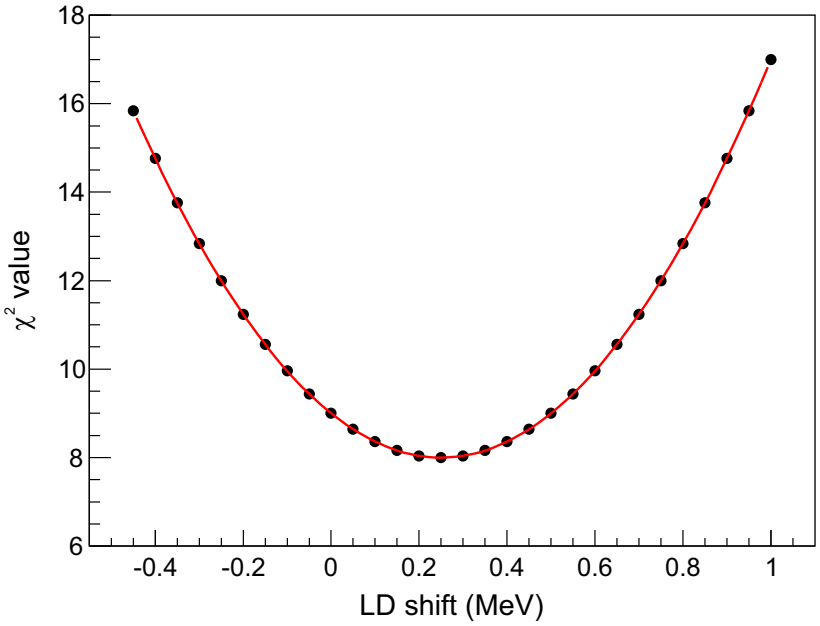

Figure 5.14: χ^2 values for different E_x shifts of the calculated cumulative levels compared to the known cumulative levels for ^{71}Ni.

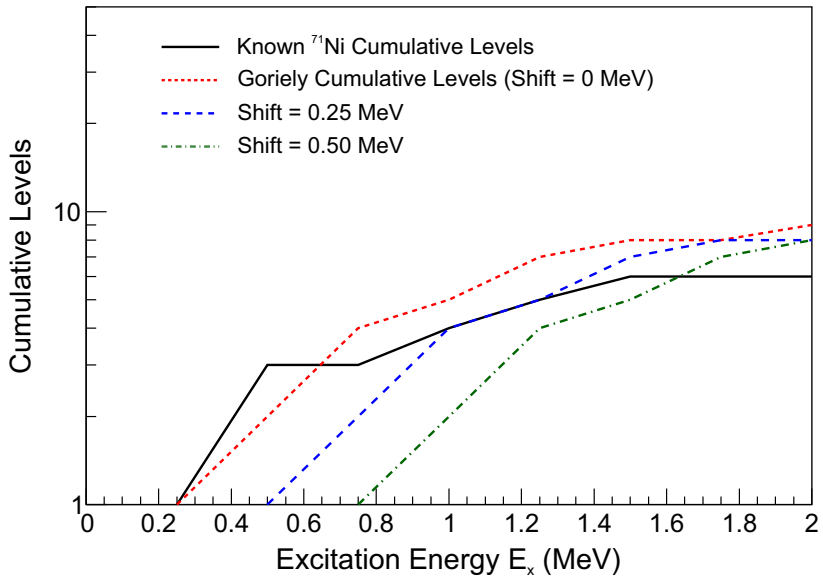

Figure 5.15: Unshifted (red line) and shifted calculated cumulative levels (blue and green lines) compared to the known cumulative levels (black line). The best shift value of 0.25 MeV with an error of 0.25 MeV led to only two shifts needed, as the lower limit shift is 0 MeV.

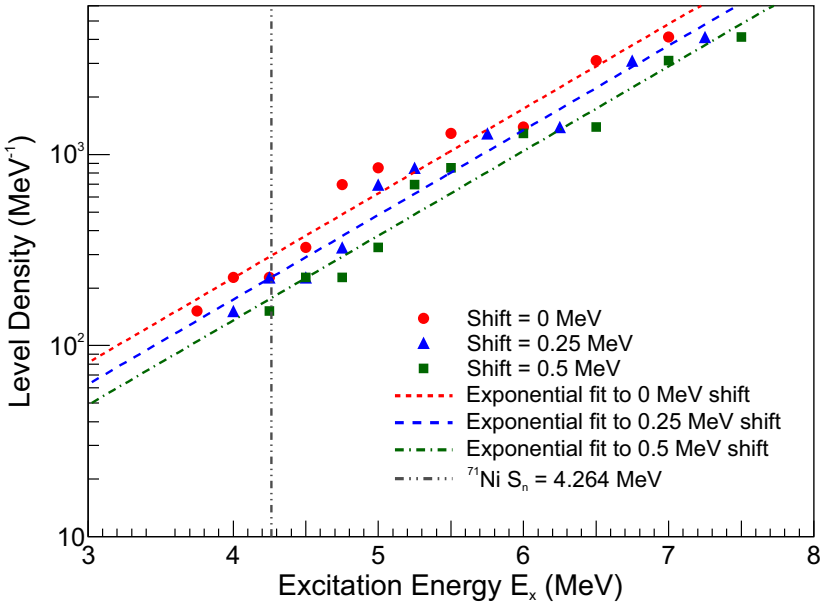

Figure 5.16: Shifted calculated level densities (upper, mid, and lower) near S_n used to determine $\rho(S_n)$ values for the NLD normalization.

^{74}Zn data. The percentage of the total NLD at the neutron separation energy as a function of spin is shown in Fig. 5.17. The indicated spins comprise 50.7(5)% of the total NLD, which led to reduced $\rho(S_n)$ values of 90(46), 116(58), and 150(73) MeV^{-1}.

With the two normalization points (the known low-energy levels and the reduced $\rho(S_n)$), the experimental NLD was normalized to match both. The normalization was performed three times, with the upper and lower limits from the shift uncertainty as well as the central value. The upper, lower, and middle normalized NLD are shown in Fig. 5.18, along with the three shifted Goriely calculated NLDs, which were reduced to include only spins in the range of interest.

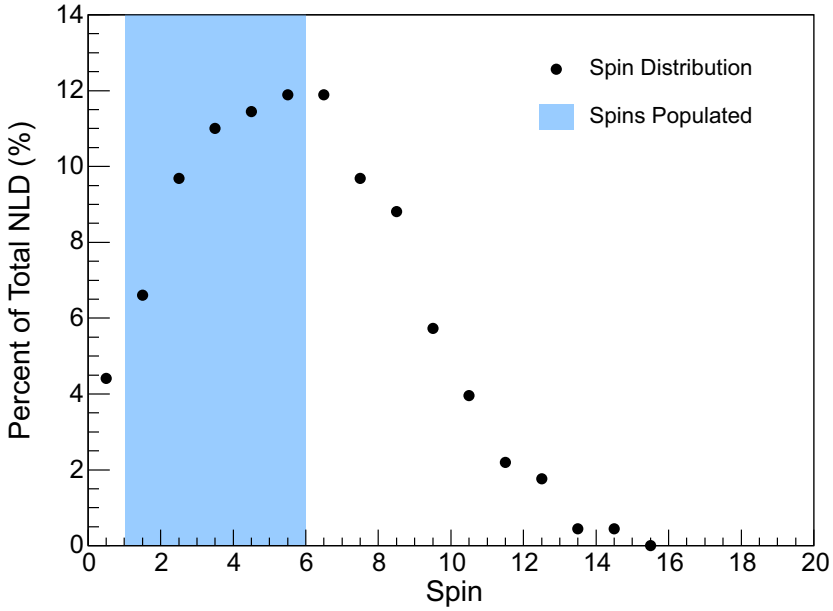

Figure 5.17: Distribution of spins for the levels in ^{71}Ni around the neutron separation energy based on tabulated spin- and parity-dependent NLD from Ref. [30]. Spins highlighted in blue are populated following an allowed β decay of ^{71}Co and one dipole photon transition. The ground state of ^{71}Co has been tentatively assigned a value of $(7/2^-)$.

5.2.3 γSF normalization

For the value of B, previous β-Oslo data on ^{69,70}Ni was used. The ^{70}Ni γSF was previously normalized to Coulomb dissociation data for ^{68}Ni [100], and then the ^{69}Ni γSF was normalized to the ^{70}Ni data. For the new ^{71}Ni data, the average of the two data sets was used for normalization along the entire energy range where ^{71}Ni data was available (1-4.5 MeV). The normalized ^{71}Ni γSF was also compared to the ^{68}Ni Coulomb dissociation data, as well as more recent data on the γSF of ^{70}Ni [101]. The normalized γSF for ^{71}Ni, along with the γSFs obtained for ^{69,70}Ni using the β-Oslo method and the Coulomb dissociation data for ^{68,70}Ni is shown in Fig. 5.19.

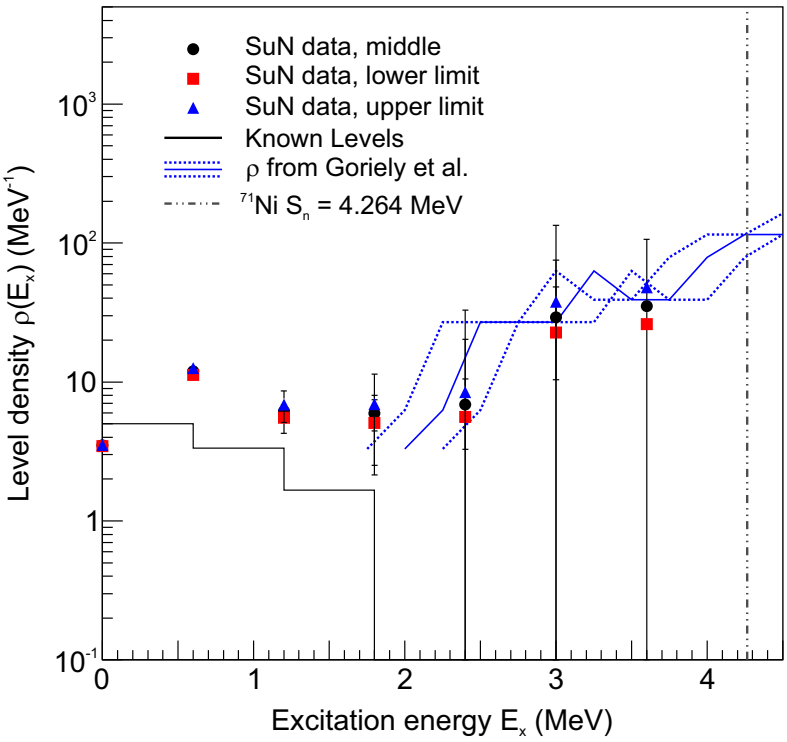

Figure 5.18: Normalized NLD for ^{71}Ni, with the known levels and Goriely calculated NLD (shifts of 0 MeV, 0.25 MeV, and 0.5 MeV).

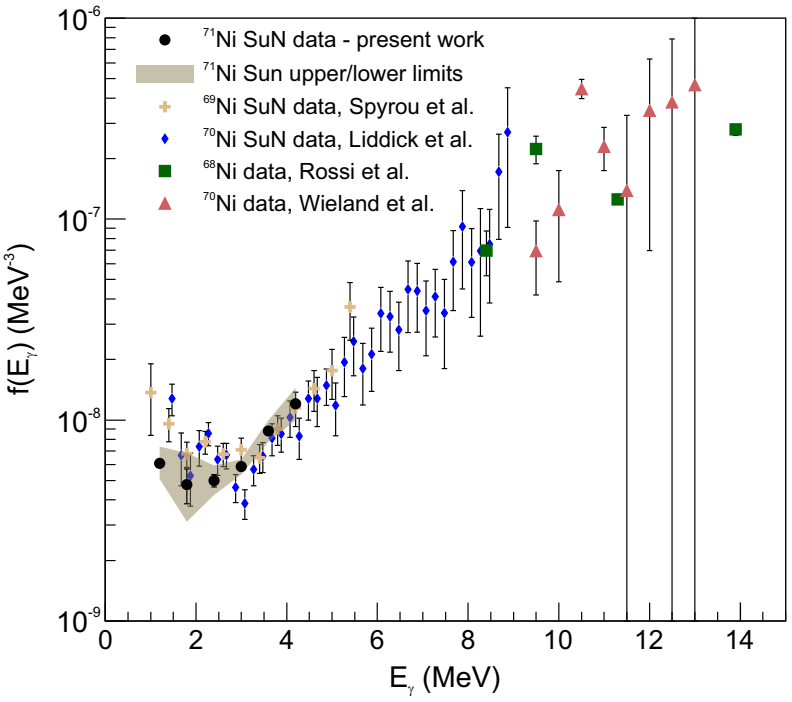

Figure 5.19: Normalized γSF for ^{71}Ni (black dots, uncertainty indicated by grey band) compared to γSF data on ^{69,70}Ni from the β-Oslo method, as well as higher-energy Coulomb dissociation data for ^{68,70}Ni.

5.3 ^{72}Co decay

From previous studies, it has been shown that when ^{72}Co is produced by fragmentation, both the ground state and a low-energy isomeric state are produced [102]. The energy of the isomeric state is unknown, but both states β decay to excited states in ^{72}Ni. The measured half-lives of the two states are very similar: 51.5(3) ms and 47.8(5) ms [103]. However, the spins of the two states are very different, with a high-spin state tentatively assigned a spin and parity of $(6^-, 7^-)$ and a low-spin state with a tentative spin and parity of $(0^+, 1^+)$ [103]. The high-spin state assignment is based on systematics of even-even Co isotopes [104, 99], while the low spin-state was suggested due to known long-lived isomers in lighter Co isotopes [104] as well as observed β feeding to levels with low spins in ^{72}Ni [103].

Characteristic γ-rays from the decay of both states were observed in the present experiment. The population ratio between the high-spin and low-spin β-decaying states was determined using the characteristic γ-rays and their respective absolute intensities as reported in Ref. [103]. For the high-spin ground state, the 1194.2(12) keV transition was the best separated characteristic γ ray (see Fig. 5.20 for a simplified level scheme of the high-spin decay). For the low-spin isomer, the 3039.6(19) keV and 3383.4(18) keV γ rays were used (see Fig. 5.21 for the low-spin decay scheme). These γ rays were fit in the experimental segments spectrum following the decay of ^{72}Co, but needed to be corrected using the efficiency of SuN. The known low-spin and high-spin decay schemes were used to model the GEANT4 response of SuN and to determine the detection efficiency for the 1194 keV, 3039 keV, and 3383 keV transitions, see Table 5.5. The results of the simulation of the response to the high spin ground state can be seen in Fig. 5.22, along with the fit to the simulated data that was used to determine the efficiency of the 1194 keV γ ray based on the number

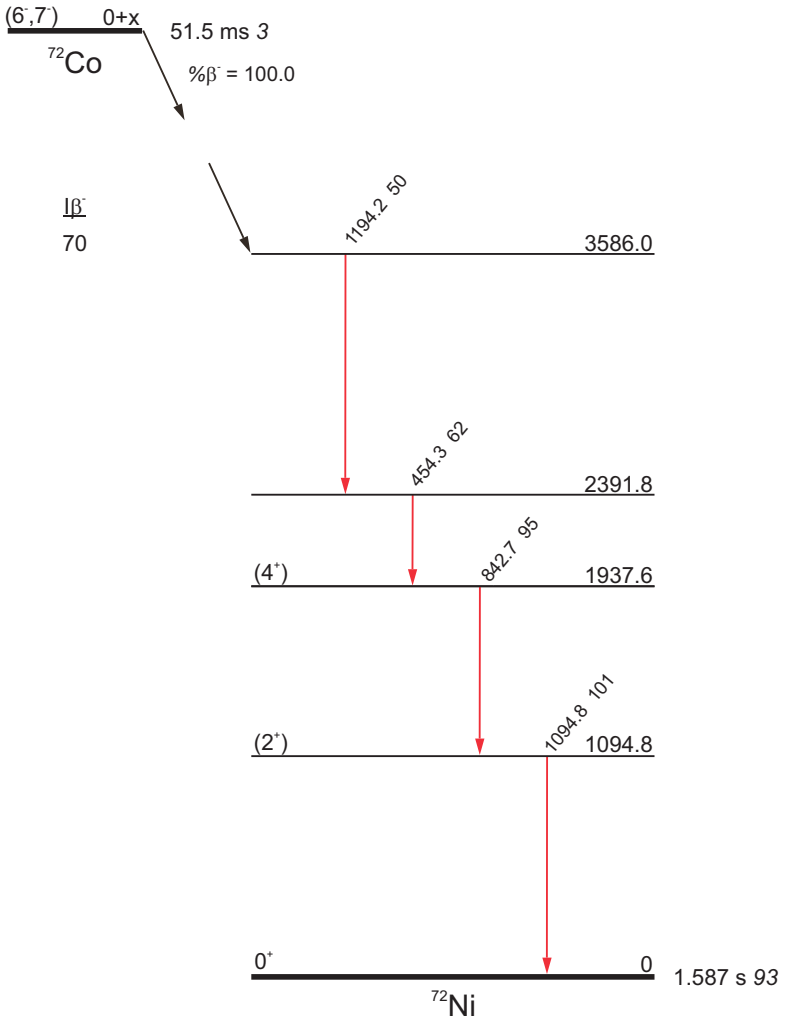

Figure 5.20: Simplified level scheme for the β decay of the high spin state in ^{72}Co. Only the four strongest transitions, originating from the strongly populated 3586.0 keV level, are shown for clarity and account for 70% of the β-decay feeding intensity.

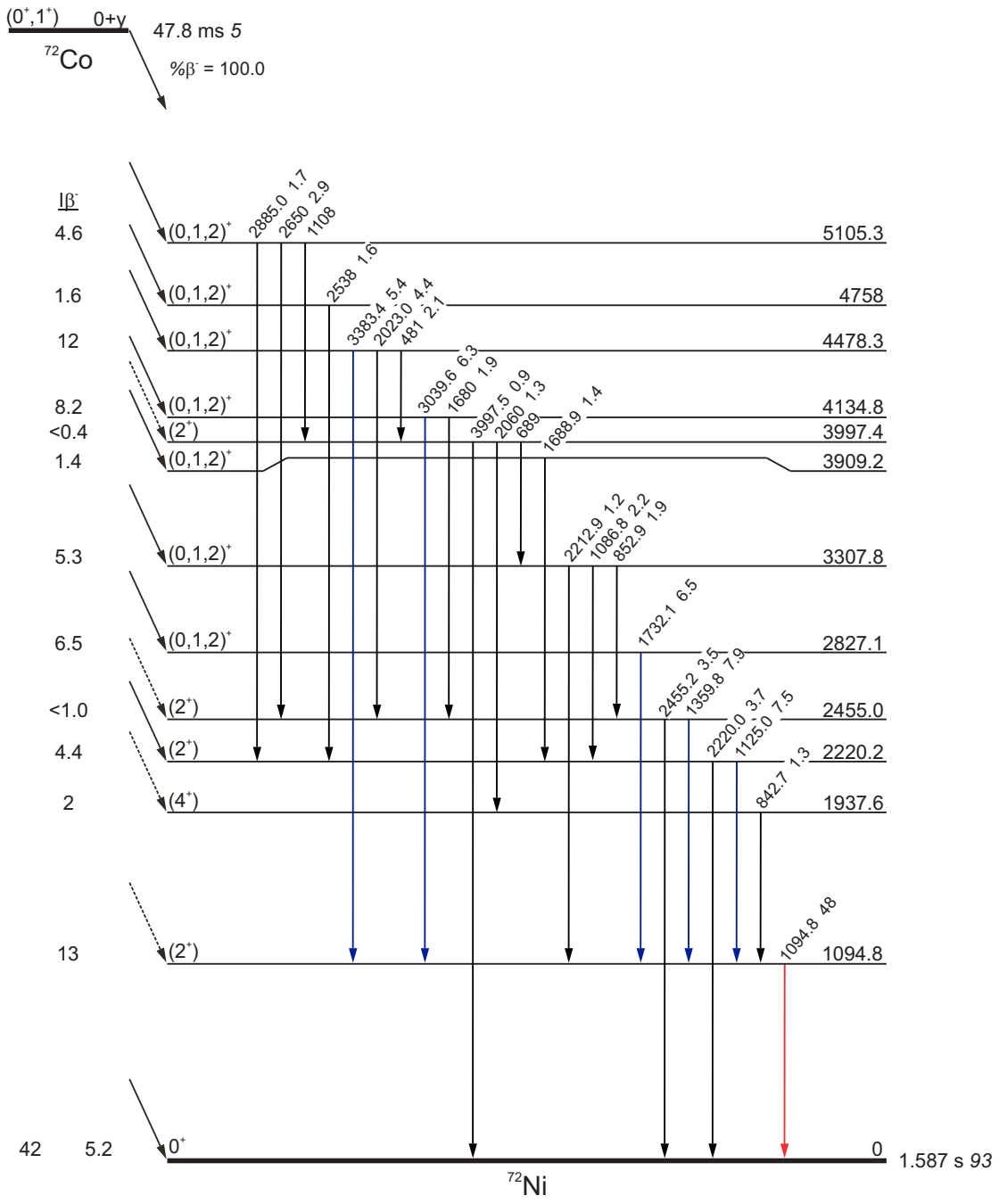

Figure 5.21: Known level scheme for the β decay of the low spin state in ^{72}Co. All known transitions are shown.

Table 5.5: Efficiency for detecting the full energy of select γ rays in one segment of SuN, determined from GEANT4 simulations.

γ-ray energy (keV)	Efficiency (%)
1194.2	16(1)
3039.6	24(4)
3383.4	22(4)

of counts compared to the number of β decays simulated. Three main peaks were fit–842.7 keV (A), 1094.8 keV (B), and 1194.2 keV (C). The 1194 keV γ ray is actually a shoulder on the strong 1095 keV transition from the first excited state to the ground state in ^{72}Ni, but it was the only γ ray from the high-spin decay that was well separated, which was why multiple peaks were fitted simultaneously. The results of the simulation of the response to the low spin isomer can be seen in Fig. 5.23. This figure focuses on the high-energy γ rays; the fit to the 3040 keV γ ray (D), the 3383 keV γ ray (E), and the surrounding γ rays is shown. The 3383 keV γ ray had smaller fitting uncertainties, so it was used for the isomer ratio determination.

The experimental data for the same energy ranges can be seen in Fig. 5.24 (1194 keV, characteristic high-spin decay) and Fig. 5.25 (3383 keV, characteristic low-spin decay). The same peripheral peaks were fit in the experimental data as in the GEANT4 simulation (when possible) to help determine the number of counts in the peaks of interest. By correcting for the efficiency and the absolute intensity of each γ-ray, the number of decays of the high-spin ground state was calculated to be 164000(21000), while the number of decays of the low-spin isomer was calculated to be 104000(27000). Adding these values together gives the total number of ^{72}Co decays to be 268000(34000), which matched within error to the number extracted from the decay curve fit shown in Fig. 5.26 (and described below). Therefore,

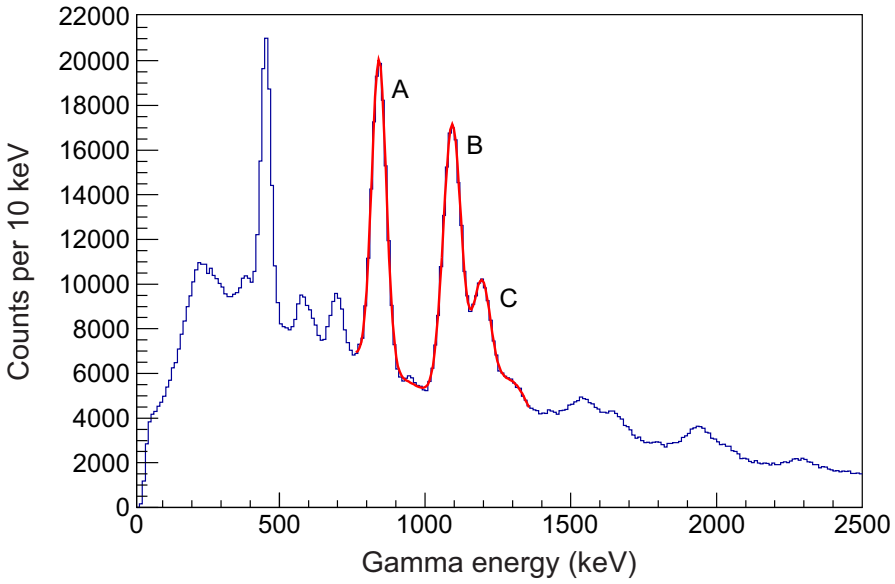

Figure 5.22: GEANT4 simulation of the decay of the ^{72}Co high spin isomer, with the fit used to extract the efficiency of the 1194.2 keV γ ray.

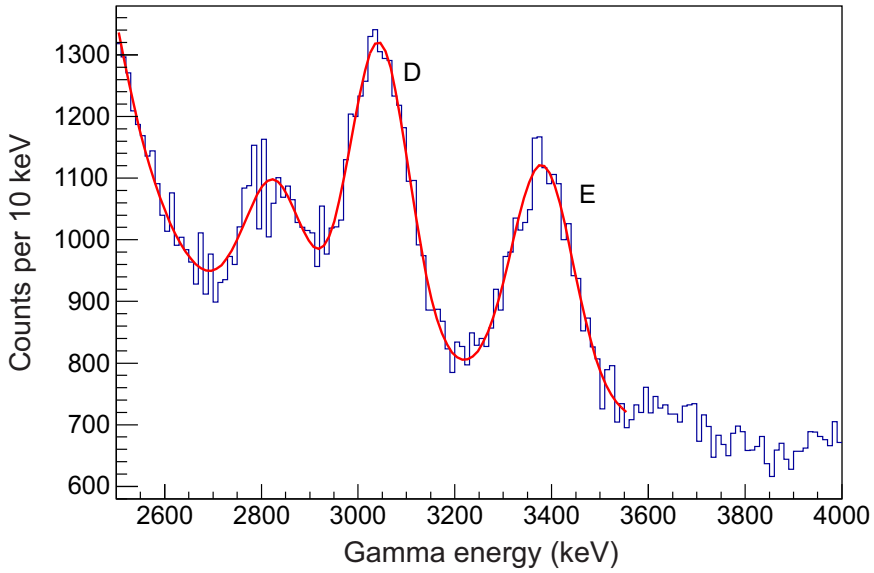

Figure 5.23: GEANT4 simulation of the decay of the ^{72}Co low spin isomer at high γ energies, with the fit used to extract the efficiency of the 3383.4 keV γ ray.

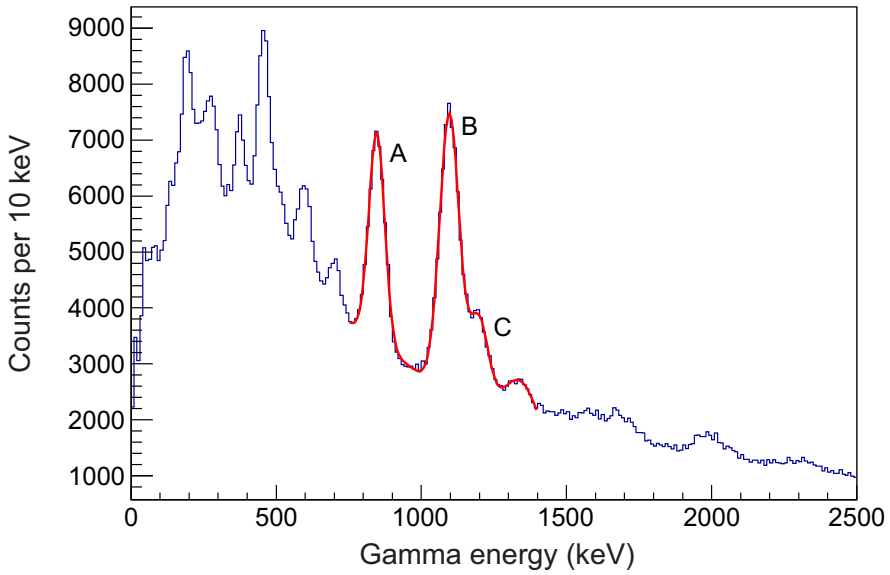

Figure 5.24: Low energy raw SuN spectrum with the fit used to extract the number of 1194.2 keV counts seen in the experiment.

60(20)% of the decays were from the high-spin state, while 40(20)% of the decays were from the low-spin state.

The ratio was tested with a GEANT4 simulation of a mixed decay scheme, shown in Fig. 5.27. The differences between the data and the simulation at low energies indicates that the β-decay feeding intensities to highly excited states (e.g. the 70% feeding at 3.586 MeV) is too large, which is commonly seen when the intensities were determined using low-efficiency high-purity Ge detectors [105, 106]. It is likely that some of the feeding intensity attributed to these levels is actually going to higher-lying, unknown excited states, as the highest known level in ^{72}Ni is just above 5 MeV but the neutron separation energy is 6.891 MeV. To investigate the impact of feeding to high excited states, two new levels were added in the simulation: a hypothetical level at 5.085 MeV that was assumed to de-excite by a 1.5 MeV γ ray to the 3.856 MeV level, and another hypothetical level at 5.978 MeV that also de-excited by a 1.5 MeV γ ray, but to the 4.478 MeV level. To test the impact of moving β-feeding

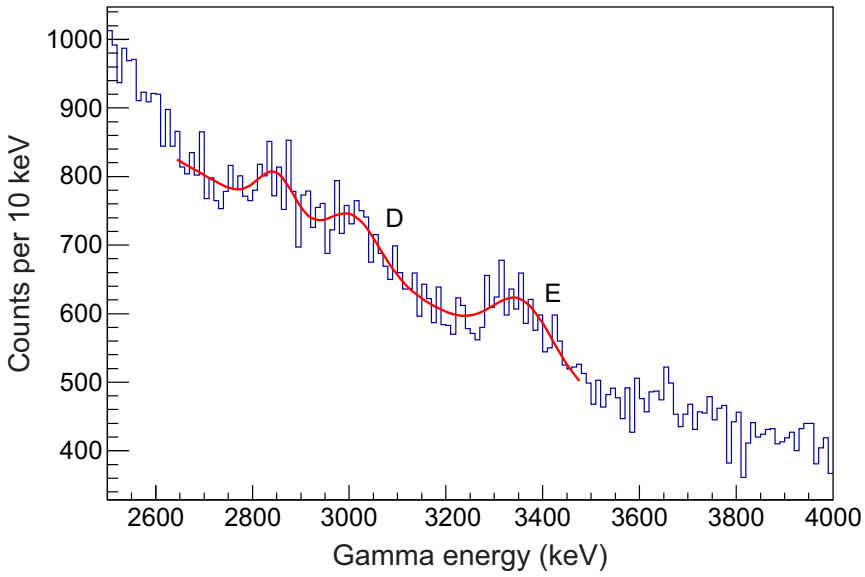

Figure 5.25: High energy raw SuN spectrum with the fit used to extract the number of 3383.4 keV counts seen in the experiment.

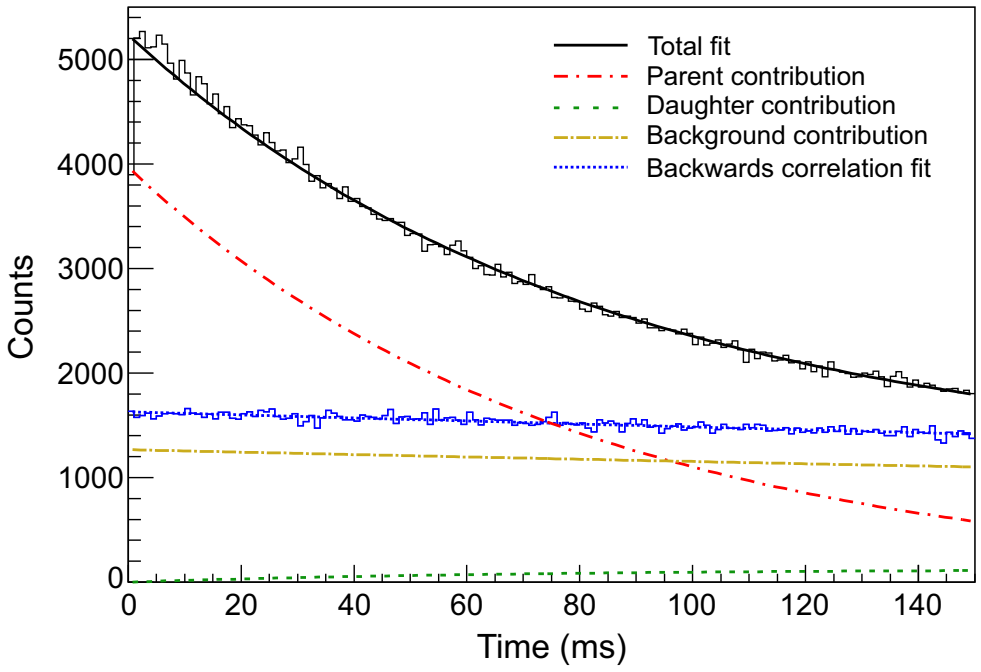

Figure 5.26: Full decay curve fit for the decay of ^{72}Co.

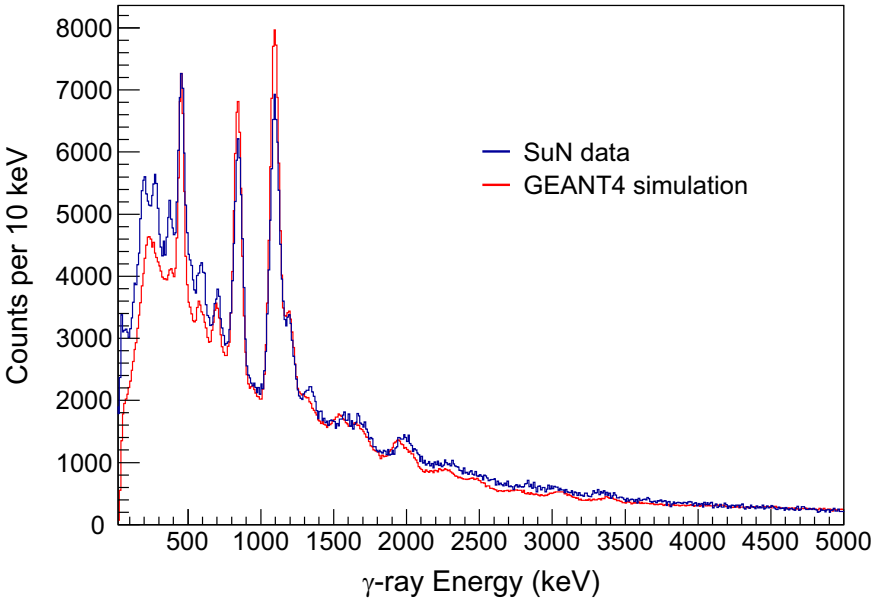

Figure 5.27: Low energy GEANT4 simulation with 60% high spin and 40% low spin decays compared to the SuN spectrum. The simulation has been scaled to match the SuN data between 4 and 6 MeV.

strength to higher excitation energies, an arbitrary amount (25%) of the β-decay feeding to the levels being populated by the new γ rays was removed and attributed to the new levels. For the new 5.086 MeV level, a β-decay feeding intensity of 17.5% was assigned (this was 25% of the 70% β-feeding intensity assigned to the 3.586 MeV level), while a β-decay feeding intensity of 3% was assigned to the new 5.978 MeV level (25% of the 12% β-decay feeding intensity assigned to the 4.478 MeV level). This is the simplest case, where the β feeding is going to just one highly excited state instead of being spread out among many states. With the new levels, the efficiency of detecting the γ-rays of interest (for determining the ratio of high-spin ground state to low-spin isomer populated in fragmentation) decreased due to the higher γ-ray multiplicity. The efficiency of detecting the 1194.2 keV γ ray in a single segment of SuN decreased from 16(1)% to 15(1)%, while the efficiency of detecting the 3383.4 keV γ ray in a single segment decreased from 22(4)% to 14(3)%. A smaller decrease in the efficiency

Table 5.6: Results of decay curve fit for ^{72}Co decay using a 150 ms correlation time (see Fig. 5.26).

Number of parent decays	252670(570)
Number of daughter decays	10566(25)
Number of random correlations	189650(40)
Number of events in backwards correlation	228329(36)

Table 5.7: Results of decay curve fit for ^{72}Co decay using a 5 sec correlation time (see Fig. 5.28).

Number of daughter decays in subtraction region	10560(270)
Number of random correlations in subtraction region	99280(240)

of the 1194.2 keV γ ray compared to the 3383.4 keV γ ray was expected, as the 1194.2 keV γ ray is in a multiplicity four (M=4) cascade, while the 3383.4 keV γ ray is in a multiplicity two (M=2) cascade. The decrease in efficiency between M=4 and M=5 is small, while the decrease in efficiency between M=2 and M=3 is larger [60], so adding a single γ ray to each cascade affected the efficiency as expected. The change in efficiency had a small impact on the calculated amounts of each β-decaying state populated in fragmentation, within the uncertainty, so the 60% high spin and 40% low spin population was used.

With the relative amounts of each β-decay state determined, the effective half-life of ^{72}Co was calculated to be 50.1(79) ms. The decay curve fit, following the procedure described for ^{71}Co, is shown in Fig. 5.26. The extracted half-life of 52(1) ms agreed well with the expected effective half-life of the mixed ground state/isomer decay.

The number of parent decays, daughter decays, background counts, and counts in the backwards correlator for the 150 ms correlation are detailed in Table 5.6. As with ^{71}Co, these values were used to perform an appropriate subtraction of the daughter and background

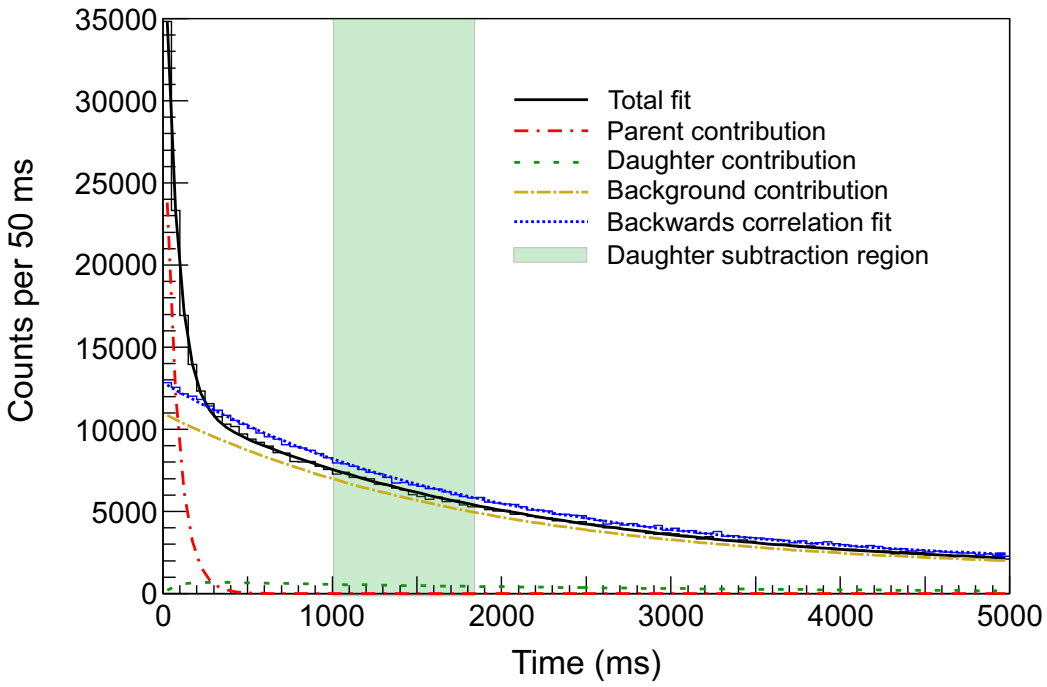

Figure 5.28: Long correlation time decay curve fit for the decay of ^{72}Co. The green band shows the time region used to remove the daughter contribution to the SuN spectra.

from the raw SuN spectra. In the 5 second correlation window, a time window from 1000 ms to 1841 ms yielded 10560(270) daughter decays, matching the 10566(25) in the 150 ms correlator, with 99280(240) random correlations in that time window (see Table 5.7). Subtracting the spectra obtained from this time window left 90370(240) background counts to be removed in the 150 ms correlation. The backwards correlation was scaled appropriately to remove the correct amount of background remaining in the spectra.

The strongest transitions in ^{72}Ni were described above (see Figs. 5.20 and 5.21), and were clearly observed in the parent contribution spectrum in Fig. 5.29. The 1094.8 keV peak [A], with an absolute intensity of 101% for the high-spin decay and 48% for the low-spin decay, is by far the strongest transition. The other strong transitions at 842.7 keV [B] (I_γ = 95% high spin, 1.3% low spin) and 454.3 keV [C] (I_γ = 62% high spin) are also clearly

present. There is a 70% β-decay feeding to the 3586.0 keV level [D] in the high spin decay, which can be best seen in the TAS spectrum, and there are no other strongly fed levels.

5.3.1 β-Oslo matrices

As with the ^{71}Co decay, the raw 2D Oslo matrix was constructed using the daughter- and background-subtracted SuN spectra, which can be seen in Appendix B. The raw matrix can be seen in Fig. 5.30, with 10 keV wide bins on both axis. The unfolded matrix, in Fig. 5.31, has 120 keV wide bins to reflect the resolution of SuN, as does the primary matrix (Fig. 5.32). The region of the primary matrix used to extract the NLD and γSF is highlighted in Fig. 5.32, and was restricted to $E_\gamma > 3000$ keV and $E_x \in (3000, 7000)$ keV. The upper E_x limit was chosen to be very close to the $\rho(S_n)$ of ^{72}Ni of 6.891(3) MeV [107]. The first excited state of ^{71}Ni is at 280.5(2) keV [67], which allowed for the upper E$_x$ limit to be increased to 7 MeV ($\sim$100 keV above S_n) without the possibility of contamination from the β-delayed neutron daughter.

5.3.2 NLD normalization

The NLD normalization followed the same procedure as for ^{71}Ni, with the spin-reduced calculated cumulative levels shifted in excitation energy to match the known levels. The χ^2 minimization, shown in Fig. 5.33, resulted in shift values of 0.25 $\pm$ 0.2 MeV. The shifted calculated cumulative levels can be seen compared to the known levels in Fig. 5.34. The shifts were then applied to the calculated NLD around S_n, which is shown in Fig. 5.35, along with the exponential fits to each shift. The results for the fitted parameters are given in Table 5.8 and resulted in $\rho(S_n)$ values of 1055(85), 1300(100), and 1600(120) MeV^{-1}.

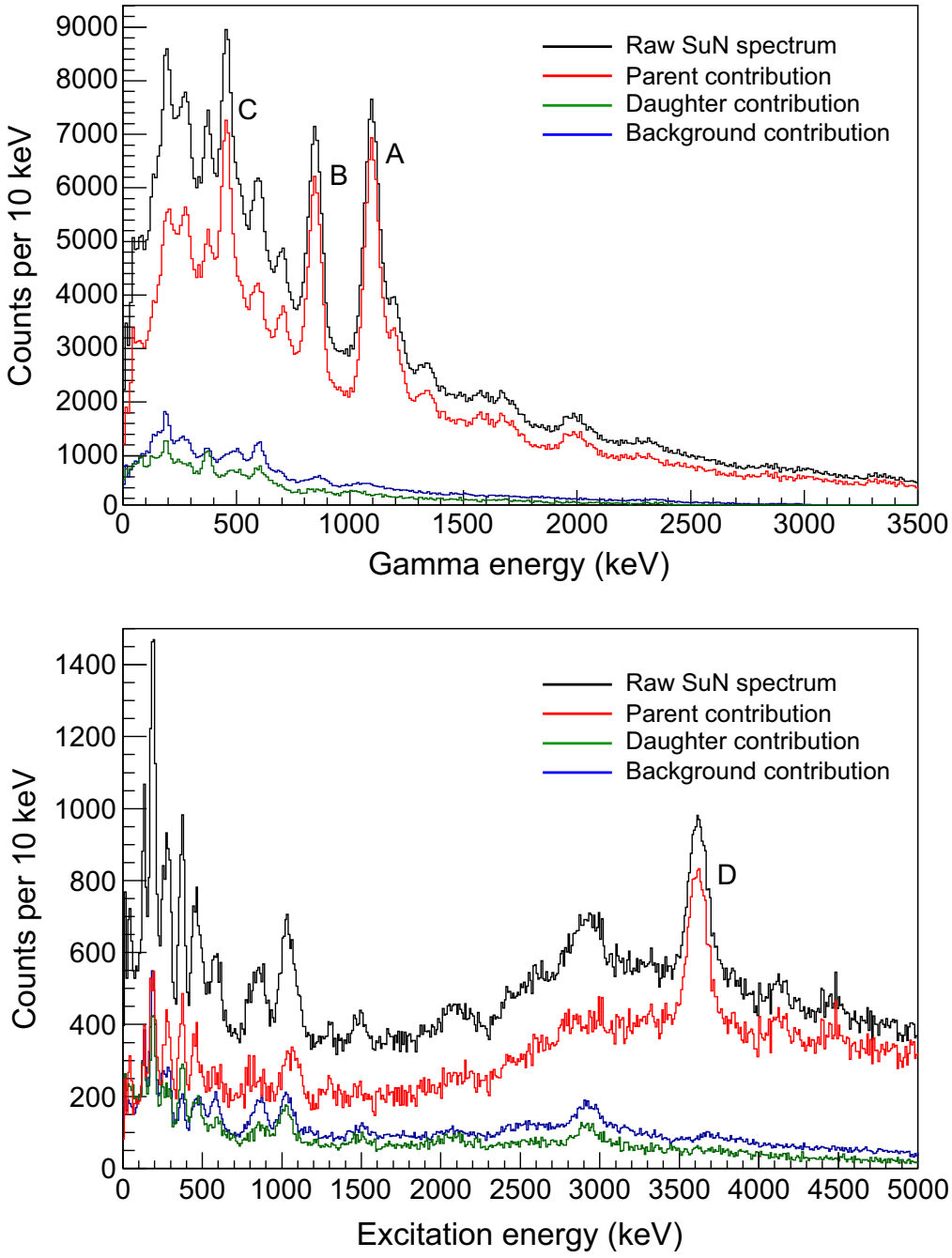

Figure 5.29: ^{72}Co SuN spectra showing the raw spectrum, daughter decay contribution, background contribution, and final γ-ray (top) and TAS (bottom) spectra for the de-excitation of ^{72}Ni.

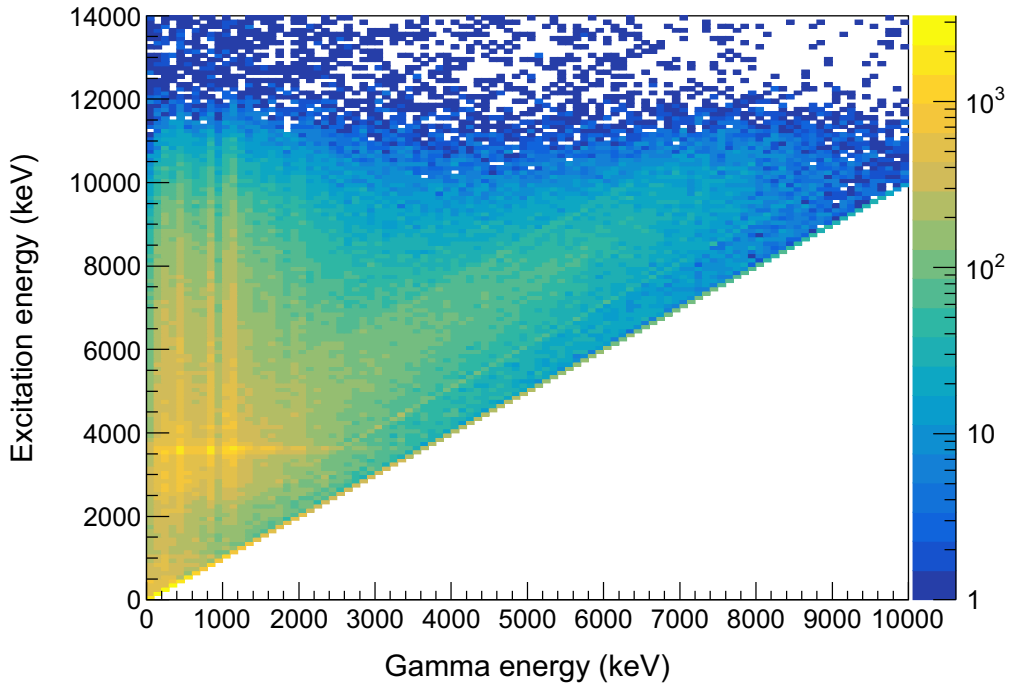

Figure 5.30: Raw 2D Oslo matrix for the decay of ^{72}Co into excited states of ^{72}Ni. The γ-ray energies obtained from the segments of SuN are plotted on the x-axis, while the excitation energy of the daughter nucleus, obtained from the total energy in the detector, is plotted on the y-axis.

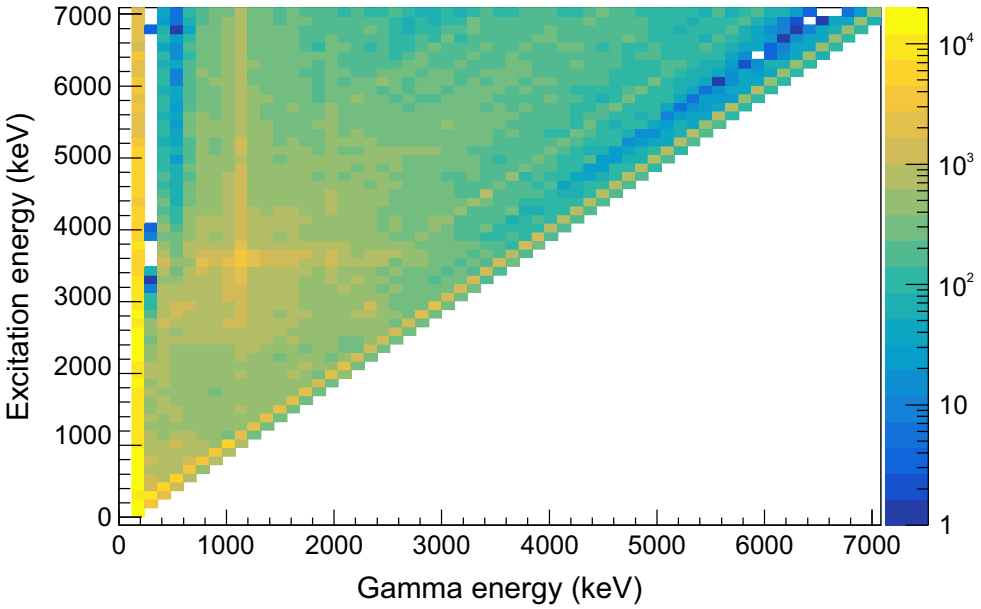

Figure 5.31: Unfolded 2D matrix for ^{72}Ni with 120 keV binning on both axis.

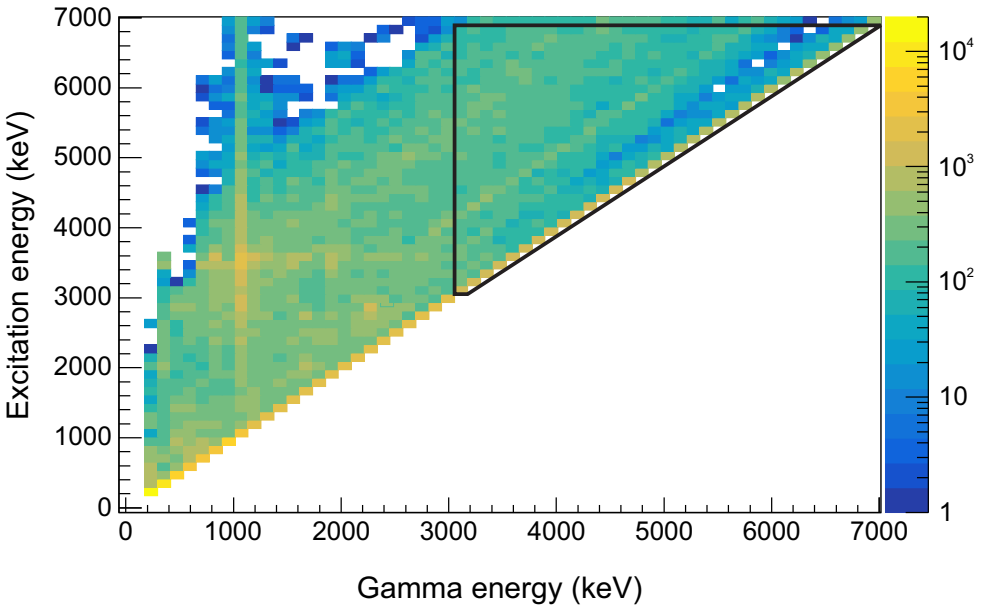

Figure 5.32: Primary 2D matrix for ^{72}Ni with 120 keV binning on both axis. The extraction region used for the NLD and γSF is outlined by the black lines.

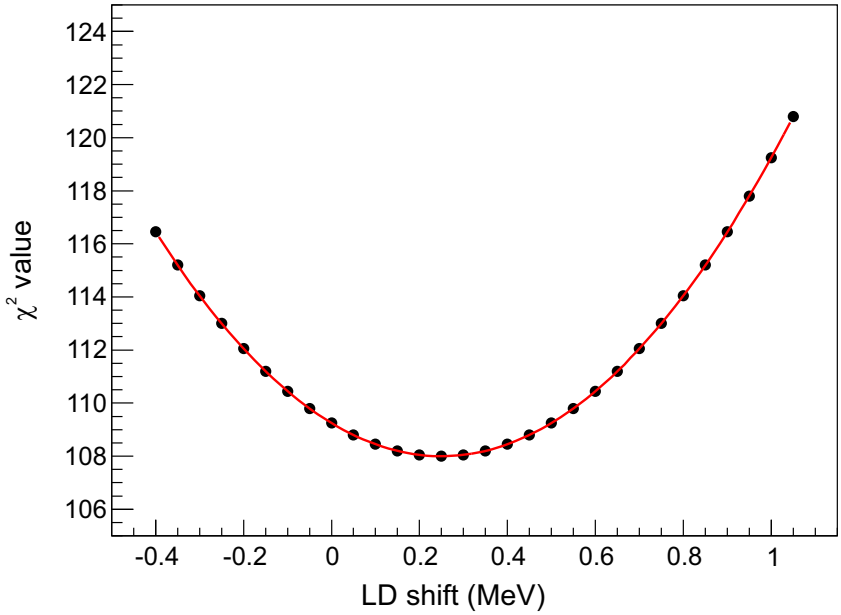

Figure 5.33: χ^2 values for different E_x shifts of the calculated cumulative levels compared to the known cumulative levels for ^{72}Ni.

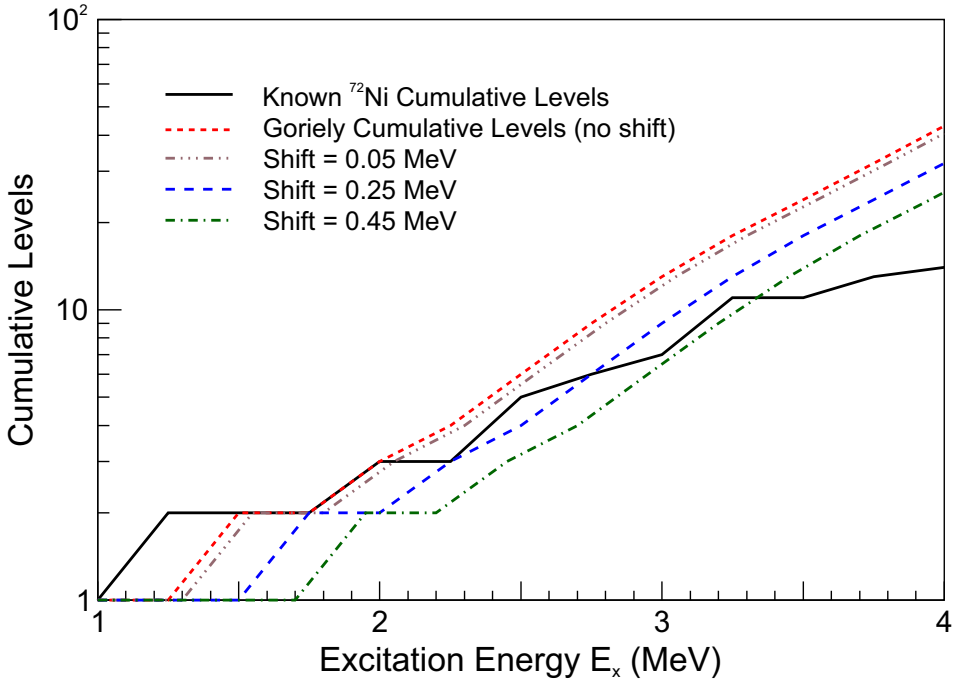

Figure 5.34: Shifted calculated cumulative levels compared to the known cumulative levels.

Table 5.8: Parameters used in exponential fit to shifted calculated NLD for ^{72}Ni.

Shift Value	Constant	Slope	$\rho(S_n)$ (MeV^{-1})
0.05 MeV	1.29(7)	1.034(8)	1600(120)
0.25 MeV	1.05(6)	1.034(8)	1300(100)
0.45 MeV	0.85(5)	1.034(8)	1055(84)

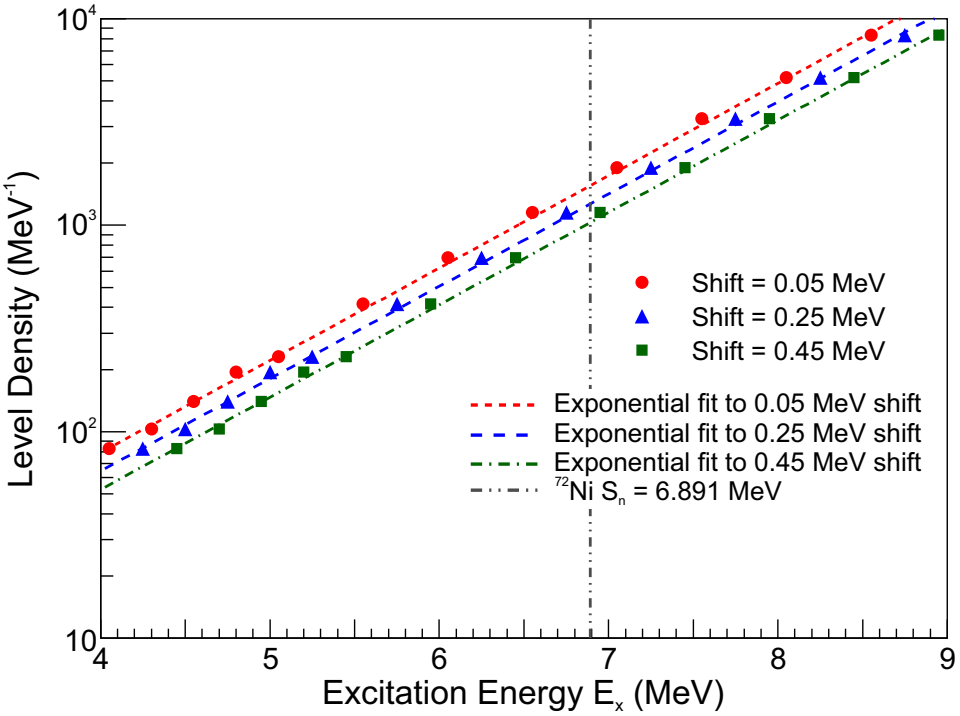

Figure 5.35: Shifted calculated level densities (upper, mid, and lower) near S_n used to determine $\rho(S_n)$ values for the NLD normalization.

Once again, the NLD needed to be reduced due to the lack of non-β decay data. The two possibilities for the ground state spin, 6^- or 7^-, account for different percentages of $\rho(S_n)$ due to the different spin ranges they cover: 4 to 8 (both parities) from a 6^- state, and 5 to 9 (both parities) from a 7^- state. The population of the NLD around S_n as a function of the spin is shown in Fig. 5.36 for both cases. The case of a 6^- ground state would populate 56% of the full $\rho(S_n)$, while the case of a 7^- ground state would populate 46%.

The high-spin ground state was found to be only 60% of the decays, however, so the low-spin isomer decay also needed to be considered. The suggested spins are (0^+, 1^+), but lighter Co isotopes have been found to have 1^+ isomers, so only a spin of 1^+ was considered. The percentage of $\rho(S_n)$ populated by the low-spin decay was found to be 33%, covering spins of 0 to 3, both parities. The spin range covered by the mixed high spin and low spin decay is shown in Fig. 5.37 for both high spin options. For a 6^- ground state with a 1^+ isomeric state, spins of 0 to 8, both parities, are covered. For a 7^- ground state with a 1^+ isomeric state, spins of 0 to 3 and 5 to 9, both parities, are covered. The percentage of $\rho(S_n)$ populated by the combined ground state and isomeric state decay (for each ground state spin case) was calculated by combining the percentage of $\rho(S_n)$ populated due to the combined spin range and the ratio of the ground state to isomeric state produced in fragmentation. Assuming that the β-decay branching ratio to high excitation energies is the same for both β-decaying states, a 6^- ground state populated 60% of the time in fragmentation combined with a 1^+ isomeric state populated 40% of the time in fragmentation would populate 76(11)% of $\rho(S_n)$, while a 7^- ground state with a 1^+ isomeric state would populate 67(10)%. That resulted in lower, middle, and upper reduced $\rho(S_n)$ values of 810(130), 990(160) and 1220(200) MeV^{-1} for the case of a 6^- ground state, and 710(120), 870(140), and 1070(170) MeV^{-1} for the case of a 7^- ground state.

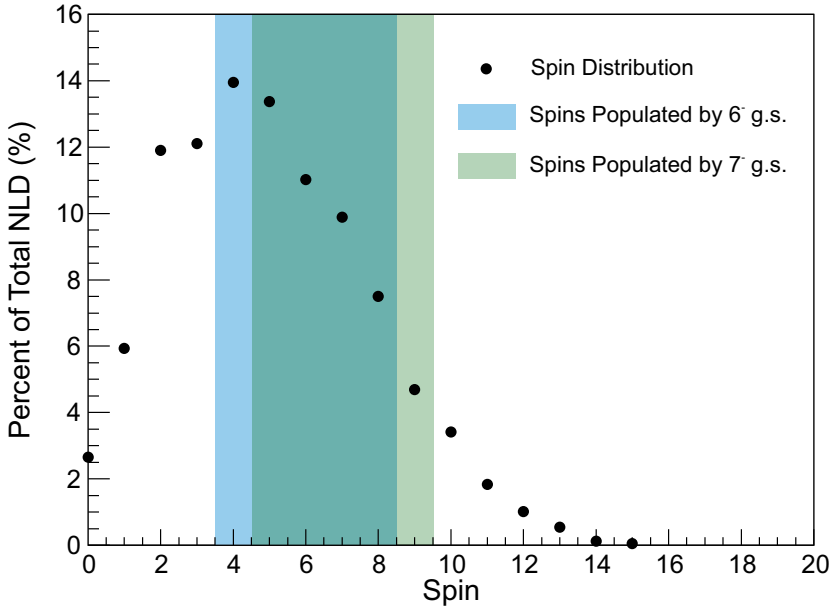

Figure 5.36: Distribution of spins for the levels in ^{72}Ni around the neutron separation energy based on tabulated spin- and parity-dependent NLD from Ref. [30]. The ground state of ^{72}Co has been tentatively assigned a value of (6^-,7^-). Spins highlighted in blue are populated following an allowed β decay of ^{72}Co from a 6^- ground state and one dipole photon transition, while spins highlighted in green are populated following an allowed β decay from a 7^- ground state and one dipole transition.

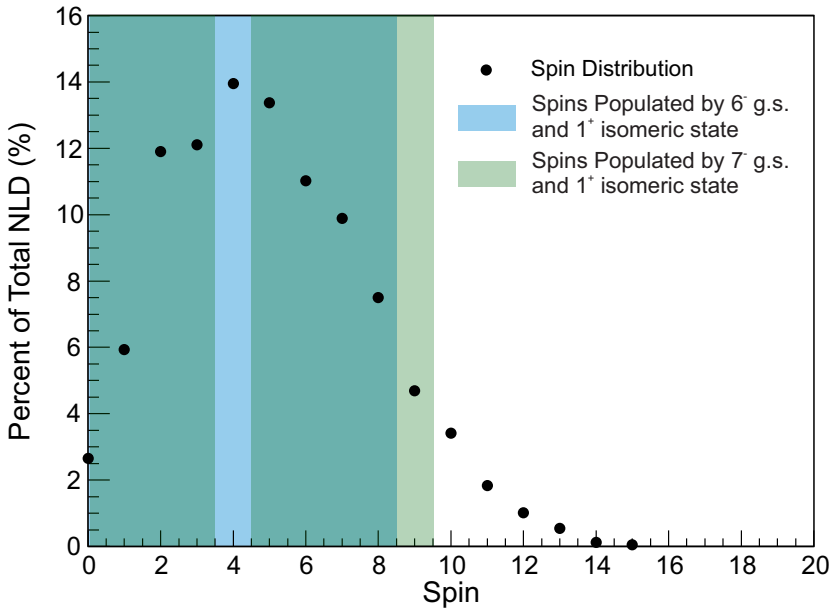

Figure 5.37: Same as in Fig. 5.36, including the spins populated in an allowed β decay from a 1^+ isomeric state and one dipole transition in addition to the ground state decay.

The reduced $\rho(S_n)$ values are modified if the low-spin and high-spin decays do not equally feed the states around S_n. The low-spin isomer has a reported ground-state β-decay branch of 42(13)% [103]. Accounting for the direct ground state decay, 68(10)% of $\rho(S_n)$ would be populated for the case of a 6^- ground state populated 60% of the time in fragmentation combined with a 1^+ isomer populated 40% of the time in fragmentation, while 58(9)% would be populated for the case of a 7^- ground state combined with a 1^+ isomer. The new reduced $\rho(S_n)$ values would therefore be 720(130), 880(160), and 1080(190) MeV^{-1} for a 6^- ground state and 620(110), 760(140), and 930(170) MeV^{-1} for a 7^- ground state. The other extreme, where 100% of the low-spin decay goes to the ground state, would result in 56% of $\rho(S_n)$ for a 6^- ground state and 46% for a 7^- ground state (the same values as above, before accounting for the fact that a β-decaying isomer was produced). With those values, the reduced $\rho(S_n)$ values were found to be 588(47), 724(57), and 890(69) MeV^{-1} for a 6^- ground state, and 490(140), 600(170), and 740(200) MeV^{-1} for a 7^- ground state. The $\rho(S_n)$ values for each case are detailed in Table 5.9.

The case of 0% β-decay feeding to the ground state from the 1^+ isomer results in the largest reduced $\rho(S_n)$ values, so this case was used as an upper limit for the normalization. The lower, middle, and upper normalized NLD for ^{72}Ni are shown in Fig. 5.38 for both high-spin cases. The shifted calculated NLD, which were reduced to contain only the spins in the ranges of interest, are included in the figure as well.

5.3.3 γSF normalization

The two ground state spin possibilities led to two different $\rho(S_n)$ reductions, so the γSF was normalized twice. The resulting γSF for both a 6^- and 7^- ground state are shown in Fig. 5.39.

Table 5.9: Lower, middle, and upper values for $\rho(S_n)$ for different spin population reductions. The full $\rho(S_n)$ was reduced using several assumptions about the β feeding to the ground state in ^{72}Ni from the low spin isomer: 0% (upper limit for populating $\rho(S_n)$), 42% (measured ground state feeding), and 100% (lower limit for populating $\rho(S_n)$, where only the high-spin ground state of ^{72}Co is responsible for populating levels around S_n).

Low spin isomer ground state I_β	High spin ground state J^π	Lower $\rho(S_n)$ (MeV^{-1})	Middle $\rho(S_n)$ (MeV^{-1})	Upper $\rho(S_n)$ (MeV^{-1})
0%	6^-	810(130)	990(160)	1220(200)
0%	7^-	710(120)	870(140)	1070(170)
42%	6^-	720(130)	880(160)	1080(190)
42%	7^-	620(110)	760(140)	930(170)
100%	6^-	588(47)	724(57)	890(69)
100%	7^-	490(140)	600(170)	740(210)

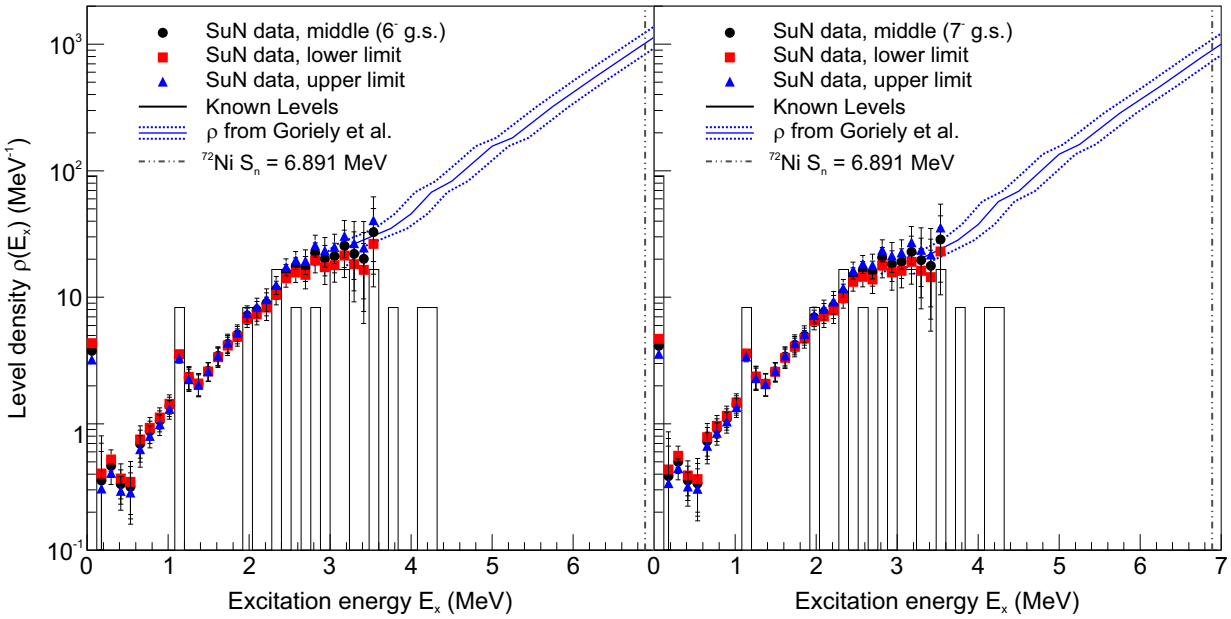

Figure 5.38: Normalized NLD for ^{72}Ni, with the known levels and Goriely calculated NLD (shifts of 0.05 MeV, 0.25 MeV, and 0.45 MeV).

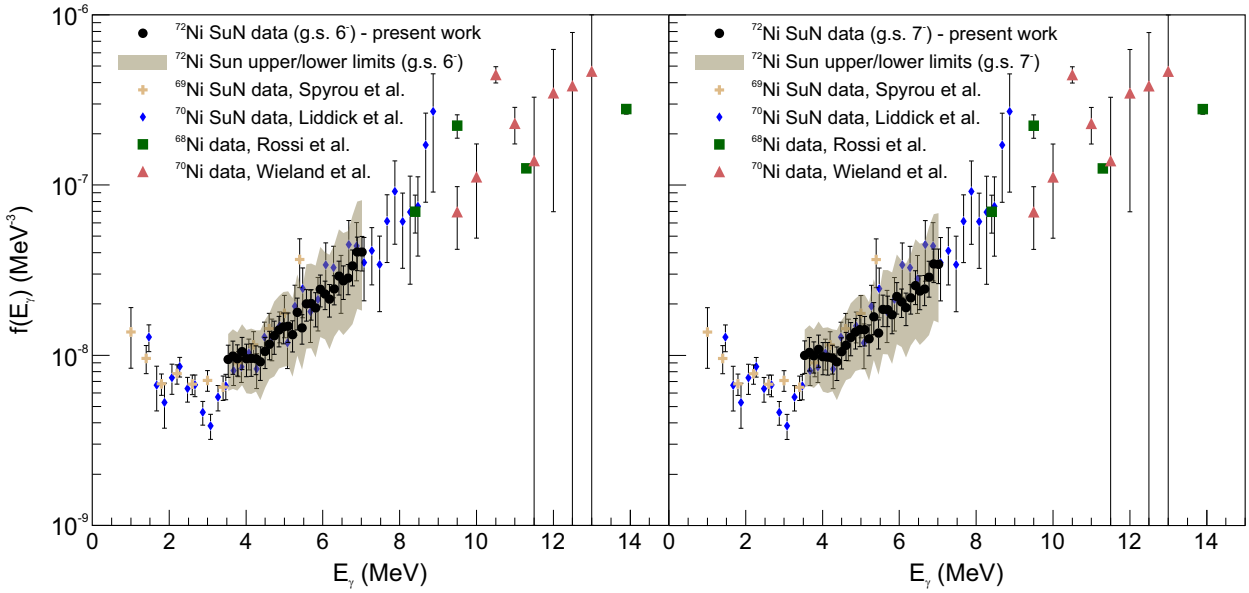

Figure 5.39: Normalized γSF for ^{72}Ni for both spin possibilities for the ground state of ^{72}Co compared to γSF data on ^{69,70}Ni from the β-Oslo method, as well as higher-energy Coulomb dissociation data for ^{68,70}Ni.

5.4 ^{73}Co decay

The decay of ^{73}Co is free of any known isomers, which made it the simplest case for fitting the decay curve. The known half-life of ^{73}Co is 40.7(13) ms [66], while the known half-life of ^{73}Ni is 840(30) ms [66]. As with the other Co isotopes, the decay curve was fit with a combination of parent decays, daughter decays with a fixed half-life, and a background component with a decay constant fixed by the backwards correlator decay curve. This fit is shown in Fig. 5.40. The half-life of ^{73}Co extracted from the fit was 41(1) ms, which matches the known half-life well.

The same procedure as described for ^{71,72}Co was used to remove the daughter and background contributions to the SuN spectra. Table 5.10 details the number of parent decays, daughter decays, and background counts from the decay curve fit.

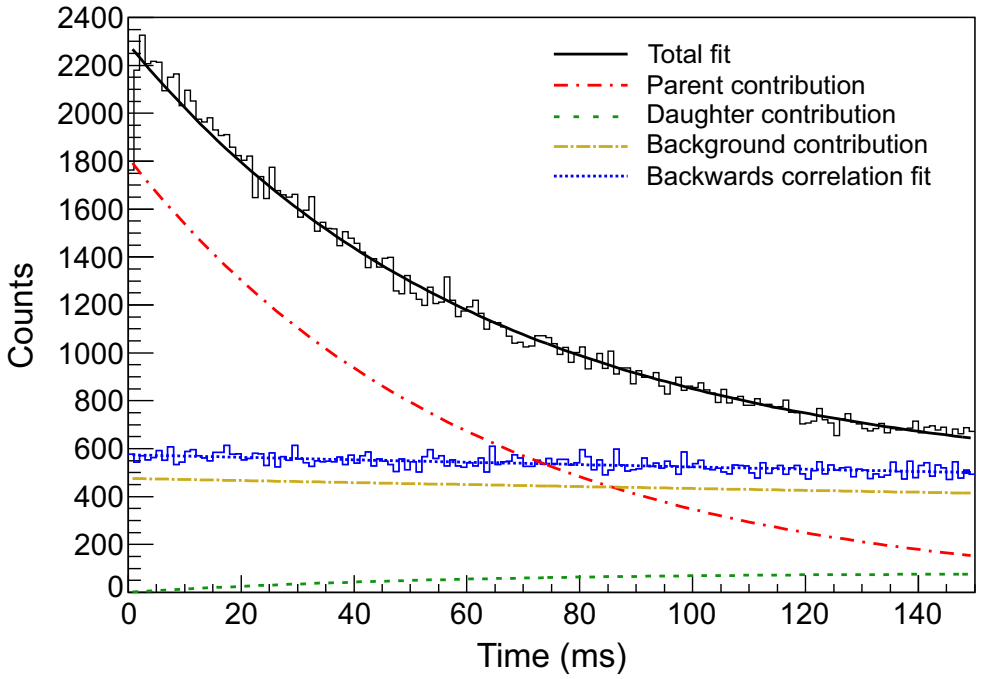

Figure 5.40: Full decay curve fit for the decay of ^{73}Co.

Table 5.10: Results of decay curve fit for ^{73}Co decay using a 150 ms correlation time (see Fig. 5.40).

Number of parent decays	97980(350)
Number of daughter decays	7966(17)
Number of random correlations	69383(30)
Number of events in backwards correlation	80511(28)

Table 5.11: Results of decay curve fit for ^{73}Co decay using a 5 sec correlation time (see Fig. 5.41).

Number of daughter decays in subtraction region	7970(120)
Number of random correlations in subtraction region	57100(100)

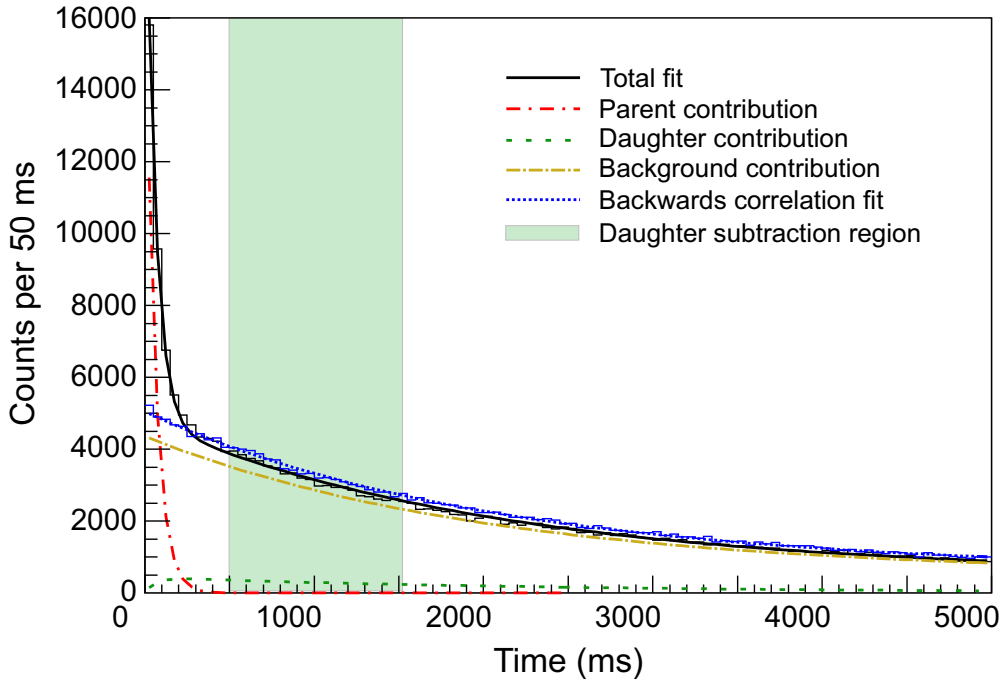

Figure 5.41: Long correlation time decay curve fit for the decay of ^{73}Co. The green band shows the time region used to remove the daughter contribution to the SuN spectra.

From the 5 second correlator, a time window of 500 ms to 1523 ms was found to have the appropriate number of daughter decays, 7970(120), to match the number of daughter decays in the 150 ms correlator. This time window contained 57100(100) background counts (see Table 5.11), leaving 12290(100) background counts left in the 150 ms correlator after removing the daughter spectrum. The backwards correlation was scaled appropriately to remove the correct amount of background remaining in the spectra.

The SuN spectra for the β decay of ^{73}Co can be seen in Fig. 5.42, and the known level scheme can be seen in Fig. 5.43. The strongest transition in ^{73}Ni, with an absolute intensity of ~70%, is at 239.2 keV, which was clearly apparent in the parent component of the γ-ray spectrum. There are only three more known transitions, at 284.8 keV ($I_\gamma \sim 34\%$), 524.6 keV ($I_\gamma \sim 18\%$), and 774.7 keV ($I_\gamma \sim 53\%$). There are two strongly fed levels, at 1299.0 keV and 239.2 keV, which were clearly seen in the TAS spectrum.

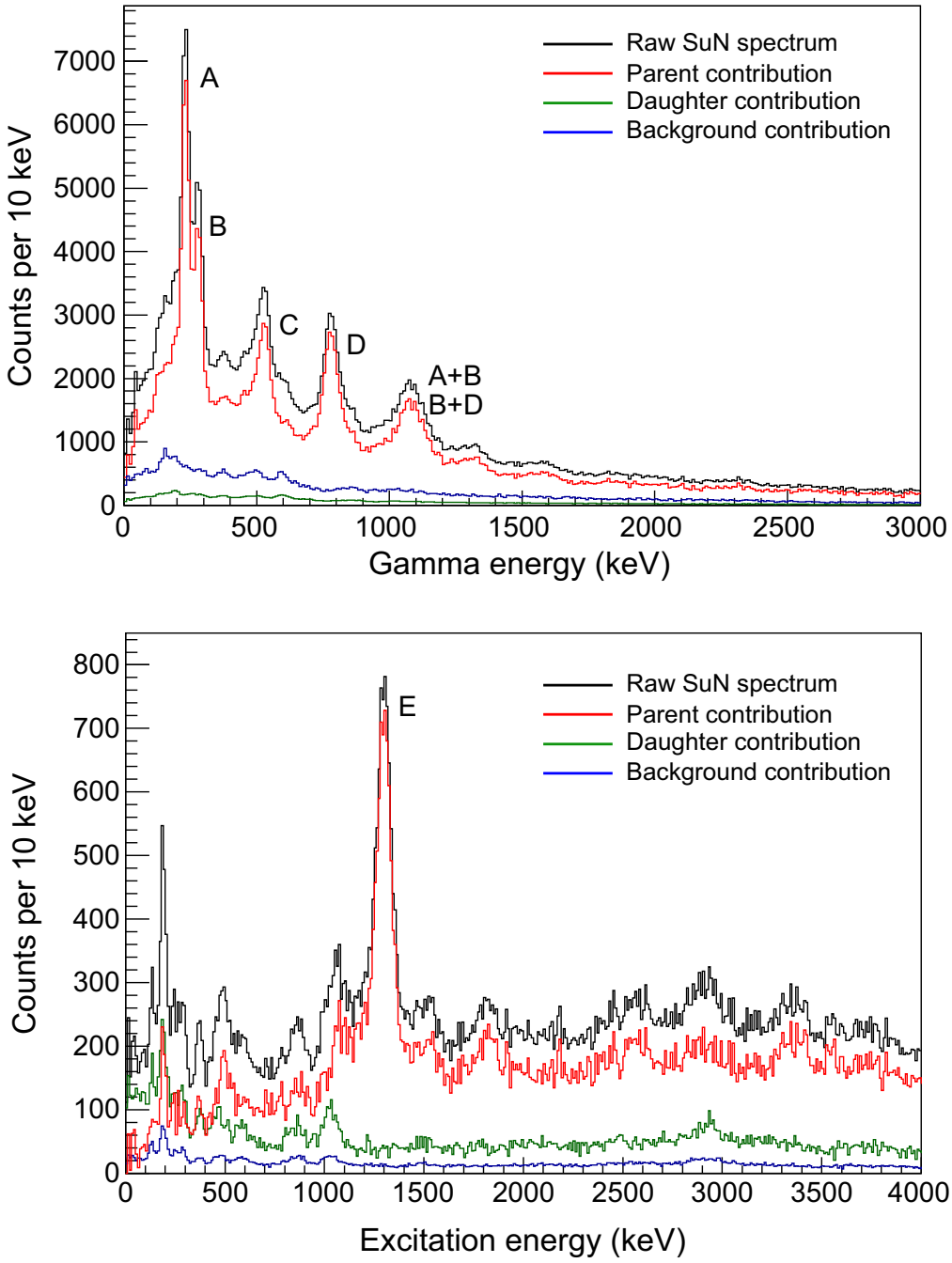

Figure 5.42: ^{73}Co SuN spectra showing the raw spectrum, daughter decay contribution, background contribution, and final γ-ray (top) and TAS (bottom) spectra for the de-excitation of ^{73}Ni.

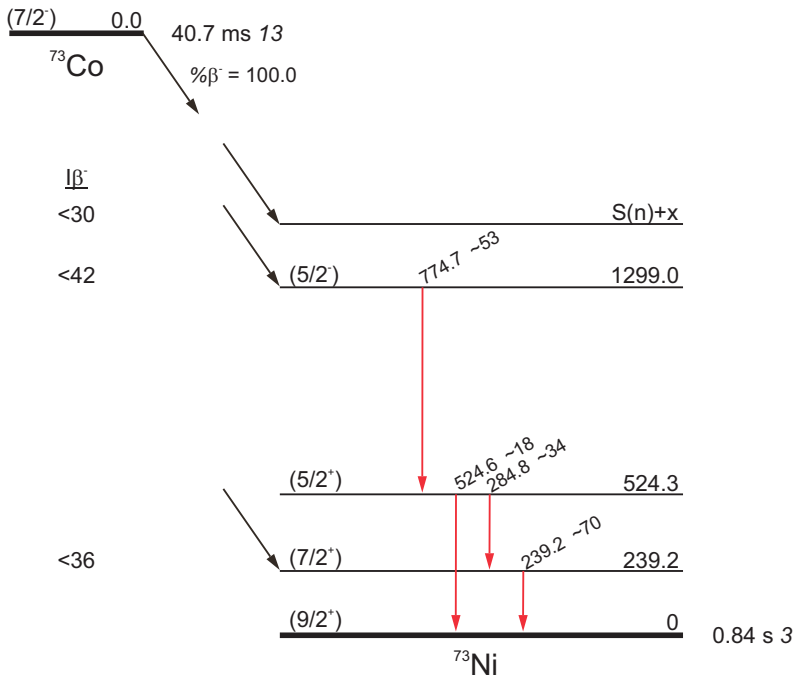

Figure 5.43: Known level scheme for the β decay of ^{73}Co.

5.4.1 β-Oslo matrices

The raw 2D Oslo matrix for the β decay of ^{73}Co is shown in Fig. 5.44 with 10 keV wide bins, while the starting matrix, daughter component matrix, and background component matrix can be found in Appendix B. The unfolded matrix is shown in Fig. 5.45, with 120 kev binning, and the primary matrix is shown in Fig. 5.46. The extraction range for the NLD and γSF was $E_\gamma > 1700$ keV, $E_x \in (2800, 4000)$ keV. Even though the first excited state of the β-delayed neutron daughter, ^{72}Ni, is relatively high in energy (1.0950(9) MeV [68]), the upper E_x limit was not raised further above S_n due to a lack of statistics.

5.4.2 NLD normalization

The NLD normalization procedure followed those described for ^{71,72}Ni. The χ^2 minimization to determine the shift value for the calculated cumulative levels (once again restricted to levels that fall within the spin range populated in β decay) is shown in Fig. 5.47, and resulted

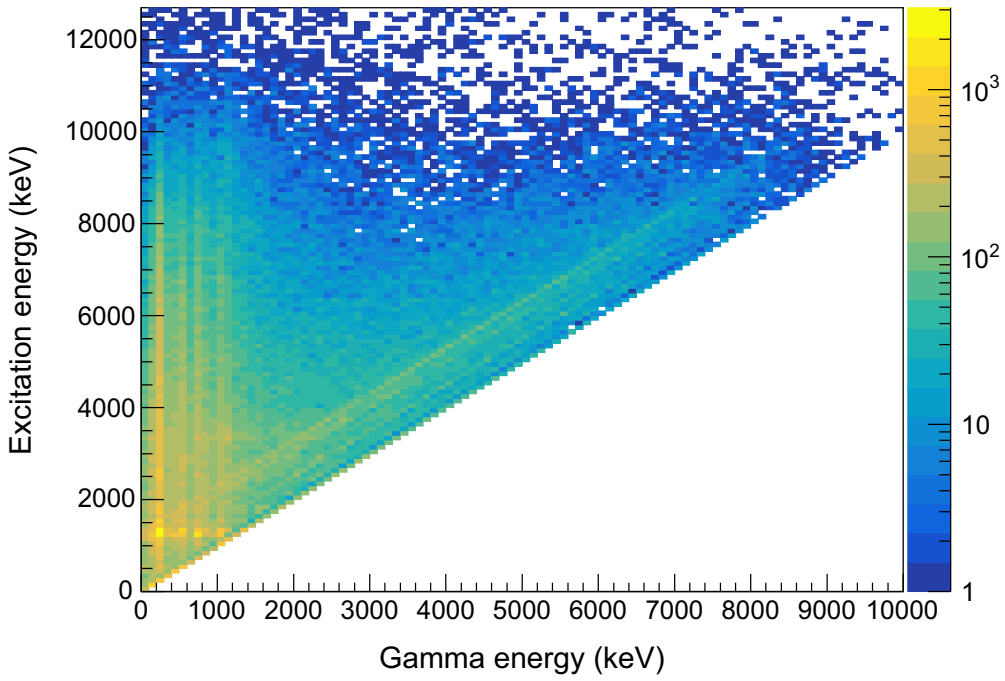

Figure 5.44: Raw 2D Oslo matrix for the decay of ^{73}Co into excited states of ^{73}Ni. The γ-ray energies obtained from the segments of SuN are plotted on the x-axis, while the excitation energy of the daughter nucleus, obtained from the total energy in the detector, is plotted on the y-axis.

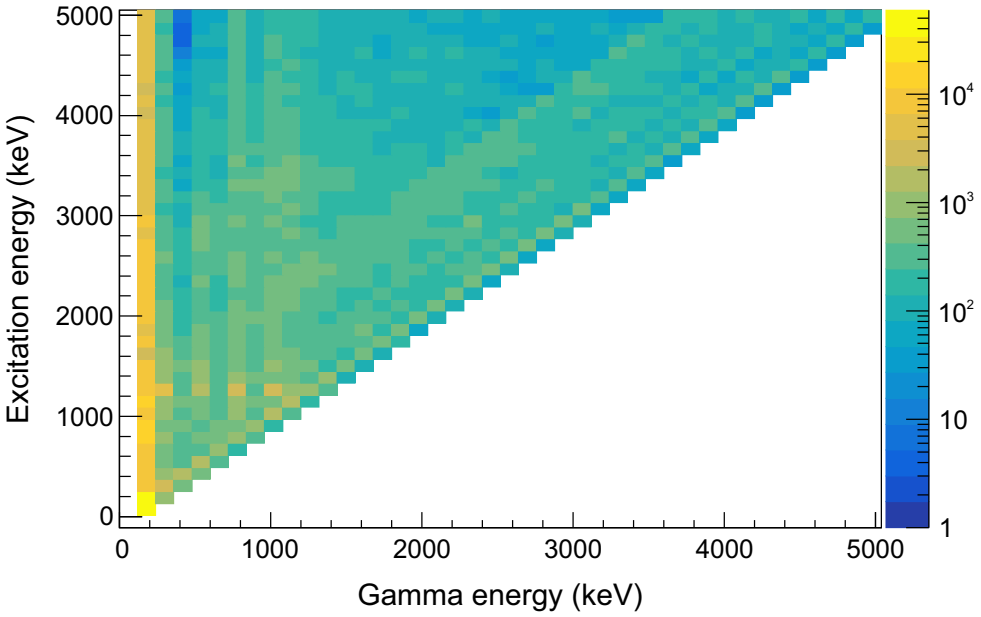

Figure 5.45: Unfolded 2D matrix for ^{73}Ni with 120 keV binning on both axis.

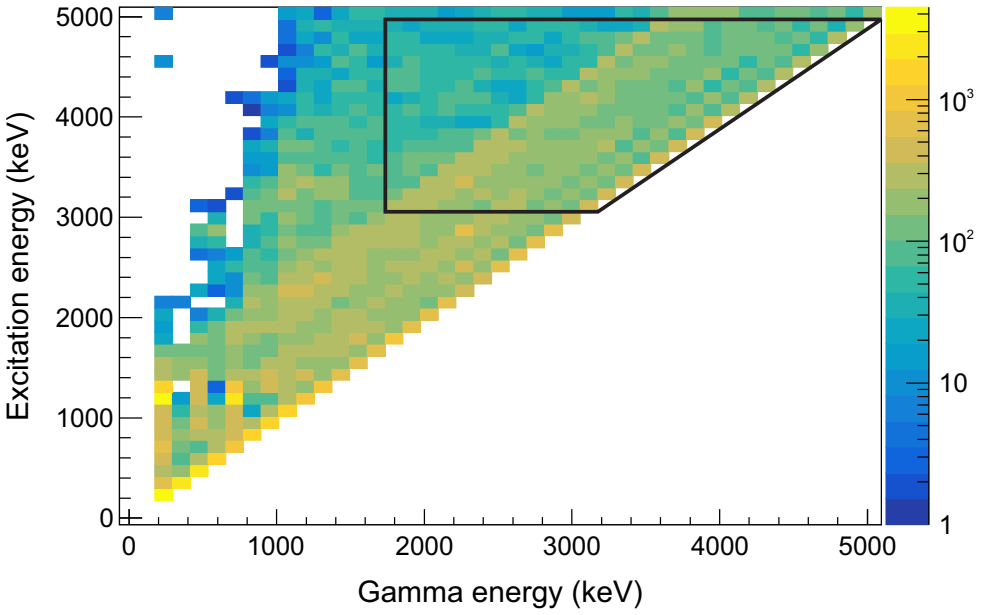

Figure 5.46: Primary 2D matrix for ^{73}Ni with 120 keV binning on both axis. The extraction region used for the NLD and γSF is outlined by the black lines.

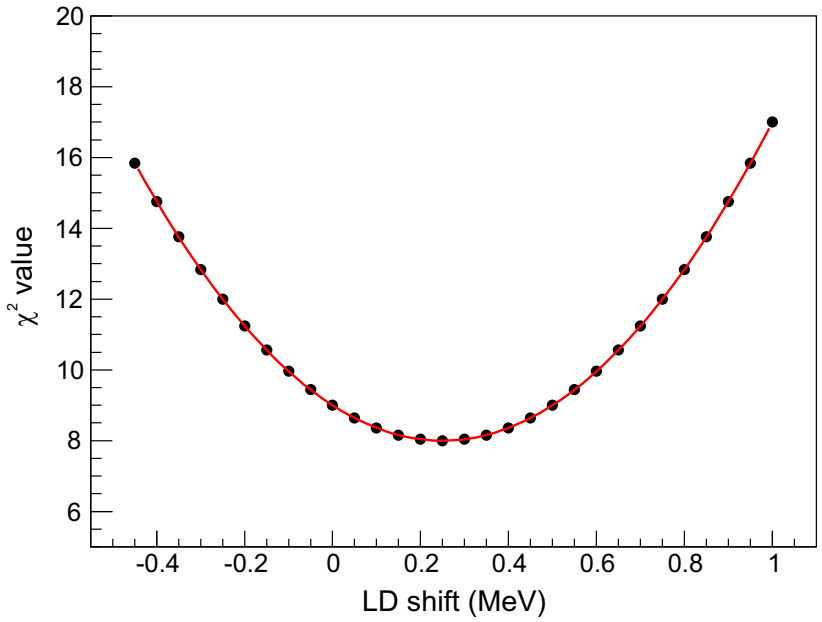

Figure 5.47: χ^2 values for different E_x shifts of the calculated cumulative levels compared to the known cumulative levels for ^{73}Ni.

Table 5.12: Parameters used in exponential fit to shifted calculated NLD for ^{73}Ni.

Shift Value	Constant	Slope	$\rho(S_n)$ (MeV^{-1})
0 MeV	1.7(1)	1.06(1)	161(17)
0.25 MeV	1.3(1)	1.06(1)	124(14)
0.5 MeV	0.99(9)	1.06(1)	95(11)

in shifts of 0.25 $\pm$ 0.25 MeV. The resulting shifted calculated NLD are shown compared to the known levels in Fig. 5.48, and the shifted calculated NLD around S_n is shown in Fig. 5.49. The low S_n value (3.953(3) MeV [107]) was less of an issue for this isotope than for ^{71}Ni, as the calculated NLD had a more exponential shape at low energies. The exponential fits to the shifted calculated NLD are shown in Fig. 5.49, while the parameters for the fits are detailed in Table 5.12. The fits resulted in $\rho(S_n)$ values of 95(11), 124(14), and 161(17) MeV^{-1}.

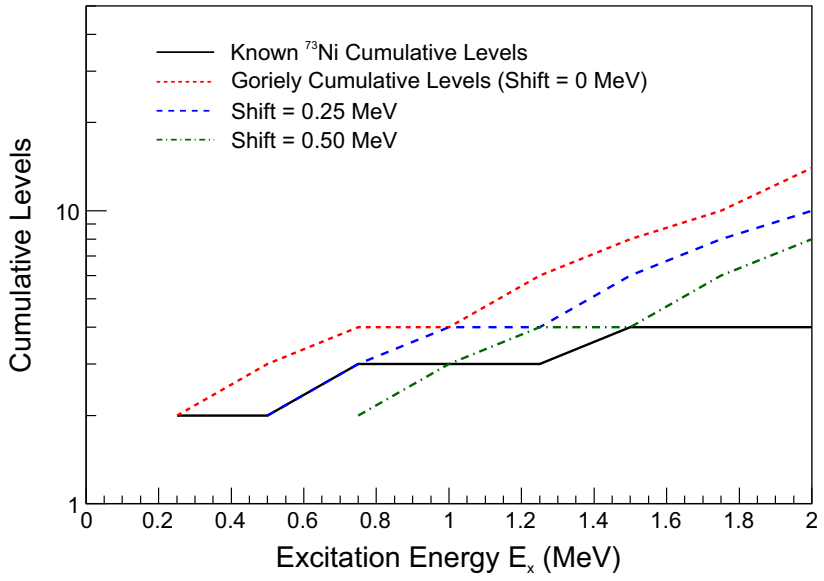

Figure 5.48: Shifted calculated cumulative levels compared to the known cumulative levels.

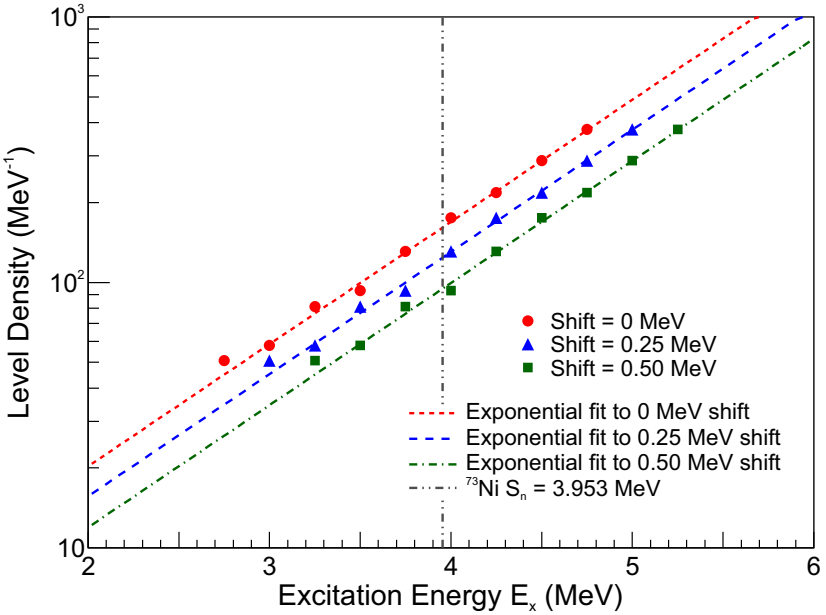

Figure 5.49: Shifted calculated level densities (upper, mid, and lower) near S_n used to determine $\rho(S_n)$ values for the NLD normalization.

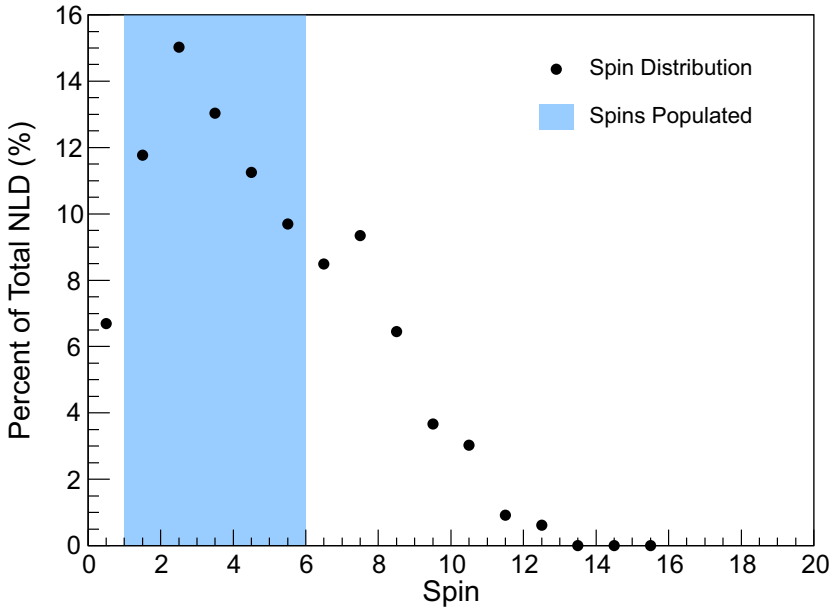

Figure 5.50: Distribution of spins for the levels in ^{73}Ni around the neutron separation energy based on tabulated spin- and parity-dependent NLD from Ref. [30]. Spins highlighted in blue are populated following an allowed β decay of ^{73}Co and one dipole photon transition. The ground state of ^{73}Co has been tentatively assigned a value of $(7/2^-)$.

The NLD reduction due to the limited experimental information was necessary for ^{73}Ni as well. The spin distribution around S_n, with the populated spins of 3/2 to 11/2 (both parities) highlighted is shown in Fig. 5.50. This represented 60.8(6)% of the total NLD, leading to reduced $\rho(S_n)$ values of 58(7), 75(8), and 98(11) MeV^{-1}. The upper, middle, and lower normalized NLD is shown in Fig. 5.51, along with the three shifted Goriely calculated NLDs, reduced to only the spin range of interest.

5.4.3 γSF normalization

As with the other two Ni isotopes, the ^{73}Ni γSF was normalized using data from ^{68,69,70}Ni. The normalized γSF is shown in Fig. 5.52.

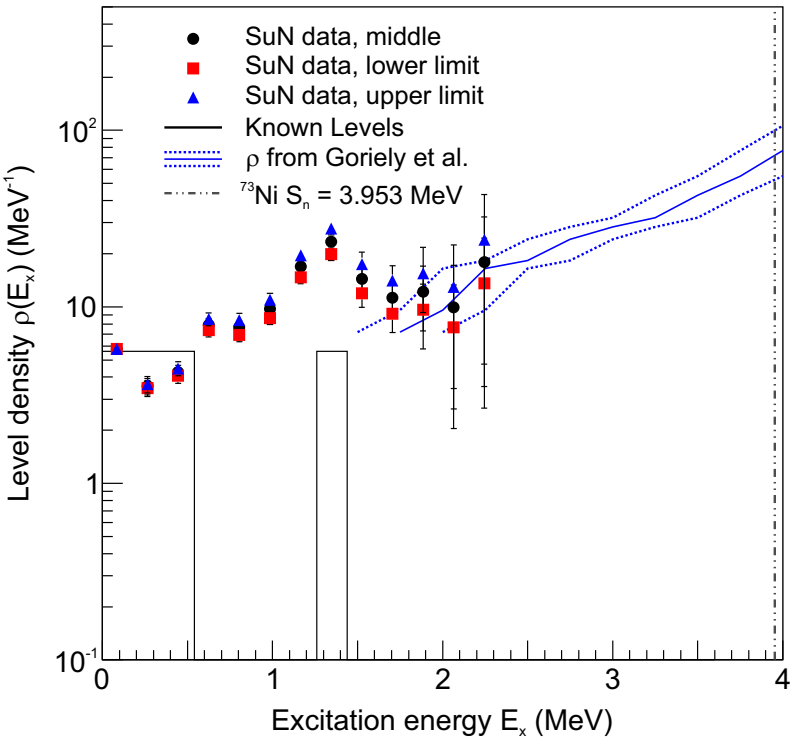

Figure 5.51: Normalized NLD for ^{73}Ni, with the known levels and Goriely calculated NLD (shifts of 0 MeV, 0.25 MeV, and 0.5 MeV).

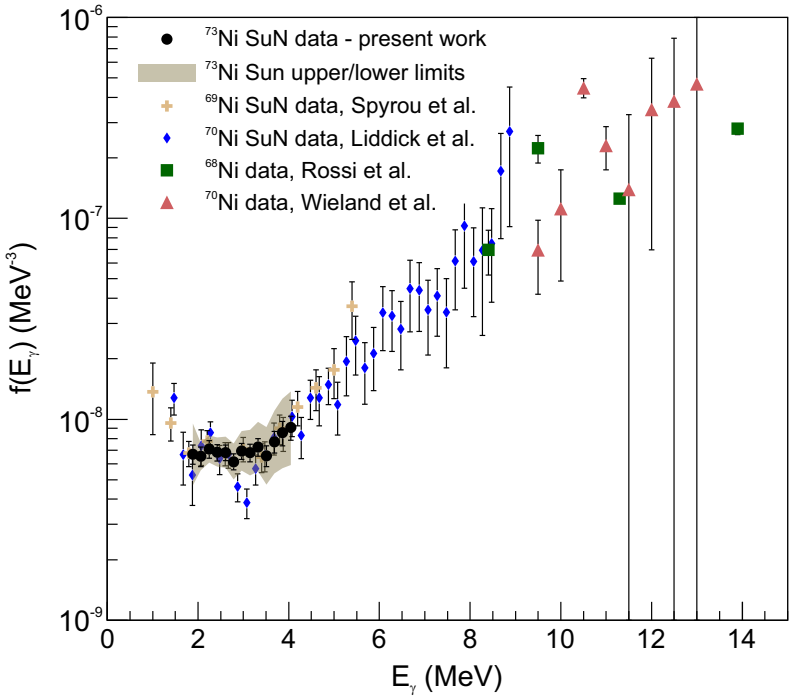

Figure 5.52: Normalized γSF for ^{73}Ni (black dots) compared to γSF data on ^{69,70}Ni from the β-Oslo method, as well as higher-energy Coulomb dissociation data for ^{68,70}Ni.

Chapter 6

Results and Discussion

6.1 TALYS calculations

The γSF data for each isotope was fitted with a combination of a Hartree-Fock BCS model ("strength 3" option in TALYS) and an exponential upbend. The strength 3 table was chosen because it represented the γSF of all three isotopes well at higher energies (above 2 MeV) and was easy to shift in magnitude in the code. The upbend needed to be added directly to the source code. The shift value and the parameters for the exponential upbend were determined by a combined fit to the experimental data. The best results can be seen in Figs. 6.1, 6.2 (fitted for both the 6^- and 7^- ^{72}Co parent spin possibilities), and 6.3. Only the middle values are shown in this section, but the lower limit and upper limit for each isotope were also obtained and incorporated into the TALYS calculation as well. All of the results from this procedure are provided in Appendix C. The fitted parameters are given in Table 6.1.

The neutron-capture cross sections and reaction rates for the ^{70}Ni$(n,\gamma)^{71}$Ni, ^{71}Ni$(n,\gamma)^{72}$Ni, and ^{72}Ni$(n,\gamma)^{73}$Ni reactions were then calculated in TALYS. All combinations of the NLD and γSF models in Table 3.4 were first used to determine the model uncertainty, which can be seen in Fig. 6.4 as the light grey band. The procedure described above was used to incorporate the experimental γSF, while the experimental NLD was converted to a spin-dependent

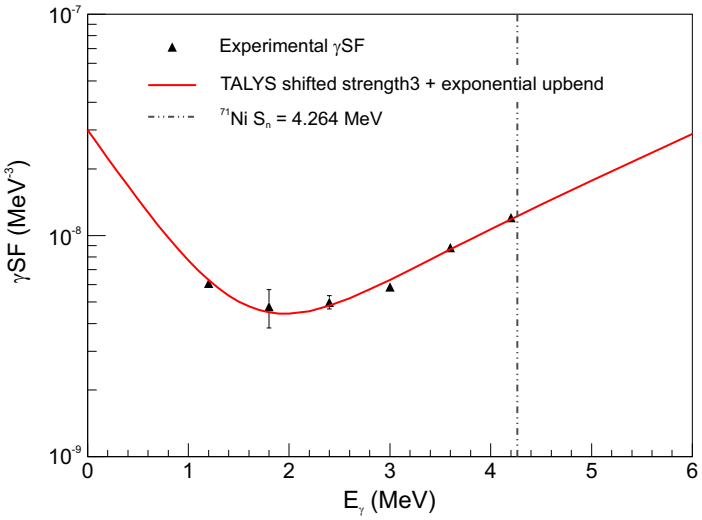

Figure 6.1: Fit to experimental γSF for ^{71}Ni using the HFBCS model (strength 3 in TALYS) and an exponential upbend.

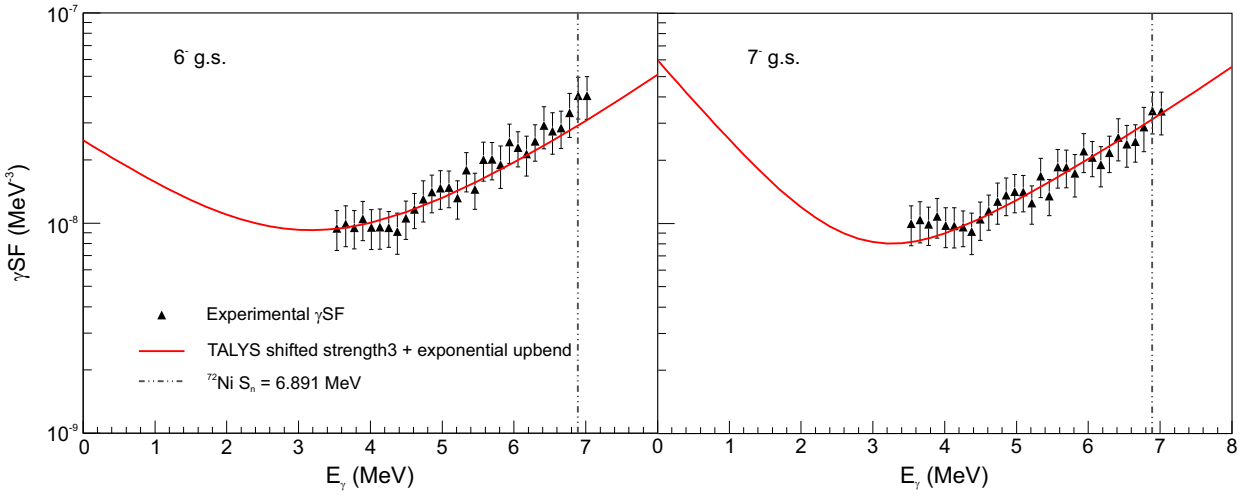

Figure 6.2: Fit to experimental γSF for ^{72}Ni using the HFBCS model (strength 3 in TALYS) and an exponential upbend. The γSF obtained from a 6^- ^{72}Co parent is on the left, while the γSF obtained from a 7^- parent is on the right.

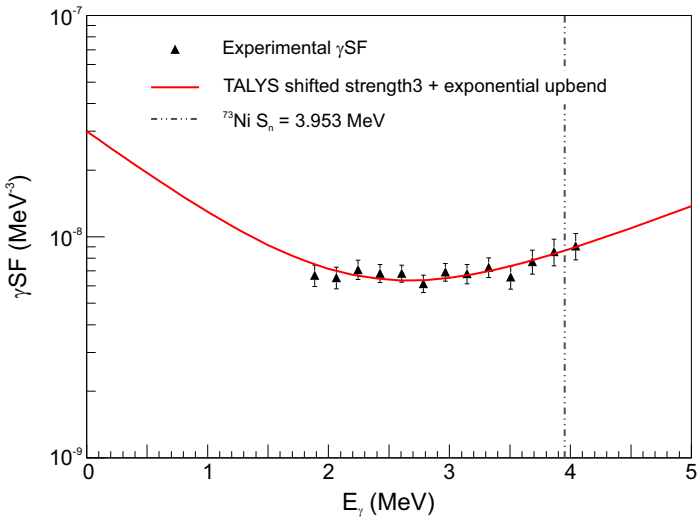

Figure 6.3: Fit to experimental γSF for ^{73}Ni using the HFBCS model (strength 3 in TALYS) and an exponential upbend.

Table 6.1: Parameters used to fit the experimental γSF with a scaled HFBCS table (strength 3 in TALYS) and exponential upbend. Fits are shown in Figs. 6.1, 6.2, and 6.3 for the middle values.

Isotope	Strength 3 scaling factor	Exponential constant	Exponential slope
^{71}Ni lower limit	1.4	3E-8	-1.2
^{71}Ni middle	1.6	3E-8	-1.5
^{71}Ni upper limit	1.8	3E-8	-1.8
^{72}Ni (6^- g.s.) lower limit	0.8	4E-8	-0.7
^{72}Ni (6^- g.s.) middle	1.2	5E-8	-0.9
^{72}Ni (6^- g.s.) upper limit	1.7	2E-8	-1.1
^{72}Ni (7^- g.s.) lower limit	0.8	3E-8	-0.5
^{72}Ni (7^- g.s.) middle	1.1	6E-8	-0.9
^{72}Ni (7^- g.s.) upper limit	1.6	5E-8	-1.2
^{73}Ni lower limit	1.0	3E-8	-0.8
^{73}Ni middle	1.3	3E-8	-0.9
^{73}Ni upper limit	1.8	4E-8	-1.2

Table 6.2: Range of neutron-capture cross sections and reaction rates (maximum/minimum at each energy or temperature) for all three reactions. In each case, the cross sections and reaction rates were reduced to under a factor of 3 (under a factor of 2 for the ^{70}Ni reaction).

Reaction	Input	Cross section range (max/min)	Reaction rate range (max/min)
^{70}Ni(n,γ)	TALYS NLD and γSF models	28	52
	experimental NLD and γSF	1.8	1.8
^{71}Ni(n,γ)	TALYS NLD and γSF models	30	28
	experimental NLD and γSF	2.9	2.4
^{72}Ni(n,γ)	TALYS NLD and γSF models	90	77
	experimental NLD and γSF	2.9	2.4

table as described in Chapter 3. All combinations of experimental NLD and γSF were run through TALYS to determine the experimentally-constrained uncertainty. The results for each isotope can be seen in Fig. 6.4 (for the ^{71}Ni$(n,\gamma)^{72}$Ni reaction, the uncertainty from both potential ^{72}Co ground state spins are combined) as the dark grey band. In all three reactions, the uncertainties were dramatically decreased when the experimental NLD and γSF were incorporated (see Table 6.2).

The ^{71,72,73}Ni neutron-capture cross sections were also compared to the ^{68,69}Ni neutron-capture cross sections previously constrained using the β-Oslo method [108, 77]. The full ranges for all five nuclei can be seen in Fig. 6.5. The three cross sections for even mass isotopes (^{68,70,72}Ni) are very similar, while the cross sections for odd mass isotopes (^{69,71}Ni) are higher. The γSF of ^{72}Ni, which is the result of the ^{71}Ni(n,γ) reaction, is larger at lower γ-ray energies than ^{71,73}Ni (see Fig. 6.6), which may explain the difference between the even-mass and odd-mass cross sections. Other potential causes have not yet been investigated, including the nuclear structure information that was used for each reaction.

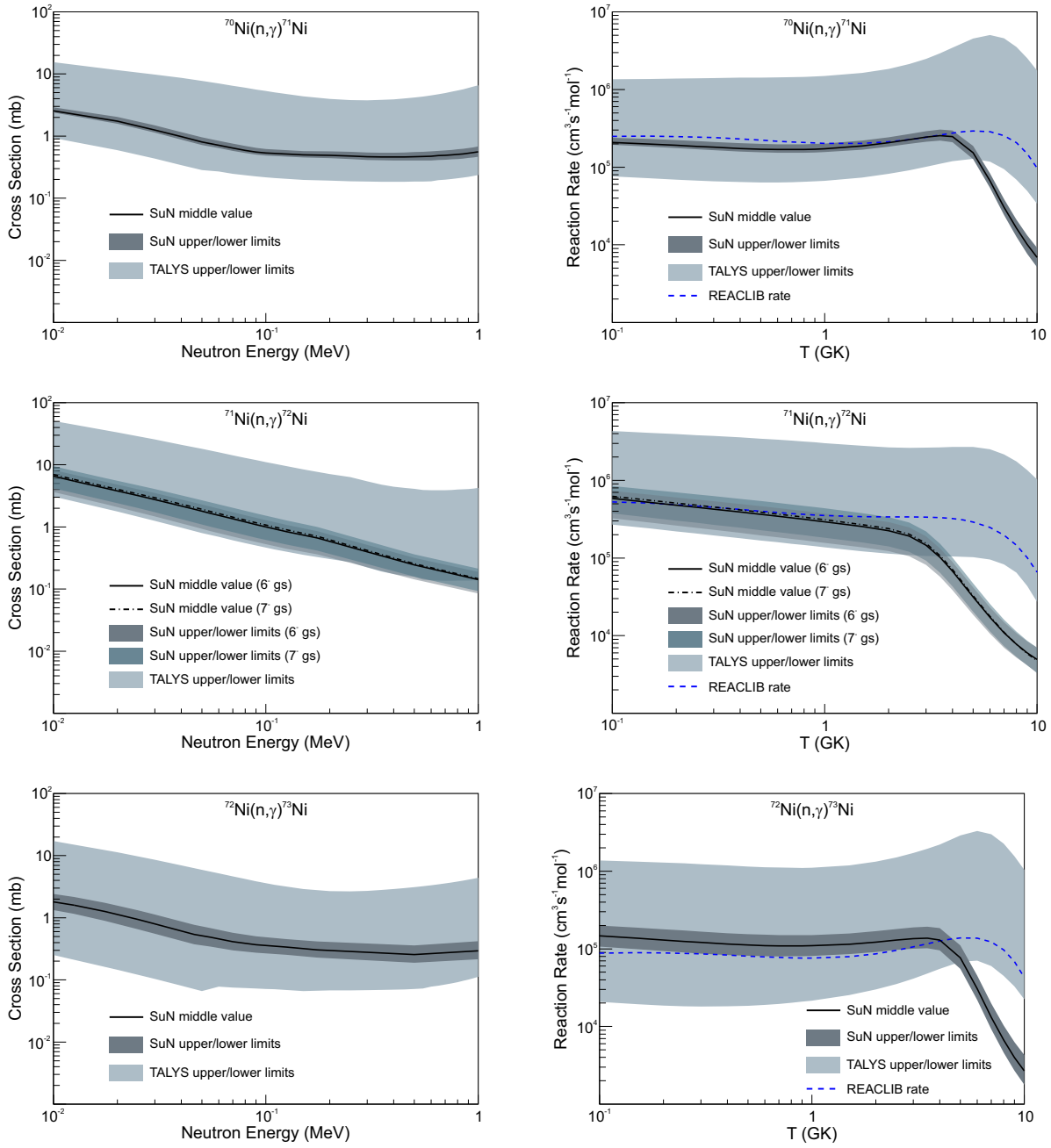

Figure 6.4: (Left) TALYS cross section calculations (reactions are labeled). The light band is the uncertainty in the cross section when considering all combinations of the NLD and γSF models available (excluding the temperature-dependent HFB NLD and SLO γSF). The darker band is the uncertainty when including the experimentally constrained NLD and γSF, along with their associated uncertainties. (Right) TALYS reaction rate calculations (reactions are labeled). The light and dark bands are the same as for the cross section, while the blue dashed line is the JINA REACLIB rate for the reaction (also calculated in TALYS) [15].

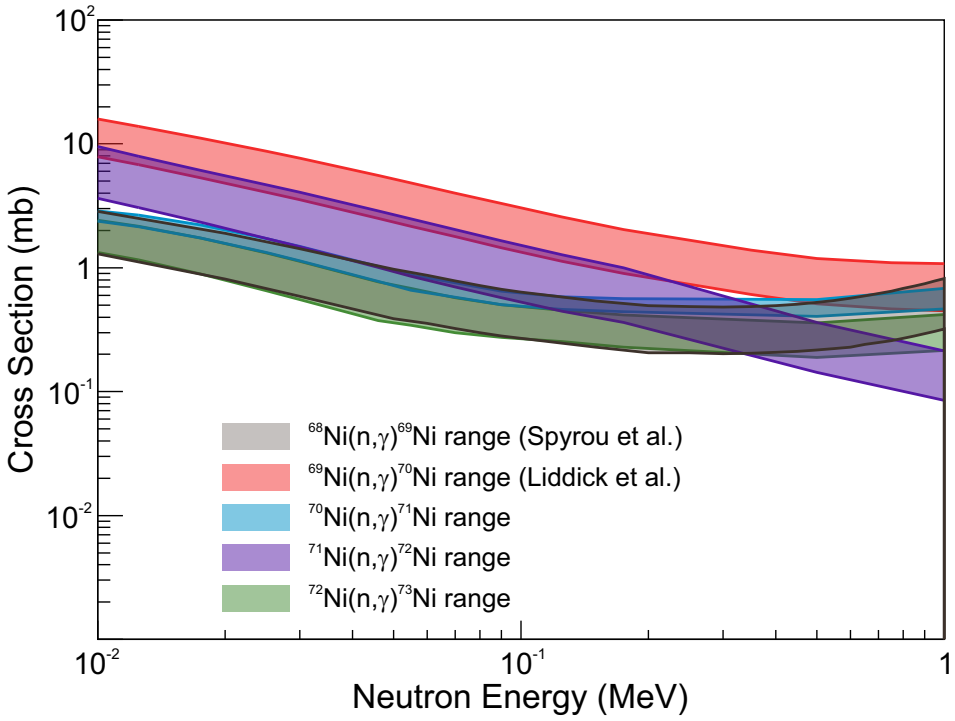

Figure 6.5: Comparison of the five Ni cross sections calculated in TALYS.

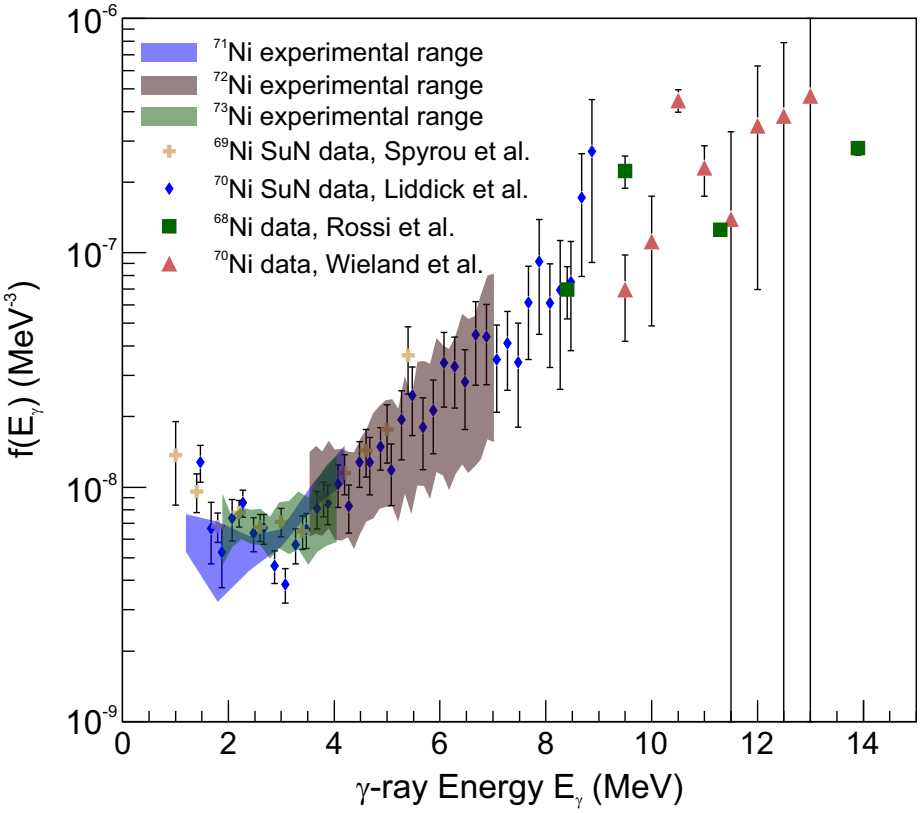

Figure 6.6: Experimentally constrained γSF for ^{71,72,73}Ni.

Chapter 7

Conclusions and Outlook

A more complete understanding of the astrophysical location of the r-process, and in particular the weak r-process, relies on detailed information about the nuclei that are involved in the process. In particular, neutron-capture cross sections are important but can have large uncertainties due to the lack of direct experimental data at the present time. For the very neutron-rich nuclei involved in the r-process, indirect methods such as the β-Oslo method are the only way to constrain neutron-capture cross section calculations using experimental data. By extracting the NLD and γSF of the nucleus formed in a neutron-capture reaction from β-decay experimental data the uncertainty in a Hauser-Feshbach calculation of the neutron-capture cross section can be reduced significantly, as these properties are the main sources of uncertainty in such calculations. Smaller uncertainties for neutron-capture cross sections propagate through astrophysics models of the r-process and result in reduced uncertainties on the predicted abundance patterns, which allows for a more direct comparison between modeled and observed abundances.

The choice of a Hauser-Feshbach model code can also contribute to the overall uncertainty in the calculated cross sections. The assumptions and choices made to describe the nuclear physics within each code, including the NLD, γSF, and known levels, can influence the cross section. When different codes start from different assumptions the resulting cross sections can very very different. Comparing the neutron-capture cross sections from multiple codes

for every nucleus involved in the r-process is not feasible, but the discrepancies between them can be reduced with a better understanding of the shape of the NLD and γSF far from stability, as well as more information about the structure of neutron-rich nuclei.

Experiments to obtain information about the NLD and γSF, even those that utilize indirect methods, are possible only in select regions of the nuclear chart. That means that our reliance on models to describe both properties for all of the other nuclei involved in the r-process remains, but the models can be improved using the select data that is available. When models of the NLD and γSF are better able to describe the neutron-rich nuclei that are possible to study, such as the Ni isotopes presented in this work, then there is less uncertainty in how to describe the NLD and γSF of even more neutron-rich nuclei. As more β-Oslo experiments are performed, larger-scale systematic studies of the NLD and γSF as a function of both the proton number and neutron number will be possible and will also contribute to an increased understanding of both properties. Some theoretical work to understand the dependence of the γSF as a function of neutron number has begun, but with more data the theory can be improved [109].

The reduced uncertainties in the neutron-capture cross sections of all five Ni isotopes (70-74) can now be used to investigate the impact on the overall uncertainty in calculated abundance patterns in weak r-process models. The reduced uncertainty in just the ^{69}Ni$(n,\gamma)^{70}$Ni reaction was previously shown to reduce the uncertainty in abundances in the mass 70 region as well as up to mass 130, so incorporating the reduced uncertainties of four more reactions should have a larger impact.

APPENDICES

Appendix A

Default NLD and γSF tables

Table A.1: TALYS default NLD for ^{74}Zn including spin-dependent NLD for J=0-4. An equal parity distribution is assumed.

E_x (MeV)	Total NLD (MeV^{-1})	J=0	J=1	J=2	J=3	J=4
0.25	2.93E-01	2.15E-02	5.55E-02	6.86E-02	6.14E-02	4.34E-02
0.50	3.98E-01	2.82E-02	7.33E-02	9.15E-02	8.31E-02	6.00E-02
0.75	5.41E-01	3.71E-02	9.69E-02	1.22E-01	1.13E-01	8.27E-02
1.00	7.36E-01	4.89E-02	1.28E-01	1.63E-01	1.52E-01	1.14E-01
1.25	1.00E+00	6.45E-02	1.70E-01	2.18E-01	2.06E-01	1.57E-01
1.50	1.36E+00	8.50E-02	2.25E-01	2.90E-01	2.78E-01	2.15E-01
1.75	1.85E+00	1.12E-01	2.98E-01	3.88E-01	3.75E-01	2.94E-01
2.00	2.51E+00	1.48E-01	3.95E-01	5.18E-01	5.06E-01	4.02E-01
2.25	3.41E+00	1.96E-01	5.24E-01	6.91E-01	6.82E-01	5.50E-01
2.50	4.64E+00	2.60E-01	6.95E-01	9.24E-01	9.20E-01	7.51E-01
2.75	6.30E+00	3.44E-01	9.24E-01	1.23E+00	1.24E+00	1.02E+00
3.00	8.57E+00	4.56E-01	1.23E+00	1.65E+00	1.67E+00	1.40E+00
3.25	1.17E+01	6.04E-01	1.63E+00	2.20E+00	2.25E+00	1.90E+00
3.50	1.58E+01	8.02E-01	2.17E+00	2.95E+00	3.03E+00	2.59E+00
3.75	2.15E+01	1.07E+00	2.89E+00	3.94E+00	4.08E+00	3.52E+00
4.00	2.92E+01	1.41E+00	3.85E+00	5.27E+00	5.50E+00	4.78E+00
4.25	3.97E+01	1.88E+00	5.12E+00	7.05E+00	7.41E+00	6.49E+00
4.50	5.40E+01	2.50E+00	6.83E+00	9.44E+00	9.98E+00	8.82E+00
4.75	7.34E+01	3.32E+00	9.10E+00	1.26E+01	1.34E+01	1.20E+01
5.00	9.98E+01	4.42E+00	1.21E+01	1.69E+01	1.81E+01	1.62E+01
5.50	1.84E+02	7.85E+00	2.16E+01	3.03E+01	3.28E+01	2.99E+01

Continued on next page

Table A.1 – continued from previous page

E_x (MeV)	Total NLD (MeV^{-1})	J=0	J=1	J=2	J=3	J=4
6.00	3.41E+02	1.39E+01	3.85E+01	5.44E+01	5.94E+01	5.49E+01
6.50	6.29E+02	2.48E+01	6.87E+01	9.76E+01	1.08E+02	1.01E+02
7.00	1.16E+03	4.42E+01	1.23E+02	1.75E+02	1.95E+02	1.85E+02
7.50	2.15E+03	7.88E+01	2.19E+02	3.15E+02	3.54E+02	3.38E+02
8.00	3.91E+03	1.37E+02	3.82E+02	5.53E+02	6.27E+02	6.08E+02
8.50	6.95E+03	2.33E+02	6.53E+02	9.51E+02	1.09E+03	1.07E+03
9.00	1.21E+04	3.89E+02	1.09E+03	1.60E+03	1.85E+03	1.83E+03
9.50	2.06E+04	6.40E+02	1.80E+03	2.65E+03	3.08E+03	3.08E+03
10.0	3.46E+04	1.04E+03	2.93E+03	4.32E+03	5.05E+03	5.10E+03
11.0	9.25E+04	2.61E+03	7.39E+03	1.10E+04	1.30E+04	1.33E+04
12.0	2.34E+05	6.26E+03	1.78E+04	2.66E+04	3.17E+04	3.29E+04
13.0	5.67E+05	1.44E+04	4.11E+04	6.19E+04	7.43E+04	7.78E+04
14.0	1.32E+06	3.21E+04	9.16E+04	1.39E+05	1.67E+05	1.77E+05
15.0	2.95E+06	6.91E+04	1.98E+05	3.00E+05	3.65E+05	3.89E+05
16.0	6.42E+06	1.45E+05	4.15E+05	6.32E+05	7.72E+05	8.28E+05
17.0	1.36E+07	2.96E+05	8.49E+05	1.30E+06	1.59E+06	1.72E+06
18.0	2.80E+07	5.91E+05	1.70E+06	2.60E+06	3.21E+06	3.48E+06
19.0	5.64E+07	1.16E+06	3.33E+06	5.11E+06	6.32E+06	6.89E+06
20.0	1.11E+08	2.22E+06	6.40E+06	9.85E+06	1.22E+07	1.34E+07
22.5	5.65E+08	1.06E+07	3.05E+07	4.72E+07	5.90E+07	6.53E+07
25.0	2.60E+09	4.61E+07	1.33E+08	2.07E+08	2.61E+08	2.91E+08
30.0	4.42E+10	7.11E+08	2.07E+09	3.23E+09	4.10E+09	4.63E+09

Continued on next page

Table A.1 – continued from previous page

E_x (MeV)	Total NLD (MeV^{-1})	J=0	J=1	J=2	J=3	J=4
40.0	6.69E+12	9.31E+10	2.72E+11	4.28E+11	5.51E+11	6.34E+11
50.0	5.66E+14	7.03E+12	2.06E+13	3.26E+13	4.24E+13	4.93E+13
60.0	3.19E+16	3.61E+14	1.06E+15	1.69E+15	2.21E+15	2.59E+15
70.0	1.32E+18	1.39E+16	4.07E+16	6.50E+16	8.54E+16	1.01E+17
80.0	4.28E+19	4.20E+17	1.24E+18	1.98E+18	2.61E+18	3.11E+18
90.0	1.14E+21	1.05E+19	3.10E+19	4.97E+19	6.58E+19	7.86E+19
100	2.55E+22	2.24E+20	6.59E+20	1.06E+21	1.41E+21	1.69E+21
110	4.94E+23	4.13E+21	1.22E+22	1.96E+22	2.62E+22	3.14E+22
120	8.45E+24	6.76E+22	2.00E+23	3.22E+23	4.30E+23	5.18E+23
130	1.29E+26	9.93E+23	2.94E+24	4.74E+24	6.34E+24	7.66E+24
140	1.79E+27	1.33E+25	3.92E+25	6.34E+25	8.49E+25	1.03E+26
150	2.27E+28	1.63E+26	4.81E+26	7.78E+26	1.04E+27	1.27E+27
160	2.66E+29	1.84E+27	5.45E+27	8.83E+27	1.19E+28	1.44E+28
170	2.89E+30	1.94E+28	5.75E+28	9.33E+28	1.26E+29	1.53E+29
180	2.94E+31	1.92E+29	5.69E+29	9.24E+29	1.24E+30	1.52E+30
190	2.82E+32	1.79E+30	5.30E+30	8.62E+30	1.16E+31	1.42E+31
200	2.55E+33	1.58E+31	4.68E+31	7.60E+31	1.03E+32	1.25E+32

Table A.2: TALYS default NLD for ^{74}Zn including spin-dependent NLD for J=5-8. An equal parity distribution is assumed.

E_x (MeV)	Total NLD (MeV^{-1})	J=5	J=6	J=7	J=8
0.25	2.93E-01	2.51E-02	1.21E-02	4.92E-03	1.69E-03
0.50	3.98E-01	3.56E-02	1.77E-02	7.44E-03	2.66E-03
0.75	5.41E-01	5.03E-02	2.57E-02	1.12E-02	4.14E-03
1.00	7.36E-01	7.08E-02	3.72E-02	1.67E-02	6.40E-03
1.25	1.00E+00	9.93E-02	5.35E-02	2.47E-02	9.80E-03
1.50	1.36E+00	1.39E-01	7.66E-02	3.63E-02	1.49E-02
1.75	1.85E+00	1.94E-01	1.09E-01	5.31E-02	2.24E-02
2.00	2.51E+00	2.70E-01	1.55E-01	7.74E-02	3.36E-02
2.25	3.41E+00	3.75E-01	2.20E-01	1.12E-01	5.00E-02
2.50	4.64E+00	5.20E-01	3.11E-01	1.62E-01	7.40E-02
2.75	6.30E+00	7.20E-01	4.38E-01	2.33E-01	1.09E-01
3.00	8.57E+00	9.95E-01	6.16E-01	3.34E-01	1.60E-01
3.25	1.17E+01	1.37E+00	8.63E-01	4.77E-01	2.33E-01
3.50	1.58E+01	1.89E+00	1.21E+00	6.79E-01	3.39E-01
3.75	2.15E+01	2.60E+00	1.69E+00	9.65E-01	4.91E-01
4.00	2.92E+01	3.58E+00	2.35E+00	1.37E+00	7.08E-01
4.25	3.97E+01	4.92E+00	3.27E+00	1.93E+00	1.02E+00
4.50	5.40E+01	6.75E+00	4.55E+00	2.73E+00	1.46E+00
4.75	7.34E+01	9.25E+00	6.31E+00	3.84E+00	2.09E+00
5.00	9.98E+01	1.27E+01	8.75E+00	5.39E+00	2.98E+00
5.50	1.84E+02	2.37E+01	1.67E+01	1.06E+01	6.02E+00
6.00	3.41E+02	4.43E+01	3.19E+01	2.06E+01	1.21E+01
6.50	6.29E+02	8.26E+01	6.06E+01	4.00E+01	2.40E+01
7.00	1.16E+03	1.54E+02	1.15E+02	7.72E+01	4.74E+01
7.50	2.15E+03	2.85E+02	2.16E+02	1.49E+02	9.31E+01
8.00	3.91E+03	5.22E+02	4.04E+02	2.85E+02	1.83E+02
8.50	6.95E+03	9.30E+02	7.33E+02	5.27E+02	3.48E+02
9.00	1.21E+04	1.62E+03	1.30E+03	9.49E+02	6.40E+02
9.50	2.06E+04	2.76E+03	2.24E+03	1.67E+03	1.15E+03
10.0	3.46E+04	4.60E+03	3.79E+03	2.86E+03	2.00E+03

Continued on next page

Table A.2 – continued from previous page

E_x (MeV)	Total NLD (MeV^{-1})	J=5	J=6	J=7	J=8
11.0	9.25E+04	1.22E+04	1.03E+04	7.98E+03	5.74E+03
12.0	2.34E+05	3.07E+04	2.63E+04	2.08E+04	1.54E+04
13.0	5.67E+05	7.36E+04	6.40E+04	5.16E+04	3.88E+04
14.0	1.32E+06	1.69E+05	1.49E+05	1.22E+05	9.34E+04
15.0	2.95E+06	3.75E+05	3.34E+05	2.78E+05	2.16E+05
16.0	6.42E+06	8.07E+05	7.26E+05	6.10E+05	4.81E+05
17.0	1.36E+07	1.69E+06	1.53E+06	1.30E+06	1.04E+06
18.0	2.80E+07	3.44E+06	3.15E+06	2.70E+06	2.18E+06
19.0	5.64E+07	6.85E+06	6.33E+06	5.47E+06	4.46E+06
20.0	1.11E+08	1.34E+07	1.24E+07	1.08E+07	8.92E+06
22.5	5.65E+08	6.61E+07	6.24E+07	5.53E+07	4.64E+07
25.0	2.60E+09	2.97E+08	2.84E+08	2.55E+08	2.18E+08
30.0	4.42E+10	4.82E+09	4.69E+09	4.31E+09	3.77E+09
40.0	6.69E+12	6.74E+11	6.73E+11	6.39E+11	5.79E+11
50.0	5.66E+14	5.32E+13	5.42E+13	5.25E+13	4.87E+13
60.0	3.19E+16	2.83E+15	2.91E+15	2.87E+15	2.71E+15
70.0	1.32E+18	1.11E+17	1.16E+17	1.15E+17	1.10E+17
80.0	4.28E+19	3.44E+18	3.61E+18	3.63E+18	3.52E+18
90.0	1.14E+21	8.76E+19	9.26E+19	9.38E+19	9.17E+19
100	2.55E+22	1.89E+21	2.01E+21	2.05E+21	2.02E+21
110	4.94E+23	3.53E+22	3.78E+22	3.88E+22	3.84E+22
120	8.45E+24	5.85E+23	6.28E+23	6.47E+23	6.45E+23
130	1.29E+26	8.67E+24	9.34E+24	9.68E+24	9.70E+24
140	1.79E+27	1.17E+26	1.26E+26	1.31E+26	1.32E+26
150	2.27E+28	1.44E+27	1.56E+27	1.63E+27	1.65E+27
160	2.66E+29	1.64E+28	1.79E+28	1.87E+28	1.90E+28
170	2.89E+30	1.75E+29	1.90E+29	2.00E+29	2.03E+29
180	2.94E+31	1.74E+30	1.90E+30	2.00E+30	2.04E+30
190	2.82E+32	1.63E+31	1.78E+31	1.88E+31	1.92E+31
200	2.55E+33	1.44E+32	1.58E+32	1.67E+32	1.72E+32

Table A.3: CoH default NLD for ^{74}Zn including spin-dependent NLD for J=0-3. An equal parity distribution is assumed.

E_x (MeV)	Total NLD (MeV^{-1})	J=0	J=1	J=2	J=3
2.46E-02	5.61E-01	5.25E-02	1.40E-01	1.85E-01	1.83E-01
4.46E-02	5.72E-01	5.35E-02	1.43E-01	1.89E-01	1.87E-01
6.46E-02	5.83E-01	5.46E-02	1.46E-01	1.93E-01	1.90E-01
8.46E-02	5.95E-01	5.56E-02	1.49E-01	1.96E-01	1.94E-01
1.05E-01	6.06E-01	5.67E-02	1.51E-01	2.00E-01	1.98E-01
1.25E-01	6.18E-01	5.78E-02	1.54E-01	2.04E-01	2.02E-01
1.45E-01	6.30E-01	5.89E-02	1.57E-01	2.08E-01	2.06E-01
1.65E-01	6.42E-01	6.00E-02	1.60E-01	2.12E-01	2.10E-01
1.85E-01	6.54E-01	6.12E-02	1.64E-01	2.16E-01	2.14E-01
2.05E-01	6.67E-01	6.24E-02	1.67E-01	2.20E-01	2.18E-01
2.25E-01	6.80E-01	6.36E-02	1.70E-01	2.25E-01	2.22E-01
2.45E-01	6.93E-01	6.48E-02	1.73E-01	2.29E-01	2.26E-01
2.65E-01	7.07E-01	6.61E-02	1.77E-01	2.33E-01	2.31E-01
2.85E-01	7.20E-01	6.74E-02	1.80E-01	2.38E-01	2.35E-01
3.05E-01	7.34E-01	6.87E-02	1.83E-01	2.42E-01	2.40E-01
3.25E-01	7.48E-01	7.00E-02	1.87E-01	2.47E-01	2.44E-01
3.45E-01	7.63E-01	7.13E-02	1.91E-01	2.52E-01	2.49E-01
3.65E-01	7.78E-01	7.27E-02	1.94E-01	2.57E-01	2.54E-01
3.85E-01	7.93E-01	7.41E-02	1.98E-01	2.62E-01	2.59E-01
4.05E-01	8.08E-01	7.56E-02	2.02E-01	2.67E-01	2.64E-01
4.25E-01	8.24E-01	7.70E-02	2.06E-01	2.72E-01	2.69E-01
4.45E-01	8.40E-01	7.85E-02	2.10E-01	2.77E-01	2.74E-01
4.65E-01	8.56E-01	8.00E-02	2.14E-01	2.83E-01	2.79E-01
4.85E-01	8.73E-01	8.16E-02	2.18E-01	2.88E-01	2.85E-01
5.05E-01	8.89E-01	8.32E-02	2.22E-01	2.94E-01	2.90E-01
5.25E-01	9.07E-01	8.48E-02	2.26E-01	2.99E-01	2.96E-01
5.45E-01	9.24E-01	8.64E-02	2.31E-01	3.05E-01	3.02E-01
5.65E-01	9.42E-01	8.81E-02	2.35E-01	3.11E-01	3.08E-01
5.85E-01	9.60E-01	8.98E-02	2.40E-01	3.17E-01	3.14E-01
6.05E-01	9.79E-01	9.15E-02	2.45E-01	3.23E-01	3.20E-01

Continued on next page

Table A.3 – continued from previous page

E_x (MeV)	Total NLD (MeV^{-1})	J=0	J=1	J=2	J=3
6.25E-01	9.98E-01	9.33E-02	2.49E-01	3.29E-01	3.26E-01
6.45E-01	1.02E+00	9.51E-02	2.54E-01	3.36E-01	3.32E-01
6.65E-01	1.04E+00	9.70E-02	2.59E-01	3.42E-01	3.38E-01
6.85E-01	1.06E+00	9.88E-02	2.64E-01	3.49E-01	3.45E-01
7.05E-01	1.08E+00	1.01E-01	2.69E-01	3.56E-01	3.52E-01
7.25E-01	1.10E+00	1.03E-01	2.74E-01	3.63E-01	3.59E-01
7.45E-01	1.12E+00	1.05E-01	2.80E-01	3.70E-01	3.65E-01
7.65E-01	1.14E+00	1.07E-01	2.85E-01	3.77E-01	3.73E-01
7.85E-01	1.16E+00	1.09E-01	2.91E-01	3.84E-01	3.80E-01
8.05E-01	1.19E+00	1.11E-01	2.96E-01	3.92E-01	3.87E-01
8.25E-01	1.21E+00	1.13E-01	3.02E-01	3.99E-01	3.95E-01
8.45E-01	1.23E+00	1.15E-01	3.08E-01	4.07E-01	4.02E-01
8.65E-01	1.26E+00	1.17E-01	3.14E-01	4.15E-01	4.10E-01
8.85E-01	1.28E+00	1.20E-01	3.20E-01	4.23E-01	4.18E-01
9.05E-01	1.31E+00	1.22E-01	3.26E-01	4.31E-01	4.26E-01
9.25E-01	1.33E+00	1.24E-01	3.32E-01	4.39E-01	4.34E-01
9.45E-01	1.36E+00	1.27E-01	3.39E-01	4.48E-01	4.43E-01
9.65E-01	1.38E+00	1.29E-01	3.45E-01	4.56E-01	4.51E-01
9.85E-01	1.41E+00	1.32E-01	3.52E-01	4.65E-01	4.60E-01
1.01E+00	1.44E+00	1.34E-01	3.59E-01	4.74E-01	4.69E-01
1.03E+00	1.46E+00	1.37E-01	3.66E-01	4.83E-01	4.78E-01
1.05E+00	1.49E+00	1.40E-01	3.73E-01	4.93E-01	4.87E-01
1.07E+00	1.52E+00	1.42E-01	3.80E-01	5.02E-01	4.97E-01
1.09E+00	1.55E+00	1.45E-01	3.87E-01	5.12E-01	5.06E-01
1.11E+00	1.58E+00	1.48E-01	3.95E-01	5.22E-01	5.16E-01
1.13E+00	1.61E+00	1.51E-01	4.03E-01	5.32E-01	5.26E-01
1.15E+00	1.64E+00	1.54E-01	4.10E-01	5.42E-01	5.36E-01
1.17E+00	1.67E+00	1.57E-01	4.18E-01	5.53E-01	5.47E-01
1.19E+00	1.71E+00	1.60E-01	4.26E-01	5.64E-01	5.57E-01
1.21E+00	1.74E+00	1.63E-01	4.35E-01	5.74E-01	5.68E-01
1.23E+00	1.77E+00	1.66E-01	4.43E-01	5.86E-01	5.79E-01

Continued on next page

Table A.3 – continued from previous page

E_x (MeV)	Total NLD (MeV^{-1})	J=0	J=1	J=2	J=3
1.25E+00	1.81E+00	1.69E-01	4.52E-01	5.97E-01	5.90E-01
1.27E+00	1.84E+00	1.72E-01	4.60E-01	6.08E-01	6.02E-01
1.29E+00	1.88E+00	1.76E-01	4.69E-01	6.20E-01	6.13E-01
1.31E+00	1.91E+00	1.79E-01	4.78E-01	6.32E-01	6.25E-01
1.33E+00	1.95E+00	1.83E-01	4.88E-01	6.45E-01	6.37E-01
1.35E+00	1.99E+00	1.86E-01	4.97E-01	6.57E-01	6.50E-01
1.37E+00	2.03E+00	1.90E-01	5.07E-01	6.70E-01	6.62E-01
1.39E+00	2.07E+00	1.93E-01	5.16E-01	6.83E-01	6.75E-01
1.41E+00	2.11E+00	1.97E-01	5.26E-01	6.96E-01	6.88E-01
1.43E+00	2.15E+00	2.01E-01	5.37E-01	7.09E-01	7.01E-01
1.45E+00	2.19E+00	2.05E-01	5.47E-01	7.23E-01	7.15E-01
1.47E+00	2.23E+00	2.09E-01	5.58E-01	7.37E-01	7.29E-01
1.49E+00	2.28E+00	2.13E-01	5.68E-01	7.51E-01	7.43E-01
1.51E+00	2.32E+00	2.17E-01	5.79E-01	7.66E-01	7.57E-01
1.53E+00	2.36E+00	2.21E-01	5.91E-01	7.81E-01	7.72E-01
1.55E+00	2.41E+00	2.25E-01	6.02E-01	7.96E-01	7.87E-01
1.57E+00	2.46E+00	2.30E-01	6.14E-01	8.11E-01	8.02E-01
1.59E+00	2.50E+00	2.34E-01	6.26E-01	8.27E-01	8.18E-01
1.61E+00	2.55E+00	2.39E-01	6.38E-01	8.43E-01	8.33E-01
1.63E+00	2.60E+00	2.43E-01	6.50E-01	8.59E-01	8.50E-01
1.65E+00	2.65E+00	2.48E-01	6.63E-01	8.76E-01	8.66E-01
1.67E+00	2.70E+00	2.53E-01	6.76E-01	8.93E-01	8.83E-01
1.69E+00	2.76E+00	2.58E-01	6.89E-01	9.10E-01	9.00E-01
1.71E+00	2.81E+00	2.63E-01	7.02E-01	9.28E-01	9.17E-01
1.73E+00	2.86E+00	2.68E-01	7.15E-01	9.46E-01	9.35E-01
1.75E+00	2.92E+00	2.73E-01	7.29E-01	9.64E-01	9.53E-01
1.77E+00	2.98E+00	2.78E-01	7.43E-01	9.83E-01	9.72E-01
1.79E+00	3.03E+00	2.84E-01	7.58E-01	1.00E+00	9.90E-01
1.81E+00	3.09E+00	2.89E-01	7.73E-01	1.02E+00	1.01E+00
1.83E+00	3.15E+00	2.95E-01	7.87E-01	1.04E+00	1.03E+00
1.85E+00	3.21E+00	3.00E-01	8.03E-01	1.06E+00	1.05E+00

Continued on next page

Table A.3 – continued from previous page

E_x (MeV)	Total NLD (MeV^{-1})	J=0	J=1	J=2	J=3
1.87E+00	3.28E+00	3.06E-01	8.18E-01	1.08E+00	1.07E+00
1.89E+00	3.34E+00	3.12E-01	8.34E-01	1.10E+00	1.09E+00
1.91E+00	3.40E+00	3.18E-01	8.50E-01	1.12E+00	1.11E+00
1.93E+00	3.47E+00	3.24E-01	8.67E-01	1.15E+00	1.13E+00
1.95E+00	3.54E+00	3.31E-01	8.83E-01	1.17E+00	1.15E+00
1.97E+00	3.60E+00	3.37E-01	9.01E-01	1.19E+00	1.18E+00
1.99E+00	3.67E+00	3.44E-01	9.18E-01	1.21E+00	1.20E+00
2.01E+00	3.75E+00	3.50E-01	9.36E-01	1.24E+00	1.22E+00
2.03E+00	3.82E+00	3.57E-01	9.54E-01	1.26E+00	1.25E+00
2.05E+00	3.89E+00	3.64E-01	9.72E-01	1.29E+00	1.27E+00
2.07E+00	3.97E+00	3.71E-01	9.91E-01	1.31E+00	1.30E+00
2.09E+00	4.04E+00	3.78E-01	1.01E+00	1.34E+00	1.32E+00
2.11E+00	4.12E+00	3.86E-01	1.03E+00	1.36E+00	1.35E+00
2.13E+00	4.20E+00	3.93E-01	1.05E+00	1.39E+00	1.37E+00
2.15E+00	4.28E+00	4.01E-01	1.07E+00	1.41E+00	1.40E+00
2.17E+00	4.37E+00	4.08E-01	1.09E+00	1.44E+00	1.43E+00
2.19E+00	4.45E+00	4.16E-01	1.11E+00	1.47E+00	1.45E+00
2.21E+00	4.54E+00	4.24E-01	1.13E+00	1.50E+00	1.48E+00
2.23E+00	4.63E+00	4.32E-01	1.16E+00	1.53E+00	1.51E+00
2.25E+00	4.71E+00	4.41E-01	1.18E+00	1.56E+00	1.54E+00
2.27E+00	4.81E+00	4.49E-01	1.20E+00	1.59E+00	1.57E+00
2.29E+00	4.90E+00	4.58E-01	1.22E+00	1.62E+00	1.60E+00
2.31E+00	4.99E+00	4.67E-01	1.25E+00	1.65E+00	1.63E+00
2.33E+00	5.09E+00	4.76E-01	1.27E+00	1.68E+00	1.66E+00
2.35E+00	5.19E+00	4.85E-01	1.30E+00	1.71E+00	1.69E+00
2.37E+00	5.29E+00	4.95E-01	1.32E+00	1.75E+00	1.73E+00
2.39E+00	5.39E+00	5.04E-01	1.35E+00	1.78E+00	1.76E+00
2.41E+00	5.50E+00	5.14E-01	1.37E+00	1.81E+00	1.79E+00
2.43E+00	5.60E+00	5.24E-01	1.40E+00	1.85E+00	1.83E+00
2.45E+00	5.71E+00	5.34E-01	1.43E+00	1.89E+00	1.86E+00
2.47E+00	5.82E+00	5.44E-01	1.45E+00	1.92E+00	1.90E+00

Continued on next page

Table A.3 – continued from previous page

E_x (MeV)	Total NLD (MeV^{-1})	J=0	J=1	J=2	J=3
2.49E+00	5.93E+00	5.55E-01	1.48E+00	1.96E+00	1.94E+00
2.51E+00	6.05E+00	5.66E-01	1.51E+00	2.00E+00	1.97E+00
2.53E+00	6.17E+00	5.77E-01	1.54E+00	2.04E+00	2.01E+00
2.55E+00	6.29E+00	5.88E-01	1.57E+00	2.08E+00	2.05E+00
2.57E+00	6.41E+00	5.99E-01	1.60E+00	2.12E+00	2.09E+00
2.59E+00	6.53E+00	6.11E-01	1.63E+00	2.16E+00	2.13E+00
2.61E+00	6.66E+00	6.23E-01	1.66E+00	2.20E+00	2.17E+00
2.63E+00	6.79E+00	6.35E-01	1.70E+00	2.24E+00	2.22E+00
2.65E+00	6.92E+00	6.47E-01	1.73E+00	2.28E+00	2.26E+00
2.67E+00	7.05E+00	6.59E-01	1.76E+00	2.33E+00	2.30E+00
2.69E+00	7.19E+00	6.72E-01	1.80E+00	2.37E+00	2.35E+00
2.71E+00	7.33E+00	6.85E-01	1.83E+00	2.42E+00	2.39E+00
2.73E+00	7.47E+00	6.98E-01	1.87E+00	2.47E+00	2.44E+00
2.75E+00	7.61E+00	7.12E-01	1.90E+00	2.51E+00	2.49E+00
2.77E+00	7.76E+00	7.26E-01	1.94E+00	2.56E+00	2.53E+00
2.79E+00	7.91E+00	7.40E-01	1.98E+00	2.61E+00	2.58E+00
2.81E+00	8.06E+00	7.54E-01	2.01E+00	2.66E+00	2.63E+00
2.83E+00	8.22E+00	7.69E-01	2.05E+00	2.71E+00	2.68E+00
2.85E+00	8.38E+00	7.84E-01	2.09E+00	2.77E+00	2.74E+00
2.87E+00	8.54E+00	7.99E-01	2.13E+00	2.82E+00	2.79E+00
2.89E+00	8.71E+00	8.14E-01	2.18E+00	2.88E+00	2.84E+00
2.91E+00	8.88E+00	8.30E-01	2.22E+00	2.93E+00	2.90E+00
2.93E+00	9.05E+00	8.46E-01	2.26E+00	2.99E+00	2.95E+00
2.95E+00	9.22E+00	8.62E-01	2.30E+00	3.05E+00	3.01E+00
2.97E+00	9.40E+00	8.79E-01	2.35E+00	3.10E+00	3.07E+00
2.99E+00	9.58E+00	8.96E-01	2.39E+00	3.16E+00	3.13E+00
3.01E+00	9.77E+00	9.13E-01	2.44E+00	3.23E+00	3.19E+00
3.03E+00	9.96E+00	9.31E-01	2.49E+00	3.29E+00	3.25E+00
3.05E+00	1.02E+01	9.49E-01	2.54E+00	3.35E+00	3.31E+00
3.07E+00	1.03E+01	9.68E-01	2.58E+00	3.42E+00	3.38E+00
3.09E+00	1.05E+01	9.86E-01	2.63E+00	3.48E+00	3.44E+00

Continued on next page

Table A.3 – continued from previous page

E_x (MeV)	Total NLD (MeV^{-1})	J=0	J=1	J=2	J=3
3.11E+00	1.08E+01	1.01E+00	2.69E+00	3.55E+00	3.51E+00
3.13E+00	1.10E+01	1.02E+00	2.74E+00	3.62E+00	3.58E+00
3.15E+00	1.12E+01	1.04E+00	2.79E+00	3.69E+00	3.65E+00
3.17E+00	1.14E+01	1.06E+00	2.84E+00	3.76E+00	3.72E+00
3.19E+00	1.16E+01	1.09E+00	2.90E+00	3.83E+00	3.79E+00
3.21E+00	1.18E+01	1.11E+00	2.96E+00	3.91E+00	3.86E+00
3.23E+00	1.21E+01	1.13E+00	3.01E+00	3.98E+00	3.94E+00
3.25E+00	1.23E+01	1.15E+00	3.07E+00	4.06E+00	4.01E+00
3.27E+00	1.25E+01	1.17E+00	3.13E+00	4.14E+00	4.09E+00
3.29E+00	1.28E+01	1.19E+00	3.19E+00	4.22E+00	4.17E+00
3.31E+00	1.30E+01	1.22E+00	3.25E+00	4.30E+00	4.25E+00
3.33E+00	1.33E+01	1.24E+00	3.32E+00	4.38E+00	4.33E+00
3.35E+00	1.35E+01	1.27E+00	3.38E+00	4.47E+00	4.42E+00
3.37E+00	1.38E+01	1.29E+00	3.45E+00	4.55E+00	4.50E+00
3.39E+00	1.41E+01	1.31E+00	3.51E+00	4.64E+00	4.59E+00
3.41E+00	1.43E+01	1.34E+00	3.58E+00	4.73E+00	4.68E+00
3.43E+00	1.46E+01	1.37E+00	3.65E+00	4.82E+00	4.77E+00
3.45E+00	1.49E+01	1.39E+00	3.72E+00	4.92E+00	4.86E+00
3.47E+00	1.52E+01	1.42E+00	3.79E+00	5.01E+00	4.96E+00
3.49E+00	1.55E+01	1.45E+00	3.87E+00	5.11E+00	5.05E+00
3.51E+00	1.58E+01	1.48E+00	3.94E+00	5.21E+00	5.15E+00
3.53E+00	1.61E+01	1.50E+00	4.02E+00	5.31E+00	5.25E+00
3.55E+00	1.64E+01	1.53E+00	4.09E+00	5.41E+00	5.35E+00
3.57E+00	1.67E+01	1.56E+00	4.17E+00	5.52E+00	5.45E+00
3.59E+00	1.70E+01	1.59E+00	4.25E+00	5.62E+00	5.56E+00
3.61E+00	1.74E+01	1.62E+00	4.34E+00	5.73E+00	5.67E+00
3.63E+00	1.77E+01	1.65E+00	4.42E+00	5.84E+00	5.78E+00
3.65E+00	1.80E+01	1.69E+00	4.51E+00	5.96E+00	5.89E+00
3.67E+00	1.84E+01	1.72E+00	4.59E+00	6.07E+00	6.00E+00
3.69E+00	1.87E+01	1.75E+00	4.68E+00	6.19E+00	6.12E+00
3.71E+00	1.91E+01	1.79E+00	4.77E+00	6.31E+00	6.24E+00

Continued on next page

Table A.3 – continued from previous page

E_x (MeV)	Total NLD (MeV^{-1})	J=0	J=1	J=2	J=3
3.73E+00	1.95E+01	1.82E+00	4.87E+00	6.43E+00	6.36E+00
3.75E+00	1.99E+01	1.86E+00	4.96E+00	6.56E+00	6.48E+00
3.77E+00	2.02E+01	1.89E+00	5.06E+00	6.68E+00	6.61E+00
3.79E+00	2.06E+01	1.93E+00	5.15E+00	6.81E+00	6.74E+00
3.81E+00	2.10E+01	1.97E+00	5.25E+00	6.94E+00	6.87E+00
3.83E+00	2.14E+01	2.00E+00	5.36E+00	7.08E+00	7.00E+00
3.85E+00	2.19E+01	2.04E+00	5.46E+00	7.22E+00	7.13E+00
3.87E+00	2.23E+01	2.08E+00	5.56E+00	7.36E+00	7.27E+00
3.89E+00	2.27E+01	2.12E+00	5.67E+00	7.50E+00	7.41E+00
3.91E+00	2.31E+01	2.16E+00	5.78E+00	7.64E+00	7.56E+00
3.93E+00	2.36E+01	2.21E+00	5.89E+00	7.79E+00	7.70E+00
3.95E+00	2.41E+01	2.25E+00	6.01E+00	7.94E+00	7.85E+00
3.97E+00	2.45E+01	2.29E+00	6.12E+00	8.10E+00	8.00E+00
3.99E+00	2.50E+01	2.34E+00	6.24E+00	8.25E+00	8.16E+00
4.01E+00	2.55E+01	2.38E+00	6.36E+00	8.41E+00	8.32E+00
4.03E+00	2.60E+01	2.43E+00	6.49E+00	8.57E+00	8.48E+00
4.05E+00	2.65E+01	2.48E+00	6.61E+00	8.74E+00	8.64E+00
4.07E+00	2.70E+01	2.52E+00	6.74E+00	8.91E+00	8.81E+00
4.09E+00	2.75E+01	2.57E+00	6.87E+00	9.08E+00	8.98E+00
4.11E+00	2.80E+01	2.62E+00	7.00E+00	9.26E+00	9.15E+00
4.13E+00	2.86E+01	2.67E+00	7.14E+00	9.44E+00	9.33E+00
4.15E+00	2.91E+01	2.72E+00	7.28E+00	9.62E+00	9.51E+00
4.17E+00	2.97E+01	2.78E+00	7.42E+00	9.81E+00	9.70E+00
4.19E+00	3.03E+01	2.83E+00	7.56E+00	1.00E+01	9.88E+00
4.21E+00	3.09E+01	2.89E+00	7.71E+00	1.02E+01	1.01E+01
4.23E+00	3.15E+01	2.94E+00	7.86E+00	1.04E+01	1.03E+01
4.25E+00	3.21E+01	3.00E+00	8.01E+00	1.06E+01	1.05E+01
4.27E+00	3.27E+01	3.06E+00	8.17E+00	1.08E+01	1.07E+01
4.29E+00	3.33E+01	3.12E+00	8.32E+00	1.10E+01	1.09E+01
4.31E+00	3.40E+01	3.18E+00	8.48E+00	1.12E+01	1.11E+01
4.33E+00	3.46E+01	3.24E+00	8.65E+00	1.14E+01	1.13E+01

Continued on next page

Table A.3 – continued from previous page

E_x (MeV)	Total NLD (MeV^{-1})	J=0	J=1	J=2	J=3
4.35E+00	3.53E+01	3.30E+00	8.82E+00	1.17E+01	1.15E+01
4.37E+00	3.60E+01	3.36E+00	8.99E+00	1.19E+01	1.17E+01
4.39E+00	3.67E+01	3.43E+00	9.16E+00	1.21E+01	1.20E+01
4.41E+00	3.74E+01	3.50E+00	9.34E+00	1.23E+01	1.22E+01
4.43E+00	3.81E+01	3.56E+00	9.52E+00	1.26E+01	1.24E+01
4.45E+00	3.88E+01	3.63E+00	9.70E+00	1.28E+01	1.27E+01
4.47E+00	3.96E+01	3.70E+00	9.89E+00	1.31E+01	1.29E+01
4.49E+00	4.04E+01	3.77E+00	1.01E+01	1.33E+01	1.32E+01
4.51E+00	4.11E+01	3.85E+00	1.03E+01	1.36E+01	1.34E+01
4.53E+00	4.19E+01	3.92E+00	1.05E+01	1.38E+01	1.37E+01
4.55E+00	4.27E+01	4.00E+00	1.07E+01	1.41E+01	1.40E+01
4.57E+00	4.36E+01	4.07E+00	1.09E+01	1.44E+01	1.42E+01
4.59E+00	4.44E+01	4.15E+00	1.11E+01	1.47E+01	1.45E+01
4.61E+00	4.53E+01	4.23E+00	1.13E+01	1.50E+01	1.48E+01
4.63E+00	4.62E+01	4.32E+00	1.15E+01	1.52E+01	1.51E+01
4.65E+00	4.70E+01	4.40E+00	1.18E+01	1.55E+01	1.54E+01
4.67E+00	4.80E+01	4.48E+00	1.20E+01	1.58E+01	1.57E+01
4.69E+00	4.89E+01	4.57E+00	1.22E+01	1.61E+01	1.60E+01
4.71E+00	4.98E+01	4.66E+00	1.24E+01	1.65E+01	1.63E+01
4.73E+00	5.08E+01	4.75E+00	1.27E+01	1.68E+01	1.66E+01
4.75E+00	5.18E+01	4.84E+00	1.29E+01	1.71E+01	1.69E+01
4.77E+00	5.28E+01	4.94E+00	1.32E+01	1.74E+01	1.72E+01
4.79E+00	5.38E+01	5.03E+00	1.34E+01	1.78E+01	1.76E+01
4.81E+00	5.48E+01	5.13E+00	1.37E+01	1.81E+01	1.79E+01
4.83E+00	5.59E+01	5.23E+00	1.40E+01	1.85E+01	1.83E+01
4.85E+00	5.70E+01	5.33E+00	1.42E+01	1.88E+01	1.86E+01
4.87E+00	5.81E+01	5.43E+00	1.45E+01	1.92E+01	1.90E+01
4.89E+00	5.92E+01	5.54E+00	1.48E+01	1.96E+01	1.93E+01
4.91E+00	6.04E+01	5.64E+00	1.51E+01	1.99E+01	1.97E+01
4.93E+00	6.15E+01	5.75E+00	1.54E+01	2.03E+01	2.01E+01
4.95E+00	6.27E+01	5.87E+00	1.57E+01	2.07E+01	2.05E+01

Continued on next page

Table A.3 – continued from previous page

E_x (MeV)	Total NLD (MeV^{-1})	J=0	J=1	J=2	J=3
4.97E+00	6.39E+01	5.98E+00	1.60E+01	2.11E+01	2.09E+01
4.99E+00	6.52E+01	6.09E+00	1.63E+01	2.15E+01	2.13E+01
5.01E+00	6.64E+01	6.21E+00	1.66E+01	2.19E+01	2.17E+01
5.03E+00	6.77E+01	6.33E+00	1.69E+01	2.24E+01	2.21E+01
5.05E+00	6.90E+01	6.46E+00	1.72E+01	2.28E+01	2.25E+01
5.07E+00	7.04E+01	6.58E+00	1.76E+01	2.32E+01	2.30E+01
5.09E+00	7.17E+01	6.71E+00	1.79E+01	2.37E+01	2.34E+01
5.11E+00	7.31E+01	6.84E+00	1.83E+01	2.41E+01	2.39E+01
5.13E+00	7.45E+01	6.97E+00	1.86E+01	2.46E+01	2.43E+01
5.15E+00	7.60E+01	7.10E+00	1.90E+01	2.51E+01	2.48E+01
5.17E+00	7.74E+01	7.24E+00	1.93E+01	2.56E+01	2.53E+01
5.19E+00	7.89E+01	7.38E+00	1.97E+01	2.61E+01	2.58E+01
5.21E+00	8.05E+01	7.53E+00	2.01E+01	2.66E+01	2.63E+01
5.23E+00	8.20E+01	7.67E+00	2.05E+01	2.71E+01	2.68E+01
5.25E+00	8.36E+01	7.82E+00	2.09E+01	2.76E+01	2.73E+01
5.27E+00	8.52E+01	7.97E+00	2.13E+01	2.81E+01	2.78E+01
5.29E+00	8.69E+01	8.12E+00	2.17E+01	2.87E+01	2.84E+01
5.31E+00	8.86E+01	8.28E+00	2.21E+01	2.92E+01	2.89E+01
5.33E+00	9.03E+01	8.44E+00	2.26E+01	2.98E+01	2.95E+01
5.35E+00	9.20E+01	8.61E+00	2.30E+01	3.04E+01	3.00E+01
5.37E+00	9.38E+01	8.77E+00	2.34E+01	3.10E+01	3.06E+01
5.39E+00	9.56E+01	8.94E+00	2.39E+01	3.16E+01	3.12E+01
5.41E+00	9.75E+01	9.12E+00	2.44E+01	3.22E+01	3.18E+01
5.43E+00	9.94E+01	9.29E+00	2.48E+01	3.28E+01	3.24E+01
5.45E+00	1.01E+02	9.47E+00	2.53E+01	3.34E+01	3.31E+01
5.47E+00	1.03E+02	9.65E+00	2.58E+01	3.41E+01	3.37E+01
5.49E+00	1.05E+02	9.84E+00	2.63E+01	3.48E+01	3.44E+01
5.51E+00	1.07E+02	1.00E+01	2.68E+01	3.54E+01	3.50E+01
5.53E+00	1.09E+02	1.02E+01	2.73E+01	3.61E+01	3.57E+01
5.55E+00	1.11E+02	1.04E+01	2.78E+01	3.68E+01	3.64E+01
5.57E+00	1.14E+02	1.06E+01	2.84E+01	3.75E+01	3.71E+01

Continued on next page

Table A.3 – continued from previous page

E_x (MeV)	Total NLD (MeV^{-1})	J=0	J=1	J=2	J=3
5.59E+00	1.16E+02	1.08E+01	2.89E+01	3.82E+01	3.78E+01
5.61E+00	1.18E+02	1.10E+01	2.95E+01	3.90E+01	3.85E+01
5.63E+00	1.20E+02	1.13E+01	3.01E+01	3.97E+01	3.93E+01
5.65E+00	1.23E+02	1.15E+01	3.07E+01	4.05E+01	4.01E+01
5.67E+00	1.25E+02	1.17E+01	3.12E+01	4.13E+01	4.08E+01
5.69E+00	1.27E+02	1.19E+01	3.18E+01	4.21E+01	4.16E+01
5.71E+00	1.30E+02	1.22E+01	3.25E+01	4.29E+01	4.24E+01
5.73E+00	1.32E+02	1.24E+01	3.31E+01	4.37E+01	4.32E+01
5.75E+00	1.35E+02	1.26E+01	3.37E+01	4.46E+01	4.41E+01
5.77E+00	1.38E+02	1.29E+01	3.44E+01	4.55E+01	4.49E+01
5.79E+00	1.40E+02	1.31E+01	3.51E+01	4.63E+01	4.58E+01
5.81E+00	1.43E+02	1.34E+01	3.57E+01	4.72E+01	4.67E+01
5.83E+00	1.46E+02	1.36E+01	3.64E+01	4.81E+01	4.76E+01
5.85E+00	1.49E+02	1.39E+01	3.71E+01	4.91E+01	4.85E+01
5.87E+00	1.51E+02	1.42E+01	3.78E+01	5.00E+01	4.95E+01
5.89E+00	1.54E+02	1.44E+01	3.86E+01	5.10E+01	5.04E+01
5.91E+00	1.57E+02	1.47E+01	3.93E+01	5.20E+01	5.14E+01
5.93E+00	1.60E+02	1.50E+01	4.01E+01	5.30E+01	5.24E+01
5.95E+00	1.64E+02	1.53E+01	4.09E+01	5.40E+01	5.34E+01
5.97E+00	1.67E+02	1.56E+01	4.17E+01	5.51E+01	5.44E+01
5.99E+00	1.70E+02	1.59E+01	4.25E+01	5.61E+01	5.55E+01
6.01E+00	1.73E+02	1.62E+01	4.33E+01	5.72E+01	5.66E+01
6.03E+00	1.77E+02	1.65E+01	4.41E+01	5.83E+01	5.77E+01
6.05E+00	1.80E+02	1.68E+01	4.50E+01	5.94E+01	5.88E+01
6.07E+00	1.84E+02	1.72E+01	4.58E+01	6.06E+01	5.99E+01
6.09E+00	1.87E+02	1.75E+01	4.67E+01	6.18E+01	6.11E+01
6.11E+00	1.91E+02	1.78E+01	4.76E+01	6.30E+01	6.23E+01
6.13E+00	1.94E+02	1.82E+01	4.86E+01	6.42E+01	6.35E+01
6.15E+00	1.98E+02	1.85E+01	4.95E+01	6.54E+01	6.47E+01
6.17E+00	2.02E+02	1.89E+01	5.05E+01	6.67E+01	6.59E+01
6.19E+00	2.06E+02	1.93E+01	5.14E+01	6.80E+01	6.72E+01

Continued on next page

Table A.3 – continued from previous page

E_x (MeV)	Total NLD (MeV^{-1})	J=0	J=1	J=2	J=3
6.21E+00	2.10E+02	1.96E+01	5.24E+01	6.93E+01	6.85E+01
6.23E+00	2.14E+02	2.00E+01	5.34E+01	7.06E+01	6.98E+01
6.25E+00	2.18E+02	2.04E+01	5.45E+01	7.20E+01	7.12E+01
6.27E+00	2.22E+02	2.08E+01	5.55E+01	7.34E+01	7.26E+01
6.29E+00	2.27E+02	2.12E+01	5.66E+01	7.48E+01	7.40E+01
6.31E+00	2.31E+02	2.16E+01	5.77E+01	7.63E+01	7.54E+01
6.33E+00	2.35E+02	2.20E+01	5.88E+01	7.77E+01	7.69E+01
6.35E+00	2.40E+02	2.24E+01	6.00E+01	7.92E+01	7.84E+01
6.37E+00	2.45E+02	2.29E+01	6.11E+01	8.08E+01	7.99E+01
6.39E+00	2.49E+02	2.33E+01	6.23E+01	8.23E+01	8.14E+01
6.41E+00	2.54E+02	2.38E+01	6.35E+01	8.39E+01	8.30E+01
6.43E+00	2.59E+02	2.42E+01	6.47E+01	8.56E+01	8.46E+01
6.45E+00	2.64E+02	2.47E+01	6.60E+01	8.72E+01	8.62E+01
6.47E+00	2.69E+02	2.52E+01	6.73E+01	8.89E+01	8.79E+01
6.49E+00	2.74E+02	2.57E+01	6.86E+01	9.06E+01	8.96E+01
6.51E+00	2.80E+02	2.62E+01	6.99E+01	9.24E+01	9.13E+01
6.53E+00	2.85E+02	2.67E+01	7.12E+01	9.42E+01	9.31E+01
6.55E+00	2.91E+02	2.72E+01	7.26E+01	9.60E+01	9.49E+01
6.57E+00	2.96E+02	2.77E+01	7.40E+01	9.79E+01	9.67E+01
6.59E+00	3.02E+02	2.82E+01	7.55E+01	9.97E+01	9.86E+01
6.61E+00	3.08E+02	2.88E+01	7.69E+01	1.02E+02	1.01E+02
6.63E+00	3.14E+02	2.94E+01	7.84E+01	1.04E+02	1.02E+02
6.65E+00	3.20E+02	2.99E+01	7.99E+01	1.06E+02	1.04E+02
6.67E+00	3.26E+02	3.05E+01	8.15E+01	1.08E+02	1.06E+02
6.69E+00	3.32E+02	3.11E+01	8.31E+01	1.10E+02	1.09E+02
6.71E+00	3.39E+02	3.17E+01	8.47E+01	1.12E+02	1.11E+02
6.73E+00	3.45E+02	3.23E+01	8.63E+01	1.14E+02	1.13E+02
6.75E+00	3.52E+02	3.29E+01	8.80E+01	1.16E+02	1.15E+02
6.77E+00	3.59E+02	3.36E+01	8.97E+01	1.19E+02	1.17E+02
6.79E+00	3.66E+02	3.42E+01	9.14E+01	1.21E+02	1.19E+02
6.81E+00	3.73E+02	3.49E+01	9.32E+01	1.23E+02	1.22E+02

Continued on next page

Table A.3 – continued from previous page

E_x (MeV)	Total NLD (MeV^{-1})	J=0	J=1	J=2	J=3
6.83E+00	3.80E+02	3.56E+01	9.50E+01	1.26E+02	1.24E+02
6.85E+00	3.88E+02	3.62E+01	9.68E+01	1.28E+02	1.27E+02
6.87E+00	3.95E+02	3.69E+01	9.87E+01	1.30E+02	1.29E+02
6.89E+00	4.03E+02	3.77E+01	1.01E+02	1.33E+02	1.31E+02
6.91E+00	4.11E+02	3.84E+01	1.03E+02	1.36E+02	1.34E+02
6.93E+00	4.18E+02	3.91E+01	1.05E+02	1.38E+02	1.37E+02
6.95E+00	4.27E+02	3.99E+01	1.07E+02	1.41E+02	1.39E+02
6.97E+00	4.35E+02	4.07E+01	1.09E+02	1.44E+02	1.42E+02
6.99E+00	4.43E+02	4.14E+01	1.11E+02	1.46E+02	1.45E+02
7.01E+00	4.52E+02	4.22E+01	1.13E+02	1.49E+02	1.48E+02
7.03E+00	4.61E+02	4.31E+01	1.15E+02	1.52E+02	1.50E+02
7.05E+00	4.69E+02	4.39E+01	1.17E+02	1.55E+02	1.53E+02
7.07E+00	4.79E+02	4.48E+01	1.20E+02	1.58E+02	1.56E+02
7.09E+00	4.88E+02	4.56E+01	1.22E+02	1.61E+02	1.59E+02
7.11E+00	4.97E+02	4.65E+01	1.24E+02	1.64E+02	1.62E+02
7.13E+00	5.07E+02	4.74E+01	1.27E+02	1.67E+02	1.65E+02
7.15E+00	5.17E+02	4.83E+01	1.29E+02	1.71E+02	1.69E+02
7.17E+00	5.27E+02	4.93E+01	1.32E+02	1.74E+02	1.72E+02
7.19E+00	5.37E+02	5.02E+01	1.34E+02	1.77E+02	1.75E+02
7.21E+00	5.47E+02	5.12E+01	1.37E+02	1.81E+02	1.79E+02
7.23E+00	5.58E+02	5.22E+01	1.39E+02	1.84E+02	1.82E+02
7.25E+00	5.69E+02	5.32E+01	1.42E+02	1.88E+02	1.86E+02
7.27E+00	5.80E+02	5.42E+01	1.45E+02	1.91E+02	1.89E+02
7.29E+00	5.91E+02	5.53E+01	1.48E+02	1.95E+02	1.93E+02
7.31E+00	6.02E+02	5.63E+01	1.50E+02	1.99E+02	1.97E+02
7.33E+00	6.14E+02	5.74E+01	1.53E+02	2.03E+02	2.00E+02
7.35E+00	6.26E+02	5.85E+01	1.56E+02	2.07E+02	2.04E+02
7.37E+00	6.38E+02	5.97E+01	1.59E+02	2.11E+02	2.08E+02
7.39E+00	6.50E+02	6.08E+01	1.62E+02	2.15E+02	2.12E+02
7.41E+00	6.63E+02	6.20E+01	1.66E+02	2.19E+02	2.16E+02
7.43E+00	6.76E+02	6.32E+01	1.69E+02	2.23E+02	2.21E+02

Continued on next page

Table A.3 – continued from previous page

E_x (MeV)	Total NLD (MeV^{-1})	J=0	J=1	J=2	J=3
7.45E+00	6.89E+02	6.44E+01	1.72E+02	2.27E+02	2.25E+02
7.47E+00	7.02E+02	6.57E+01	1.75E+02	2.32E+02	2.29E+02
7.49E+00	7.16E+02	6.69E+01	1.79E+02	2.36E+02	2.34E+02
7.51E+00	7.30E+02	6.82E+01	1.82E+02	2.41E+02	2.38E+02
7.53E+00	7.44E+02	6.95E+01	1.86E+02	2.46E+02	2.43E+02
7.55E+00	7.58E+02	7.09E+01	1.89E+02	2.50E+02	2.48E+02
7.57E+00	7.73E+02	7.23E+01	1.93E+02	2.55E+02	2.52E+02
7.59E+00	7.88E+02	7.37E+01	1.97E+02	2.60E+02	2.57E+02
7.61E+00	8.03E+02	7.51E+01	2.01E+02	2.65E+02	2.62E+02
7.63E+00	8.19E+02	7.65E+01	2.04E+02	2.70E+02	2.67E+02
7.65E+00	8.34E+02	7.80E+01	2.08E+02	2.76E+02	2.72E+02
7.67E+00	8.51E+02	7.95E+01	2.12E+02	2.81E+02	2.78E+02
7.69E+00	8.67E+02	8.11E+01	2.17E+02	2.86E+02	2.83E+02
7.71E+00	8.84E+02	8.26E+01	2.21E+02	2.92E+02	2.89E+02
7.73E+00	9.01E+02	8.42E+01	2.25E+02	2.97E+02	2.94E+02
7.75E+00	9.18E+02	8.59E+01	2.29E+02	3.03E+02	3.00E+02
7.77E+00	9.36E+02	8.75E+01	2.34E+02	3.09E+02	3.06E+02
7.79E+00	9.54E+02	8.92E+01	2.38E+02	3.15E+02	3.12E+02
7.81E+00	9.73E+02	9.10E+01	2.43E+02	3.21E+02	3.18E+02
7.83E+00	9.92E+02	9.27E+01	2.48E+02	3.27E+02	3.24E+02
7.85E+00	1.01E+03	9.45E+01	2.53E+02	3.34E+02	3.30E+02
7.87E+00	1.03E+03	9.63E+01	2.57E+02	3.40E+02	3.36E+02
7.89E+00	1.05E+03	9.82E+01	2.62E+02	3.47E+02	3.43E+02
7.91E+00	1.07E+03	1.00E+02	2.67E+02	3.54E+02	3.50E+02
7.93E+00	1.09E+03	1.02E+02	2.73E+02	3.60E+02	3.56E+02
7.95E+00	1.11E+03	1.04E+02	2.78E+02	3.67E+02	3.63E+02
7.97E+00	1.13E+03	1.06E+02	2.83E+02	3.74E+02	3.70E+02
7.99E+00	1.16E+03	1.08E+02	2.89E+02	3.82E+02	3.77E+02
8.01E+00	1.18E+03	1.10E+02	2.94E+02	3.89E+02	3.85E+02
8.03E+00	1.20E+03	1.12E+02	3.00E+02	3.97E+02	3.92E+02
8.05E+00	1.22E+03	1.14E+02	3.06E+02	4.04E+02	4.00E+02

Continued on next page

Table A.3 – continued from previous page

E_x (MeV)	Total NLD (MeV^{-1})	J=0	J=1	J=2	J=3
8.07E+00	1.25E+03	1.17E+02	3.12E+02	4.12E+02	4.07E+02
8.09E+00	1.27E+03	1.19E+02	3.18E+02	4.20E+02	4.15E+02
8.11E+00	1.30E+03	1.21E+02	3.24E+02	4.28E+02	4.23E+02
8.13E+00	1.32E+03	1.24E+02	3.30E+02	4.36E+02	4.32E+02
8.15E+00	1.35E+03	1.26E+02	3.37E+02	4.45E+02	4.40E+02
8.17E+00	1.37E+03	1.28E+02	3.43E+02	4.54E+02	4.48E+02
8.19E+00	1.40E+03	1.31E+02	3.50E+02	4.62E+02	4.57E+02
8.21E+00	1.43E+03	1.33E+02	3.57E+02	4.71E+02	4.66E+02
8.23E+00	1.45E+03	1.36E+02	3.63E+02	4.80E+02	4.75E+02
8.25E+00	1.48E+03	1.39E+02	3.70E+02	4.90E+02	4.84E+02

Table A.4: EMPIRE default NLD for ^{74}Zn including spin-dependent NLD for J=0-5. An equal parity distribution is assumed.

E_x (MeV)	Total NLD (MeV^{-1})	J=0	J=1	J=2	J=3	J=4	J=5
0.000	0.00E+00	0.00E+00	0.00E+00	0.00E+00	0.00E+00	0.00E+00	0.00E+00
0.106	8.86E-02	3.73E-02	4.13E-02	9.39E-03	6.63E-04	1.59E-05	1.35E-07
0.212	9.59E-02	2.97E-02	4.44E-02	1.84E-02	3.18E-03	2.52E-04	9.52E-06
0.318	1.16E-01	2.93E-02	5.03E-02	2.75E-02	7.25E-03	1.01E-03	7.62E-05
0.424	1.44E-01	3.13E-02	5.85E-02	3.80E-02	1.29E-02	2.52E-03	2.93E-04
0.530	1.80E-01	3.47E-02	6.89E-02	5.03E-02	2.05E-02	5.06E-03	7.89E-04
0.637	2.27E-01	3.93E-02	8.15E-02	6.50E-02	3.02E-02	8.90E-03	1.73E-03
0.743	2.85E-01	4.51E-02	9.68E-02	8.27E-02	4.26E-02	1.44E-02	3.32E-03
0.849	3.58E-01	5.21E-02	1.15E-01	1.04E-01	5.81E-02	2.20E-02	5.83E-03
0.955	4.49E-01	6.06E-02	1.37E-01	1.30E-01	7.75E-02	3.22E-02	9.56E-03
1.061	5.60E-01	7.06E-02	1.63E-01	1.60E-01	1.02E-01	4.55E-02	1.49E-02
1.167	6.96E-01	8.25E-02	1.93E-01	1.97E-01	1.31E-01	6.28E-02	2.24E-02
1.273	8.63E-01	9.65E-02	2.29E-01	2.40E-01	1.67E-01	8.49E-02	3.25E-02
1.379	1.07E+00	1.13E-01	2.72E-01	2.92E-01	2.11E-01	1.13E-01	4.60E-02
1.485	1.31E+00	1.32E-01	3.22E-01	3.53E-01	2.65E-01	1.48E-01	6.37E-02
1.591	1.61E+00	1.55E-01	3.80E-01	4.26E-01	3.29E-01	1.91E-01	8.67E-02
1.697	1.97E+00	1.81E-01	4.49E-01	5.12E-01	4.06E-01	2.45E-01	1.16E-01
1.803	2.40E+00	2.11E-01	5.29E-01	6.13E-01	4.98E-01	3.11E-01	1.54E-01
1.909	2.93E+00	2.47E-01	6.22E-01	7.33E-01	6.09E-01	3.91E-01	2.01E-01
2.016	3.55E+00	2.88E-01	7.31E-01	8.73E-01	7.40E-01	4.88E-01	2.59E-01
2.122	4.30E+00	3.36E-01	8.58E-01	1.04E+00	8.97E-01	6.06E-01	3.32E-01

Continued on next page

Table A.4 – continued from previous page

E_x (MeV)	Total NLD (MeV^{-1})	J=0	J=1	J=2	J=3	J=4	J=5
2.228	5.19E+00	3.91E-01	1.01E+00	1.23E+00	1.08E+00	7.49E-01	4.22E-01
2.334	6.25E+00	4.56E-01	1.18E+00	1.45E+00	1.30E+00	9.19E-01	5.33E-01
2.440	7.51E+00	5.30E-01	1.38E+00	1.72E+00	1.56E+00	1.12E+00	6.67E-01
2.546	9.01E+00	6.16E-01	1.61E+00	2.02E+00	1.86E+00	1.37E+00	8.31E-01
2.652	1.08E+01	7.15E-01	1.87E+00	2.38E+00	2.22E+00	1.66E+00	1.03E+00
2.758	1.29E+01	8.29E-01	2.18E+00	2.79E+00	2.64E+00	2.00E+00	1.27E+00
2.864	1.54E+01	9.60E-01	2.54E+00	3.27E+00	3.12E+00	2.41E+00	1.56E+00
2.970	1.83E+01	1.11E+00	2.95E+00	3.83E+00	3.69E+00	2.89E+00	1.90E+00
3.076	2.17E+01	1.29E+00	3.42E+00	4.47E+00	4.36E+00	3.46E+00	2.31E+00
3.182	2.58E+01	1.49E+00	3.96E+00	5.22E+00	5.13E+00	4.12E+00	2.80E+00
3.288	3.05E+01	1.72E+00	4.59E+00	6.08E+00	6.03E+00	4.91E+00	3.38E+00
3.395	3.61E+01	1.98E+00	5.31E+00	7.07E+00	7.08E+00	5.82E+00	4.07E+00
3.501	4.26E+01	2.28E+00	6.13E+00	8.22E+00	8.29E+00	6.89E+00	4.89E+00
3.607	5.02E+01	2.63E+00	7.08E+00	9.53E+00	9.70E+00	8.14E+00	5.85E+00
3.713	5.91E+01	3.02E+00	8.17E+00	1.11E+01	1.13E+01	9.60E+00	6.98E+00
3.819	6.95E+01	3.47E+00	9.41E+00	1.28E+01	1.32E+01	1.13E+01	8.30E+00
3.925	8.15E+01	3.99E+00	1.08E+01	1.48E+01	1.54E+01	1.33E+01	9.86E+00
4.031	9.56E+01	4.58E+00	1.25E+01	1.71E+01	1.79E+01	1.56E+01	1.17E+01
4.137	1.12E+02	5.25E+00	1.43E+01	1.97E+01	2.07E+01	1.82E+01	1.38E+01
4.243	1.31E+02	6.02E+00	1.64E+01	2.27E+01	2.40E+01	2.13E+01	1.63E+01
4.349	1.53E+02	6.89E+00	1.89E+01	2.62E+01	2.78E+01	2.48E+01	1.92E+01
4.455	1.78E+02	7.89E+00	2.16E+01	3.01E+01	3.22E+01	2.89E+01	2.26E+01

Continued on next page

Table A.4 – continued from previous page

E_x (MeV)	Total NLD (MeV^{-1})	J=0	J=1	J=2	J=3	J=4	J=5
4.561	2.08E+02	9.02E+00	2.48E+01	3.46E+01	3.72E+01	3.36E+01	2.65E+01
4.668	2.42E+02	1.03E+01	2.84E+01	3.98E+01	4.30E+01	3.91E+01	3.10E+01
4.774	2.82E+02	1.18E+01	3.25E+01	4.56E+01	4.95E+01	4.53E+01	3.63E+01
4.880	3.27E+02	1.34E+01	3.71E+01	5.23E+01	5.70E+01	5.26E+01	4.24E+01
4.986	3.80E+02	1.53E+01	4.24E+01	6.00E+01	6.56E+01	6.08E+01	4.94E+01
5.092	4.41E+02	1.75E+01	4.84E+01	6.86E+01	7.55E+01	7.03E+01	5.75E+01
5.198	5.10E+02	1.99E+01	5.52E+01	7.85E+01	8.67E+01	8.12E+01	6.69E+01
5.304	5.91E+02	2.27E+01	6.29E+01	8.98E+01	9.95E+01	9.37E+01	7.76E+01
5.410	6.83E+02	2.58E+01	7.17E+01	1.03E+02	1.14E+02	1.08E+02	9.01E+01
5.516	7.90E+02	2.94E+01	8.17E+01	1.17E+02	1.31E+02	1.24E+02	1.04E+02
5.622	9.12E+02	3.34E+01	9.29E+01	1.34E+02	1.50E+02	1.43E+02	1.21E+02
5.728	1.05E+03	3.79E+01	1.06E+02	1.52E+02	1.71E+02	1.64E+02	1.40E+02
5.834	1.21E+03	4.31E+01	1.20E+02	1.74E+02	1.96E+02	1.89E+02	1.61E+02
5.940	1.40E+03	4.89E+01	1.37E+02	1.98E+02	2.24E+02	2.17E+02	1.86E+02
6.047	1.61E+03	5.54E+01	1.55E+02	2.25E+02	2.55E+02	2.48E+02	2.14E+02
6.153	1.85E+03	6.29E+01	1.76E+02	2.56E+02	2.91E+02	2.85E+02	2.47E+02
6.259	2.13E+03	7.13E+01	2.00E+02	2.91E+02	3.32E+02	3.26E+02	2.84E+02
6.365	2.45E+03	8.08E+01	2.27E+02	3.30E+02	3.79E+02	3.73E+02	3.26E+02
6.471	2.79E+03	9.08E+01	2.55E+02	3.73E+02	4.28E+02	4.23E+02	3.72E+02
6.577	3.11E+03	9.99E+01	2.81E+02	4.11E+02	4.74E+02	4.70E+02	4.15E+02
6.683	3.47E+03	1.10E+02	3.09E+02	4.53E+02	5.23E+02	5.20E+02	4.62E+02
6.789	3.85E+03	1.21E+02	3.40E+02	4.98E+02	5.77E+02	5.76E+02	5.12E+02

Continued on next page

Table A.4 – continued from previous page

E_x (MeV)	Total NLD (MeV^{-1})	J=0	J=1	J=2	J=3	J=4	J=5
6.895	4.27E+03	1.32E+02	3.72E+02	5.47E+02	6.35E+02	6.35E+02	5.68E+02
7.001	4.72E+03	1.45E+02	4.08E+02	6.00E+02	6.98E+02	7.00E+02	6.28E+02
7.107	5.22E+03	1.58E+02	4.46E+02	6.57E+02	7.66E+02	7.70E+02	6.93E+02
7.213	5.75E+03	1.72E+02	4.87E+02	7.18E+02	8.39E+02	8.46E+02	7.64E+02
7.319	6.33E+03	1.88E+02	5.30E+02	7.84E+02	9.17E+02	9.27E+02	8.40E+02
7.426	6.96E+03	2.04E+02	5.77E+02	8.54E+02	1.00E+03	1.02E+03	9.22E+02
7.532	7.63E+03	2.22E+02	6.27E+02	9.29E+02	1.09E+03	1.11E+03	1.01E+03
7.638	8.36E+03	2.40E+02	6.80E+02	1.01E+03	1.19E+03	1.21E+03	1.11E+03
7.744	9.14E+03	2.60E+02	7.37E+02	1.09E+03	1.29E+03	1.32E+03	1.21E+03
7.850	9.97E+03	2.81E+02	7.97E+02	1.19E+03	1.40E+03	1.43E+03	1.32E+03
7.956	1.09E+04	3.03E+02	8.60E+02	1.28E+03	1.51E+03	1.55E+03	1.43E+03
8.062	1.18E+04	3.27E+02	9.27E+02	1.38E+03	1.64E+03	1.68E+03	1.55E+03
8.168	1.28E+04	3.52E+02	9.98E+02	1.49E+03	1.77E+03	1.82E+03	1.68E+03
8.274	1.39E+04	3.78E+02	1.07E+03	1.60E+03	1.90E+03	1.96E+03	1.82E+03
8.380	1.50E+04	4.05E+02	1.15E+03	1.72E+03	2.05E+03	2.12E+03	1.97E+03

Table A.5: EMPIRE default NLD for ^{74}Zn including spin-dependent NLD for J=6-10. An equal parity distribution is assumed.

E_x (MeV)	Total NLD (MeV^{-1})	J=6	J=7	J=8	J=9	J=10
0.000	0.00E+00	0.00E+00	0.00E+00	0.00E+00	0.00E+00	0.00E+00
0.106	8.86E-02	0.00E+00	0.00E+00	0.00E+00	0.00E+00	0.00E+00
0.212	9.59E-02	1.74E-07	1.55E-09	0.00E+00	0.00E+00	0.00E+00
0.318	1.16E-01	3.21E-06	7.59E-08	0.00E+00	0.00E+00	0.00E+00
0.424	1.44E-01	2.06E-05	8.84E-07	2.34E-08	0.00E+00	0.00E+00
0.530	1.80E-01	7.90E-05	5.13E-06	2.18E-07	6.08E-09	0.00E+00
0.637	2.27E-01	2.26E-04	1.99E-05	1.20E-06	4.97E-08	0.00E+00
0.743	2.85E-01	5.32E-04	5.98E-05	4.74E-06	2.67E-07	1.07E-08
0.849	3.58E-01	1.10E-03	1.50E-04	1.49E-05	1.07E-06	5.67E-08
0.955	4.49E-01	2.07E-03	3.32E-04	3.94E-05	3.50E-06	2.32E-07
1.061	5.60E-01	3.63E-03	6.66E-04	9.23E-05	9.74E-06	7.85E-07
1.167	6.96E-01	6.02E-03	1.24E-03	1.96E-04	2.40E-05	2.28E-06
1.273	8.63E-01	9.54E-03	2.17E-03	3.86E-04	5.38E-05	5.90E-06
1.379	1.07E+00	1.46E-02	3.62E-03	7.13E-04	1.11E-04	1.39E-05
1.485	1.31E+00	2.16E-02	5.81E-03	1.25E-03	2.16E-04	3.01E-05
1.591	1.61E+00	3.12E-02	9.01E-03	2.10E-03	3.97E-04	6.10E-05
1.697	1.97E+00	4.41E-02	1.36E-02	3.40E-03	6.97E-04	1.17E-04
1.803	2.40E+00	6.13E-02	2.00E-02	5.34E-03	1.18E-03	2.15E-04
1.909	2.93E+00	8.37E-02	2.87E-02	8.15E-03	1.92E-03	3.78E-04
2.016	3.55E+00	1.13E-01	4.06E-02	1.22E-02	3.05E-03	6.42E-04
2.122	4.30E+00	1.50E-01	5.64E-02	1.78E-02	4.71E-03	1.06E-03

Continued on next page

Table A.5 – continued from previous page

E_x (MeV)	Total NLD (MeV^{-1})	J=6	J=7	J=8	J=9	J=10
2.228	5.19E+00	1.97E-01	7.72E-02	2.55E-02	7.12E-03	1.69E-03
2.334	6.25E+00	2.57E-01	1.04E-01	3.60E-02	1.05E-02	2.64E-03
2.440	7.51E+00	3.32E-01	1.40E-01	5.00E-02	1.53E-02	4.03E-03
2.546	9.01E+00	4.25E-01	1.85E-01	6.86E-02	2.19E-02	6.03E-03
2.652	1.08E+01	5.40E-01	2.42E-01	9.30E-02	3.09E-02	8.87E-03
2.758	1.29E+01	6.82E-01	3.14E-01	1.25E-01	4.29E-02	1.28E-02
2.864	1.54E+01	8.55E-01	4.05E-01	1.66E-01	5.90E-02	1.83E-02
2.970	1.83E+01	1.07E+00	5.18E-01	2.18E-01	8.01E-02	2.58E-02
3.076	2.17E+01	1.33E+00	6.58E-01	2.85E-01	1.08E-01	3.59E-02
3.182	2.58E+01	1.64E+00	8.30E-01	3.69E-01	1.44E-01	4.93E-02
3.288	3.05E+01	2.01E+00	1.04E+00	4.74E-01	1.90E-01	6.71E-02
3.395	3.61E+01	2.46E+00	1.30E+00	6.05E-01	2.49E-01	9.05E-02
3.501	4.26E+01	3.00E+00	1.62E+00	7.69E-01	3.23E-01	1.21E-01
3.607	5.02E+01	3.65E+00	2.00E+00	9.71E-01	4.18E-01	1.60E-01
3.713	5.91E+01	4.42E+00	2.47E+00	1.22E+00	5.36E-01	2.11E-01
3.819	6.95E+01	5.34E+00	3.03E+00	1.52E+00	6.84E-01	2.75E-01
3.925	8.15E+01	6.42E+00	3.70E+00	1.90E+00	8.68E-01	3.57E-01
4.031	9.56E+01	7.70E+00	4.50E+00	2.35E+00	1.10E+00	4.60E-01
4.137	1.12E+02	9.22E+00	5.47E+00	2.90E+00	1.38E+00	5.90E-01
4.243	1.31E+02	1.10E+01	6.61E+00	3.56E+00	1.72E+00	7.51E-01
4.349	1.53E+02	1.31E+01	7.98E+00	4.36E+00	2.14E+00	9.53E-01
4.455	1.78E+02	1.56E+01	9.59E+00	5.31E+00	2.66E+00	1.20E+00

Continued on next page

Table A.5 – continued from previous page

E_x (MeV)	Total NLD (MeV^{-1})	J=6	J=7	J=8	J=9	J=10
4.561	2.08E+02	1.85E+01	1.15E+01	6.46E+00	3.28E+00	1.51E+00
4.668	2.42E+02	2.18E+01	1.38E+01	7.83E+00	4.04E+00	1.89E+00
4.774	2.82E+02	2.58E+01	1.64E+01	9.47E+00	4.95E+00	2.35E+00
4.880	3.27E+02	3.04E+01	1.96E+01	1.14E+01	6.05E+00	2.92E+00
4.986	3.80E+02	3.57E+01	2.33E+01	1.37E+01	7.36E+00	3.61E+00
5.092	4.41E+02	4.20E+01	2.76E+01	1.65E+01	8.94E+00	4.44E+00
5.198	5.10E+02	4.92E+01	3.27E+01	1.97E+01	1.08E+01	5.45E+00
5.304	5.91E+02	5.76E+01	3.86E+01	2.35E+01	1.31E+01	6.67E+00
5.410	6.83E+02	6.73E+01	4.55E+01	2.80E+01	1.58E+01	8.14E+00
5.516	7.90E+02	7.85E+01	5.35E+01	3.33E+01	1.89E+01	9.90E+00
5.622	9.12E+02	9.15E+01	6.29E+01	3.95E+01	2.27E+01	1.20E+01
5.728	1.05E+03	1.07E+02	7.38E+01	4.67E+01	2.72E+01	1.45E+01
5.834	1.21E+03	1.24E+02	8.65E+01	5.52E+01	3.24E+01	1.75E+01
5.940	1.40E+03	1.44E+02	1.01E+02	6.52E+01	3.86E+01	2.11E+01
6.047	1.61E+03	1.67E+02	1.18E+02	7.68E+01	4.59E+01	2.54E+01
6.153	1.85E+03	1.93E+02	1.38E+02	9.03E+01	5.45E+01	3.04E+01
6.259	2.13E+03	2.23E+02	1.61E+02	1.06E+02	6.45E+01	3.64E+01
6.365	2.45E+03	2.58E+02	1.87E+02	1.24E+02	7.63E+01	4.34E+01
6.471	2.79E+03	2.97E+02	2.16E+02	1.45E+02	9.00E+01	5.17E+01
6.577	3.11E+03	3.32E+02	2.44E+02	1.65E+02	1.03E+02	5.95E+01
6.683	3.47E+03	3.71E+02	2.74E+02	1.86E+02	1.17E+02	6.83E+01
6.789	3.85E+03	4.14E+02	3.07E+02	2.10E+02	1.33E+02	7.82E+01

Continued on next page

Table A.5 – continued from previous page

E_x (MeV)	Total NLD (MeV^{-1})	J=6	J=7	J=8	J=9	J=10
6.895	4.27E+03	4.61E+02	3.43E+02	2.36E+02	1.50E+02	8.92E+01
7.001	4.72E+03	5.12E+02	3.83E+02	2.65E+02	1.70E+02	1.01E+02
7.107	5.22E+03	5.67E+02	4.27E+02	2.97E+02	1.92E+02	1.15E+02
7.213	5.75E+03	6.28E+02	4.74E+02	3.32E+02	2.15E+02	1.30E+02
7.319	6.33E+03	6.93E+02	5.26E+02	3.70E+02	2.41E+02	1.47E+02
7.426	6.96E+03	7.64E+02	5.82E+02	4.11E+02	2.70E+02	1.65E+02
7.532	7.63E+03	8.40E+02	6.43E+02	4.56E+02	3.01E+02	1.86E+02
7.638	8.36E+03	9.22E+02	7.09E+02	5.05E+02	3.35E+02	2.08E+02
7.744	9.14E+03	1.01E+03	7.79E+02	5.58E+02	3.72E+02	2.32E+02
7.850	9.97E+03	1.10E+03	8.55E+02	6.15E+02	4.13E+02	2.59E+02
7.956	1.09E+04	1.21E+03	9.37E+02	6.77E+02	4.56E+02	2.87E+02
8.062	1.18E+04	1.31E+03	1.03E+03	7.43E+02	5.03E+02	3.19E+02
8.168	1.28E+04	1.43E+03	1.12E+03	8.15E+02	5.54E+02	3.53E+02
8.274	1.39E+04	1.55E+03	1.22E+03	8.91E+02	6.09E+02	3.89E+02
8.380	1.50E+04	1.68E+03	1.33E+03	9.73E+02	6.67E+02	4.29E+02

Table A.6: TALYS default γSF for ^{74}Zn.

γ-ray Energy (MeV)	f(M1) (MeV^{-3})	f(E1) (MeV^{-3})	γSF (MeV^{-3})
0.001	0.000E+00	1.108E-08	1.108E-08
0.002	1.532E-12	1.108E-08	1.108E-08
0.005	3.830E-12	1.108E-08	1.109E-08
0.010	7.660E-12	1.109E-08	1.109E-08
0.020	1.532E-11	1.110E-08	1.111E-08
0.050	3.830E-11	1.112E-08	1.116E-08
0.100	7.661E-11	1.117E-08	1.125E-08
0.200	1.533E-10	1.126E-08	1.141E-08
0.300	2.302E-10	1.135E-08	1.158E-08
0.400	3.073E-10	1.144E-08	1.175E-08
0.500	3.848E-10	1.154E-08	1.192E-08
0.600	4.628E-10	1.163E-08	1.210E-08
0.700	5.413E-10	1.173E-08	1.227E-08
0.800	6.204E-10	1.183E-08	1.245E-08
0.900	7.002E-10	1.193E-08	1.263E-08
1.000	7.809E-10	1.204E-08	1.282E-08
1.100	8.625E-10	1.214E-08	1.301E-08
1.200	9.451E-10	1.226E-08	1.320E-08
1.300	1.029E-09	1.237E-08	1.340E-08
1.400	1.114E-09	1.249E-08	1.361E-08
1.500	1.200E-09	1.262E-08	1.382E-08
1.600	1.288E-09	1.275E-08	1.403E-08
1.700	1.377E-09	1.288E-08	1.426E-08
1.800	1.468E-09	1.302E-08	1.449E-08
1.900	1.561E-09	1.317E-08	1.473E-08
2.000	1.656E-09	1.332E-08	1.498E-08
2.200	1.853E-09	1.365E-08	1.550E-08
2.400	2.059E-09	1.401E-08	1.606E-08
2.600	2.276E-09	1.440E-08	1.667E-08
2.800	2.505E-09	1.483E-08	1.733E-08
3.000	2.749E-09	1.530E-08	1.805E-08

Continued on next page

Table A.6 – continued from previous page

γ-ray Energy (MeV)	f(M1) (MeV^{-3})	f(E1) (MeV^{-3})	γSF (MeV^{-3})
3.200	3.008E-09	1.582E-08	1.883E-08
3.400	3.286E-09	1.639E-08	1.967E-08
3.600	3.584E-09	1.701E-08	2.059E-08
3.800	3.904E-09	1.769E-08	2.160E-08
4.000	4.251E-09	1.844E-08	2.269E-08
4.500	5.254E-09	2.064E-08	2.589E-08
5.000	6.509E-09	2.338E-08	2.989E-08
5.500	8.110E-09	2.679E-08	3.490E-08
6.000	1.019E-08	3.103E-08	4.122E-08
6.500	1.295E-08	3.628E-08	4.922E-08
7.000	1.662E-08	4.278E-08	5.940E-08
7.500	2.150E-08	5.083E-08	7.233E-08
8.000	2.776E-08	6.083E-08	8.858E-08
8.500	3.503E-08	7.326E-08	1.083E-07
9.000	4.173E-08	8.877E-08	1.305E-07
9.500	4.502E-08	1.082E-07	1.532E-07

Table A.7: CoH default γSF for ^{74}Zn.

γ-ray Energy (MeV)	f(M1) (MeV^{-3})	f(E1) (MeV^{-3})	γSF (MeV^{-3})
0.05	5.419E-12	5.542E-09	5.548E-09
0.10	1.084E-11	5.531E-09	5.542E-09
0.15	1.626E-11	5.519E-09	5.535E-09
0.20	2.169E-11	5.507E-09	5.529E-09
0.25	2.713E-11	5.495E-09	5.522E-09
0.30	3.257E-11	5.483E-09	5.515E-09
0.35	3.802E-11	5.470E-09	5.508E-09
0.40	4.348E-11	5.457E-09	5.501E-09
0.45	4.896E-11	5.444E-09	5.493E-09

Continued on next page

Table A.7 – continued from previous page

γ-ray Energy (MeV)	f(M1) (MeV^{-3})	f(E1) (MeV^{-3})	γSF (MeV^{-3})
0.50	5.445E-11	5.431E-09	5.485E-09
0.55	5.995E-11	5.418E-09	5.478E-09
0.60	6.547E-11	5.404E-09	5.470E-09
0.65	7.102E-11	5.391E-09	5.462E-09
0.70	7.658E-11	5.377E-09	5.453E-09
0.75	8.216E-11	5.363E-09	5.445E-09
0.80	8.777E-11	5.349E-09	5.437E-09
0.85	9.341E-11	5.335E-09	5.429E-09
0.90	9.907E-11	5.321E-09	5.420E-09
0.95	1.048E-10	5.307E-09	5.412E-09
1.00	1.105E-10	5.293E-09	5.403E-09
1.05	1.162E-10	5.278E-09	5.394E-09
1.10	1.220E-10	5.264E-09	5.386E-09
1.15	1.279E-10	5.250E-09	5.377E-09
1.20	1.337E-10	5.235E-09	5.369E-09
1.25	1.396E-10	5.221E-09	5.360E-09
1.30	1.456E-10	5.206E-09	5.352E-09
1.35	1.516E-10	5.192E-09	5.343E-09
1.40	1.576E-10	5.178E-09	5.335E-09
1.45	1.637E-10	5.163E-09	5.327E-09
1.50	1.698E-10	5.149E-09	5.319E-09
1.55	1.760E-10	5.135E-09	5.311E-09
1.60	1.822E-10	5.121E-09	5.303E-09
1.65	1.885E-10	5.107E-09	5.295E-09
1.70	1.949E-10	5.093E-09	5.288E-09
1.75	2.013E-10	5.079E-09	5.280E-09
1.80	2.078E-10	5.065E-09	5.273E-09
1.85	2.143E-10	5.052E-09	5.266E-09
1.90	2.209E-10	5.038E-09	5.259E-09
1.95	2.276E-10	5.025E-09	5.252E-09
2.00	2.343E-10	5.012E-09	5.246E-09

Continued on next page

Table A.7 – continued from previous page

γ-ray Energy (MeV)	f(M1) (MeV^{-3})	f(E1) (MeV^{-3})	γSF (MeV^{-3})
2.05	2.412E-10	4.999E-09	5.240E-09
2.10	2.481E-10	4.986E-09	5.234E-09
2.15	2.550E-10	4.974E-09	5.229E-09
2.20	2.621E-10	4.961E-09	5.224E-09
2.25	2.693E-10	4.949E-09	5.219E-09
2.30	2.765E-10	4.938E-09	5.214E-09
2.35	2.838E-10	4.926E-09	5.210E-09
2.40	2.913E-10	4.915E-09	5.206E-09
2.45	2.988E-10	4.904E-09	5.202E-09
2.50	3.064E-10	4.893E-09	5.199E-09
2.55	3.141E-10	4.883E-09	5.197E-09
2.60	3.220E-10	4.872E-09	5.194E-09
2.65	3.299E-10	4.863E-09	5.193E-09
2.70	3.380E-10	4.853E-09	5.191E-09
2.75	3.461E-10	4.844E-09	5.190E-09
2.80	3.544E-10	4.836E-09	5.190E-09
2.85	3.628E-10	4.827E-09	5.190E-09
2.90	3.714E-10	4.820E-09	5.191E-09
2.95	3.801E-10	4.812E-09	5.192E-09
3.00	3.889E-10	4.805E-09	5.194E-09
3.05	3.978E-10	4.799E-09	5.196E-09
3.10	4.069E-10	4.792E-09	5.199E-09
3.15	4.162E-10	4.787E-09	5.203E-09
3.20	4.256E-10	4.782E-09	5.207E-09
3.25	4.352E-10	4.777E-09	5.212E-09
3.30	4.449E-10	4.773E-09	5.218E-09
3.35	4.548E-10	4.770E-09	5.224E-09
3.40	4.649E-10	4.767E-09	5.232E-09
3.45	4.751E-10	4.764E-09	5.239E-09
3.50	4.856E-10	4.763E-09	5.248E-09
3.55	4.962E-10	4.761E-09	5.258E-09

Continued on next page

Table A.7 – continued from previous page

γ-ray Energy (MeV)	f(M1) (MeV^{-3})	f(E1) (MeV^{-3})	γSF (MeV^{-3})
3.60	5.070E-10	4.761E-09	5.268E-09
3.65	5.180E-10	4.761E-09	5.279E-09
3.70	5.293E-10	4.762E-09	5.291E-09
3.75	5.407E-10	4.763E-09	5.304E-09
3.80	5.524E-10	4.765E-09	5.318E-09
3.85	5.643E-10	4.768E-09	5.333E-09
3.90	5.764E-10	4.772E-09	5.348E-09
3.95	5.888E-10	4.776E-09	5.365E-09
4.00	6.014E-10	4.782E-09	5.383E-09
4.05	6.143E-10	4.788E-09	5.402E-09
4.10	6.275E-10	4.794E-09	5.422E-09
4.15	6.409E-10	4.802E-09	5.443E-09
4.20	6.546E-10	4.810E-09	5.465E-09
4.25	6.686E-10	4.820E-09	5.488E-09
4.30	6.829E-10	4.830E-09	5.513E-09
4.35	6.975E-10	4.841E-09	5.539E-09
4.40	7.125E-10	4.854E-09	5.566E-09
4.45	7.277E-10	4.867E-09	5.594E-09
4.50	7.433E-10	4.881E-09	5.624E-09
4.55	7.593E-10	4.896E-09	5.655E-09
4.60	7.756E-10	4.912E-09	5.688E-09
4.65	7.923E-10	4.930E-09	5.722E-09
4.70	8.094E-10	4.948E-09	5.757E-09
4.75	8.269E-10	4.967E-09	5.794E-09
4.80	8.448E-10	4.988E-09	5.833E-09
4.85	8.631E-10	5.010E-09	5.873E-09
4.90	8.819E-10	5.033E-09	5.915E-09
4.95	9.012E-10	5.057E-09	5.958E-09
5.00	9.209E-10	5.083E-09	6.004E-09
5.05	9.410E-10	5.110E-09	6.051E-09
5.10	9.617E-10	5.138E-09	6.100E-09

Continued on next page

Table A.7 – continued from previous page

γ-ray Energy (MeV)	f(M1) (MeV^{-3})	f(E1) (MeV^{-3})	γSF (MeV^{-3})
5.15	9.829E-10	5.167E-09	6.150E-09
5.20	1.005E-09	5.198E-09	6.203E-09
5.25	1.027E-09	5.231E-09	6.258E-09
5.30	1.050E-09	5.264E-09	6.314E-09
5.35	1.073E-09	5.300E-09	6.373E-09
5.40	1.097E-09	5.336E-09	6.434E-09
5.45	1.122E-09	5.375E-09	6.497E-09
5.50	1.147E-09	5.414E-09	6.562E-09
5.55	1.174E-09	5.456E-09	6.629E-09
5.60	1.200E-09	5.499E-09	6.699E-09
5.65	1.228E-09	5.544E-09	6.771E-09
5.70	1.256E-09	5.590E-09	6.846E-09
5.75	1.285E-09	5.639E-09	6.924E-09
5.80	1.315E-09	5.689E-09	7.004E-09
5.85	1.345E-09	5.741E-09	7.086E-09
5.90	1.377E-09	5.795E-09	7.171E-09
5.95	1.409E-09	5.851E-09	7.260E-09
6.00	1.442E-09	5.908E-09	7.351E-09
6.05	1.476E-09	5.968E-09	7.445E-09
6.10	1.512E-09	6.030E-09	7.542E-09
6.15	1.548E-09	6.094E-09	7.642E-09
6.20	1.585E-09	6.160E-09	7.745E-09
6.25	1.623E-09	6.229E-09	7.852E-09
6.30	1.662E-09	6.299E-09	7.962E-09
6.35	1.703E-09	6.372E-09	8.075E-09
6.40	1.745E-09	6.448E-09	8.192E-09
6.45	1.788E-09	6.525E-09	8.313E-09
6.50	1.832E-09	6.606E-09	8.437E-09
6.55	1.877E-09	6.688E-09	8.566E-09
6.60	1.924E-09	6.774E-09	8.698E-09
6.65	1.972E-09	6.862E-09	8.834E-09

Continued on next page

Table A.7 – continued from previous page

γ-ray Energy (MeV)	f(M1) (MeV^{-3})	f(E1) (MeV^{-3})	γSF (MeV^{-3})
6.70	2.022E-09	6.953E-09	8.974E-09
6.75	2.073E-09	7.046E-09	9.119E-09
6.80	2.125E-09	7.142E-09	9.268E-09
6.85	2.180E-09	7.242E-09	9.421E-09

Table A.8: EMPIRE default γSF for ^{74}Zn.

γ-ray Energy (MeV)	γSF (MeV^{-3})	γSF (mb/MeV)
0.106	3.223E-12	3.942E-06
0.212	1.290E-11	3.154E-05
0.318	2.903E-11	1.065E-04
0.424	5.163E-11	2.526E-04
0.530	8.073E-11	4.936E-04
0.636	1.163E-10	8.537E-04
0.743	1.585E-10	1.357E-03
0.849	2.073E-10	2.028E-03
0.955	2.626E-10	2.891E-03
1.061	3.247E-10	3.971E-03
1.167	3.935E-10	5.294E-03
1.273	4.691E-10	6.885E-03
1.379	5.516E-10	8.769E-03
1.485	6.410E-10	1.097E-02
1.591	7.374E-10	1.353E-02
1.697	8.410E-10	1.646E-02
1.803	9.517E-10	1.979E-02
1.909	1.070E-09	2.355E-02
2.016	1.195E-09	2.777E-02
2.122	1.328E-09	3.249E-02
2.228	1.469E-09	3.773E-02

Continued on next page

Table A.8 – continued from previous page

γ-ray Energy (MeV)	γSF (MeV^{-3})	γSF (mb/MeV)
2.334	1.617E-09	4.352E-02
2.440	1.774E-09	4.989E-02
2.546	1.938E-09	5.689E-02
2.652	2.111E-09	6.454E-02
2.758	2.292E-09	7.288E-02
2.864	2.482E-09	8.194E-02
2.970	2.680E-09	9.177E-02
3.076	2.887E-09	1.024E-01
3.182	3.104E-09	1.139E-01
3.288	3.330E-09	1.262E-01
3.395	3.565E-09	1.395E-01
3.501	3.810E-09	1.538E-01
3.607	4.066E-09	1.690E-01
3.713	4.331E-09	1.854E-01
3.819	4.607E-09	2.028E-01
3.925	4.894E-09	2.215E-01
4.031	5.193E-09	2.413E-01
4.137	5.502E-09	2.624E-01
4.243	5.824E-09	2.849E-01
4.349	6.157E-09	3.087E-01
4.455	6.503E-09	3.340E-01
4.561	6.862E-09	3.609E-01
4.668	7.235E-09	3.893E-01
4.774	7.620E-09	4.194E-01
4.880	8.020E-09	4.512E-01
4.986	8.435E-09	4.848E-01
5.092	8.864E-09	5.204E-01
5.198	9.309E-09	5.579E-01
5.304	9.770E-09	5.974E-01
5.410	1.025E-08	6.392E-01
5.516	1.074E-08	6.832E-01

Continued on next page

Table A.8 – continued from previous page

γ-ray Energy (MeV)	γSF (MeV^{-3})	γSF (mb/MeV)
5.622	1.125E-08	7.295E-01
5.728	1.179E-08	7.783E-01
5.834	1.234E-08	8.297E-01
5.940	1.290E-08	8.838E-01
6.047	1.349E-08	9.406E-01
6.153	1.410E-08	1.000E+00
6.259	1.474E-08	1.063E+00
6.365	1.539E-08	1.129E+00
6.471	1.607E-08	1.199E+00
6.577	1.677E-08	1.272E+00
6.683	1.750E-08	1.348E+00
6.789	1.826E-08	1.429E+00
6.895	1.904E-08	1.513E+00
7.001	1.985E-08	1.602E+00
7.107	2.069E-08	1.695E+00
7.213	2.156E-08	1.793E+00
7.319	2.246E-08	1.895E+00
7.426	2.340E-08	2.003E+00
7.532	2.437E-08	2.116E+00
7.638	2.538E-08	2.234E+00
7.744	2.642E-08	2.359E+00
7.850	2.751E-08	2.489E+00
7.956	2.863E-08	2.626E+00
8.062	2.980E-08	2.770E+00
8.168	3.101E-08	2.920E+00
8.274	3.227E-08	3.078E+00
8.380	3.358E-08	3.244E+00

Appendix B

Matrices used in the daughter and background subtraction for the decay of ^{71,72,73}Co

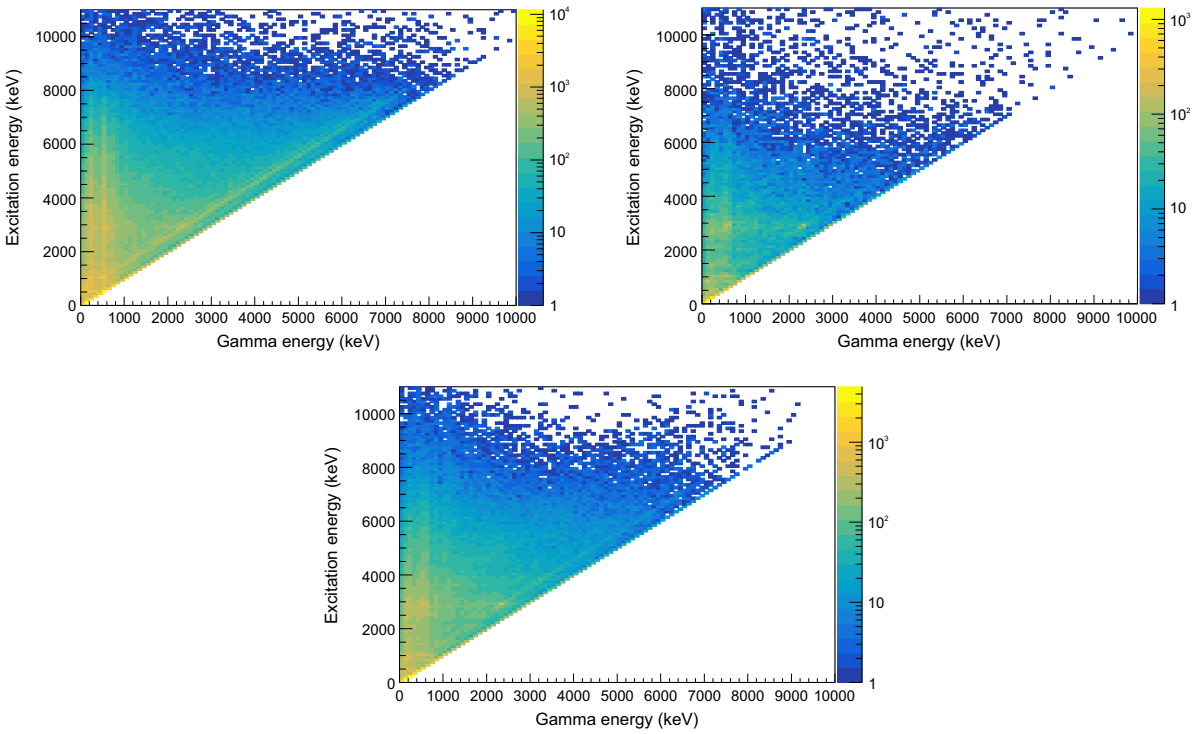

Figure B.1: (Top Left) Starting 2D matrix for the analysis of the β decay of ^{71}Co using the β-Oslo method (includes daughter decay and random correlation, or background, contributions). (Top Right) Matrix with daughter decay component that was subtracted from the starting matrix. (Bottom) Matrix with the background component from random correlations that was subtracted from the starting matrix.

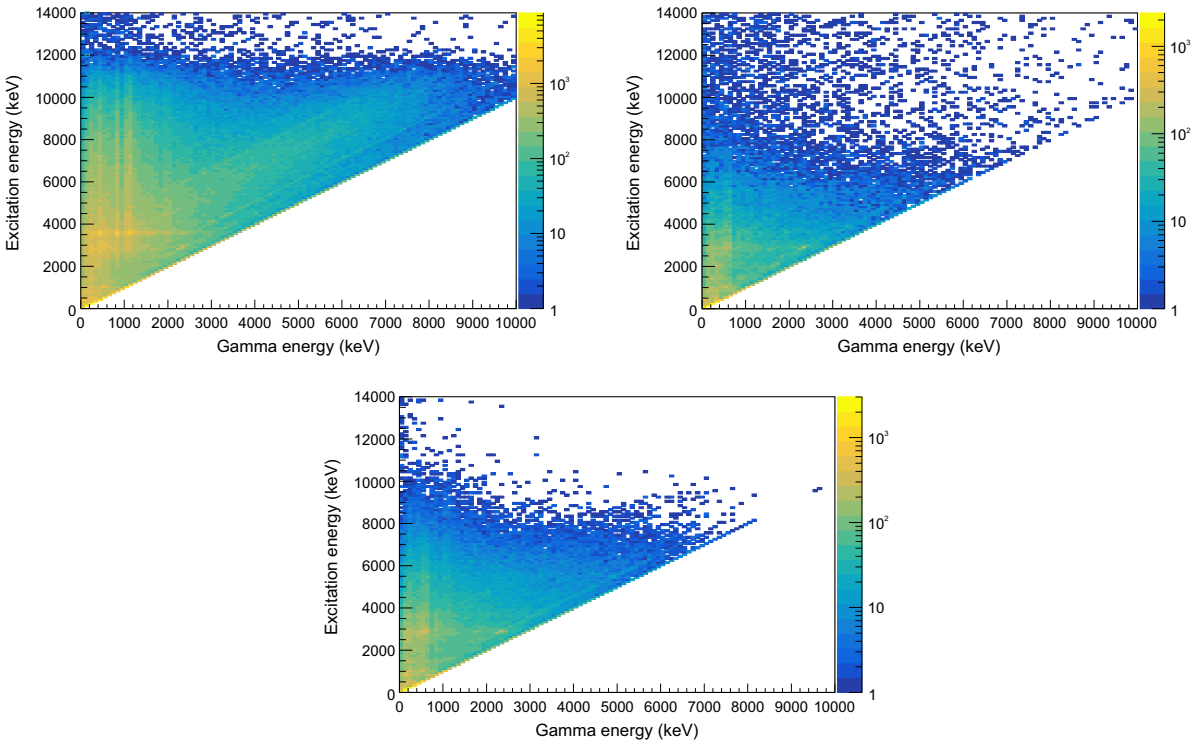

Figure B.2: (Top Left) Starting 2D matrix for the analysis of the β decay of ^{72}Co using the β-Oslo method (includes daughter decay and random correlation, or background, contributions). (Top Right) Matrix with daughter decay component that was subtracted from the starting matrix. (Bottom) Matrix with the background component from random correlations that was subtracted from the starting matrix.

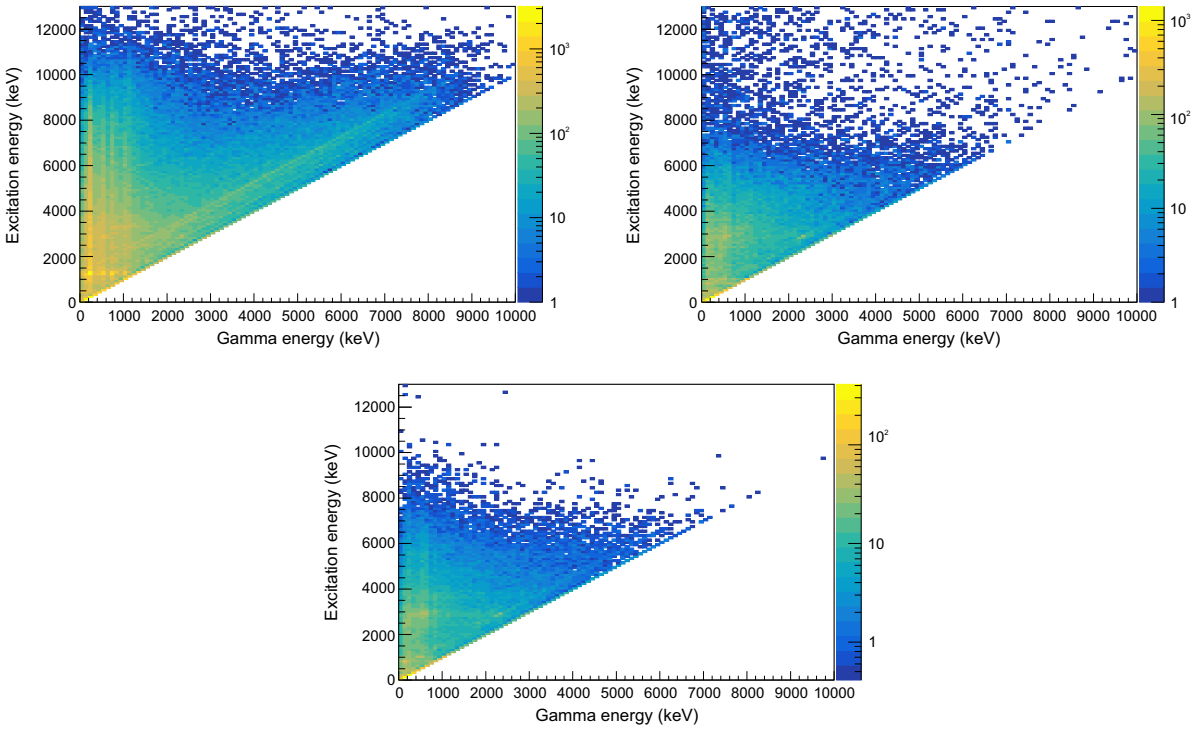

Figure B.3: (Top Left) Starting 2D matrix for the analysis of the β decay of ^{73}Co using the β-Oslo method (includes daughter decay and random correlation, or background, contributions). (Top Right) Matrix with daughter decay component that was subtracted from the starting matrix. (Bottom) Matrix with the background component from random correlations that was subtracted from the starting matrix.

Appendix C

Fits to experimental γSF (upper and lower limits)

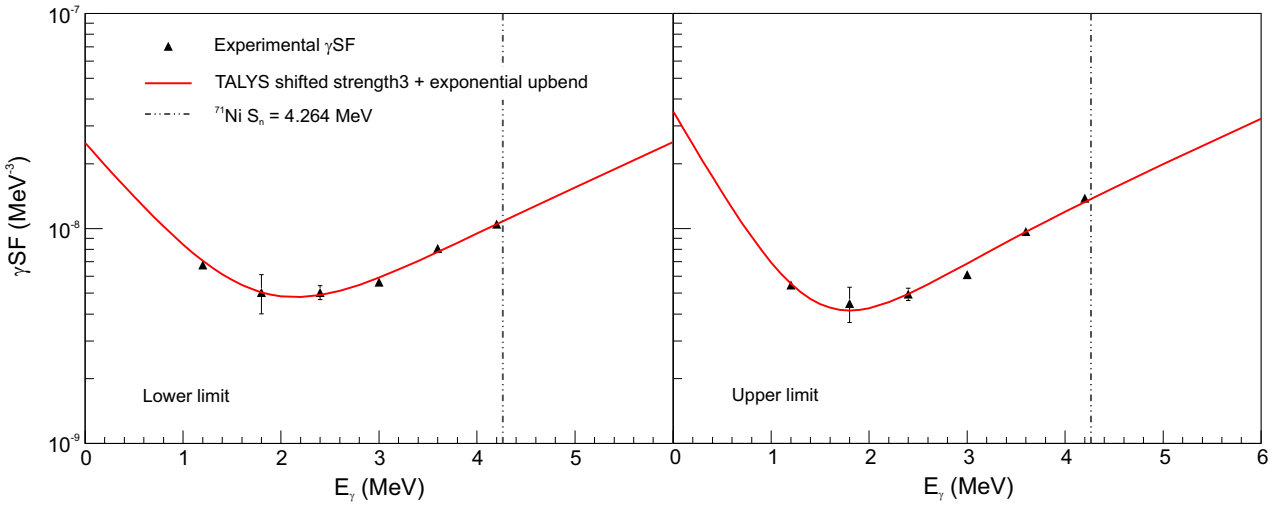

Figure C.1: Fit to experimental γSFs for ^{71}Ni using the HFBCS model (strength 3 in TALYS) and an exponential upbend. The lower limit data set is on the right, while the upper limit data set is on the left.

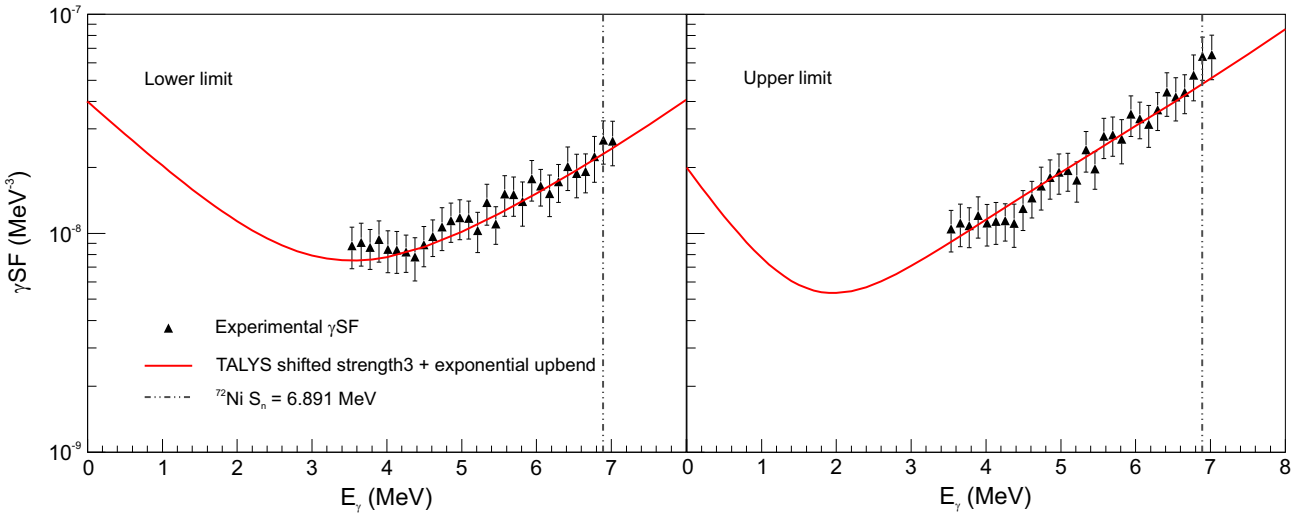

Figure C.2: Fit to experimental γSFs for ^{72}Ni, (6^- ground state of ^{72}Co) using the HFBCS model (strength 3 in TALYS) and an exponential upbend. The lower limit data set is on the right, while the upper limit data set is on the left.

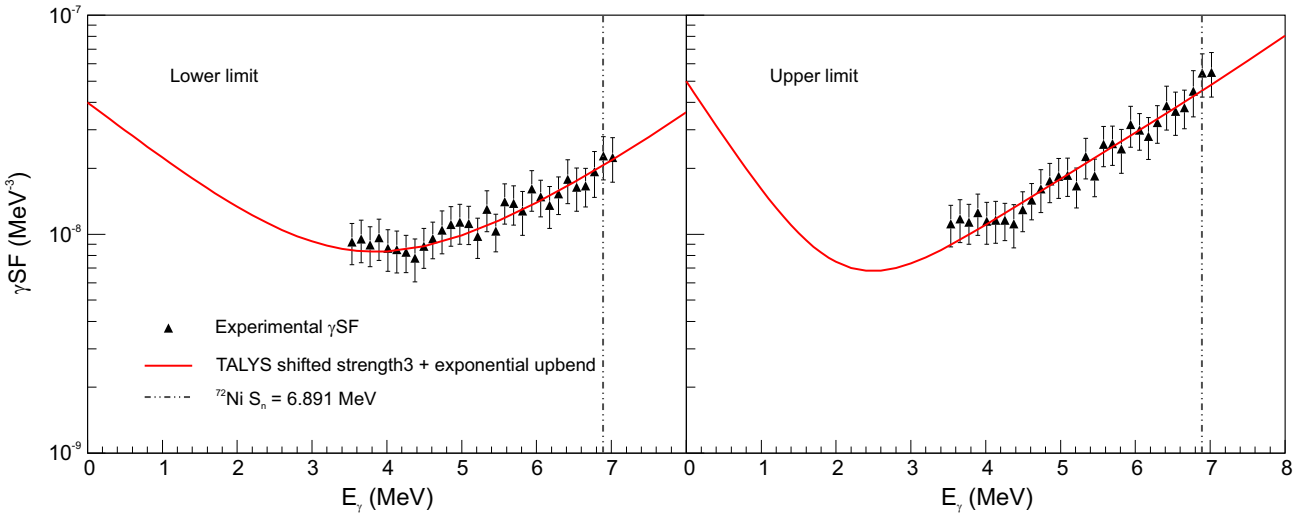

Figure C.3: Fit to experimental γSFs for ^{72}Ni (7^- ground state of ^{72}Co) using the HFBCS model (strength 3 in TALYS) and an exponential upbend. The lower limit data set is on the right, while the upper limit data set is on the left.

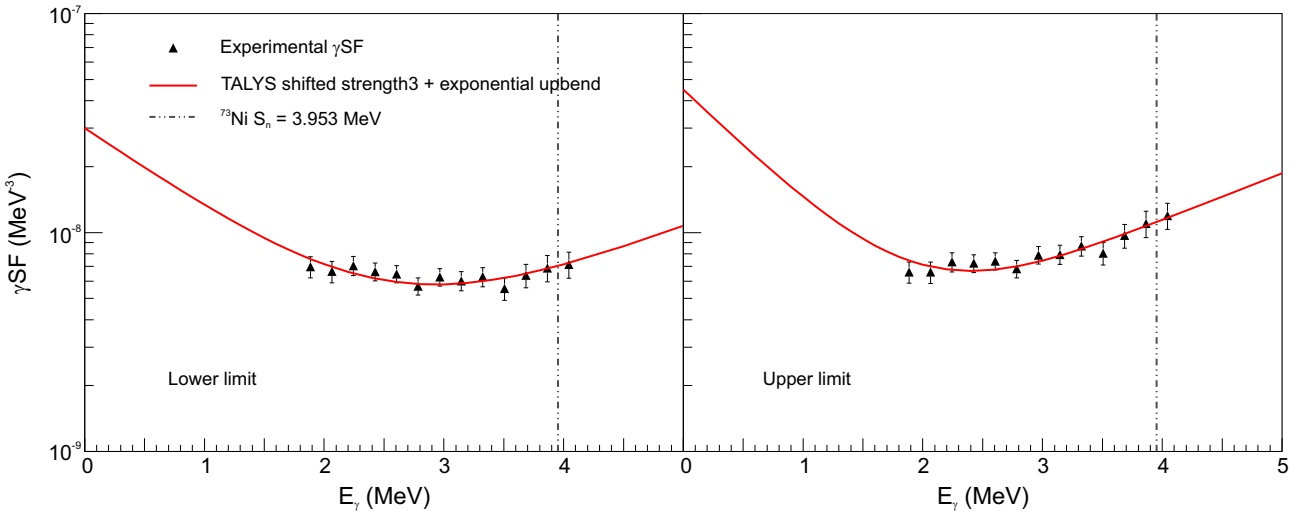

Figure C.4: Fit to experimental γSFs for ^{73}Ni using the HFBCS model (strength 3 in TALYS) and an exponential upbend. The lower limit data set is on the right, while the upper limit data set is on the left.

BIBLIOGRAPHY

[1] M. Weigand, T. A. Bredeweg, A. Couture, K. Göbel, T. Heftrich, M. Jandel, F. Käppeler, C. Lederer, N. Kivel, G. Korschinek, M. Krtička, J. M. O'Donnell, J. Ostermöller, R. Plag, R. Reifarth, D. Schumann, J. L. Ullmann, and A. Wallner. Ni 63 (n,γ) cross sections measured with DANCE. *Physical Review C - Nuclear Physics*, 92(4):045810, 2015.

[2] C. Sneden, J.J. Cowan, and R. Gallino. Neutron-Capture Elements in the Early Galaxy. *Annual Review of Astronomy and Astrophysics*, 46:241–288, 9 2008.

[3] M. Arnould, S. Goriely, and K. Takahashi. The r-process of stellar nucleosynthesis: Astrophysics and nuclear physics achievements and mysteries. *Physics Reports*, 450:97–213, 2007.

[4] LIGO Scientific Collaboration and Virgo Collaboration. GW170817: Observation of Gravitational Waves from a Binary Neutron Star Inspiral. *Phys. Rev. Lett.*, 119(16):30–33, 2017.

[5] M. R. Drout, A. L. Piro, B. J. Shappee, C. D. Kilpatrick, J. D. Simon, C. Contreras, D. A. Coulter, R. J. Foley, M. R. Siebert, N. Morrell, K. Boutsia, F. Di Mille, T. W.S. Holoien, D. Kasen, J. A. Kollmeier, B. F. Madore, A. J. Monson, A. Murguia-Berthier, Y.-C. Pan, J. X. Prochaska, E. Ramirez-Ruiz, A. Rest, C. Adams, K. Alatalo, E. Bañados, J. Baughman, T. C. Beers, R. A. Bernstein, T. Bitsakis, A. Campillay, T. T. Hansen, C. R. Higgs, A. P. Ji, G. Maravelias, J. L. Marshall, C. Moni Bidin, J. L. Prieto, K. C. Rasmussen, C. Rojas-Bravo, A. L. Strom, N. Ulloa, J. Vargas-González, Z. Wan, and D. D. Whitten. Light curves of the neutron star merger GW170817/SSS17a: Implications for r-process nucleosynthesis. *Science*, 358(6370):1570–1574, 12 2017.

[6] D. Kasen, B. Metzger, J. Barnes, E. Quataert, and E. Ramirez-Ruiz. Origin of the heavy elements in binary neutron-star mergers from a gravitational-wave event. *Nature*, 551(7678):80–84, 2017.

[7] B.D. Metzger, G. Martínez-Pinedo, S. Darbha, E. Quataert, A. Arcones, D. Kasen, R. Thomas, P. Nugent, I.V. Panov, and N.T. Zinner. Electromagnetic counterparts of compact object mergers powered by the radioactive decay of r-process nuclei. *Monthly Notices of the Royal Astronomical Society*, 406:2650–2662, 2010.

[8] G.J. Wasserburg and Y.-Z. Qian. Prompt iron enrichment, two r-process components, and abundanced in very metal-poor stars. *The Astrophysical Journal*, 529:L21, 2000.

[9] Y. Z. Qian and G. J. Wasserburg. Stellar abundances in the early galaxy and two r-process components. *Physics Reports*, 333-334(4-6):77–108, 2000.

[10] Y Z Qian and G J Wasserburg. A model for abundances in metal-poor stars. *The Astrophysical Journal*, 559(2):925–941, 2001.

[11] Y. Z. Qian and G. J. Wasserburg. Determination of Nucleosynthetic Yields of Supernovae and Very Massive Stars from Abundances in Metal-Poor Stars. *The Astrophysical Journal*, 567:515, 2001.

[12] F. Montes, T. C. Beers, J. Cowan, T. Elliot, K. Farouqi, R. Gallino, M. Heil, K.L. Kratz, B. Pfeiffer, M. Pignatari, and H. Schatz. Nucleosynthesis in the Early Galaxy. *The Astrophysical Journal*, 671(2):1685–1695, 2007.

[13] M. R. Mumpower, R. Surman, G. C. McLaughlin, and A. Aprahamian. The impact of individual nuclear properties on r-process nucleosynthesis. *Prog. Part. Nucl. Phys.*, 86:86, 2016.

[14] R. Surman, M. Mumpower, R. Sinclair, K. L. Jones, W. R. Hix, and G. C. McLaughlin. Sensitivity studies for the weak r process: Neutron capture rates. *AIP Advances*, 4:041008, 2014.

[15] R.H. Cyburt, A. M. Amthor, R. Ferguson, Z. Meisel, K. Smith, S. Warren, A. Heger, R. D. Hoffman, T. Rauscher, A. Sakharuk, H. Schatz, F. K. Thielemann, and M. Wiescher. the Jina Reaclib Database: Its Recent Updates and Impact on Type-I X-Ray Bursts. *The Astrophysical Journal Supplement Series*, 189(1):240–252, 2010.

[16] A. C. Larsen, A. Spyrou, S. N. Liddick, M. Guttormsen, V. W. Ingeberg, S. Siem, M. Wiedeking, B. P. Crider, F. Naqvi, G. Perdikakis, M. R. Mumpower, R. Surman, G. M. Tveten, D. L. Bleuel, A. Couture, L. Crespo Campo, A. C. Dombos, A. Görgen, R. Lewis, S. M. Mosby, S. Nikas, C. J. Prokop, S. J. Quinn, T. Renstrøm, and B. Rubio. Novel techniques for constraining neutron-capture rates relevant to heavy-element nucleosynthesis. *Progress in Particle and Nuclear Physics*, In Press, 2019.

[17] S. M. Grimes. Hauser-Feshbach calculations in deformed nuclei. *Phys. Rev. C*, 88(2):1–10, 2013.

[18] A. J. Koning and J. P. Delaroche. Local and global nucleon optical models from 1 keV to 200 MeV. *Nucl. Phys. A*, 713:231, 2003.

[19] J.-P. Jeukenne, A. Lejeune, and C. Mahaux. Microscopic calculation of the symmetry and Coulomb components of the complex optical-model potential. *Physical Review*, 15:10, 1977.

[20] T. Ericson. The statistical model and nuclear level densities. *Advances in Physics*, 9(36):425–511, 1960.

[21] A. Gilbert and A.G.W. Cameron. A composite nuclear level density formula with shell corrections. *Can. J. Phys.*, 43:1446, 1965.

[22] T. Von Egidy and D. Bucurescu. Experimental energy-dependent nuclear spin distributions. *Phys. Rev. C*, 80:054310, 2009.

[23] H.A. Bethe. Nuclear Physics B. Nuclear Dynamics, Theoretical. *Rev. Mod. Phys.*, 9:69, 1937.

[24] TALYS User Manual (v. 1.6).

[25] T. D. Newton. Shell Effects on the Spacing of Nuclear Levels. *Can. J. Phys.*, 34:804–829, 1956.

[26] A.G.W. Cameron. Nuclear Level Spacings. *Can. J. Phys.*, 36:1040, 1958.

[27] A. Gilbert, F.S. Chen, and A.G.W Cameron. Level densities in lighter nuclei. *Can. J. Phys.*, 43(7):1248–1258, 1965.

[28] R. Capote, M. Herman, P. Obložinský, P. G. Young, S. Goriely, T. Belgya, A. V. Ignatyuk, A. J. Koning, S. Hilaire, V. A. Plujko, M. Avrigeanu, O. Bersillon, M. B. Chadwick, T. Fukahori, Zhigang Ge, Yinlu Han, S. Kailas, J. Kopecky, V. M. Maslov, G. Reffo, M. Sin, E. Sh Soukhovitskii, and P. Talou. RIPL - Reference Input Parameter Library for Calculation of Nuclear Reactions and Nuclear Data Evaluations. *Nuclear Data Sheets*, 110(12):3107–3214, 2009.

[29] S. Goriely, F. Tondeur, and J.M. Pearson. A Hartree-Fock Nuclear Mass Table. *Atomic Data and Nuclear Data Tables*, 77:311, 2001.

[30] S. Goriely, S. Hilaire, and A. J. Koning. Improved microscopic nuclear level densities within the Hartree-Fock-Bogoliubov plus combinatorial method. *Phys. Rev. C*, 78:064307, 2008.

[31] S. Hilaire, M. Girod, S. Goriely, and A. J. Koning. Temperature-dependent combinatorial level densities with the D1M Gogny force. *Phys. Rev. C*, 86:064317, 2012.

[32] D.M. Brink. Individual Particle and Collective Aspects of the Nuclear Photoeffect. *Nuclear Physics*, 4:215, 1957.

[33] P. Axel. Electric Dipole Ground-State Transition Width Strength Function and 7-Mev Photon Interactions. *Physical Review*, 126(2):671–683, 1962.

[34] M. Krtička and F. Bečvář. What do we really know about photon strength functions? *Journal of Physics G*, 35:014025, 2008.

[35] J. Kopecky and M. Uhl. Test of gamma-ray strength functions in nuclear reaction model calculations. *Phys. Rev. C*, 41:1941, 1990.

[36] A.C. Larsen and S. Goriely. Impact of a low-energy enhancement in the γ -ray strength function on the neutron-capture cross section. *Phys. Rev. C*, 82:014318, 2010.

[37] S. Goriely and E. Khan. Large-scale QRPA calculation of E1-strength and its impact on the neutron capture cross section. *Nuclear Physics A*, 706:217–232, 2002.

[38] S. Goriely, E. Khan, and M. Samyn. Microscopic HFB + QRPA predictions of dipole strength for astrophysics applications. *Nuclear Physics A*, 739:331–352, 2004.

[39] A. Koning, S. Hilaire, and M.C. Duijvestijn. No Title. In *TALYS-1.6: Proceedings of the International Conference on Nuclear Data for Science and Technology 2007*. EDP Sciences, Nice, France, 2007, 2007.

[40] A. J. Koning and D. Rochman. Modern Nuclear Data Evaluation with the TALYS Code System. *Nuclear Data Sheets*, 113:2927, 2012.

[41] A. Voinov, E. Algin, U. Agvaanluvsan, T. Belgya, R. Chankova, M. Guttormsen, G.E. Mitchell, J. Rekstad, A. Schiller, and S. Siem. Large enhancement of radiative strength for soft transitions in the quasicontinuum. *Phys. Rev. Lett.*, pages 7–10, 2004.

[42] M. Guttormsen, R. Chankova, U. Agvaanluvsan, E. Algin, L. A. Bernstein, F. Ingebretsen, T. Lönnroth, S. Messelt, G. E. Mitchell, J. Rekstad, A. Schiller, S. Siem, A. C. Sunde, A. Voinov, and S. Ødegård. Radiative strength functions in 93-98Mo. *Phys. Rev. C*, 71(4):044307, 2005.

[43] A. C. Larsen, M. Guttormsen, R. Chankova, F. Ingebretsen, T. Lönnroth, S. Messelt, J. Rekstad, A. Schiller, S. Siem, N. U. H. Syed, and A. Voinov. Nuclear level densities and γ-ray strength functions in 44,45Sc. *Phys. Rev. C*, 76(4):044303, 2007.

[44] M. Wiedeking, L.A. Bernstein, M. Krtička, D.L. Bleuel, J.M. Allmond, M.S. Basunia, J.T. Burke, P. Fallon, R.B. Firestone, B.L. Goldblum, R. Hatarik, P.T. Lake, I-Y. Lee, S.R. Lesher, S. Paschalis, M. Petri, L. Phair, and N.D. Scielzo. Low-Energy Enhancement in the Photon Strength of Mo95. *Phys. Rev. Lett.*, 108(16):162503, 2012.

[45] A. Bürger, A. C. Larsen, S. Hilaire, M. Guttormsen, S. Harissopulos, M. Kmiecik, T. Konstantinopoulos, M. Krtička, A. Lagoyannis, T. Lönnroth, K. Mazurek, M. Norrby, H. T. Nyhus, G. Perdikakis, S. Siem, A. Spyrou, and N. U.H. Syed. Nuclear level density and γ-ray strength function of 43Sc. *Phys. Rev. C*, 85(6):064328, 2012.

[46] A. C. Larsen, N. Blasi, A. Bracco, F. Camera, T. K. Eriksen, A. Görgen, M. Guttormsen, T. W. Hagen, S. Leoni, B. Million, H. T. Nyhus, T. Renstrøm, S. J. Rose, I. E. Ruud, S. Siem, T. Tornyi, G. M. Tveten, A. V. Voinov, and M. Wiedeking. Evidence for the dipole nature of the low-energy g enhancement in Fe56. *Phys. Rev. Lett.*, 111:242504, 2013.

[47] B. V. Kheswa, M. Wiedeking, F. Giacoppo, S. Goriely, M. Guttormsen, A. C. Larsen, F. L. Bello Garrote, T. K. Eriksen, A. Görgen, T. W. Hagen, P. E. Koehler, M. Klintefjord, H. T. Nyhus, P. Papka, T. Renstrøm, S. Rose, E. Sahin, S. Siem, and T. Tornyi. Galactic production of138La: Impact of138,139La statistical properties. *Phys. Lett. B*, 744:268–272, 2015.

[48] A. Simon, M. Guttormsen, A. C. Larsen, C. W. Beausang, P. Humby, J. T. Burke, R. J. Casperson, R. O. Hughes, T. J. Ross, J. M. Allmond, R. Chyzh, M. Dag, J. Koglin, E. McCleskey, M. McCleskey, S. Ota, and A. Saastamoinen. First observation of low-energy γ -ray enhancement in the rare-earth region. *Phys. Rev. C*, 93(3):034303, 2016.

[49] S. Paschalis, I. Y. Lee, A. O. MacChiavelli, C. M. Campbell, M. Cromaz, S. Gros, J. Pavan, J. Qian, R. M. Clark, H. L. Crawford, D. Doering, P. Fallon, C. Lionberger, T. Loew, M. Petri, T. Stezelberger, S. Zimmermann, D. C. Radford, K. Lagergren, D. Weisshaar, R. Winkler, T. Glasmacher, J. T. Anderson, and C. W. Beausang. The performance of the Gamma-Ray Energy Tracking In-beam Nuclear Array GRETINA. *Nucl. Instr. Meth. Phys. Res. A*, 709:44–55, 2013.

[50] M. D. Jones, A. O. MacChiavelli, M. Wiedeking, L. A. Bernstein, H. L. Crawford, C. M. Campbell, R. M. Clark, M. Cromaz, P. Fallon, I. Y. Lee, M. Salathe, A. Wiens, A. D. Ayangeakaa, D. L. Bleuel, S. Bottoni, M. P. Carpenter, H. M. Davids, J. Elson, A. Görgen, M. Guttormsen, R. V.F. Janssens, J. E. Kinnison, L. Kirsch, A. C. Larsen, T. Lauritsen, W. Reviol, D. G. Sarantites, S. Siem, A. V. Voinov, and S. Zhu. Examination of the low-energy enhancement of the γ -ray strength function of Fe 56. *Phys. Rev. C*, 97(2):024327, 2018.

[51] M. Guttormsen, T.S. Tveter, L. Bergholt, F. Ingebretsen, and J. Rekstad. The unfolding of continuum y-ray spectra. *Nucl. Instr. Meth. Phys. Res. A*, 374:371, 1996.

[52] M. Guttormsen, T. Ramsøy, and J. Rekstad. The first generation of γ-rays from hot nuclei. *Nucl. Instr. Meth. Phys. Res. A*, 255(3):518–523, 4 1987.

[53] A Schiller, L Bergholt, M Guttormsen, E Melby, J Rekstad, and S Siem. Extraction of level density and γ strength function from primary γ spectra. *Nucl. Instr. Meth. Phys. Res. A*, 447(3):498–511, 2000.

[54] A. C. Larsen, M. Guttormsen, M. Krtička, E. Běták, A. Bürger, A. Görgen, H. T. Nyhus, J. Rekstad, A. Schiller, S. Siem, H. K. Toft, G. M. Tveten, A. V. Voinov, and K. Wikan. Analysis of possible systematic errors in the Oslo method. *Phys. Rev. C*, 83:034315, 2011.

[55] A Spyrou, S N Liddick, A C Larsen, M Guttormsen, K Cooper, A C Dombos, D J Morrissey, F Naqvi, G Perdikakis, S J Quinn, T Renstrøm, J A Rodriguez, A Simon, C S Sumithrarachchi, and R G T Zegers. Novel technique for Constraining r-Process (n, γ) Reaction Rates. *Phys. Rev. Lett.*, 113:232502, 2014.

[56] J. E. Escher, J. T. Burke, R. O. Hughes, N. D. Scielzo, R. J. Casperson, S. Ota, H. I. Park, A. Saastamoinen, and T. J. Ross. Constraining Neutron Capture Cross Sections for Unstable Nuclei with Surrogate Reaction Data and Theory. *Phys. Rev. Lett.*, 121(5):52501, 2018.

[57] H. Utsunomiya, S. Goriely, H. Akimune, H. Harada, F. Kitatani, S. Goko, H. Toyokawa, K. Yamada, T. Kondo, O. Itoh, M. Kamata, T. Yamagata, Y.-W. Lui, I. Daoutidis,

D.P. Arteaga, S. Hilaire, and A.J. Koning. γ-ray strength function method and its application to 107 Pd. *Phys. Rev. C*, 82:064610, 2010.

[58] H. Utsunomiya, S. Goriely, T. Kondo, C. Iwamoto, H. Akimune, T. Yamagata, H. Toyokawa, H. Harada, F. Kitatani, Y. W. Lui, A. C. Larsen, M. Guttormsen, P. E. Koehler, S. Hilaire, S. Péru, M. Martini, and A. J. Koning. Photoneutron cross sections for Mo isotopes: A step toward a unified understanding of (γ,n) and (n,γ) reactions. *Phys. Rev. C*, 88(1):015805, 2013.

[59] D. J. Morrissey, B. M. Sherrill, M. Steiner, A. Stolz, and I. Wiedenhoever. Commissioning the A1900 projectile fragment separator. *Nucl. Instr. Meth. Phys. Res. B*, 204:90–96, 2003.

[60] A. Simon, S. J. Quinn, A. Spyrou, A. Battaglia, I. Beskin, A. Best, B. Bucher, M. Couder, P. A. Deyoung, X. Fang, J. Görres, A. Kontos, Q. Li, S. N. Liddick, A. Long, S. Lyons, K. Padmanabhan, J. Peace, A. Roberts, D. Robertson, K. Smith, M. K. Smith, E. Stech, B. Stefanek, W. P. Tan, X. D. Tang, and M. Wiescher. SuN: Summing NaI(Tl) gamma-ray detector for capture reaction measurements. *Nucl. Instr. Meth. Phys. Res. A*, 703:16, 2013.

[61] M. S. Basunia. Nuclear Data Sheets for A = 237. *Nuclear Data Sheets*, 107(8):2323–2422, 2006.

[62] F. G. Kondev and S. Lalkovski. Nuclear Data Sheets for A = 207. *Nuclear Data Sheets*, 112(3):707–853, 2011.

[63] E. Browne and J. K. Tuli. Nuclear Data Sheets for A = 137. *Nuclear Data Sheets*, 108(10):2173–2318, 2007.

[64] R.G. Helmer. Nuclear Data Sheets for A = 60. *Nuclear Data Sheets*, 114(12):51849–2022, 2013.

[65] M. J. Martin. Nuclear Data Sheets for A = 208. *Nuclear Data Sheets*, 108(8):1583–1806, 2007.

[66] B. Singh and A.R. Farhan. Nuclear Data Sheets for A=74. *Nuclear Data Sheets*, 107(7):1923–2102, 2006.

[67] K. Abusaleem and B. Singh. Nuclear Data Sheets for A=71. *Nuclear Data Sheets*, 112:113, 2011.

[68] D. Abriola and A.A. Sonzogni. Nuclear Data Sheets for A = 72. *Nuclear Data Sheets*, 111(1):1–140, 2010.

[69] M. M. Rajabali, R. Grzywacz, S. N. Liddick, C. Mazzocchi, J. C. Batchelder, T. Baumann, C. R. Bingham, I. G. Darby, T. N. Ginter, S. V. Ilyushkin, M. Karny, W. Królas, P. F. Mantica, K. Miernik, M. Pfützner, K. P. Rykaczewski, D. Weisshaar, and J. A. Winger. β decay of 71,73Co: Probing single-particle states approaching doubly magic 78Ni. *Phys. Rev. C*, 85(3):034326, 2012.

[70] T. Kurtukian-Nieto, J. Benlliure, and K. H. Schmidt. A new analysis method to determine β-decay half-lives in experiments with complex background. *Nucl. Instr. Meth. Phys. Res. A*, 589(3):472–483, 2008.

[71] M. Guttormsen. Matrix Manipulation Program (MAMA), Oslo Method v1.1.2, 2018.

[72] M. Guttormsen, A. C. Larsen, A. Görgen, T. Renstrøm, S. Siem, T. G. Tornyi, and G. M. Tveten. Validity of the Generalized Brink-Axel Hypothesis in Np 238. *Phys. Rev. Lett.*, 116:012502, 2016.

[73] J. Allison, K. Amako, J. Apostolakis, P. Arce, M. Asai, T. Aso, E. Bagli, A. Bagulya, S. Banerjee, G. Barrand, B. R. Beck, A. G. Bogdanov, D. Brandt, J. M.C. Brown, H. Burkhardt, Ph Canal, D. Cano-Ott, S. Chauvie, K. Cho, G. A.P. Cirrone, G. Cooperman, M. A. Cortés-Giraldo, G. Cosmo, G. Cuttone, G. Depaola, L. Desorgher, X. Dong, A. Dotti, V. D. Elvira, G. Folger, Z. Francis, A. Galoyan, L. Garnier, M. Gayer, K. L. Genser, V. M. Grichine, S. Guatelli, P. Guèye, P. Gumplinger, A. S. Howard, I. Hřivnáčová, S. Hwang, S. Incerti, A. Ivanchenko, V. N. Ivanchenko, F. W. Jones, S. Y. Jun, P. Kaitaniemi, N. Karakatsanis, M. Karamitrosi, M. Kelsey, A. Kimura, T. Koi, H. Kurashige, A. Lechner, S. B. Lee, F. Longo, M. Maire, D. Mancusi, A. Mantero, E. Mendoza, B. Morgan, K. Murakami, T. Nikitina, L. Pandola, P. Paprocki, J. Perl, I. Petrović, M. G. Pia, W. Pokorski, J. M. Quesada, M. Raine, M. A. Reis, A. Ribon, A. Ristić Fira, F. Romano, G. Russo, G. Santin, T. Sasaki, D. Sawkey, J. I. Shin, I. I. Strakovsky, A. Taborda, S. Tanaka, B. Tomé, T. Toshito, H. N. Tran, P. R. Truscott, L. Urban, V. Uzhinsky, J. M. Verbeke, M. Verderi, B. L. Wendt, H. Wenzel, D. H. Wright, D. M. Wright, T. Yamashita, J. Yarba, and H. Yoshida. Recent developments in GEANT4. *Nucl. Instr. Meth. Phys. Res. A*, 835:186–225, 2016.

[74] R.P. de Groote, J. Billowes, C. L. Binnersley, S. Franchoo, K. T. Flanagan, S. Rothe, R. P. de Groote, K. M. Lynch, K. D. A. Wendt, T. Day Goodacre, F. Nowacki, Y. Tsunoda, A. R. Vernon, T. Otsuka, M. L. Bissell, R. F. Garcia Ruiz, X. F. Yang, T. E. Cocolios, H. H. Stroke, . Koszorús, S. G. Wilkins, Z. Y. Xu, D. V. Fedorov, G. Neyens, and G. J. Farooq-Smith. Dipole and quadrupole moments of Cu7378 as a test of the robustness of the Z=28 shell closure near Ni78. *Physical Review C*, 96(4):041302(R), 2017.

[75] K.T. Flanagan, P. Vingerhoets, M.L. Bissell, K. Blaum, B.A. Brown, B. Cheal, M. De Rydt, D.H. Forest, C. Geppert, M. Honma, M. Kowalska, J. Krämer, A. Krieger, E. Mané, R. Neugart, G. Neyens, W. Nörtershäuser, M. Schug, H.H. Stroke, and D.T. Yordanov. Experimental determination of an I $\pi = 2$ ground state in 72,74 Cu. *Phys. Rev. C*, 82:041302(R), 2010.

[76] A.M. Goryachev and G.N. Zalesnyy. The studying of the photoneutron reactions cross sections in the region of the giant dipole resonance in zinc, germanium, selenium, and strontium isotopes. *Voprosy Teoreticheskoy i Yadernoy Fiziki*, 8:121, 1982.

[77] S. N. Liddick, A. Spyrou, B. P. Crider, F. Naqvi, A. C. Larsen, M. Guttormsen, M. Mumpower, R. Surman, G. Perdikakis, D. L. Bleuel, A. Couture, L. Crespo Campo, A. C. Dombos, R. Lewis, S. Mosby, S. Nikas, C. J. Prokop, T. Renstrom, B. Rubio, S. Siem, and S. J. Quinn. Experimental Neutron Capture Rate Constraint Far from Stability. *Phys. Rev. Lett.*, 116:242502, 2016.

[78] W. Dilg, W. Schantl, H. Vonach, and M. Uhl. Level density parameters for the Back-Shifted Fermi Gas model in the mass range 40¡A¡250. *Nuclear Physics, Section A*, 217(2):269–298, 1973.

[79] A.V. Ignatyuk, J.L. Weil, S. Raman, and S. Kahane. Density of discrete levels in 116Sn. *Phys. Rev. C*, 47:1504, 1993.

[80] S. Goriely. Radiative neutron captures by neutron-rich nuclei and the r-process nucleosynthesis. *Phys. Lett. B*, 436:10–18, 1998.

[81] M. Herman, R. Capote, B. V. Carlson, P. Obložinský, M. Sin, A. Trkov, H. Wienke, and V. Zerkin. EMPIRE: Nuclear Reaction Model Code System for Data Evaluation. *Nuclear Data Sheets*, 108:2655, 2007.

[82] T. Rauscher and F.-K. Thielemann. Astrophysical Reaction Rates From Statistical Model Calculations. *At. Data Nucl. Data Tables*, 75:1, 2000.

[83] T. Rauscher and F.-K. Thielemann. *Stellar Evolution, Stellar Explosions, and Galactic Chemical Evolution*. IOP, Bristol, 1998.

[84] T. Kawano, R. Capote, S. Hilaire, and P. Chau Huu-Tai. Statistical Hauser-Feshbach theory with width-fluctuation correction including direct reaction channels for neutron-induced reactions at low energies. *Phys. Rev. C*, 94:014612, 2016.

[85] S. I. Al-Quraishi, S. M. Grimes, T. N. Massey, and D. A. Resler. Are the level densities for r - and rp -process nuclei different from nearby nuclei in the valley of stability? *Phys. Rev. C*, 63(6):065803, 2001.

[86] D. Savran, T. Aumann, and A. Zilges. Experimental studies of the Pygmy Dipole Resonance. *Prog. Part. Nucl. Phys.*, 70:210, 2013.

[87] M. Beard, E. Uberseder, R. Crowter, and M. Wiescher. Comparison of statistical model calculations for stable isotope neutron capture. *Phys. Rev. C*, 90:034619, 2014.

[88] R. Capote, S. Hilaire, O. Iwamoto, T. Kawano, and M. Sin. Inter-comparison of Hauser-Feshbach model codes toward better actinide evaluations. *EPJ Web of Conferences*, 146:12034, 2017.

[89] E. Uberseder, T. Adachi, T. Aumann, S. Beceiro-Novo, K. Boretzky, C. Caesar, I. Dillmann, O. Ershova, A. Estrade, F. Farinon, J. Hagdahl, T. Heftrich, M. Heil, M. Heine, M. Holl, A. Ignatov, H. T. Johansson, N. Kalantar, C. Langer, T. Le Bleis, Yu A. Litvinov, J. Marganiec, A. Movsesyan, M. A. Najafi, T. Nilsson, C. Nociforo, V. Panin, S. Pietri, R. Plag, A. Prochazka, G. Rastrepina, R. Reifarth, V. Ricciardi, C. Rigollet,

D. M. Rossi, D. Savran, H. Simon, K. Sonnabend, B. Streicher, S. Terashima, R. Thies, Y. Togano, V. Volkov, F. Wamers, H. Weick, M. Weigand, M. Wiescher, C. Wimmer, N. Winckler, and P. J. Woods. First experimental constraint on the 59Fe(n,γ)60Fe reaction cross section at astrophysical energies via the coulomb dissociation of 60Fe. *Phys. Rev. Lett.*, 112:1211101, 2014.

[90] O. Iwamoto. Development of a Comprehensive Code for Nuclear Data Evaluation, CCONE, and Validation Using Neutron-Induced Cross Sections for Uranium Isotopes. *J. of Nucl. Science and Tech.*, 44:687, 2007.

[91] V.A. Plujko, O.M. Gorbachenko, E.V. Kulich, V.M. Bondar, and O.I. Davidovskaya. Testing simple models of E1 radiative strength functions. In *Proceedings of Science*, page PSF07, 2008.

[92] B. Singh. Nuclear Data Sheets for A = 73. *Nuclear Data Sheets*, 101:193, 2004.

[93] J. Van De Walle, F. Aksouh, T. Behrens, V. Bildstein, A. Blazhev, J. Cederkäll, E. Clément, T. E. Cocolios, T. Davinson, P. Delahaye, J. Eberth, A. Ekström, D. V. Fedorov, V. N. Fedosseev, L. M. Fraile, S. Franchoo, R. Gernhauser, G. Georgiev, D. Habs, K. Heyde, G. Huber, M. Huyse, F. Ibrahim, O. Ivanov, J. Iwanicki, J. Jolie, O. Kester, U. Köster, T. Kröll, R. Krücken, M. Lauer, A. F. Lisetskiy, R. Lutter, B. A. Marsh, P. Mayet, O. Niedermaier, M. Pantea, R. Raabe, P. Reiter, M. Sawicka, H. Scheit, G. Schrieder, D. Schwalm, M. D. Seliverstov, T. Sieber, G. Sletten, N. Smirnova, M. Stanoiu, I. Stefanescu, J. C. Thomas, J. J. Valiente-Dobón, P. Van Duppen, D. Verney, D. Voulot, N. Warr, D. Weisshaar, F. Wenander, B. H. Wolf, and M. Zielińska. Low-energy Coulomb excitation of neutron-rich zinc isotopes. *Phys. Rev. C*, 79:014309, 2009.

[94] T. Kawano, P. Talou, M.B. Chadwick, and T. Watanabe. Monte Carlo Simulation for Particle and -Ray Emissions in Statistical Hauser-Feshbach Model. *J. of Nucl. Science and Tech.*, 47:462, 2010.

[95] P. A. Moldauer. Statistics and the average cross section. *Nuclear Physics A*, 344:185–195, 1980.

[96] T. Kawano and P. Talou. Numerical simulations for low energy nuclear reactions to validate statistical models. *Nuclear Data Sheets*, 118(1):183–186, 2014.

[97] S. Hilaire, C. Lagrange, and A.J. Koning. Comparisons between various width fluctuation correction factors for compound nucleus reactions. *Annals of Physics*, 306(2):209–231, 2003.

[98] I. Stefanescu, D. Pauwels, N. Bree, T. E. Cocolios, J. Diriken, S. Franchoo, M. Huyse, O. Ivanov, Y. Kudryavtsev, N. Patronis, J. Van De Walle, P. Van Duppen, and W. B. Walters. Evidence for a β-decaying 1/2- isomer in 71Ni. *Phys. Rev. C*, 79(4):044325, 2009.

[99] G. Gürdal and E. A. McCutchan. Nuclear Data Sheets for A=70. *Nuclear Data Sheets*, 136:1–162, 2016.

[100] D. M. Rossi, P. Adrich, F. Aksouh, H. Alvarez-Pol, T. Aumann, J. Benlliure, M. Böhmer, K. Boretzky, E. Casarejos, M. Chartier, A. Chatillon, D. Cortina-Gil, U. Datta Pramanik, H. Emling, O. Ershova, B. Fernandez-Dominguez, H. Geissel, M. Gorska, M. Heil, H. T. Johansson, A. Junghans, A. Kelic-Heil, O. Kiselev, A. Klimkiewicz, J. V. Kratz, R. Krücken, N. Kurz, M. Labiche, T. Le Bleis, R. Lemmon, Yu A. Litvinov, K. Mahata, P. Maierbeck, A. Movsesyan, T. Nilsson, C. Nociforo, R. Palit, S. Paschalis, R. Plag, R. Reifarth, D. Savran, H. Scheit, H. Simon, K. Sümmerer, A. Wagner, W. Walua, H. Weick, and M. Winkler. Measurement of the dipole polarizability of the unstable neutron-rich nucleus 68Ni. *Phys. Rev. Lett.*, 111(24):1–6, 2013.

[101] O. Wieland, A. Bracco, F. Camera, R. Avigo, H. Baba, N. Nakatsuka, T. Aumann, S. R. Banerjee, G. Benzoni, K. Boretzky, C. Caesar, S. Ceruti, S. Chen, F. C. L. Crespi, V. Derya, P. Doornenbal, N. Fukuda, A. Giaz, K. Ieki, N. Kobayashi, Y. Kondo, S. Koyama, T. Kubo, M. Matsushita, B. Million, T. Motobayashi, T. Nakamura, M. Nishimura, H. Otsu, T. Ozaki, A. T. Saito, H. Sakurai, H. Scheit, F. Schindler, P. Schrock, Y. Shiga, M. Shikata, S. Shimoura, D. Steppenbeck, T. Sumikama, S. Takeuchi, R. Taniuchi, Y. Togano, J. Tscheuschner, J. Tsubota, H. Wang, K. Wimmer, and K. Yoneda. Low-lying dipole response in the unstable 70Ni nucleus. *Phys. Rev. C*, 98(6):064313, 2018.

[102] M. M. Rajabali, R. Grzywacz, S. N. Liddick, C. Mazzocchi, J. C. Batchelder, T. Baumann, C. R. Bingham, I. G. Darby, T. N. Ginter, S. V. Ilyushkin, M. Karny, W. Królas, P. F. Mantica, K. Miernik, M. Pfützner, K. P. Rykaczewski, D. Weisshaar, and J. A. Winger. β decay of72Co and microsecond isomers in even-mass neutron-rich nickel isotopes. *Journal of Physics G*, 41(11), 2014.

[103] A. I. Morales, G. Benzoni, H. Watanabe, S. Nishimura, F. Browne, R. Daido, P. Doornenbal, Y. Fang, G. Lorusso, Z. Patel, S. Rice, L. Sinclair, P. A. Söderström, T. Sumikama, J. Wu, Z. Y. Xu, A. Yagi, R. Yokoyama, H. Baba, R. Avigo, F. L. Bello Garrote, N. Blasi, A. Bracco, F. Camera, S. Ceruti, F. C.L. Crespi, G. De Angelis, M. C. Delattre, Zs Dombradi, A. Gottardo, T. Isobe, I. Kojouharov, N. Kurz, I. Kuti, K. Matsui, B. Melon, D. Mengoni, T. Miyazaki, V. Modamio-Hoyborg, S. Momiyama, D. R. Napoli, M. Niikura, R. Orlandi, H. Sakurai, E. Sahin, D. Sohler, H. Shaffner, R. Taniuchi, J. Taprogge, Zs Vajta, J. J. Valiente-Dobón, O. Wieland, and M. Yalcinkaya. Low-lying excitations in Ni 72. *Phys. Rev. C*, 93:034328, 2016.

[104] E. A. McCutchan. Nuclear Data Sheets for A=68. *Nuclear Data Sheets*, 113:1735–1870, 2012.

[105] J. C. Hardy, L. C. Carraz, B. Jonson, and P. G. Hansen. The essential decay of pandemonium: A demonstration of errors in complex beta-decay schemes. *Physics Letters B*, 71(2):307–310, 1977.

[106] B. Rubio, W. Gelletly, E. Nácher, A. Algora, J. L. Taín, A. Pérez, and L. Caballero. Beta decay studies with the total absorption technique: Past, present and future. *Journal of Physics G: Nuclear and Particle Physics*, 31(10):S1477, 2005.

[107] M. Wang, G. Audi, F.G. Kondev, W.J. Huang, S. Naimi, and X. Xu. The Ame2016 atomic mass evaluation. *Chinese Physics C*, 41:030003, 2017.

[108] A. Spyrou, A. C. Larsen, S. N. Liddick, F. Naqvi, B. P. Crider, A. C. Dombos, M. Guttormsen, D. L. Bleuel, A. Couture, L. Crespo Campo, R. Lewis, S. Mosby, M. R. Mumpower, G. Perdikakis, C. J. Prokop, S. J. Quinn, T. Renstrøm, S. Siem, and R. Surman. Neutron-capture rates for explosive nucleosynthesis: the case of 68Ni(n, γ)69Ni. *Journal of Physics G*, 44:044002, 2017.

[109] R. Schwengner, S. Frauendorf, and B. A. Brown. Low-Energy Magnetic Dipole Radiation in Open-Shell Nuclei. *Physical Review Letters*, 118(9):092502, 2017.